

High-impedance circuit quantum electrodynamics with semiconductor quantum dots

Inauguraldissertation

zur

Erlangung der Würde eines Doktors der Philosophie
vorgelegt der
Philosophisch-Naturwissenschaftlichen Fakultät
der Universität Basel

von

Jann Hinnerk Ungerer

2023

Originaldokument gespeichert auf dem Dokumentenserver der
Universität Basel edoc.unibas.ch

Genehmigt von der Philosophisch-Naturwissenschaftlichen Fakultät
auf Antrag von
Erstbetreuer:
Prof. Dr. Christian Schönenberger
Zweitbetreuer:
Prof. Dr. Martino Poggio
externe Experten:
Prof. Dr. Ferdinand Kuemmeth, Prof. Dr. Jason Petta

Basel, den 13.12.2022

Prof. Dr. Marcel Mayor
Dekan

Für meine Tochter Juliane

Contents

1. Introduction	1
1.1. Outline of this thesis	3
2. Combining superconducting resonators with semiconductor quantum dots	5
2.1. Light-matter interaction	5
2.1.1. Quantum Rabi and Jaynes-Cummings model . . .	5
2.2. Photons in superconducting resonators	7
2.2.1. LC harmonic oscillator	8
2.2.2. Resonator impedance	9
2.2.3. Josephson-junction and SQUID array resonator . .	9
2.2.4. Transmission line resonator	15
2.2.5. Kinetic inductance	16
2.2.6. Resonance lineshapes	18
2.3. Double quantum dots	22
2.3.1. Material platforms	23
2.3.2. Charge-stability diagram	26
2.3.3. Charge and spin qubits	29
3. Designing high-impedance microwave circuits	37
3.1. Spurious modes	37
3.2. Losses through the dc lines connected to the device	38
3.3. Losses through the tap	39
3.3.1. QUCS simulations	41
3.3.2. Sonnet simulations	43
3.4. Designing the coupling capacitor	45
3.5. Cryogenic microwave setup	47
4. The effect of dielectrics on the quality of high-impedance resonators	51
4.1. Introduction	53
4.2. Experimental setup	54

4.3. Sample preparation	56
4.4. Determining loss due to two-level fluctuators	58
4.5. Resonator stability at elevated temperatures and fields	62
4.6. Conclusions	65
5. Charge noise protection and ultrastrong coupling	67
5.1. Introduction	70
5.2. Double quantum dot charge qubit	72
5.3. Increasing charge qubit coherence	79
5.4. Ultrastrong coupling with a junction array resonator	86
5.5. Conclusions	88
6. Charge-sensing of a GeSi nanowire double quantum dot	91
6.1. Introduction	93
6.2. Device description	95
6.3. Charge sensing	97
6.4. Conclusions	104
7. Dispersive interaction between a crystal-phase defined double quantum dot and a microwave photon	107
7.1. Device description	108
7.2. Device characterization	109
7.3. From double-dot to single dot	111
7.4. Resonator response versus tunnel rate.	112
7.5. Bloch-Siegert shift in the strong dispersive regime	116
7.6. Entering the resonant regime	117
7.7. Conclusions and Outlook	118
8. Strong coupling between a single photon and a singlet-triplet qubit	121
8.1. Introduction	124
8.2. Device characterization	125
8.3. Strong spin-photon coupling	128
8.4. Magneto spectroscopy	130
8.5. Conclusion and Outlook	134
9. Conclusions and Outlook	137
9.1. Outlook	139

Bibliography	141
A. Fabrication protocols	157
A.1. Fabrication of resonator devices with GaAs dots	157
A.2. Fabrication of high-impedance NbTiN resonators	157
A.2.1. Wafer characteristics	157
A.2.2. Cleaning of wafer with capping layer	157
A.2.3. Cleaning of wafer without capping layer	158
A.2.4. Sputtering	158
A.2.5. Two-step e-beam lithography	159
A.2.6. Dry-etching	160
A.2.7. Resist removal	160
A.3. Fabrication of nanowire devices	161
A.3.1. Fabrication of Ge/Si core/shell nanowire device . .	161
A.3.2. Fabrication of InAs nanowire device	161
B. Supplementary information: Designing high-impedance microwave circuits	163
B.1. Designing the coupling capacitor	163
B.2. Alternative measurement setup	164
C. Supplementary information: The effect of dielectrics on the quality of high-impedance resonators	167
C.1. Investigation of sputtering parameters	167
C.2. Frequency shift in power dependence	169
D. Supplementary information: Charge noise protection and ultra-strong coupling	171
D.1. Determining the system capacitances	171
D.2. Considerations about definition of dipole strength η . . .	177
D.3. Detuning sensitivity to charge and voltage fluctuations . .	178
D.4. SQUID and junction array high impedance resonators . .	180
D.5. Dissipative dynamics of DQD and resonator	181
D.5.1. Hamiltonian	183
D.5.2. Dissipative processes	183
D.5.3. SLH model - driven, dissipative dynamics of DQD and resonator	184
D.5.4. Visibility of vacuum Rabi splitting	185

D.5.5. Fits	186
D.6. System Cooperativity	186
D.7. Renormalization of the coupling strengths (Eq. 5.13)	187
D.8. Additional data	189
E. Supplementary information: Charge-sensing of a GeSi nanowire double quantum dot	193
E.1. Additional data	193
F. Supplementary information: Dispersive interaction between a crystal-phase defined double quantum dot and a microwave photon	195
F.1. Bias triangle	195
F.2. Extracted capacitances of five inter-dot configurations	195
G. Strong coupling between a single photon and a singlet-triplet qubit	197
G.1. Resonator characterization and analysis	197
G.2. Charge parity determination	199
G.3. Jaynes-Cummings model	200
G.4. Effective two-electron Hamiltonian model	201
G.5. Hamiltonian in the odd charge parity	203
G.6. Singlet-triplet hybridization at low fields	204
G.7. Linear dependence between tunnel rate and linewidth	207
Curriculum Vitae	209
Publications	211
Acknowledgements	215

1 Introduction

We live exciting times in which several quantum bit (qubit) hardware implementations are in competition for a useful quantum computer. Among other quantum technologies based on trapped ions, solid-state qubit platforms based on semiconductor quantum dots and superconducting circuits are the most promising contenders for building a scalable hardware platform [1, 2].

In semiconductors, the charge or spin degree of freedom of a single electron or hole in a quantum dot is used to form a qubit [3]. The advantages of these qubits include their small footprint, their potential for fast gate operations and the well established fabrication techniques [3, 4]. In the past decades, some key experiments have showcased single qubit rotations [5, 6] and two-qubit gate operations [7–9] of electron spins in quantum dots. In a state of the art quantum processor based on spins in semiconductors, up to six qubits can already be universally controlled [10], illustrating the rapid development of the field. However, the used entangling gates between semiconductor qubits are short range, limiting scaling up towards larger quantum processors.

A solution for long range qubit entanglement can be obtained in the scope of circuit quantum electrodynamics (QED) [11, 12]. This approach has been very fruitful for the superconducting qubits, where it enabled building of large processors with hundreds of qubits [13]. Combining circuit QED with semiconductor qubits can make use of the advantages of both qubit hardware platforms. But implementing circuit QED techniques with semiconductor qubits is challenging, because of the small electric and magnetic dipole moments of a single electron (or hole) [14, 15].

Nonetheless, early experiments demonstrated a dipolar coupling between the charge [16–20] or spin [21] of a single electron and the microwave field of a superconducting coplanar waveguide resonator. Recently, circuit QED experiments with quantum dots have made a leap and the strong

1

coupling regime between a single microwave photon and a charge qubit was demonstrated [22–24]. Shortly after, similar results were achieved between a single photon and a spin qubit by making use of the magnetic-field gradient of a micromagnet [25, 26] or of the exchange interaction of electrons in a triple quantum dot [27]. In the strong coupling regime, the coupling term is larger than the damping of the individual elements, i.e., the qubit and photon are able to coherently exchange information [12]. Strong coupling therefore constitutes a first step towards implementing a quantum bus enabling entanglement of distant quantum objects [28].

Attempts of implementing entangling gates between distant semiconductor qubits based on circuit QED have resulted in coherent interactions between distant charge and distant spin qubits, both in the resonant and virtual-photon mediated regimes [29–31]. However, the demonstration of an entangling gate between distant semiconductor qubits remains an open challenge, because the coupling strengths of the involved systems are still relatively small compared to the decoherence rates of the qubits. In past experiments that realized distant spin-spin coupling mediated by the microwave field of a superconducting resonator [30, 31], the spin-photon coupling was based on micromagnets resulting in relatively low spin-photon coupling strengths. Moreover, micromagnets complicate scalability because they limit the tunability of the spin-orbit interaction strength and the Landé g -factors.

In this thesis, we attempt to address both the coupling strength between semiconductor qubits and resonator, as well as the scalability of spin-based qubits.

First, the coupling strength fundamentally scales proportionally to the vacuum electric-field fluctuations of the resonator, in turn given by the square root of its impedance [12]. This observation is the main motivation to develop a circuit QED infrastructure based on high-impedance resonators [32], and is therefore one of the main focus points of this thesis. To this end, we engineer a well-characterized circuit QED platform that is compatible with various types of nanowire-based semiconducting qubits incorporating magnetic field resilient, high impedance NbTiN superconducting thin-film resonators.

Second, the coupling of spin qubits to superconducting resonators relies on a hybridization of spin and charge degree of freedom [21, 33, 34]. Therefore, a systematic understanding of the coherence of a charge qubit as well as its coupling to the resonator are essential. Here, we explore how

the coherence time and the charge-photon coupling strength of a GaAs double-quantum dot (DQD) coupled to a high-impedance resonator [35] can be enhanced by engineering the electro-static potential of the DQD.

Third, we address the scalability challenge imposed by the micromagnets by making use of the intrinsic spin-orbit interaction naturally present in semiconductor nanowires.

1.1. Outline of this thesis

The thesis begins in Chapter 2 with an introduction to the fundamental aspects of the various types of high-impedance resonators [32, 36, 37] and the three different material systems used to implement DQDs in this thesis, namely a two-dimensional electron gas in GaAs [38], a Ge/Si core/shell nanowire [39] and an InAs nanowire with a crystal-phase defined DQD [40].

In Chapter 3, we discuss the design considerations when implementing high-impedance, half-wave resonators with semiconductor nanowires and elaborate on the experimental setup.

Superconducting resonators are susceptible to two-level fluctuators that are predominantly present at substrate interfaces and in lossy dielectrics [41], but well-established fabrication protocols of semiconductor nanowires rely on these oxides [21, 42–46]. We therefore investigate the quality of high-impedance NbTiN resonators fabricated in various dielectric configurations and report the results in Chapter 4.

In Chapter 5, we describe experiments performed with a DQD in GaAs coupled to high-impedance resonators [35] based on arrays of Josephson junctions (JJs) [37] or superconducting quantum interference devices (SQUIDs) [36]. We achieve record high charge qubit coherence times and charge-qubit resonator coupling strengths.

After having demonstrated these results that focused on charge qubits with the magnetic field vulnerable resonators, we switch to the integration of magnetic-field resilient, high-impedance NbTiN resonators with DQDs in nanowires with strong spin-orbit interaction. In Chapter 6, we utilise a Ge/Si core/shell nanowire [39] and use the high-impedance resonator for detecting charging and discharging of single holes from the DQD. Thus, we extend charge-sensing protocols in this material system [43, 44, 47, 48] to a regime of low hole occupancy where no current through the DQD can be measured.

Chapter 7 and Chapter 8 focus on the integration of crystal-phase defined DQDs in zincblende InAs nanowires with strong spin-orbit interaction [49] with the magnetic field resilient high-impedance resonators. In Chapter 7, we first explore the charge qubit-photon coupling in the dispersive regime, while in Chapter 8, we make use of the magnetic-field resilience of the resonator by turning on a large magnetic-field. This enables us to operate the DQD as a singlet-triplet qubit, and to measure the coupling to a resonator mode in the single-photon limit.

We draw a conclusion of our results in Chapter 9 where we also provide an outlook. Detailed fabrication protocols are given in Appendix A and additional information for the individual chapters is found in the further appendices.

2 Combining superconducting resonators with semiconductor quantum dots

2.1. Light-matter interaction

This chapter aims on laying the basis for the work presented in later chapters. First, the theoretical framework of dipolar coupling between a quantum light-field and a quantum bit (qubit) is introduced in Section 2.1.1. The consecutive sections introduce the host systems of the light field and the qubit: Section 2.2 explains the working principle of the various types of superconducting resonators hosting single microwave photons that were used in this work, and in Section 2.3 the qubit host, namely semiconductor double-quantum dots (DQDs) are treated.

2.1.1. Quantum Rabi and Jaynes-Cummings model

The Rabi model describes the dipolar interaction between a two-level system (TLS) and a classical radiation field mode [50]. In its quantized version, it is called quantum Rabi model (QRM) and described by the QRM Hamiltonian [51]

$$\mathcal{H}_R = \underbrace{\hbar\omega_r \left(\hat{a}^\dagger \hat{a} + \frac{1}{2} \right)}_{\text{bosonic mode}} + \underbrace{\hbar \frac{\omega_q}{2} \hat{\sigma}_z}_{\text{qubit}} - \underbrace{\vec{d} \cdot \vec{E} \hat{\sigma}_x}_{\text{dipolar interaction}} (\hat{a} + \hat{a}^\dagger) \quad (2.1)$$

As indicated by the brackets, the Hamiltonian consists of three parts. The first part describes a single, quantized bosonic mode with eigenfrequency ω_r , whose annihilation and creation operators are \hat{a} and \hat{a}^\dagger . In this thesis, the bosonic mode is realized by superconducting resonators as described in section 2.2. The second part, describes a TLS (qubit) with transition frequency ω_q which is described as a fermionic spin by the Pauli operators $\hat{\sigma}_{x,y,z}$. In the work presented in this thesis, qubits are realized by

semiconductor QDs which are discussed in detail in section 2.3. Finally, the last term describes the dipolar interaction between the bosonic mode and the qubit. $\vec{E}(\hat{a} + \hat{a}^\dagger)$ are the vacuum electric-field fluctuations of the bosonic mode and \vec{d} is the transition dipole moment of the qubit. The strength of the dipolar interaction is usually characterized by the coupling strength $g = \vec{d} \cdot \vec{E}/\hbar$.

By expressing the dipolar coupling in terms of fermionic ladder operators as $\hat{\sigma}_x = (\hat{\sigma}_+ + \hat{\sigma}_-)/2$, the dipolar energy takes the form

$$\mathcal{H}_{\text{int}} = \hbar g \left[\underbrace{\hat{\sigma}_- \hat{a}^\dagger + \hat{\sigma}_+ \hat{a}}_{\text{resonant}} + \underbrace{\hat{\sigma}_+ \hat{a}^\dagger + \hat{\sigma}_- \hat{a}}_{\text{anti-resonant}} \right]. \quad (2.2)$$

Assuming that the transition frequency of the qubit is similar to the bosonic transition frequency, $\omega_q \approx \omega_r$, the resonant terms, proportional to $\hat{\sigma}_- \hat{a}^\dagger$ and $\hat{\sigma}_+ \hat{a}$, correspond to transitions of states with small energy difference $\hbar|\omega_r - \omega_q|$. The anti-resonant terms, proportional to $\hat{\sigma}_+ \hat{a}^\dagger$ and $\hat{\sigma}_- \hat{a}$, correspond to transitions of states with large energy difference $\hbar|\omega_r + \omega_q|$. If the coupling strength is much smaller than the involved transition frequencies, $g \ll \omega_r, \omega_q$, the mixing of the states with large energy difference is small and the anti-resonant terms can be neglected. This procedure is called rotating-wave approximation and results in the Jaynes-Cummings (JC) Hamiltonian [52]

$$\mathcal{H}_{\text{JC}} = \hbar\omega_r \left(\hat{a}^\dagger \hat{a} + \frac{1}{2} \right) + \hbar \frac{\omega_q}{2} \hat{\sigma}_z + \hbar g (\hat{\sigma}_- \hat{a}^\dagger + \hat{\sigma}_+ \hat{a}). \quad (2.3)$$

Exact diagonalization of the JC Hamiltonian yields the ground state $|\downarrow, 0\rangle$ and the dressed states [12, 53]

$$|+, n\rangle = \cos \theta_n |\uparrow, n\rangle + \sin \theta_n |\downarrow, n+1\rangle \quad (2.4)$$

$$|-, n\rangle = -\sin \theta_n |\uparrow, n\rangle + \cos \theta_n |\downarrow, n+1\rangle \quad (2.5)$$

with corresponding eigenenergies

$$E_{\downarrow, 0} = \hbar \frac{\omega_r - \omega_q}{2} \quad (2.6)$$

$$E_{\pm, n} = (n+1)\hbar\omega_r \pm \frac{\hbar}{2} \sqrt{4g^2(n+1) + (\omega_r - \omega_q)^2} \quad (2.7)$$

In these equations, the argument of the trigonometric function is the mixing angle

$$\theta_n = \frac{1}{2} \tan^{-1} \left(\frac{2g\sqrt{n+1}}{\omega_q - \omega_r} \right). \quad (2.8)$$

The low-energy excitations with $n = 0$ are plotted in Fig. 2.1a). In the experiments described below, we probe the transitions from the ground state to the dressed states involving one photonic excitation. In this case, $n = 0$ and the transition frequencies as plotted in Fig. 2.1b) are given by

$$\omega_t = (E_{\pm,0} - E_{\downarrow,0})/\hbar. \quad (2.9)$$

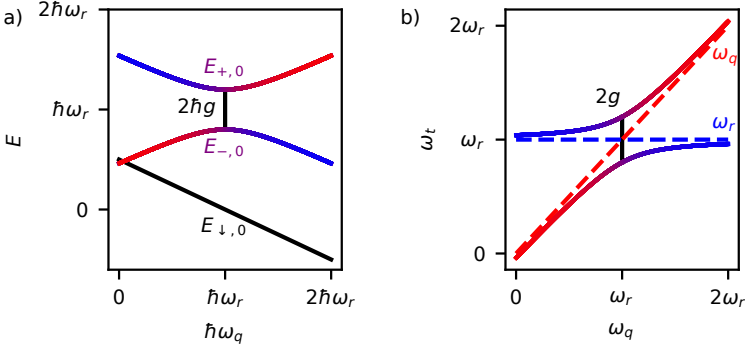


Figure 2.1. Jaynes-Cummings excitations. a) Lowest energy levels according to Eq. (2.6) and Eq. (2.7) with $n = 0$. b) Transition frequencies given by the difference of the energy levels according to Eq. (2.9). Here, a blue color corresponds to an excitation of the resonator and a red color to a qubit excitation.

2.2. Photons in superconducting resonators

In this thesis, photon cavities are realized by high-impedance superconducting resonators whose quantum-mechanical description is elaborated in

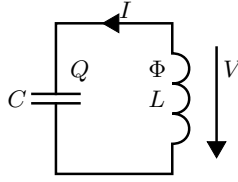


Figure 2.2. Schematic representation of an LC oscillator. The capacitor with capacitance C hosts a charge Q and the inductor with inductance L is threaded by a flux Φ . I denotes the current through the capacitor and V the voltage over the circuit. Q , Φ , I and V are time-dependent quantities.

this section. Section 2.2.1 contains the quantum-mechanical description of an LC circuit and Section 2.2.2 introduces the meaning of the resonator impedance. Then in the following Section 2.2.3 and Section 2.2.4, we elaborate the working principles of the various types of superconducting resonators used throughout this thesis and how they can be mapped onto the LC circuit. Finally Section 2.2.6 discusses the resonance lineshape of the resonators.

2.2.1. LC harmonic oscillator

By connecting a capacitor C and an inductor L in a loop configuration as depicted in Fig. 2.2, the most fundamental resonant circuit is created. A current I passing through the inductor L creates a flux $\Phi = LI$ and leads to a voltage drop $V = -L\dot{I}$. This voltage drops over the parallel capacitor creating a charge $Q = CV$ whose derivative is the current $I = \dot{Q}$. The total energy in the circuit can be separated into a inductive energy $E_L = \Phi^2/2L$ and a charging energy $E_C = Q^2/2C$. We write the Hamiltonian of the system

$$H = E_L + E_C = \frac{\Phi^2}{2L} + \frac{Q^2}{2C} \quad (2.10)$$

and, in analogy to a harmonic pendulum, identify Φ and Q as canonical variables as $\dot{Q} = \partial H/\partial\Phi$ and $\dot{\Phi} = -\partial H/\partial Q$. We can therefore introduce the quantum mechanical operators $\hat{\Phi}$ and \hat{Q} satisfying the commutation

relation $[\hat{\Phi}, \hat{Q}] = i\hbar$. Introducing the annihilation operator

$$\hat{a} = \frac{1}{\sqrt{2\hbar}} \left(\sqrt{\frac{C}{L}} \hat{\Phi} - i\sqrt{\frac{L}{C}} \hat{Q} \right), \quad (2.11)$$

and its hermitian adjoint \hat{a}^\dagger yields the quantum mechanical Hamiltonian of the circuit

$$\hat{H} = \hbar\omega_r \left(\hat{a}^\dagger \hat{a} + \frac{1}{2} \right). \quad (2.12)$$

The Hamiltonian represents the harmonic oscillator with resonance frequency $\omega_r = 1/\sqrt{LC}$. The photon number operator is given by $\hat{a}^\dagger \hat{a}$. Therefore, excitations of the circuit are photons of frequency ω_r .

2.2.2. Resonator impedance

As discussed in section 2.1.1, the light-matter coupling is proportional to both the electric dipole moment of the qubit and the strength of the electric-field fluctuations of the cavity. The typically very small electric dipole of a quantum system therefore calls for maximizing the strength of the vacuum electric field fluctuations, i.e. the vacuum voltage fluctuations on the resonator in the GHz domain. The vacuum voltage fluctuations can be expressed as [12]

$$\delta\hat{V} = \sqrt{\langle V^2 \rangle} = \sqrt{\hbar\omega_r} \sqrt{\frac{L}{C}}. \quad (2.13)$$

Thus, to enhance the coupling between a dipole moment and a resonator with fixed frequency ω_r , the impedance $Z = \sqrt{L/C}$ has to be increased [32, 34]. Resonators with large impedance were realized in several ways in the scope of this thesis. In section 2.2.3 we discuss how Josephson junctions (JJs) and superconducting quantum interference devices (SQUIDs) form circuit-elements of high-impedance resonators. Section 2.2.4 treats transmission line resonators and in particular how to make use of the large kinetic inductance of NbTiN to form a high-impedance resonator.

2.2.3. Josephson-junction and SQUID array resonator

The impedance of a resonator can be made large by exploiting a superconductor based on JJs [37] or SQUIDs [54, 55]. We have incorporated both

of these types of resonators in the experiments described in Chapter 5. The aim of this subsection is providing a fundamental understanding of the microwave properties of JJs and of SQUIDs based on the more lengthy discussion given in the references [56–58].

Josephson effect

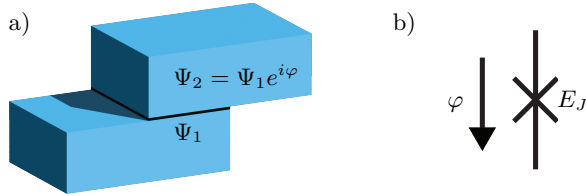


Figure 2.3. Schematic of a Josephson junction. a) Two superconductors (blue) with condensates Ψ_1 and Ψ_2 are tunnel coupled to each other via a thin barrier (black). b) Circuit representation of a JJ with phase drop φ and Josephson energy E_J .

The most important macroscopic manifestation of the quantum coherence of a superconductor is the Josephson effect which is highly important for precision metrology [59, 60] and forms the basis of superconducting quantum computers [61]. The Josephson effect occurs when two superconductors are connected by a tunnel junction as schematically depicted in Fig. 2.3 allowing them to exchange Cooper pairs with each other. Josephson predicted the effect in 1962 and it was experimentally verified shortly after by Anderson and Rowell [62, 63].

A superconducting condensate is described by its wave function

$$\Psi = \sqrt{n_{\text{cp}}} e^{i\phi} , \quad (2.14)$$

where n_{cp} is the density of Cooper pairs. The superconducting wavefunction satisfies the Schrödinger equation

$$i\hbar \frac{\partial \Psi}{\partial t} = \hat{H} \Psi = E \Psi , \quad (2.15)$$

with E as the ground state energy. Considering two superconductors with condensates $\Psi_1 = \sqrt{n_{\text{cp},1}} e^{i\phi_1}$ and $\Psi_2 = \sqrt{n_{\text{cp},2}} e^{i\phi_2}$ being coupled to each

other, the Schrödinger equation reads

$$i\hbar \frac{\partial}{\partial t} \begin{pmatrix} \Psi_1 \\ \Psi_2 \end{pmatrix} = \hat{\mathcal{H}} \begin{pmatrix} \Psi_1 \\ \Psi_2 \end{pmatrix} = \begin{pmatrix} E_1 & T \\ T^* & E_2 \end{pmatrix} \begin{pmatrix} \Psi_1 \\ \Psi_2 \end{pmatrix}, \quad (2.16)$$

where E_1 and E_2 are the ground state energies of the uncoupled condensates and T is (without loss of generality) the real tunneling amplitude between the superconductors. For two identical superconductors, the ground state energies are identical except for an applied potential V between them. In that case, the energy difference between Cooper pairs on either side of the junction is $E_1 - E_2 = 2eV$.

The current I through the junction is given by tunneling of Cooper pairs as the derivative of the Cooper pair density as

$$I = 2e \frac{\partial n_{\text{cp},1}}{\partial t} = -2e \frac{\partial n_{\text{cp},2}}{\partial t}, \quad (2.17)$$

where e is the elementary charge. By using the complex expressions for the two condensates and Eq. (2.16), we find the dc Josephson effect

$$I = \frac{4eT}{\hbar} \sqrt{n_{\text{cp},1} n_{\text{cp},2}} \sin \varphi = I_c \sin \varphi, \quad (2.18)$$

where the maximal value of the non-dissipative current I_c is called the Josephson critical current and $\varphi = \phi_2 - \phi_1$ is the superconducting phase difference.

The Josephson effect arises by considering the evolution of φ which evolves in time as

$$\frac{\partial \varphi}{\partial t} = \frac{E_1 - E_2}{\hbar} = \frac{2e}{\hbar} V. \quad (2.19)$$

Inserting Eq. (2.19) in Eq. (2.18) results in the Josephson relation for the current

$$I(t) = I_c \sin \left(\frac{2e}{\hbar} V t \right). \quad (2.20)$$

A relation between the voltage and the current across the junction is found by combining equations (2.18) and (2.19) to be

$$V = \frac{\hbar}{4e\pi I_c} \frac{1}{\cos \varphi} \dot{I} \quad (2.21)$$

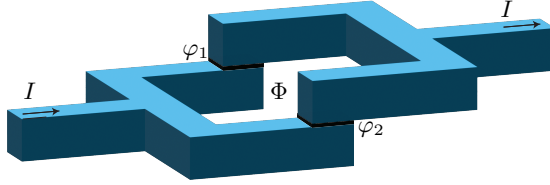


Figure 2.4. Schematic representation of a SQUID. The SQUID is threaded by a flux Φ , while a current I is passed through the device resulting in phase drops across the JJs φ_1 and φ_2 .

This leads to the definition of the specific Josephson inductance close to equilibrium, where $\varphi \approx 0$,

$$L_{\text{JJ}} = \left. \frac{V}{\dot{I}} \right|_{\varphi \approx 0} = \frac{h}{4e\pi I_c} \quad (2.22)$$

Typical critical currents on the order of 100 nA lead to specific inductances of a few pH making it possible to fabricate very compact inductors based on JJs.

Superconducting quantum interference device

A SQUID consists of two JJs in a loop enclosing a magnetic flux Φ as depicted schematically in Fig. 2.4. Analogously to the Aharonov-Bohm effect for electrons, the flux is quantized by the superconducting flux quantum $h/2e$ as

$$\varphi_1 - \varphi_2 = 2\pi \frac{\Phi}{h/2e} \pmod{2\pi}, \quad (2.23)$$

where we assumed that the loop does not contribute any inductance except of the Josephson inductances. Using the IV-characteristic of a JJ, Eq. (2.21), and the Josephson effect, Eq. (2.20), we find

$$I = I_{c1} \sin \varphi_1 + I_{c2} \sin \varphi_2 = I_{c1} \sin \left(\alpha + \frac{2\pi e \Phi}{h} \right) + I_{c2} \sin \left(\alpha - \frac{2\pi e \Phi}{h} \right), \quad (2.24)$$

with an effective phase drop α across the SQUID. When the two junctions support the same critical current, $I_{c1} = I_{c2} = I_c$, the equation simplifies

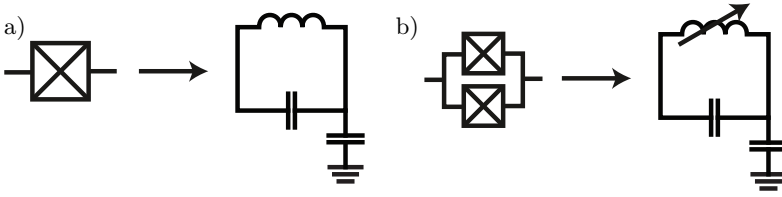


Figure 2.5. LC circuit representation a) Representation of a JJ b) Representation of a SQUID.

to

$$I = 2I_c \cos\left(\frac{2\pi e\Phi}{h}\right) \sin \alpha, \quad (2.25)$$

which is the analogy of the Josephson effect for a single junction with a modified critical current

$$I_c^{\text{SQUID}} = 2I_c \left| \cos\left(\pi \frac{2e\Phi}{h}\right) \right|. \quad (2.26)$$

In analogy to the JJ, this leads to the definition of the inductance of a single SQUID

$$L_{\text{SQUID}} = \frac{1}{2} L_{\text{JJ}} \left| \cos\left(\pi \frac{2e\Phi}{h}\right) \right| \quad (2.27)$$

which is half of the inductance of a single junction for an external flux $\Phi \approx 0$ and can be reduced further by applying an external flux Φ .

Circuit representation of Josephson-junction and SQUID array

In the experiments, presented in Chapter 5, two types of resonators are implemented. They consist of linear arrays of JJs and/or SQUIDs connected in series with each other [23, 36, 37, 54]. The aim of this subsection is to provide an understanding of the behavior of JJ-arrays and SQUID-arrays in a regime of low photon excitations.

Close to equilibrium with currents well below the critical current of the JJ, a linear approximation of the inductance can be assumed and it is then given by Eq. (2.22). When realizing a JJ as a circuit element, a stray capacitance between the superconducting leads of the JJ such as to the ground is formed. Therefore, the single JJ has to be treated as a parallel

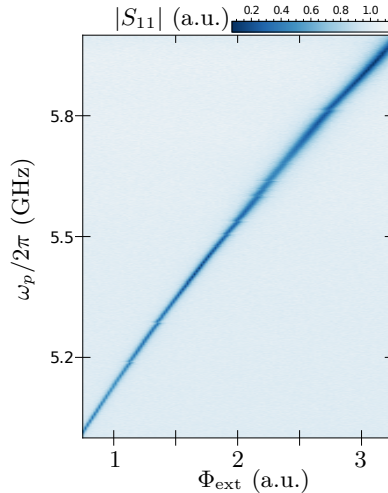


Figure 2.6. Resonance dip of a SQUID-array resonator. Plot showing the reflection amplitude $|S_{11}|$ as a function of probe frequency ω_p and externally applied flux. The SQUID-array resonance is clearly visible as a dip and its resonance frequency changes as a function of applied flux.

LC circuit as depicted in Fig. 2.5. Similarly, a single SQUID forms an LC circuit with a flux-tunable inductor.

A linear array of N JJs or SQUIDs can be treated as N coupled LC harmonic oscillators. The array, hence hosts N normal modes with effective mode inductances L_k and mode capacitances C_k [36, 64]. In the experiments presented below, we restrict ourselves to microwave excitations close to the fundamental frequency $\omega_0 = 1/\sqrt{L_0 C_0}$. This allows us to quantize the circuit as described in section 2.2.1. Restricting the excitation to a few photons being distributed across the array, in return justifies the treatment of the Josephson elements as linear inductors. Fig. 2.6 shows the resonance dip of a SQUID-array resonator probed in reflection. Its resonance frequency is changing as a function of externally applied flux, illustrating the flux-tunable inductance of the SQUID.

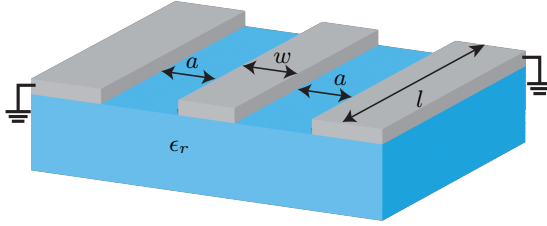


Figure 2.7. Schematic of transmission line resonator. The schematic shows a half-wave coplanar transmission line resonator with length l , center conductor width w and gap width a on a substrate with a relative permittivity ϵ_r .

2.2.4. Transmission line resonator

The experiments being described in Chapters 4, 6, 7 and 8 rely on coplanar waveguide (CPW) transmission line resonators based on NbTiN. A CPW consist of a center conductor with width w separated from the ground plane located in the same plane by a distance a as depicted in Fig. 2.7. By interrupting the center conductor on either side, a resonator of length l is formed. For a CPW resonator, the relevant wavelengths of the microwave signals are comparable to the resonator length. Therefore, in order to describe a CPW resonator in terms of a lumped element description, the resonator has to be subdivided into N segments as depicted in Fig. 2.8. Each segment of length $\Delta_x = l/N$ has a finite capacitance to ground $\Delta_x C_l$ and series inductance $\Delta_x L_l$ where we have introduced the line capacitance C_l and line inductance L_l . For a perfect transmission line, the number N tends to infinity. The description in terms of lumped elements allows us once again to find the N normal modes and, when restricting ourselves to the fundamental mode, to quantize the circuit as described in section 2.2.1. The resonance frequency is thereby given by

$$\omega_0^{\lambda/2} = \frac{1}{2l\sqrt{L_l C_l}}, \quad (2.28)$$

if both ends of the resonator have the same boundary condition, either a short to ground or an open end, a half-wave resonator is formed. For a CPW, analytic equations for the geometric contributions to the line

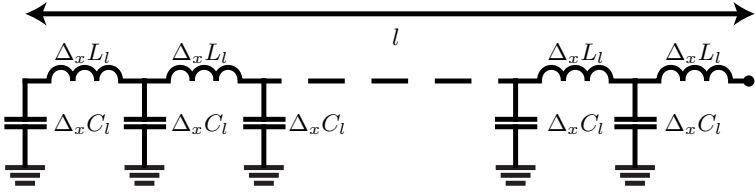


Figure 2.8. Lumped element representation of a transmission line resonator. The transmission line is subdivided into N sections of length $\Delta_x = l/N$. Each segment has an inductance $\Delta_x L_l$ and a capacitance $\Delta_x C_l$.

capacitance C_l^{geo} and line inductance L_l^{geo} can be found in Ref. [65] to be

$$C_l^{\text{geo}} = 2\epsilon_0 (1 + \epsilon_r) \frac{K[k]}{K[\sqrt{1-k^2}]}, \quad L_l^{\text{geo}} = \frac{\mu_0}{4} \frac{K[k]}{K[\sqrt{1-k^2}]}. \quad (2.29)$$

ϵ_0 describes the vacuum permittivity, ϵ_r is the relative permittivity of the substrate and μ_0 is the vacuum permeability. $K(k)$ denotes the complete elliptic integral of the first kind of the ratio of center conductor width and distance to the ground plane $k = w/(w + 2a)$. A simple approximation of the complete elliptic integral of the first kind is given by [66]

$$\frac{K[k]}{K[\sqrt{1-k^2}]} = \begin{cases} \frac{\pi}{\ln \left[2(1 + \sqrt[4]{1-k^2}) / (1 - \sqrt[4]{1-k^2}) \right]} & , \text{ if } 0 \leq k \leq 0.707 \\ \frac{1}{\pi} \ln \left[2(1 + \sqrt{k}) / (1 - \sqrt{k}) \right] & , \text{ if } 0.707 < k \leq 1. \end{cases} \quad (2.30)$$

2.2.5. Kinetic inductance

Another contribution to the inductance of a coplanar waveguide resonator lies in the inertial mass of mobile charge carriers in the superconductor. This so called kinetic inductance L_{kin} has to be added to the geometrical inductance and can be much larger than latter, hence enhancing the impedance of the resonator. The kinetic inductance is calculated by equating the total kinetic energy density of the Cooper pairs $2mv^2 n_{\text{cp}}/2$ with an equivalent inductive energy density $L_{\text{kin}} i_{\text{sc}}^2/2$. Here $2mv^2$ is the kinetic energy of a single Cooper pair, n_{cp} is the Cooper pair density and

i_{sc} describes the supercurrent density. Using BCS theory, the sheet kinetic inductance at zero temperature is found to be [56]

$$L_{\text{kin}}^{\text{sq}}(0) = \frac{R_{\text{sq}}h}{2\pi^2\Delta_0}, \quad (2.31)$$

where h is the Planck constant, R_{sq} denotes the normal state sheet resistance and Δ_0 is the superconducting gap at zero temperature.

The temperature dependence of the kinetic inductance L_{kin} is found using Mattis-Bardeen formula in the low frequency limit, $\hbar\omega < k_B T$ [56], where k_B is the Boltzmann constant. ω denotes the probe frequency and T the temperature. From this formula, the kinetic inductance per square is found to be [68]

$$L_{\text{kin}}^{\text{sq}}(T) = \frac{R_{\text{sq}}h}{2\pi^2\Delta} \frac{1}{\tanh\left(\frac{\Delta}{2k_B T}\right)}. \quad (2.32)$$

Here, the superconducting gap depends on temperature $\Delta = \Delta(T)$. NbTiN is a highly resistive metal which, when being cooled to a temperature $T < T_c$, forms a superconductor in the dirty limit, i.e., a mean free path shorter than coherence length, in the local regime, i.e., with the penetration length larger than coherence length [67]. The superconducting gap

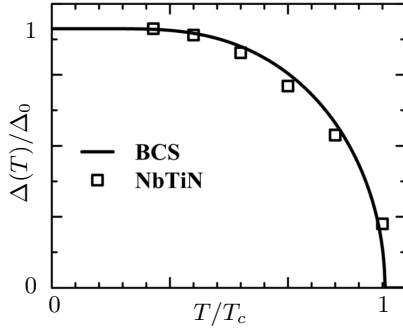


Figure 2.9. Temperature dependence of the superconducting gap of NbTiN. Squares represent experimentally determined values and the curve is derived from Bardeen–Cooper–Schrieffer (BCS) theory. Figure adapted from [67].

at zero temperature of NbTiN is $\Delta(0) = 1.86k_B T_c$ [67]. With increasing temperature, the superconducting gap $\Delta(T)$ decreases monotonically until vanishing at $T = T_c$ [56, 68]. This behavior as predicted in BCS theory in the weak coupling limit and is depicted in Fig. 2.9.

2.2.6. Resonance lineshapes

As we showed in section 2.2.1, an LC resonator is characterized by its resonance frequency $\omega_0 = 1/\sqrt{LC}$. However, any physical system is prone to loss resulting in a resonance broadening in the frequency domain due to Heisenberg uncertainty principle. Here, first we briefly mention the different origins of losses that yield resonance broadening. Then we discuss the lineshapes of a notch-type and of a transmission-type half-wave resonator.

Origins of loss

The widely used Q factor is a measure of the total loss of a resonator and defined as

$$Q_{\text{tot}} = \frac{1}{2\pi} \frac{\text{energy lost per cycle}}{\text{energy stored}}. \quad (2.33)$$

It is directly related to the linewidth $\kappa_{\text{tot}} = \frac{\omega_r}{Q_{\text{tot}}}$ of the resonator. In order to probe the resonance in a measurement, the resonator has to be coupled to a microwave feedline giving rise to photon loss of rate κ_c . Other, in general unwanted, loss channels are usually referred to by the decay rate κ_i . To highlight that losses of the resonator are not only of internal origin, but originate, e.g., from unwanted coupling to dc lines, in this thesis we use the nomenclature $\kappa_i = \kappa_{\text{loss}}$.

In the scope of high impedance resonators coupled to semiconductor devices, the loss is given by the sum rule

$$\kappa_{\text{loss}} = \kappa_{\text{rad}} + \kappa_{\text{TLS}} + \kappa_{\text{QP}} + \kappa_{\text{residual}}, \quad (2.34)$$

where all the terms in the sum are further elaborated below. κ_{rad} describes the losses attributed to the coupling between the resonator and the DC bias lines needed for operating the semiconductor device opening a photon leakage pathway [21, 69]. In Chapter 3, we describe our approach on designing the microwave environment of the resonator looking for a trade-off between minimizing κ_{rad} and device intricacy. κ_{TLS}

characterizes losses due to an interaction of the resonator with impurity TLSs in the dielectric, relevant in the limit of low-photon numbers, in which quantum devices are operated. Chapter 4 focuses on selecting an ideal dielectric environment for our hybrid devices. κ_{QP} describes additional losses originating from quasiparticles at finite temperatures and/or magnetic-fields [32, 70]. Further losses might originate from coupling to phonons [71] or the vacuum. These losses and any other loss sources are usually negligible and therefore summed up to κ_{residual} .

Reflection, notch and transmission port resonators

In this work, the coupling between the used resonator and the feedline has been realized in three different fashions. The corresponding circuits are schematically depicted in Fig. 2.10a), d) and g) where the resistor in parallel with the LC-oscillator accounts for losses. There is plenty of literature discussing the complex reflection and transmission of either of these circuits [72–78]. Especially Ref. [78] has to be highlighted as a thorough summary providing on top a github repository that enables fitting any of the mentioned resonator types, including asymmetries [78]. This framework was extensively used throughout this work. Either realization of feedline to resonator coupling has its own advantages and disadvantages which become apparent when considering their complex reflection S_{11} and transmission S_{21} . These are depicted in Fig. 2.10 for varying κ_{loss} . The middle row of the figure shows the absolute value of the scattering coefficient for either configuration and the lowest row shows the out-of phase component (Q) versus in-phase component (I). The different resonance shapes are further detailed below.

Reflection port The feedline coupling of choice for most applications is the reflection port coupling in which a single feedline is coupled capacitively to the resonator at its open end as schematically depicted in Fig. 2.10a). In this case a reflection coefficient is measured which is given by

$$S_{11}^{\text{ref}}(\omega) = \frac{\kappa_c - \kappa_{\text{loss}} + 2i(\omega - \omega_r)}{\kappa_{\text{tot}} - 2i(\omega - \omega_r)}. \quad (2.35)$$

For the reflection port a large signal in the amplitude is only visible, if $\kappa_c \approx \kappa_{\text{loss}}$, see Fig. 2.10b). On the other hand, the phase signal increases monotonically when increasing the coupling strength (see excursion in

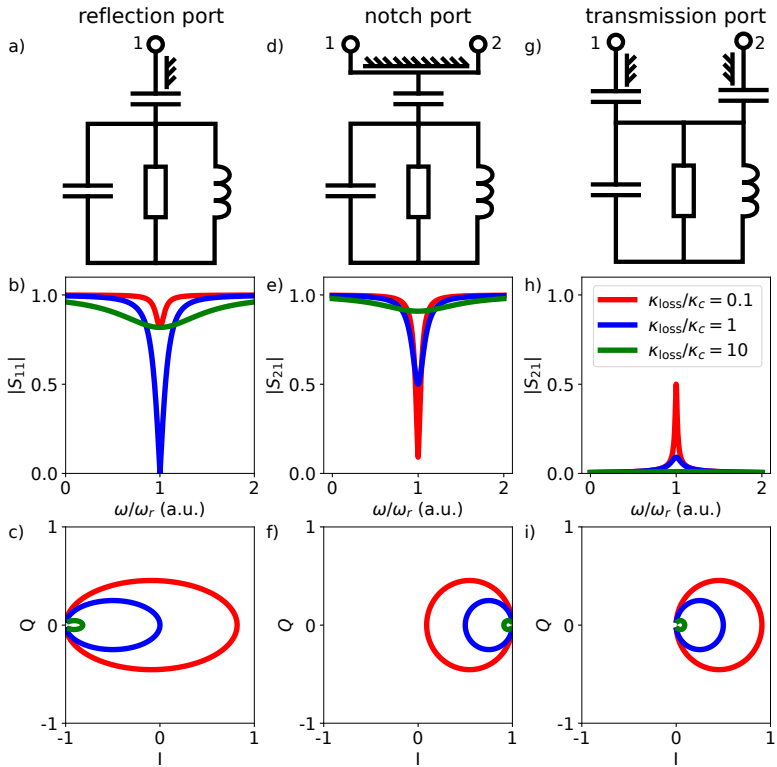


Figure 2.10. Resonance lineshapes. The columns correspond to the circuits depicted in the uppermost row. Middle row: Signal reflection or transmission amplitude (depending on the typical measurement setup) for different types of resonator - feedline coupling. For each trace $\kappa_c = 0.1\omega_r$ is fixed. κ_{loss} is varied as indicated in the legend. Lowest row: out-of phase component Q versus in-phase component I of the resonance excursion corresponding to the above panel.

the I-Q plane in Fig. 2.10c). In the limit of strong overcoupling $\kappa_c \gg \kappa_{\text{loss}}$, a 2π rotation is realized, which reflects in a large phase signal in a measurement. A reflection port resonator is used in Chapter 5.

Notch port In a notch-type, colloquially called 'hanger', configuration, the resonator is located in the vicinity of a non-interrupted feedline coupling either capacitively or inductively, see schematic in Fig. 2.10d). In the notch-port configuration, the transmission through the feedline is given by

$$S_{21}^{\text{notch}}(\omega) = \frac{1 - \kappa_c e^{i\Phi_{\text{Fano}}} / \kappa_{\text{tot}}}{1 + 2i(\omega - \omega_r) / \kappa_{\text{tot}}}, \quad (2.36)$$

where we introduced the asymmetry phase factor Φ_{Fano} accounting for a finite asymmetry as a function of frequency due to interferences of the resonator with standing waves in the feedline [77, 78]. These standing waves originate from reflections due to impedance mismatches. For the plots in this section, we set $\Phi_{\text{Fano}} = 0$ which correspond to the ideal case in the absence of any reflections.

In contrast to the reflection-port resonator, the maximum acquired phase asymptotically approaches π rather than 2π and therefore the phase signal in a measurement is smaller by a factor of 2. However, S_{21}^{notch} exhibits an increasing depth of the resonance dip as κ_c increases (see Fig. 2.10e)). This corresponds to an increasingly larger excursion in the I-Q plane (see Fig. 2.10f)). Therefore, the notch-type resonator is advantageous compared to the reflection port resonator, if $\kappa_c > \kappa_i$. Another advantage of the notch-port configuration is that due to the non-interrupted ground plane, several frequency-multiplexed resonators can be coupled to the same feedline. Notch-port resonators are used in Chapters 4, 6 and 7.

Transmission port Finally, a transmission-type resonator is capacitively coupled to the open ends of two feedlines as shown in Fig. 2.10g). The total transmission from one feedline to the other is measured and is given by

$$S_{21}^{\text{trans}}(\omega) = \frac{\kappa_c / \kappa_{\text{tot}}}{1 + 2i(\omega - \omega_r) / \kappa_{\text{tot}}}. \quad (2.37)$$

In contrast to the reflection-port and the notch-port resonator, a transmission-port resonator results in a suppression of the signal everywhere except on

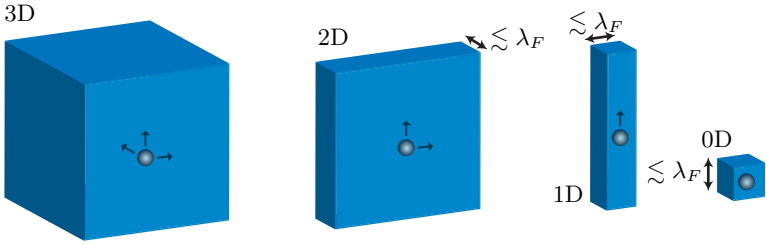


Figure 2.11. Material dimensions. The dimensionality of the system is reduced if the electron confinement in a particular direction is smaller than the Fermi wavelength λ_F . In this case, the motion of the electrons (indicated by arrows) is limited. Figure adapted from Ref. [79].

resonance (compare Fig. 2.10h)). Therefore, the transmission-port resonator is highly preferable compared to the other two types when operating in the strongly overcoupled regime $\kappa_c \gg \kappa_{\text{loss}}$, because read-out is typically performed on resonance where the signal is fully suppressed in any other configuration. The excursion in the I-Q plane behaves similar to the notch-port resonator asymptotically reaching a total phase of π as plotted in Fig. 2.10i). Another advantage of the transmission port resonator is that it enables a fully symmetrical design. A disadvantage of the transmission-port resonator is that without setup calibration, only the width of the resonance can be measured because the baseline is missing. When analyzing the lineshape this implies that only $\kappa_{\text{tot}} = \kappa_c + \kappa_{\text{loss}}$ can be measured, but not the individual components, while in the other two cases, both κ_c and κ_{loss} can be inferred from the resonance trace. A transmission port resonator is used in Chapter 8.

2.3. Double quantum dots

In a bulk metal or semiconductor, electrons can move freely in all three spatial dimensions. However, if the spatial extent of the structure is limited, an electron is confined in that particular dimension as schematically shown in Fig. 2.11. The case in which all three spatial dimensions are limited so that quantum confinement or Coulomb interaction effects become relevant [80, 81] is of particular interest; a so-called quantum dot is

formed. In a quantum dot, electrons are only allowed to occupy discrete energy levels and they are therefore often referred to as artificial atoms. In this thesis, we focus on coupled quantum dots, i.e. with a finite wave function overlap, forming a so-called DQD. In analogy to atoms forming a molecule, a DQD can be considered to be an artificial molecule, which is used as a qubit in this thesis.

2.3.1. Material platforms

Throughout this thesis, we have realized DQDs in three different material platforms. These material systems provide confinement in one, two or all three spatial dimensions and shall be introduced hereafter.

2D electron gas in GaAs

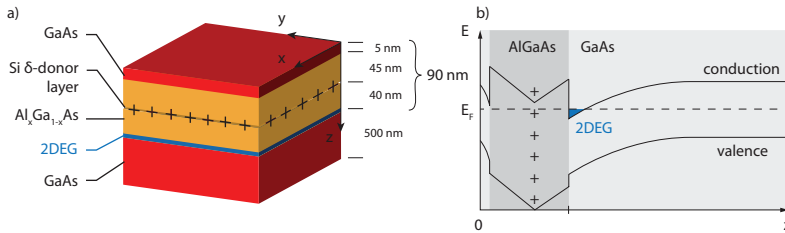


Figure 2.12. 2DEG in heterostructure. a) GaAs/ $\text{Al}_x\text{Ga}_{1-x}\text{As}$ layer sequence with a two-dimensional electron gas (2DEG) at the interface. Figure adapted from [35].

The device substrate used in the experiments presented in Chapter 5 is GaAs/ $\text{Al}_x\text{Ga}_{1-x}\text{As}$ as depicted in Fig. 2.12a). The used wafer was grown by Christian Reichl in the group of Werner Wegscheider at ETH Zurich. The substrate consists of a commercial GaAs wafer on top of which a 500 nm thick GaAs substrate layer is grown by molecular beam epitaxy. 40 nm of $\text{Al}_x\text{Ga}_{1-x}\text{As}$ spacer separate the GaAs substrate from a δ -donor layer of silicon dopants. On top of the δ -donor layer, another 45 nm of $\text{Al}_x\text{Ga}_{1-x}\text{As}$ spacer layer and a 5 nm cap layer of GaAs are grown. Fig. 2.12b) shows the resulting spatial variation of the conduction and valence band edges. The difference in the staggered band gaps of

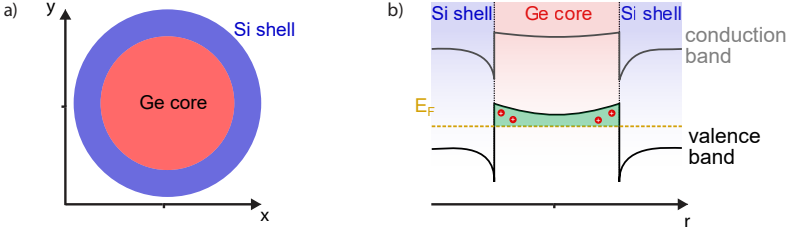


Figure 2.13. Schematic of Ge/Si core shell nanowire. a) Cross section of a Ge/Si core/shell nanowire. b) band structure alignment of a Ge/Si core/shell nanowire as a function of radial position $r = \sqrt{x^2 + y^2}$. Figure adapted from [82–84].

GaAs and $\text{Al}_x\text{Ga}_{1-x}\text{As}$ together with the positive charges introduced by the δ -dopant layer, yield a band bending as depicted in the figure. The resulting conduction band lies below the Fermi energy only in a small region at the interface between the GaAs and the AlGaAs approximately 90 nm below the surface. Therefore, the heterostructure hosts a 2DEG at this position.

In order to form a DQD, the electrons therefore have to be confined in the remaining two dimensions. This is realized by using depletion gates on top of the heterostructure surface, separated by ~ 90 nm from the 2DEG.

1D Ge/Si core/shell nanowires

In Chapter 6, we couple a superconducting resonator to a 1D Ge/Si core/shell nanowire, the latter of which was grown by Ang Li in the group of Erik Bakkers at Eindhoven University of Technology. Fig. 2.13a) shows a schematic cross section of the nanowire. Its Ge core is encapsulated by a Si shell forming a mono-crystalline system [85]. This material alignment results in a staggered type 2 band gap between Si and Ge as shown for the radial direction of the nanowire in Fig. 2.13b). Because the Fermi level gets pinned in the valence band, free holes accumulate in the core of the nanowire even in the absence of doping and gating [39, 83].

The formed one-dimensional hole gas (1DHG) has several properties that make it an exciting test bed for the implementation of spin-based

quantum computers. Firstly, Ge/Si core/shell nanowires can be grown with low defect densities [85] which allows a high degree of control of the electrostatic environment of the 1DHG. Secondly, Ge and Si are group IV materials possessing a low degree of nuclear spins which reduces hyperfine interaction and can result in long spin coherence times. The hyperfine interaction is further reduced, because holes possess a p-type wavefunction featuring a very small overlap between the hole wavefunction and the wavefunction of the remaining nuclear spins. Thirdly, Ge/Si core shell nanowires have a large, direct Rashba spin-orbit interaction (DRSOI) [86] which has enabled very fast Rabi oscillations [46] based on electric-dipole spin resonance (EDSR) [87, 88]. Moreover, the Rabi frequency is electric-field tunable [87, 89] which makes it possible to switch the qubit between an idle state and an operating state by applying a local gate potential. Fourthly, not only the strength of the EDSR, but also the Landé g-factor is electric-field tunable [86, 90] enabling an all-electric spin qubit control. Lastly, the heavy-hole light-hole mixing in the valence band of Ge is rich in physics and yet quite unexplored [86, 91].

In order to form a DQD in the 1DHG, the wire is deposited on top of a linear array of bottom gates [42, 92] where positive gate potentials confine the holes in longitudinal direction.

0D crystal-phase defined dots in InAs

In Chapters 7 and 8, we couple a superconducting resonator to a DQD defined by crystal phase engineering of an InAs nanowire. The used nanowire was grown by Sebastian Lehmann in the groups of Kimberly Dick Thelander and Claes Thelander at Lund University. The growth conditions determine whether the nanowire crystal forms a wurtzite or a zincblende phase [94]. This is utilized by changing the growth parameters during the growth so that the crystal-phase of specific wire sections can be deterministically varied [40]. Fig. 2.14 shows the formation of a DQD by using this so-called crystal-phase engineering. Because of the larger band gap of the wurtzite crystal-phase compared to the zincblende crystal-phase, the three short wurtzite segments form tunnel barriers for electrons in the conduction band and hence a DQD within the zincblende crystal-phase is formed. In other words, by stacking the different crystal phases, 0D quantum dots are formed without the need of any gates. Only plunger gates are required in order to change the quantum dot's electrochemical

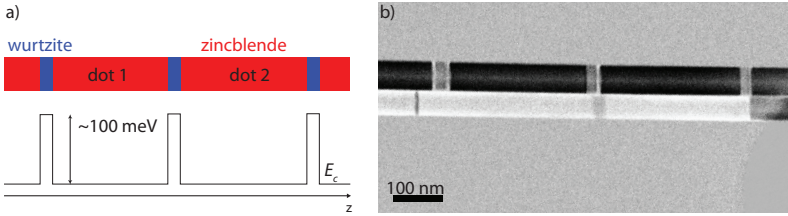


Figure 2.14. Crystal-phase defined DQD in InAs a) upper panel: Schematic of the nanowire showing zincblende segments and the wurtzite barriers. Lower panel: Corresponding conduction band edge energy. The conduction band edge of wurtzite InAs is higher by approximately 100 meV. The crystal phase therefore defines two quantum dots in the zincblende segments as indicated in the upper panel. Figure adapted from [45, 93] b) Transmission electron micrograph of two nanowires. In the upper one, the zincblende segments (black) and the wurtzite barriers (gray) are clearly visible. The image was taken by Sebastian Lehmann.

potential. Single electron transport through similar structures forming a single quantum dot [93] and DQDs [45, 95] has been demonstrated. The quantum dots are formed in the zincblende InAs segments and hence experience a large spin-orbit interaction [49, 96], which will be used in Chapter 8 to mediate a coupling between a spin qubit and a superconducting resonator.

2.3.2. Charge-stability diagram

In the DQD considered in this thesis, the Coulomb energy is the dominating energy scale. At low temperatures, Coulomb repulsion yields fully occupied dot states with energies lower than the electro-chemical potential of the source and drain and entirely empty states with energies larger than the source and drain potential. In a typical experiment, a negligible bias between source and drain is applied, $eV_{sd} \ll k_B T$. Loading and unloading of an electron or hole in a quantum dot by means of a tunneling process is then only possible, if the energy level of the quantum dot is aligned with the electro-chemical potential of the drain (Fig. 2.15a)), the source (Fig. 2.15b)) or an energy level of the second quantum dot (Fig. 2.15c)).

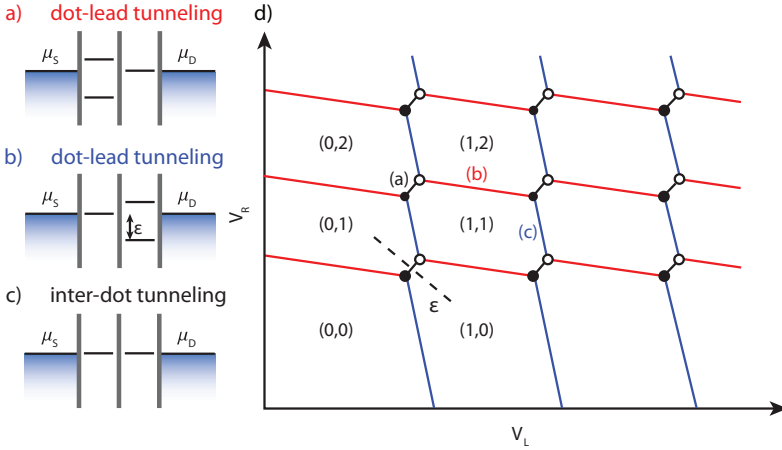


Figure 2.15. Schematic charge-stability diagram. a) Energy levels of a DQD where the right dot level is aligned with the electrochemical potential μ_D of the drain. b) Level diagram where the left dot level is aligned with the source potential μ_S . c) Level diagram where both dot levels are aligned with each other and with source and drain potentials $\mu_S = \mu_D$. Sequential tunneling from source to drain is only possible in case c), but back-and-forth tunneling is possible in all three cases. d) Color coded charge-stability diagram where the colors correspond to the resonance conditions in a), b) and c). The charge configurations are indicated in the brackets. Figure adapted from [23].

The difference of the energy levels between quantum dots, as indicated in Fig. 2.15b) is called detuning ϵ . If the levels are not aligned, the charge in either quantum dot remains constant.

Experimentally, the electro-chemical potentials of the quantum dots are individually shifted by changing the voltages V_L and V_R on the plunger gates. This results in the charge-stability diagram in the shape of a hexagon as depicted in Fig. 2.15d), where lines indicate the configurations where tunneling is possible while in the rest of the diagram the DQD is Coulomb-blockaded and has a fixed charge [97]. A dashed line in Fig. 2.15d) shows a direction along which only the detuning of the dots is

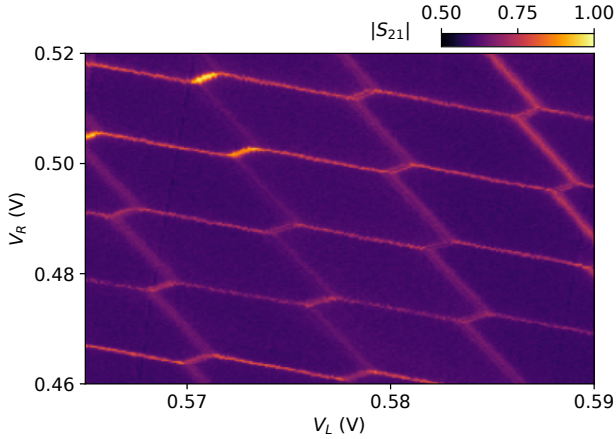


Figure 2.16. Measured charge-stability diagram of a crystal-phase defined DQD in InAs. Resonance conditions as shown in Fig. 2.15 are detected by sensing a superconducting resonator that is coupled to the DQD. The figure shows the transmission amplitude $|S_{21}|$ at the resonator frequency as a function of the plunger gate voltages.

changed. The slanting of the honeycomb pattern with respect to the voltage axes is a consequence of the finite cross capacitance between the right dot and the left gate and vice versa. Filled and empty circles indicate the triple points at which the electro-chemical potential of source and drain is aligned with the energy levels of both quantum dots. When measuring the source-drain current, the triple points are the only configurations at which sequential tunneling results in a direct transport.

In our experiments, we typically measure the charge-stability diagram by probing the response of a resonator, capacitively coupled to one of the two quantum dots, close to its resonance frequency. Fig. 2.16 shows the response $|S_{21}|$ of a notch-type resonator coupled to a DQD. The figure clearly exhibits the honeycomb pattern of the charge-stability diagram. Noteworthy is that not only the triple points are visible; all three resonance conditions as depicted in Fig. 2.15 result in a measurable resonator response, because of the dipolar coupling between the resonator and the tunneling charge. The charge-stability diagram can also be ana-

lyzed quantitatively [97] for extracting the relevant system capacitances. The way this is done throughout this thesis is described in Section D.1 in the appendix.

2.3.3. Charge and spin qubits

The structure of the charge-stability diagram is explained electrostatically using a capacitance model. However, for understanding the resonator response, a capacitance model is not sufficient and a Hamiltonian model has to be considered. When doing so, because electrons (or holes) possess a spin character, the spin-degree of freedom is relevant at non-zero magnetic fields. The spin degree of freedom is of special interest, because it can be employed as a spin qubit [5, 6, 98].

This sub-section aims on explaining how a DQD in the presence of spin-orbit interaction can be operated as a charge or a spin qubit. Describing the DQD as a qubit implies that when coupled to a microwave photon in a resonator, the Rabi and JC model can be applied as described in section 2.1.1 explaining the measured resonator response.

Because pairs of electrons progressively occupy the spin degenerate quantum dot levels, a DQD can have either a spin 1/2 or a spin 0 character with behaviour mimicking a single electron or two electrons [99]. In the following, we therefore refer to the single electron model as odd parity and to the two electron model as even parity.

We first consider the energy levels of a single electron shared among the two dots of a DQD in the presence of a magnetic field and spin-orbit interaction. A different behavior is expected in the case of two electrons shared among the two quantum dots which is explained thereafter.

Odd parity

If the electrons in the DQD have a total spin of 1/2, they can be modelled by one spin-degenerate electron. This electron can reside either on the left dot or on the right dot [100]. Therefore, a suitable basis is $\{|L \downarrow\rangle, |L \uparrow\rangle, |R \downarrow\rangle, |R \uparrow\rangle\}$, where L/R denotes whether the charge resides in the left dot or on the right dot, respectively and \downarrow/\uparrow denotes whether the spin is aligned parallel or anti-parallel with the magnetic field B .

The Hamiltonian describing the electron can be decomposed into three parts as

$$\mathcal{H}_{\text{odd}} = \mathcal{H}_{\text{odd}}^0 + \mathcal{H}_{\text{odd}}^Z + \mathcal{H}_{\text{odd}}^{\text{soi}} \quad (2.38)$$

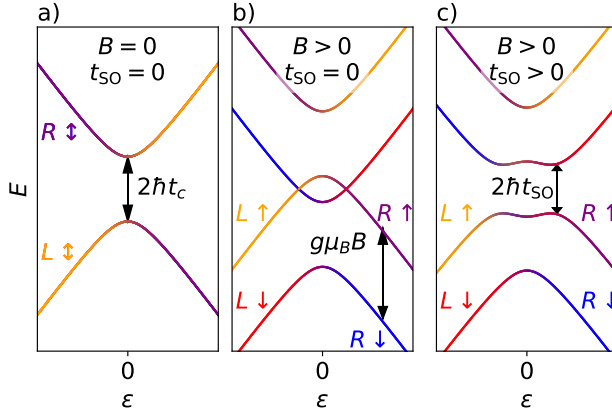


Figure 2.17. Energy levels of a single electron in a DQD. The energy levels are shown as a function of detuning ϵ and subfigures differ only in the choice of the magnetic field B and spin-flipping tunneling amplitude t_{SO} as indicated. In all figures, $g_L = g_R$. The tick on the x -axis indicates zero detuning. The color encodes the squared amplitude of the corresponding eigenstate as indicated in the figure.

The first part of the Hamiltonian describes the spin-independent charge which can be written using the the charge Pauli matrices $\hat{\tau}_{x,y,z}$ as

$$\mathcal{H}_{\text{odd}}^0 = \frac{\hbar\epsilon}{2}\hat{\tau}_z + \hbar t_c \hat{\tau}_x. \quad (2.39)$$

Here, the diagonal terms are proportional to the detuning $\hbar\epsilon = E_R - E_L$ which is the difference between the electro-static potential of the electron residing in the right and left dot, respectively. The off-diagonal terms are given by $\hbar t_c$ which is the spin-conserving tunneling amplitude. In the absence of a magnetic-field and spin-orbit interaction, $\mathcal{H}_{\text{odd}} = H_{\text{odd}}^0$ is the full Hamiltonian. The resulting energy levels are plotted in Fig. 2.17a). As visible in the figure, at $\epsilon = 0$, the spin-degenerate charge states hybridize. At this charge degeneracy, the eigenstates of the system are given by the the anti-symmetric (bonding) and symmetric (anti-bonding) superposition states, $|\pm_c\rangle = (|R\downarrow\rangle \pm |L\downarrow\rangle)/\sqrt{2}$.

In the presence of a magnetic-field, the second part of the Hamiltonian comes into effect. This term describes the Zeeman energy of the electron and is given by

$$\mathcal{H}_{\text{odd}}^Z = \frac{1}{2}g_{L,R}\mu_B B \hat{\sigma}_z, \quad (2.40)$$

where g_L and g_R are the site-dependent Landé g-factors, μ_B is the Bohr magneton and $\hat{\sigma}_{x,y,z}$ are the spin Pauli matrices. The Zeeman energy lifts the spin degeneracy and hence four spin-polarized levels are observed as shown in Fig. 2.17b). The curvature of the levels is not influenced by the Zeeman term and is still governed by the spin-conserving tunneling. Fig. 2.17b) shows the levels in the situation where the Zeeman energy exceeds the spin-conserving tunneling, $g\mu_B B > \hbar t_c$. In this situation, in the absence of spin-orbit interaction, $t_{\text{SO}} = 0$, two spin-polarized levels cross without coupling to each other (see figure).

The crossing between the spin-polarized levels is lifted in the presence of a spin-orbit field that creates a coherent mixing between the two different spin-states. The spin-orbit interaction results in a spin-flipping tunneling amplitude t_{SO} entering the third part of the Hamiltonian as [101]

$$\mathcal{H}_{\text{odd}}^{\text{SO}} = \hbar t_{\text{SO}} \hat{\tau}_y \hat{\sigma}_y \quad (2.41)$$

As depicted in Fig. 2.17c), the spin-flip tunneling amplitude results in an avoided crossing of the levels corresponding to $|L \uparrow\rangle$ and $|R \downarrow\rangle$ and of the levels corresponding to $|R \uparrow\rangle$ and $|L \downarrow\rangle$. As is apparent upon comparing Fig. 2.17b) and Fig. 2.17c), the ground state energy level remains mostly unaffected by this anti-crossing.

Even parity

If the total spin of the DQD is even, the DQD can be modelled by considering only two electrons. The spins of two electrons form singlets and triplets [3] which behave qualitatively very differently when working at non-zero magnetic fields. In the even parity, the basis is chosen to be $\{S_{1,1}, T_{1,1}^-, T_{1,1}^0, T_{1,1}^+, S_{2,0}, T_{2,0}^-, T_{2,0}^0, T_{2,0}^+\}$, where the charge configuration is indicated by the tuple of integers. The spin states are given as singlet

$$S = \frac{1}{\sqrt{2}} (|\uparrow\downarrow\rangle - |\downarrow\uparrow\rangle) \quad (2.42)$$

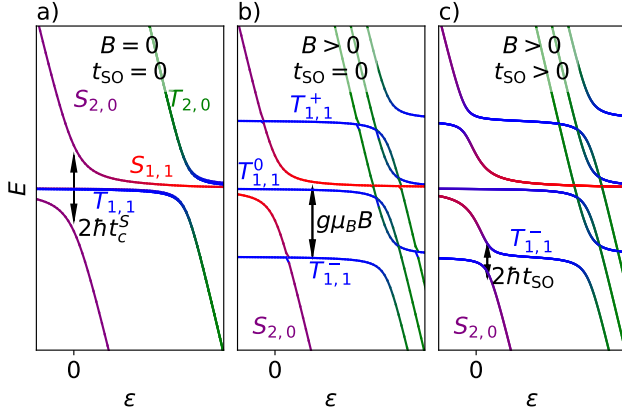


Figure 2.18. Energy levels of two electrons in a DQD. The energy levels are shown as a function of detuning ϵ and subfigures differ only in the choice of the magnetic field B and spin-flipping tunneling amplitude t_{SO} as indicated. In all figures, $g_L = g_R$. The color encodes the squared amplitude of the corresponding eigenstate as indicated in the figure.

and triplets

$$T^- = |\downarrow\downarrow\rangle, \quad T^0 = \frac{1}{\sqrt{2}} (|\uparrow\downarrow\rangle + |\downarrow\uparrow\rangle), \quad T^+ = |\uparrow\uparrow\rangle \quad (2.43)$$

Similar to the odd parity, the system Hamiltonian can be decomposed in three parts as

$$\mathcal{H}_{\text{even}} = \mathcal{H}_{\text{even}}^0 + \mathcal{H}_{\text{even}}^Z + \mathcal{H}_{\text{even}}^{\text{soi}}. \quad (2.44)$$

The first part of the Hamiltonian describes the electrostatic-potential, the singlet-triplet splitting and spin-conserving tunneling. It is given by

$$\begin{aligned} \mathcal{H}_{\text{even}}^0 = & \hbar\epsilon \left(|S_{20}\rangle \langle S_{20}| + \sum_{i \in [0\pm]} |T_{20}^i\rangle \langle T_{20}^i| \right) \\ & + \Delta_{ST} \sum_{i \in [0\pm]} |T_{20}^i\rangle \langle T_{20}^i| \\ & + \hbar t_c^S |S_{20}\rangle \langle S_{11}| + \hbar t_c^T \sum_{i \in [0,\pm]} |T_{20}^i\rangle \langle T_{11}^i| + \text{h.c.}, \end{aligned} \quad (2.45)$$

where once again $\epsilon = (E_R - E_L)/\hbar$ is the detuning and Δ_{ST} is the single dot singlet-triplet splitting separating the $T_{2,0}$ states from the $S_{2,0}$ state. The spin conserving inter-dot tunneling amplitudes are denoted $\hbar t_c^S$ and $\hbar t_c^T$ for the singlet and triplet states. In the absence of a magnetic field and spin-orbit coupling, the total Hamiltonian is given as $\mathcal{H}_{\text{even}} = \mathcal{H}_{\text{even}}^0$. The levels corresponding to this situation are plotted in Fig. 2.18a). The ground state always has a singlet character and at charge degeneracy ($\epsilon = 0$) an anti-crossing between the levels, corresponding to the $S_{2,0}$ and $S_{1,1}$ states can be seen. The hybridized singlet levels are separated by $2\hbar t_c^S$ (see arrow in figure). At zero detuning, the triplet states $T_{1,1}$ with the electrons spread among the two dots have zero energy and the triplet states $T_{2,0}$, where two electrons reside in the same dot, have energy Δ_{ST} (off-scale in the figure). For increased detuning, the energy of the $T_{2,0}$ decreases while the energy of the $T_{1,1}$ states remains constants. Therefore, they anti-cross at large positive detuning with a level separation of $2\hbar t_c^T$.

In the presence of a magnetic field B , the degeneracy between the triplet levels is lifted by the Zeeman energy which is included by the Zeeman term in the Hamiltonian

$$\mathcal{H}_{\text{even}}^Z = \mu_B B \sum_{\pm} \left(\pm \frac{g_L + g_R}{2} |T_{11}^{\pm}\rangle \langle T_{11}^{\pm}| \pm g_L |T_{20}^{\pm}\rangle \langle T_{20}^{\pm}| \right). \quad (2.46)$$

Here, g_R and g_L denote the Landé g-factors of the right and left dot, respectively. Fig. 2.18b) shows the level structure for the situation where $g\mu_B B > \hbar t_c^S$ with $g = g_R = g_L$ in the absence of spin-orbit interaction ($t_{SO} = 0$). The spin polarized triplet states are spin-split from the spin-zero triplet state by $g\mu_B B$. From the figure, it becomes clear that for

negative ϵ , the ground state of the system is not any longer given by the singlet state, but by $T_{1,1}^-$. However at large, positive detuning the ground state is $S_{2,0}$. Therefore, at an intermediately large $\epsilon > 0$, these two states cross without influencing each other.

Let us now consider non-zero spin-orbit coupling. Spin-orbit coupling results in spin-flipping tunnel transitions $t_{\text{SO}} > 0$ coupling the $S_{2,0}$ and the $T_{1,1}$ states. This is described by the third part of the Hamiltonian

$$\mathcal{H}_{\text{even}}^{\text{SO}} = \hbar t_{\text{SO}} \sum_{i \in [0, \pm]} (|S_{20}\rangle \langle T_{11}^i| + |S_{11}\rangle \langle T_{20}^i|) + \text{h.c.}, \quad (2.47)$$

Fig. 2.18c) shows the level diagram with the same parameters as in Fig. 2.18b), but with $t_{\text{SO}} > 0$. As becomes apparent from the figure, the effect of the spin-orbit coupling on the ground state is an avoided crossing between $S_{2,0}$ and $T_{1,1}$. Instead of crossing, $S_{2,0}$ and $T_{1,1}^-$ anti-cross and the levels of the fully hybridized states are separated by $2\hbar t_{\text{SO}}$.

The double-dot two-level system

At low temperatures, the DQD remains in the ground state, except if it is excited by, for instance, a microwave tone. Because higher energy excitations are irrelevant at low temperatures, close to an avoided crossing, the Hilbert space can be collapsed to the two-level subspace including only the two coupled states. This allows us to describe the DQD system as a qubit. The spin or charge nature of this qubit is determined by the character of the tunnel-coupled states. Considering the case in which the ground state is tunnel coupled by a tunnel rate t with a second state with opposite charge configuration, these two states differ solely by their charge configuration such as $|R\rangle$ and $|L\rangle$ in the odd-parity case, or $S_{2,0}$ and $S_{1,1}$ in the even-parity case. Hence, a charge qubit is realized. When considering two tunnel-coupled states with differing spin character, a spin qubit is realized. This is the case for instance for the avoided crossing between $S_{2,0}$ and $T_{1,1}^-$ due to spin-orbit interaction.

In the following, we label these two states with $|g\rangle$ and $|e\rangle$. In the two-level subspace, the Hamiltonian reads

$$\mathcal{H}_q = \frac{\hbar}{2} (\epsilon \hat{\tau}_z + 2t \hat{\tau}_x), \quad (2.48)$$

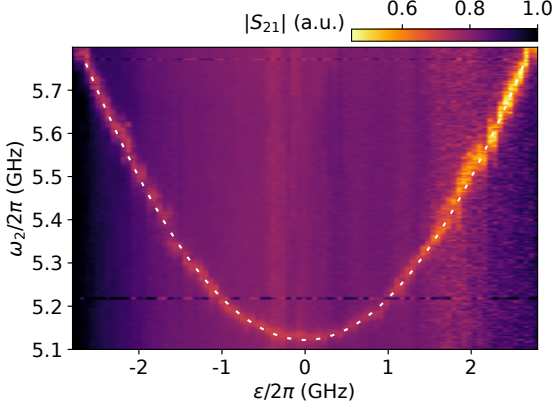


Figure 2.19. Charge qubit dispersion. The graph shows the result of a two-tone spectroscopy experiment of a GaAs DQD strongly coupled to a microwave resonator. The resonator response S_{21} is acquired at the resonator frequency $\omega_r/2\pi = 6.2581$ GHz while a second tone with frequency ω_2 is applied. We plot $|S_{21}|$ as a function of ω_2 and detuning ϵ . A change in $|S_{21}|$ is measured whenever the ω_2 is resonant with the qubit transition frequency ω_q . The white, dashed line is a fit to the transition frequency $\omega_q = \sqrt{|2t|^2 + \epsilon^2}$, where $t > 0$ is a fit parameter. A second fit parameter is the lever arm α that converts the applied voltage V to the detuning as $\epsilon = \alpha(V - V_0)$ with an offset voltage V_0 .

where ϵ is detuning of the uncoupled states. Furthermore, $\hat{\tau}_{x,z}$ are the Pauli matrices in the basis of the two coupled states with opposite charge character. Diagonalization of the Hamiltonian gives

$$\mathcal{H}'_q = \frac{\hbar\omega_q}{2} \hat{\sigma}_z, \quad (2.49)$$

where $\hbar\omega_q = \hbar\sqrt{|2t|^2 + \epsilon^2}$ is the energy separation between the hybridized states and $\hat{\sigma}_z$ is the Pauli operator in the eigenstate basis. The eigenstates of the diagonalized Hamiltonian are the bonding and anti-bonding

states [23, 102]

$$|g\rangle = \begin{cases} \sin \frac{\vartheta}{2} |0\rangle - \cos \frac{\vartheta}{2} |1\rangle, & \text{if } \vartheta > 0 \\ \cos \frac{\vartheta}{2} |0\rangle - \sin \frac{\vartheta}{2} |1\rangle, & \text{if } \vartheta < 0 \end{cases}, \quad (2.50)$$

$$|e\rangle = \begin{cases} \cos \frac{\vartheta}{2} |0\rangle + \sin \frac{\vartheta}{2} |1\rangle, & \text{if } \vartheta > 0 \\ \sin \frac{\vartheta}{2} |0\rangle + \cos \frac{\vartheta}{2} |1\rangle, & \text{if } \vartheta < 0 \end{cases} \quad (2.51)$$

and $\vartheta = \arctan(|2t|/\epsilon) \in [-\pi/2, \pi/2]$ is called mixing angle.

To demonstrate that the DQD can indeed be treated as a qubit, Fig. 2.19 shows the dispersion of a DQD qubit at zero magnetic field (charge qubit) in GaAs. The data is acquired by two-tone spectroscopy of the DQD [22, 35]: The response of a resonator coupled to the qubit is measured while a second microwave tone with frequency ω_2 is used to drive the qubit. On resonance, the qubit population changes and hence does the signal S_{21} at the resonator frequency. The white, dashed line is a fit of the data to the transition frequency $\omega_q(\epsilon)$.

3 Designing high-impedance microwave circuits

As discussed in the previous chapter, using high-impedance resonators enhances the resonator vacuum fluctuations and therefore the coupling of the resonator to electric dipoles. However, a large impedance does come at a cost and several challenges have to be addressed. One consideration is the choice of the dielectric environment of the superconducting resonator which will be discussed in Chapter 4. Detailed fabrication steps are listed in Appendix A. This chapter describes the design considerations that are taken into account when building an architecture combining half-wave resonators based on thin-film NbTiN with semiconductor nanowires. Moreover, in Section 3.5, we describe the cryogenic setup in which the experiments are performed.

3.1. Spurious modes

When modeling coplanar waveguide resonators, it is assumed that the ground plane itself is well grounded everywhere and that the back propagating currents travel only very close to the resonator [65, 103]. However, when both the center conductor and the ground plane consist of a material with large kinetic inductance, the ground plane itself has a non-negligible impedance which becomes problematic when constrictions are present, and if insufficient grounding to the environment is provided.

Figure 3.1 shows the transmission through a transmission type resonator with a resonance frequency of 4.33 GHz. Its resonance is clearly visible as a sharp peak in the transmission. However, a second, broader spurious peak, close to the resonance frequency is also visible. This peak is partly overlapping with the resonator resonance and might therefore interfere with measurements. In order to investigate the origin of this spurious mode, the experiment is repeated several times with increasing number of

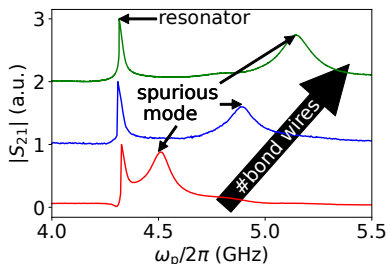


Figure 3.1. Spurious mode. Transmission amplitude $|S_{21}|$ through a NbTiN transmission-type resonator showing resonator resonance and spurious mode (see main text). The difference between the curves lies in the number of wire bonds connecting the ground plane and the printed circuit board (PCB) as indicated by the arrow. Data is offset vertically.

bond wires between the ground plane and the PCB. As a consequence, the spurious mode shifts to higher frequencies (see Fig. 3.1). We suspect this mode originates from the parallel-plate capacitor formed by the ground plane and the copper, separated by $\sim 500 \mu\text{m}$ of silicon. Using a parallel-plate capacitor model, we estimate a capacitance $C_{\text{spurious}} \approx 200 \text{ pF}$ for the $2.5 \text{ mm} \times 4.5 \text{ mm}$ chip. Combining this capacitance with the measured resonance frequency $\omega_{\text{spurious}}/2\pi = 4.5 \text{ GHz}$ allows us to estimate an inductance of $L_{\text{spurious}} \approx 500 \text{ pH}$. Given the sheet kinetic inductance of the used film of $\sim 30 \text{ pH/sq}$, L_{spurious} corresponds to approximately 20 squares which are realistically given by the geometry of the patterned ground plane.

After having identified the origin of the spurious mode, we avoid similar modes in the experiments presented in the chapters 4, 6, 7 and 8 by drilling holes in the copper holder forming the back plate of the parallel plate capacitor and thereby reducing C_{spurious} substantially.

3.2. Losses through the dc lines connected to the device

To electrostatically control a double-quantum dot (DQD), dc gate lines are required. In a hybrid architecture, where a resonator is coupled to a DQD, these unavoidably possess some stray capacitance to the resonator

and open a leakage pathway for the resonator. The leakage loss through a dc gate line can be approximated by [104, 105]

$$\kappa_g = \frac{2}{\pi} \omega_r^3 Z_g Z_r C_g^2, \quad (3.1)$$

where ω_r and Z_r are the resonance frequency and impedance of the resonator, Z_g is the impedance of the dc line, and C_g is the resonator-to-gate capacitance. Indeed, early measurements show significant microwave leakage through the dc lines [21] and the issue has been addressed by implementing superconducting, on-chip low-pass filters [106] whose performance in a high-impedance architecture was investigated rigorously [105]. In the architectures being discussed in the references [105, 106], the DQD is formed by accumulation and depletion gates on top of a two-dimensional electron gas (2DEG). This architecture unavoidably results in a large resonator-to-gate capacitance C_g and therefore, the authors decided to decrease leakage by lowering the effective gate impedance Z_g by incorporating low-pass filters. However, when incorporating one-dimensional nanowires and zero-dimensional crystal-phase defined quantum dots, the resonator-to-gate capacitance can be designed substantially smaller. This alleviates the leakage as $\kappa_g \propto C_g^2$ and hence makes the on-chip low-pass filtering dispensable. Not fabricating the low-pass filters drastically simplifies the device architecture and reduces the footprint. Nevertheless, since $\kappa_g \propto Z_r$, it is evident that the high impedance resonator does lead to a larger leakage term, but not to an extent limiting application of the resonator.

3.3. Losses through the tap

When coupling a resonator to a DQD, it is desirable to be able to apply a dc voltage to the resonator being capacitively coupled to one of the two quantum dots. This on the one hand reduces the overall number of required gate lines needed to control the DQD potentials. On the other hand, it minimizes the resonator-to-gate capacitance C_g and hence, according to Eq. (3.1), ensures a sufficient resonator quality factor. Dc biasing the resonator can be realized by connecting a tap to the position of its voltage node. For a half-wave resonator, this means connecting a dc tap to the middle of the center conductor [17, 21, 107]. However, the dc tap itself in general has a non-negligible inductance and capacitance that

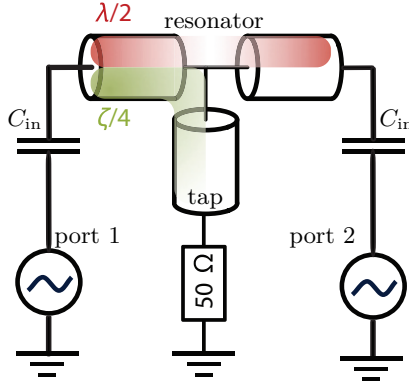


Figure 3.2. Half-wave resonator with dc tap. The figure shows a half-wave resonator probed in transmission from port 1 to port 2 with coupling capacitors C_{in} . Additionally to the mode of our interest, $\lambda/2$, the resonator hosts a $\zeta/4$ mode due to the dc biasing tap (see main text for details). The color gradient, corresponding to the two modes, represents the voltage amplitude along the resonator. For clarity the $\zeta/4$ mode is only plotted on side of the resonator. Figure adapted from Ref. [105].

can change the resonator excitation spectrum [105] and therefore requires careful engineering of the tap.

Fig. 3.2 shows a simplified schematic of a half-wave resonator including the dc tap connected to the middle of its center conductor. The resonance mode that we aim on coupling to a DQD is the half-wave mode $\lambda/2$. At the positions of the coupling capacitors C_{in} , this mode has voltage anti-nodes which oscillate out of phase. The voltage node of the $\lambda/2$ mode is positioned at the middle of the center conductor. Because a dc tap is connected to the middle of the center conductor, a second mode, labelled $\zeta/4$ forms [105]. It extends into the tap of finite inductance and therefore has a lower resonance frequency than the $\lambda/2$ mode. Because the $\zeta/4$ mode is connected to an ohmic line at its current anti-node, it has a low quality factor compared to the $\lambda/2$ mode. Therefore, engineering of the combined system aims on decoupling the two modes from each other as much as possible, preventing loss from the $\lambda/2$ mode through the tap.

Similarly to the $\lambda/2$ mode, the voltage anti-nodes of the $\zeta/4$ mode are located at the coupling capacitors of the resonator. However, in contrast to the $\lambda/2$ mode, the voltage amplitudes at the two ends oscillate in phase. The leakage from the first mode to the second mode is given by their wavefunction overlap. Therefore, if the device is fully symmetric, their different symmetries result in a cancellation of the contributions from the left and right arm of the resonator due to destructive interference. This prevents a coupling between the two modes and hence ensures the high quality of the $\lambda/2$ resonance.

3.3.1. QUCS simulations

We confirm this symmetry argument by simulating a transmission-type resonator using a quite universal circuit simulator (QUCS) [108]. Figure 3.3 shows two simulated circuits with realistic parameters corresponding to a NbTiN resonator, where the tap is represented by a lumped element inductor. The circuits are shown in Fig. 3.3a) and Fig. 3.3b) and differ only by the positioning of the tap: In Fig. 3.3a), the tap is positioned in the middle of the center conductor yielding a fully symmetric device, while in Fig. 3.3b), the device is highly asymmetric, as indicated by the lengths of the resonator segments in the blue and red box respectively. Figure 3.3c) shows the simulated transmission using either structure where the broad $\zeta/4$ mode and much sharper $\lambda/2$ mode are visible. Additionally, at ~ 12 GHz a higher order excitation of the $\zeta/4$ mode, is present.

Figure 3.3d) shows a zoom onto the $\lambda/2$ resonance. As expected in the fully symmetric case, the transmission on resonance is one, indicating that the resonance broadening is only determined by the coupling via the coupling capacitors, according to Eq. (2.37). By fitting a Lorentzian, we extract the resonance frequency $\omega_{0,\text{sym}} = 5.761$ GHz and linewidth $\kappa_{\text{sym}} = 1.089$ MHz. We repeat the same analysis in the asymmetric case, and find that the asymmetry enables a finite hybridization of the $\lambda/2$ mode with the $\zeta/4$ mode and shifts the resonance peak by 23 MHz. Moreover, we find that in the asymmetric case, the peak amplitude does not reach one, reflecting a finite loss through the tap. From a Lorentzian fit, we extract $\kappa_{\text{asym}} = 1.863$ MHz. Because no other loss sources are included in the simulation, the difference in the line widths $\kappa_{\text{tap}} = \kappa_{\text{asym}} - \kappa_{\text{sym}} = 0.773 \pm 0.001$ MHz is fully determined by the losses of the $\lambda/2$ resonance

3. Designing high-impedance microwave circuits

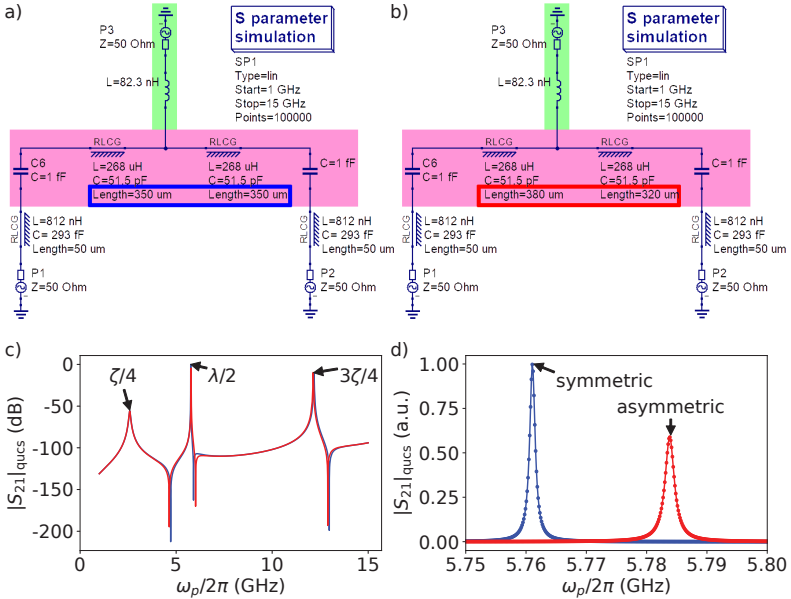


Figure 3.3. QUCS simulations of dc tap. a) Simulation schematic of a resonator probed in transmission with a dc tap simulated as a lumped-element inductor and connected to the middle of the center conductor. b) Same as a, but the tap is not connected to the middle of the center conductor (see colored boxes). c) Simulated transmission amplitude $|S_{21}|_{\text{qucs}}$. d) Zoom of the $\lambda/2$ resonance. Dots are simulated data while the solid line is a Lorentzian fit. A frequency shift and a linewidth broadening are observed for the asymmetric setup compared to the symmetric one. The color code in c) and d) correspond to the boxes' color in a) and b). Inductances and capacitances indicated in the figure are normalized per unit length.

through the tap.

We note that despite the very large asymmetry in the circuit, the loss rate through the tap κ_{tap} is relatively small, $\kappa_{\text{tap}} < 1$ MHz. We attribute this to the large detuning between the $\zeta/4$ mode and the $\lambda/2$ mode of more than 3 GHz.

3.3.2. Sonnet simulations

In the QUCS simulations presented in Section 3.3.1, we simulate the resonator tap by a single lumped element inductor. In a realistic device, such an inductor is realized by a meandered line of the high kinetic-inductance material NbTiN. To simulate a realistic device, we use Sonnet, a finite-element electromagnetic solver, which allows us to take into account the kinetic inductance of the material while performing an electromagnetic simulation. In Fig. 3.4 a-c), we plot the simulated current densities at several frequencies corresponding to the mode spectrum of the resonator. We identify the $\zeta/4$ (see Fig. 3.4a)), the $\lambda/2$ mode (see Fig. 3.4b)) and higher order $n\zeta/4$ modes, where n is an odd integer (see Fig. 3.4c) for the $3\zeta/4$ mode). The transmission as a function of frequency is plotted in Fig. 3.4d), where we indicate the peaks corresponding to either resonance mode.

Figure 3.4d) shows the simulated transmission through the resonator as a function of frequency. During the simulation, the kinetic inductance and the coplanar waveguide capacitance and inductance are chosen to match the line capacitance and inductance that are used in the simulations described in Section 3.3.1. Nonetheless, we observe that the resonance frequencies of the $n\zeta/4$ resonance modes are reduced drastically compared to the QUCS simulation results. This is explained by the fact that in the QUCS simulations, the meandered inductor is approximated by a purely inductive lumped element. In reality however, the inductor possesses a non-negligible spurious capacitance lowering the resonance frequencies of the $n\zeta/4$. Additionally, we note that the resonance frequency of the $\lambda/2$ mode is higher compared to the results of analytical equations and of the QUCS simulations. We attribute this to the gaps in the ground plane due to the tap and feedlines which effectively reduce the total capacitance of the resonator. Moreover, we note that despite the smaller detuning between the $\lambda/2$ resonance and the $3\zeta/4$ resonance of less than 1 GHz, the transmission on resonance of the $\lambda/2$ resonator is 0 dB. This signifies

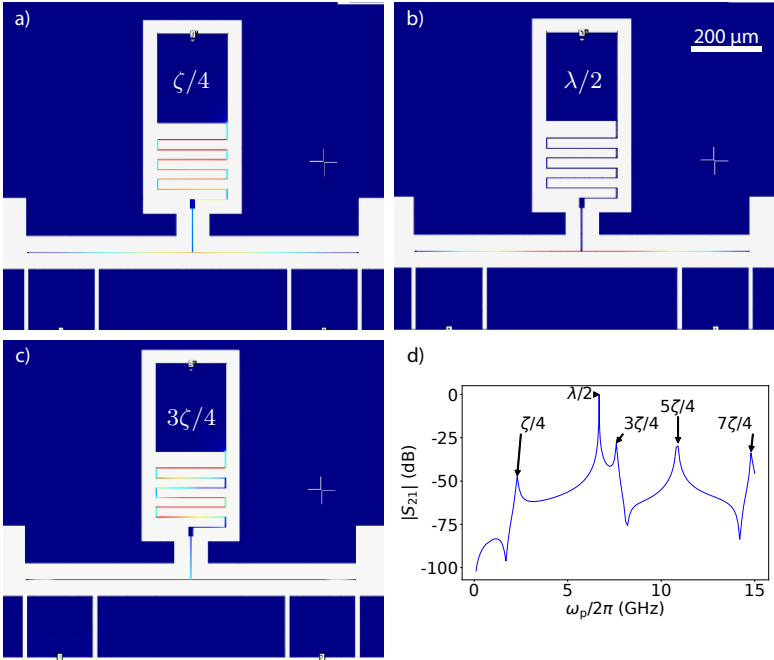


Figure 3.4. Sonnet simulation of dc tap. Simulated current density a) at ~ 2.1 GHz showing the $\zeta/4$ mode, b) at ~ 6.7 GHz showing $\lambda/2$ mode and c) at ~ 7.6 GHz showing $3\zeta/4$ mode. d) Simulated transmission amplitude $|S_{21}|$ as function of probe frequency ω_p . For the simulations, a sheet kinetic inductance of 80 pH per square is used. In the simulated current densities, a red color corresponds to a large current density in arbitrary units.

that no loss through the tap is observed, once again reflecting the fully symmetric resonator design.

3.4. Designing the coupling capacitor

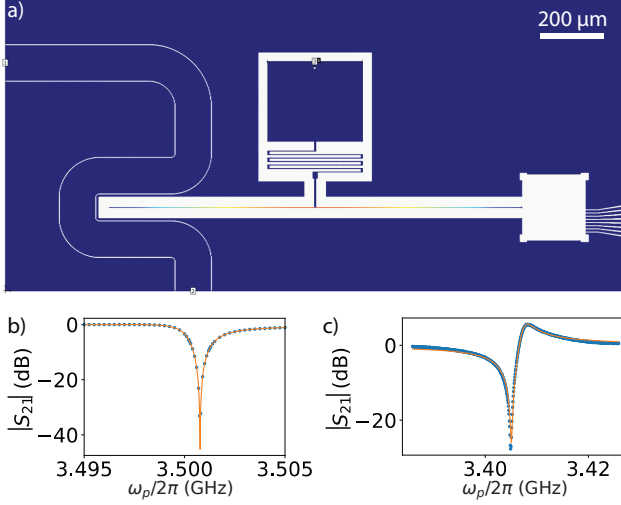


Figure 3.5. Design of coupling capacitor. a) Simulated current density distribution. A red color corresponds to a high current density. b) Simulated resonance curve (blue dots) and fit to Eq. (2.36) (orange curve). From the fit, we extract $f_c = 3.500491 \pm 0.00002$ GHz, $Q_c = 3500 \pm 200$, $\Phi_{\text{Fano}} = 0.28 \pm 0.02$. c) Measured resonance curve at a base temperature of 20 mK and fit. From the fit, we extract $f_c = 3.40734 \pm 0.00002$ GHz, $Q_c = 2490 \pm 20$, $Q_{\text{loss}} = 16500 \pm 1200$ and $\Phi_{\text{Fano}} = -1.042 \pm 0.003$.

In the previous Section 3.3.2, we showed how Sonnet can be used to engineer the dc tap of a half-wave resonator. Sonnet also proves extremely useful for engineering the coupling between the resonator and a feedline, which we briefly demonstrate here for a notch-type half-wave resonator.

Firstly, the feedline dimensions (center conductor width and gap to ground plane) are designed and adjusted to match 50Ω taking into ac-

count the previously determined kinetic induction of the superconducting film according to the equations quoted in Section 2.2.4. A $5\ \mu\text{m}$ wide NbTiN strip, which is connected to the ground plane, is located between the feedline and the resonator. This design of the coupling capacitor ensures a high symmetry of the resonator and hence suppresses losses through the dc tap as explained in Section 3.3.1. Moreover, simulations show that compared to a disconnected ground plane, this design results in a more homogeneous current density distribution in the ground plane for frequencies close to the resonance frequency.

We simulate several coupling capacitor designs. The simulation results are shown in the appendix in Section B.1.

Fig. 3.5a) shows the simulated current density of a resonator design at 3.5 GHz. One can clearly see the half-wave mode on the resonator center conductor. We simulate the complex transmission, S_{21} , through the feedline as a function of frequency, and fit the resonance curve in the complex plane [78] from which we extract the resonance linewidth κ and resonance frequency ω_r . As opposed to Because no other sources of loss are included in the simulations, the loss is purely due to the coupling to the feedline, $\kappa_c = \kappa$ and we find the coupling Q factor $Q_c = \omega_r/\kappa_c$.

To verify the simulation results, we fabricate a test resonator based on this design and probe it in a dilution refrigerator at 20 mK. For comparison, the simulation results are shown in Fig. 3.5b) and the measurement results are shown in Fig. 3.5c). We find both f_r and Q_c to be similar between the simulation and the measurement results (see figure caption). The small deviations in the resonance frequency can be explained by an inhomogeneous film thickness across the wafer. This inhomogeneity results in slightly different film properties on the test chip from which the kinetic inductance was deduced and the chip from which the resonator was fabricated. Therefore, the kinetic inductance and hence the resonance frequency differ slightly. Compared to the simulations, in the measurements we observe a larger absolute asymmetry factor Φ_{Fano} which originates from interference with a broad resonance and hence points towards a small standing wave background in the setup.

The various fabrication steps that are required to fabricate the NbTiN resonators are partly executed at the Paul Scherrer Institute and partly at the University of Basel. The detailed fabrication protocol can be found in Section A.2 in the appendix.

3.5. Cryogenic microwave setup

In order to perform measurements, all samples presented in this thesis are mounted on a PCB with direct current (DC) and/or radio frequency (RF) connectors.

The chip on the PCB is shielded from environmental radiation by a copper box with box mode resonance frequencies well above the frequencies of our interest. The PCB is then connected to the base temperature stage of a dilution refrigerator. The experiments described in Chapter 4, Chapter 6, Chapter 7 and Chapter 8 were performed in an Oxford Triton dilution refrigerator with a bottom-loader system. This cryostat makes use of the phase transition between a concentrated phase of He_3 and a diluted phase of He_3 in He_4 . By driving the He_3 from the He_3 -rich to the He_3 -poor phase, the heat attributed to this phase transition is absorbed. This process takes place in a so-called mixing chamber which is thermally anchored to a plate which, as a consequence, is cooled to a few tens of millikelvin. In order to isolate the mixing chamber plate from the environment, the cryostat has several other temperature stages. All stages are shown in the photograph in Fig. 3.6.

Figure 3.7 shows schematically the electronics used in the experiments on the different temperature stages. The room temperature measurement setup consists of DC and alternating current (AC) electronics. The DC electronics for operating the DQD DC voltages are generated by a digital-to-analog converter (DAC). The DC signal is low-pass filtered using a filter box at room temperature and by using a second low-pass filter stage at the mixing chamber plate. DC currents are measured using an current to voltage (I/V)-converter and a voltage meter. Alternatively, the low-frequency conductance through the DQD is measured using the I/V-converter combined with a lock-in amplifier.

On the AC side, first a coherent microwave signal is generated by a VNA. The signal is then attenuated at every temperature stage in order to reach microwave powers with on average less than one photon in the resonator [109]. In Fig. 3.7, the sample is illustrated exemplarily as a transmission-type resonator coupled to a DQD, corresponding to the experiments described in Chapter 8. The out coming signal passes two isolators, isolating the sample from back action noise from the cryogenic HEMT amplifier which amplifies the signal at 4 K. At room temperature, the signal is further amplified using two additional HEMT amplifiers and

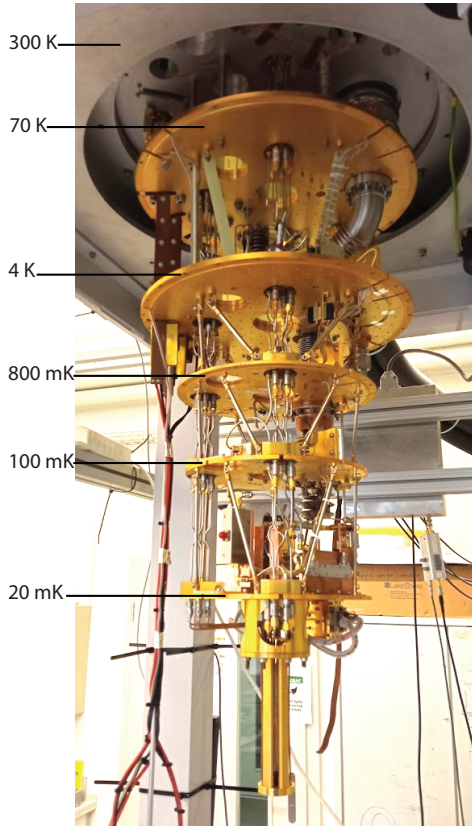


Figure 3.6. Photograph of cryogenic setup. The dilution refrigerator of the type Triton (Oxford instruments) with indicated temperature stages.

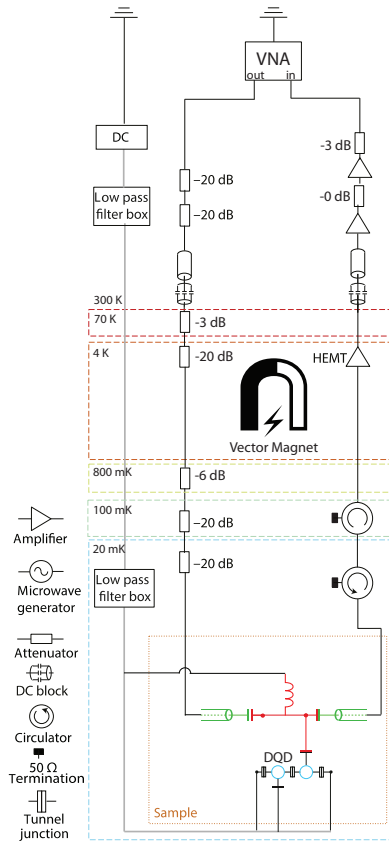


Figure 3.7. Cryogenic and room-temperature equipment. A coherent microwave signal is generated by a vector network analyzer (VNA). In order to suppress thermal radiation, the signal is attenuated at every temperature stage of the cryostat. After passing the resonator, it is amplified by a cryogenic high electron mobility transistor (HEMT) amplifier and two room-temperature HEMT amplifiers before being detected by the VNA.

then detected by the VNA.

Three superconducting Helmholtz coils are mounted at the 4 K plate forming a 3D vector magnet providing uniform magnetic fields at the sample position in any spatial direction.

The experiments described in Chapter 5 were performed in a different dilution refrigerator at ETH Zurich. In these experiments, the signal is first amplified by a Josephson parametric amplifier (JPA) and then down-converted before being acquired using an analog-to-digital converter (ADC) acquisition card. The schematic setup for this experiment is shown in Fig. B.2 in the appendix.

4 The effect of dielectrics on the quality of high-impedance resonators

After having laid-out the considerations taking place when designing magnetic-field resilient, high-impedance, superconducting half-wave resonators based on NbTiN in Chapter 3, we develop a fabrication protocol aiming on very large internal quality factors in the single-photon limit and at elevated magnetic fields. The developed protocol, which can be found in Section A.2 in the appendix, reliably results in high-impedance resonators with unloaded quality factors $Q_{\text{loss}} > 10^5$ when resonators are fabricated on top of intrinsic silicon.

However, nanowire device fabrication is well established using wafers with thermally grown silicon oxide [110–112]. Therefore, additionally to testing the resonator performance on top of intrinsic silicon, we fabricate and test resonators on top of silicon oxide. Moreover, we examine the resonator performance when aluminum oxide is deposited on top of the wafer, covering the resonator which further simplifies the fabrication of nanowire devices.

This chapter is a submitted paper [113].

Performance of high impedance resonators in dirty dielectric environments

J. H. Ungerer,^{1,2} D. Sarmah,¹ A. Kononov,¹ J. Ridderbos,¹ R. Haller,¹
L. Y. Cheung¹ and C. Schönenberger^{1,2}

¹Department of Physics, University of Basel, Klingelbergstrasse 82 CH-4056, Switzerland

²Swiss Nanoscience Institute, University of Basel, Klingelbergstrasse 82 CH-4056, Switzerland

Abstract

High-impedance resonators are a promising contender for realizing long-distance entangling gates between spin qubits. As a material system for the qubits, semiconductor nanowires with strong spin-orbit interaction are often employed, working towards large-scale spin-qubit quantum processor. Inherently, the fabrication of nanowire based qubits relies on the use of gate dielectrics which are detrimental to the quality of the resonator. Here, we investigate loss mechanisms of high-impedance NbTiN resonators in the vicinity of a variety of several commonly used dielectrics and benchmark their performance in elevated magnetic fields and at elevated temperatures. We find that the internal quality factors are indeed limited by the coupling between the resonator and two-level systems of the oxides. We show, that even for the most perfect dielectric configuration for the integration of nanowire devices, where the resonator is sandwiched between SiO₂ and Al₂O₃, which is the least ideal configuration for the resonator, the internal quality factor well exceeds 10³. This allows to integrate high-impedance resonators using established fabrication protocols of semiconductor nanowires while maintaining a high quality factor, thus paving the way for large-scale quantum computers.

4.1. Introduction

High impedance resonators have recently attracted a lot of attention because their large vacuum voltage fluctuations enable strong interactions with a weak electric dipole moment [12, 32]. Superconducting resonator have realized important breakthroughs such as a coherent coupling between a single photon and a single charge [22, 35] on a double-quantum

dot (DQD). In addition, spin-photon coupling [27, 33, 34], distant, resonant charge-to-charge [29] coupling, and spin-to-spin [30] coupling have been demonstrated. Moreover, implementation of high-impedance resonators enabled coherent, virtual-photon mediated charge-to-charge [29] and spin-to-spin [31] coupling, and rapid-gate based spin readout [114].

Investigations of high-impedance resonators have so far focused on realizing the highest quality resonators possible [32, 70, 115, 116] by removing dielectrics that cause loss in the low-photon limit [41]. However, spin qubit quality factors in hybrid devices incorporating a resonator are on the order of 10^3 [30, 31, 33, 34]. And after coupling the resonator to a device, its coherence is not limited by dielectric loss, but by photon leakage to the leads [105, 117] typically limiting their Q factors to $\sim 10^3$, too. This implies that the antecedent optimization of the dielectric environment is unnecessary in any real world device, as long as dielectric losses have a negligible impact on the Q factor. This would then allow one to use established fabrication recipes that employ an arbitrary gate dielectric aiming on electrostatic stability of quantum dot devices.

To showcase this, we investigate high-impedance NbTiN resonators in a variety of dielectric configurations that are commonly used when fabricating double-quantum dots based on semiconductor nanowires [21, 42, 43, 45, 46]. We demonstrate that despite a reduction of the resonator quality factors due to the additional dielectrics, their quality is sufficient even in a dielectric configuration ideal for nanowire integration.

We describe the crucial parameters during sputtering of the material and investigate the dominant resonator loss mechanism. A crucial criterion for resonators aiming on coupling to spin qubits is their magnetic-field resilience and recently, the community has started to operate spin qubits at elevated temperatures [118–120]. Using these arguments as a motivation, we characterize the resonator performance in large magnetic fields up to 5 T and at elevated temperatures.

4.2. Experimental setup

We fabricated a total of 16 NbTiN coplanar waveguide resonators with an impedance of $Z = \sqrt{L/C} \sim 2 \text{ k}\Omega$ distributed on four different chips with dielectric configurations depicted in the dashed, colored boxes in Fig. 4.1a). The sample preparation is described in section 4.3. Each chip hosts a feedline with four notch-type, half-wave resonators as shown in

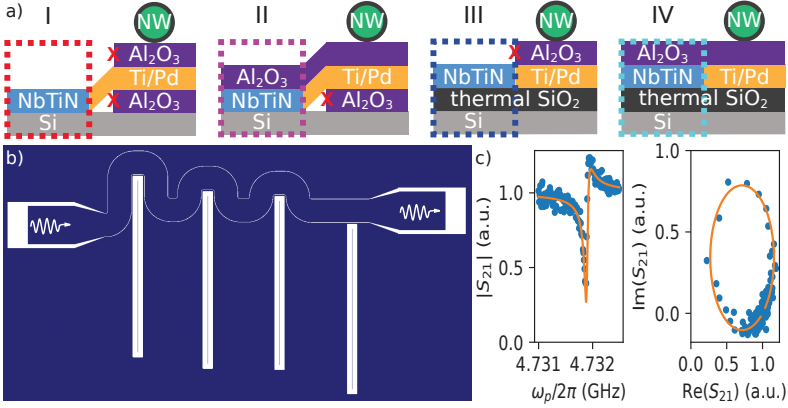


Figure 4.1. Device Overview. a) Side-view schematics of four different dielectric configurations that were investigated. The color of the dashed boxes corresponds to their respective configurations throughout the paper. The right part of each schematic illustrates how a nanowire device can be realized, given the dielectric configuration on its left. b) Top-view design of the four half-wave resonators, capacitively coupled to a much wider 50 Ω matched feedline. c) Amplitude and IQ-excursion of exemplary resonance. The orange line is a fit to the data.

Fig. 4.1b). From left to right, the different wrapping of the feedline results in coupling quality factors between $Q_c \approx 10^3$ and $Q_c \approx 10^5$ enabling us to investigate the film properties accurately for a large range of internal quality factors Q_i . Resonance frequencies are in the range between $f_r \sim 4.2$ GHz and $f_r \sim 5.6$ GHz.

For illustrative purposes, in Fig. 4.1a), we not only show the four different dielectric configurations in colored, dashed boxes, but also the corresponding dielectric configuration of a nanowire device. Case I - NbTiN on Si - is the most ideal configuration for the resonator. Fabricating bottom-gate based devices [46, 92] directly on top of intrinsic silicon comes with the problem of gate leakage, because of the small gate pitch. Moreover, on the surface of the intrinsic silicon, a native silicon oxide forms under ambient conditions which might result in a poor electrostatic device

stability. Therefore, fabrication of nanowire devices on top of intrinsic silicon involves sandwiching the bottom gates with two oxide layers grown by atomic-layer deposition (ALD). To maintain a pure dielectric environment of the resonator, the oxide has to be wet-etched or the ALD-layers have to be deposited locally by a lift-off process [121]. Wet-etching of the oxide might lead to unwanted surface-chemistry on the surface of the NbTiN [122]. And, since ALD growth is a conformal processes, the lift-off process might result in irregular, rough edges around the desired structures that may protrude significantly out of plane with respect to the substrate (red crosses in schematic). These edges in turn, may lead to step coverage issues on subsequent metal layers.

The local deposition of oxides for nanowire device integration is alleviated if the whole chip, including the resonator, can be covered with an ALD-grown oxide. We investigate this in case II - Al_2O_3 on NbTiN on Si.

For device integration, it is desirable to work with electrostatically silent oxides. Therefore, nanowire devices are commonly fabricated on top of thermally grown silicon oxide. We therefore investigate the performance of resonators on top of silicon oxide in case III - NbTiN on SiO_2 on Si. In this case bottom-gate based nanowire devices only require one local oxide deposition step as indicated in the schematic. Additionally, the remaining local oxide deposition is alleviated in case IV - Al_2O_3 on NbTiN on SiO_2 on Si.

The color codes as introduced in Fig. 4.1a) are used throughout the rest of this chapter and denote the dielectric configuration.

4.3. Sample preparation

Since this work aims to investigate resonator losses due to the choice of the dielectric configuration, the intrinsic Q of the resonators must not be limited by the NbTiN film quality. Here we summarize the steps taken to optimize the fabrication of the used films.

1. As a substrate, we select two undoped Si wafers with a resistivity larger than $10 \text{ k}\Omega\text{cm}$; one with only a layer of native SiO_2 and the other with $\sim 100 \text{ nm}$ of thermally grown SiO_2 .
2. In order to minimize the impurity density at the metal-substrate interface, the wafer with only native oxide undergoes the following etching steps: (i) a Piranha etch to oxidise the top $\sim 10 \text{ nm}$ that may contain contamination, (ii) an HF bath to remove this oxide layer, and (iii) a

second Piranha etch, followed by (iv) a second HF bath seconds before loading the wafer into the sputtering chamber. The second wafer hosts ~ 100 nm of thermally grown SiO_2 . In order to remove organic residues but keeping the oxide layer intact, we consecutively use ultrasonic cleaning of the wafer in an aqueous solution of tripotassium orthophosphat ¹, distilled water, acetone and isopropanol before loading the wafer into the sputtering chamber.

3. The vacuum quality in the sputtering chamber plays a vital role. We perform Ti pre-sputtering, resulting in a significant reduction of the chamber base pressure.

4. We pre-sputter the NbTi target to remove the top, potentially contaminated or oxidised layer [123].

5. The sputtering rate has to be maximized by choosing an ideal set of sputtering parameters. See Appendix C.1 for details. Because the impingement rates of oxygen and water decreases with increasing growth rates, higher sputtering rates result in a purer film and accordingly lower loss tangents of the resonators ².

6. We perform sputtering as close as possible to stoichiometry of NbTiN [124]. See Appendix C.1 for details.

7. The resonators are dry-etched using argon/chlorine, offering a higher selectivity against silicon etching compared to the more widely used fluorine based etching recipes [123, 125]. This makes it easier to prevent over-etching.

8. After fabrication, each film is characterized in dc measurements by measuring the critical temperature T_c^{dc} and the sheet resistance $R^{\text{sq,dc}}$ close to T_c^{dc} using etched reference structures. This allows us to determine the sheet kinetic inductance as [56]

$$L_{\text{kin}}^{\text{sq,dc}} = \frac{R^{\text{sq,dc}} h}{2\pi^2 \Delta}, \quad (4.1)$$

where Δ is the superconducting gap and $\Delta(T = 0) = 1.86k_B T_c$ [67], the superconducting gap of Nb. Table 4.1 shows the values obtained from dc measurements, T_c^{dc} and $R_{\text{sq}}^{\text{dc}}$ for the two films. From these, according to Equation (4.1), we deduce the sheet kinetic inductance $L_k^{\text{sq,dc}}$, which is also given in Table 4.1.

¹The used solution has the brand name deconex[®] 12 BASIC 2% solution.

²Discussion with Mihai Gabureac

The resonance frequency is then designed using analytical equations of coplanar waveguide resonators [65] and the coupling quality factor is estimated by simulating the structure using the electromagnetic simulation software Sonnet.

4.4. Determining loss due to two-level fluctuators

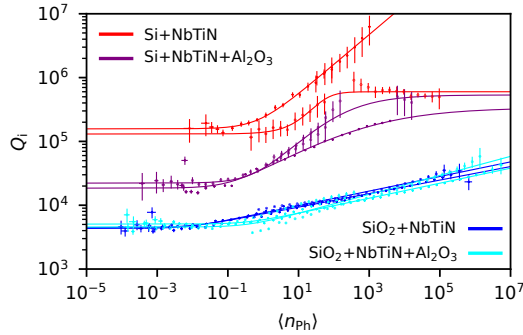


Figure 4.2. Power dependence. Internal quality factor Q_i as a function of average photon number $\langle n_{ph} \rangle$ in the resonator. The solid lines are fits to Eq. (4.4), assuming two level fluctuators as the dominating leakage mechanism at low photon numbers. The color encodes the dielectric configuration according to Figure 4.1a). Different symbols correspond to different resonators.

To benchmark the performance of the resonators in the different dielectric configurations, we probe each notch-type half-wave resonator by measuring the transmission S_{21} through the feedline at the base temperature of a dilution refrigerator $T_{base} \approx 30$ mK. Figure 4.1c) shows an exemplary resonance which is described by [73, 77]

$$S_{21} = 1 - \frac{Q_l e^{i\Phi}}{Q_c \cos(\Phi)(1 + 2iQ_l(\omega/\omega_r - 1))}. \quad (4.2)$$

Here $Q_l = 1/(Q_i^{-1} + Q_c^{-1})$ is the loaded quality factor and Φ describes

4.4. Determining loss due to two-level fluctuators

	film A: Si substrate		film B: SiO ₂ substrate	
	NbTiN	NbTiN+Al ₂ O ₃	NbTiN	NbTiN+Al ₂ O ₃
$R^{\text{sq,dc}}$ (Ω)	260 \pm 20		430 \pm 40	
T_c^{dc} (K)	5.8 \pm 0.1		6.6 \pm 0.3	
$L_k^{\text{sq,dc}}$ (pH)	56 \pm 5		85 \pm 9	
$L_k^{\text{sq,rf}}$ (pH)	79 \pm 14		61 \pm 9	
D (cm ² /s)	0.27 \pm 0.08		0.32 \pm 0.33	
Q_{TLS} (10^3)	151 \pm 20	22.9 \pm 2.4	4.8 \pm 0.8	4.6 \pm 0, 4
Q_{other} (10^6)	1.9 \pm 2.6	0.63 \pm 0.34	-	-
n_c	1.226 \pm 1.254	0.32 \pm 0.34	0.01 \pm 0.01	0.37 \pm 0.02
β	0.54 \pm 0.232	0.46 \pm 0.15	0.12 \pm 0.02	0.13 \pm 0.02

Table 4.1. Resonator properties. Extracted parameters for the two films with varying dielectric configurations. The sheet resistance $R^{\text{sq,dc}}$ and critical temperature T_c^{dc} are obtained from a dc measurement, from which the dc sheet kinetic inductance $L_k^{\text{sq,dc}}$ is determined (see Eq. 4.1). The rf sheet kinetic inductance $L_k^{\text{sq,rf}}$ is independently inferred from the 8 measured resonance frequencies of either film, where the error represents the root variance. The diffusion constant D is as well a weighted average of all resonators of either film (see main text). Q_{TLS} , Q_{other} , n_c and β are fit parameters of Eq. (4.4). Their values represent a weighted average over the data sets of 4 resonators of either dielectric configuration with weights proportional to the inverse of the error bar of the fit, resulting in a maximum weight, if $Q_c \sim Q_i$. The color code corresponds to Fig. 4.1a)

a small resonance asymmetry due to interference with a standing-wave background [77].

We identify 4 resonances on every investigated chip and assign every measured resonance frequency f_r to a physical resonator. Using the physical dimensions of the resonator for calculating its geometric inductance and capacitance [65], we deduce its kinetic inductance from the measured resonance frequency. Thereby, we use the center conductor width which we measure for every resonator by means of scanning electron microscopy after having performed the experiments presented in this work. The so obtained averaged square kinetic inductance $L_k^{\text{sq,rf}}$ is also given in Table 4.1 where the error bar represents the root variance. We find that the values of $L_k^{\text{sq,dc}}$ and $L_k^{\text{sq,rf}}$ are compatible with each other for either film.

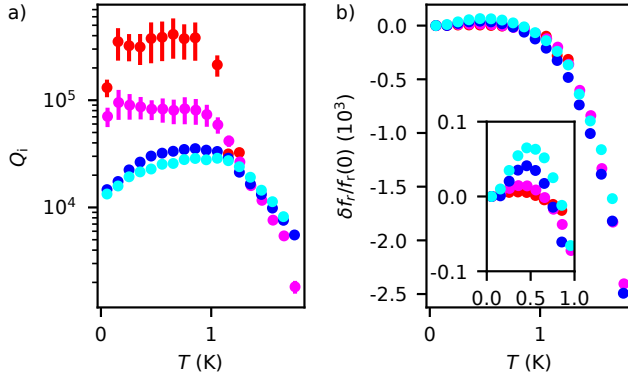


Figure 4.3. Temperature dependence of resonator properties.

a) Internal quality factor Q_i as a function of temperature. b) Relative frequency shift $\delta f_r = (f_r(T) - f_r(0))$ as a function of temperature. The inset is a zoom in onto the peak that is observed at ~ 0.5 K. In all sub-figures, the color encodes the dielectric configuration according to Figure 4.1a) and legend in Figure 4.2. The data was acquired at an average photon number of $\sim 10^4$.

The differences in $R^{\text{sq,dc}}$ and T_c^{dc} between the two films such as the large variance of $L_k^{\text{sq,rf}}$ is attributed to the small film thickness giving rise to a large effect of film thickness inhomogeneities.

In order to quantify the loss due to two-level systems (TLS) residing in the differing dielectric structures, we measure a resonance trace for every resonator in every dielectric configuration and extract Q_i as a function of power applied on the feedline by fitting equation (4.2) in a circular fit [78]. Figure 4.2 shows the fitted internal quality factor Q_i for two resonators of each configuration. We convert the applied power P_{in} on the feedline to an average photon number in the resonator using[116]

$$\langle n_{\text{ph}} \rangle = \frac{Q_c}{\omega_r} \left(\frac{Q_i}{Q_i + Q_c} \right) \frac{P_{\text{in}}}{\hbar \omega_r}, \quad (4.3)$$

where Q_i , Q_c and ω_r are extracted from fitting the resonance curve. TLS residing in the oxides close to the resonator give rise to a power dependent

dielectric loss which is usually modeled by [126–133]

$$\frac{1}{Q_i} = \frac{1}{Q_{\text{TLS}}} \frac{\tanh\left(\frac{\hbar\omega_r}{2k_B T}\right)}{\left(1 + \frac{\langle n_{\text{ph}} \rangle}{n_c}\right)^\beta} + \frac{1}{Q_{\text{other}}}. \quad (4.4)$$

In the low power limit, and at low temperatures, Q_i is approximately given by Q_{TLS} due to TLS. When increasing $\langle n_{\text{ph}} \rangle$ above a critical value n_c , Q_i increases with a characteristic scaling β until eventually saturating at Q_{other} . We fit Equation (4.4) to the data (solid lines in Fig. 4.2) and extract Q_{TLS} , Q_{other} , n_c and β as fit parameters. The weighted average of these fit parameters for each film are specified in Table 4.1.

We find that Eq. (4.4) fits well to our data in all four dielectric configurations implying that in the limit of low photon numbers, all resonators are limited by their coupling to TLS. However, the quantitative behavior for the different dielectric configurations differs by a lot. Let us first consider the low-photon limit in Fig. 4.2. At low photon numbers, the internal quality factor is determined by the coupling to TLS, $Q_i(n=0) \sim Q_{\text{TLS}}$.

In case I - NbTiN on Si, Q_i saturates at the largest value as the number of photons in the resonator approaches zero. This implies a low abundance of TLS at the interface between the intrinsic silicon and the NbTiN. In case II - Al₂O₃ on NbTiN on Si, Q_i saturates at values approximately an order of magnitude lower which we attribute to the larger abundance of TLS stemming from the ALD-grown oxide on top of the metal. For case III - NbTiN on SiO₂ - and for case IV - Al₂O₃ on NbTiN on SiO₂, the saturation of Q_i in the low-photon limit happens another order of magnitude lower than for case II. We attribute this decrease to the larger participation ratio of the interfaces below the center conductor compared to the ones above it due to the larger dielectric constant of silicon as compared to the vacuum dielectric constant. The larger importance of the oxides below the center conductor is confirmed by the negligible difference of Q_{TLS} in case III and case IV (with additional oxide on top of the resonator).

In all cases, once the average number of photons $\langle n_{\text{ph}} \rangle$ exceeds a critical value n_c , Q_i increases, because the TLS are increasingly saturated and no longer open a photon leakage path [126, 128, 129, 134].

In the high power limit in case I and case II, all TLS saturate, and Q_i asymptotically approaches Q_{other} which originates from a power independent source of loss. The origin of Q_{other} potentially lies in the interaction

with phonons or quasiparticles. In case III and case IV, Q_i does not saturate even at photon numbers on the order of 10^7 underlining the importance of losses due to TLS in these cases.

Despite the TLS being the dominant source of loss for these resonators, we highlight that Q_{TLS} well exceeds 10^3 even for the configuration where the resonator is sandwiched between SiO_2 and Al_2O_3 . This result is a central point of this chapter as it allows for easier integration of semiconductor nanowires into a resonator architecture maintaining a good resonator quality. Moreover, we stress that Q_{TLS} is larger by almost an order of magnitude when oxides are only grown on top of the metal and not below.

4.5. Resonator stability at elevated temperatures and fields

After having determined the quality of the resonators in each dielectric configuration, quantified by Q_{TLS} , we aim on benchmarking the resonator stability at elevated temperatures and magnetic fields in regimes relevant for spin-qubit operation.

Figure 4.3a) shows Q_i as a function of temperature for all dielectric configurations where the color code corresponds to the one introduced in Fig. 4.1a). For all curves, we measure an increase in Q_i for increasing temperature peaking at ~ 0.8 K. We attribute this increase in the quality factor to an increasing saturation of the TLS with temperature. When the temperature exceeds ~ 1 K, a decline in Q_i is observed which is attributed to an increasing quasiparticle population because of the closing of the superconducting gap [32, 135].

Simultaneously to measuring the quality factor, we also measure the shift in resonance frequency δf_r and plot it in Fig. 4.3b). We find that δf_r peaks at a temperature $T_0 \sim 0.5$ K (see inset of figure), which the effect being most pronounced for the resonators fabricated on top of SiO_2 (blue points in Fig. 4.3). Moreover, the positive frequency shift at increased temperature exceeds the positive frequency shift in the case of TLS saturation due to a large photon population (see Fig. C.2 in the appendix). This effect can be understood by noting that the latter only saturates TLS in a narrow band around the resonance frequency ω_r while the elevated temperature saturates TLS in a much wider frequency range [128]. The temperature of maximum positive frequency shift corresponds to a

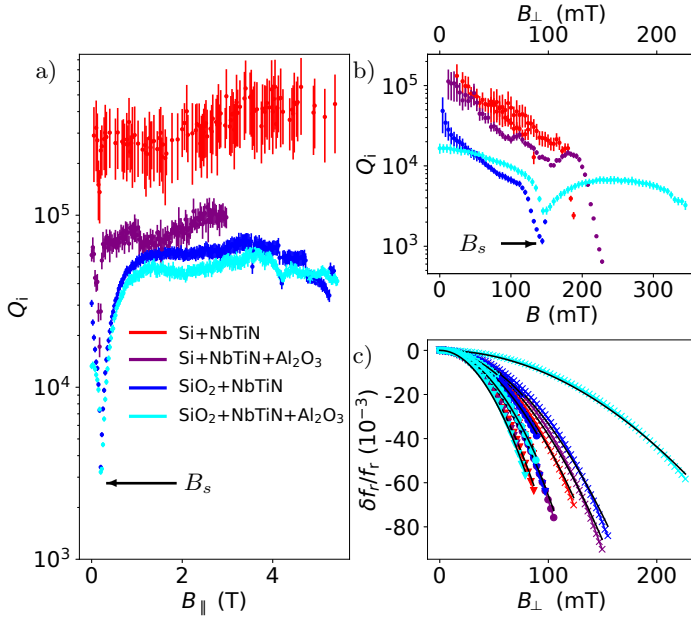


Figure 4.4. Magnetic field dependence a) Internal quality factor Q_i as a function of in-plane field amplitude $B_{||}$. A dip is observed at a field amplitude of $B = B_s = hf_r/2\mu_B \approx 150$ mT, depending on the exact resonance frequency f_r . b) Internal quality factor Q_i as a function of out-of plane field. The field B is applied with an angle of 49° with respect to the substrate and the perpendicular component B_{\perp} is indicated. Once again a dip is observed around $B = hf_r/2\mu_B$, being less pronounced for the resonator fabricated on intrinsic silicon. c) Relative frequency shift $\delta f_r = f_r(B_{\perp}) - f_r(0)$ as a function of out-of plane field component B_{\perp} . The solid lines are fits to equation (4.5). In all sub-figures, the color encodes the dielectric configuration according to Figure 4.1a).

frequency of $\omega_{\text{thermal}}/2\pi = k_{\text{B}}T_0/h \sim 10$ GHz. As $\omega_{\text{thermal}} > \omega_r$, saturation of TLS in this frequency range explains the positive resonance frequency shift due to the dispersive interaction between resonator and TLS. For larger temperature the resonance frequency starts to decrease due to the closing of the superconducting gap Δ resulting in a larger kinetic inductance according to Equation (4.1), explaining the decrease of δf_r .

In order to benchmark the stability of the NbTiN resonators in an external magnetic field, we plot Q_i as a function of in-plane field B_{\parallel} in Fig. 4.4a) and as a function of out-of plane field B_{\perp} in Fig. 4.4b). During the latter measurement, the magnetic field B was applied with an angle of 49° with respect to the sample plane as indicated by the second longitudinal axis in Fig. 4.4b). In both cases, we observe a dip in Q_i at an absolute field strength $B_s \approx 150$ mT corresponding to the Zeeman-splitting of a spin 1/2 particle with a Landé g -factor of 2, $B_s = hf_r/2\mu_B$. The dip is therefore attributed to a resonant interaction with paramagnetic impurities in the substrate [32]. Remarkably, this dip is much less pronounced for the resonator fabricated without any additional oxides, indicating that the paramagnetic impurities mainly reside within the oxides. Besides this dip, for the in-plane field, no noteworthy decline in Q_i is observed up to the very largest applied field strengths of 5 T, confirming a magnetic-field resilience for in-plane fields. This is expected because the penetration depth $\lambda \sim 260$ nm [67] is much larger than the thickness of the NbTiN film (~ 10 nm). Out-of-plane, Q_i declines monotonously for increasing field-strengths which we attribute to the increasing quasiparticle density in the film. However, Q_i remains larger than 10^3 up to $B_{\perp} \sim 100$ mT for all dielectric configurations, once again confirming their suitability for spin qubit integration.

Finally, Fig. 4.4c) shows the resonance frequency versus out-of plane field. The data is well fitted by

$$\frac{\delta f_r}{f_r(0)} = -\frac{\pi}{48} \frac{De^2}{\hbar k_{\text{B}} T_c} w^2 B_{\perp}^2 \quad (4.5)$$

which is deduced from BCS theory [32, 56]. Here, the width w of every resonator center conductor is measured by electron beam microscopy. The average width is $w = 390 \pm 120$ nm where the error bar is the root variance. D denotes the diffusion constant which is a fit parameter.

The weighted average of the fitted diffusion constants are given in Table 4.1. We note that the diffusion constants of the two investigated films are similar and slightly lower than the one in Reference [32].

4.6. Conclusions

We have investigated superconducting, high-impedance resonators based on NbTiN in four different dielectric configurations. The largest internal quality factor in the low-photon limit is found for the resonator fabricated on intrinsic silicon. Nevertheless, all other dielectric configurations result in internal quality factors $> 10^3$, sufficient for resonator integration in the context of spin qubits. Moreover, we benchmark the resonator performance at elevated temperatures and magnetic-field strengths. Since the resonators are compatible with existing fabrication protocols, our results allow for straightforward integration of these types of resonators with spin qubits defined in semiconductor nanowires.

We acknowledge very fruitful discussions with Mihai Gabureac and Sergey Amitonov. Furthermore, we thank Dario Marty for the support in wafer etching in the facilities of the Paul Scherrer Institute. This research was supported by the Swiss Nanoscience Institute (SNI), the Swiss National Science Foundation through grant 192027 and through the NCCR Spin Qubit in Silicon (NCCR-Spin). We further acknowledge funding from the European Union's Horizon 2020 research and innovation programme, specifically the FET-open project AndQC, agreement No 828948 and the FET-open project TOPSQUAD, agreement No 847471. We also acknowledge support through the Marie Skłodowska -Curie COFUNG grant QUSTEC, grant agreement N° 847471 and the Basel Quantum Center through a Georg H. Endress fellowship.

5 Charge noise protection and ultrastrong coupling

In the previous Chapter 4, we have laid the basis of magnetic-field resilient, high-impedance resonators aiming on the spin degree of freedom. These resonators will be coupled to nanowire double-quantum dots (DQDs) in chapters 6, 7 and 8.

Let us now first take a step back and consider a charge qubit defined in a GaAs-two-dimensional electron gas (2DEG) and coupled to a high-impedance superconducting quantum interference device (SQUID)-array resonator. While the SQUID-array is not magnetic-field resilient its resonance frequency can be varied by applying a small external flux as discussed in Section 2.2.3 enabling us to measure resonant interactions between the resonator and the charge qubit always close to the charge qubit sweet spot.

In the following, we demonstrate a tuning protocol enabling us to achieve record high semiconductor charge qubit coherence times. In addition, making use of the large impedance of the Josephson junction (JJ)-resonator, the same protocol in the opposite limit results in a very large coupling strength, reaching the so-called ultra-strong coupling regime where the dipolar interaction strength is non-negligible compared to the bare resonator frequency and bare charge qubit frequency.

The experiments presented in this chapter were performed by J.H. Ungerer, Pasquale Scarlino, D.J. van Woerkom and Marco Mancini in the laboratory of Andreas Wallraff [136] at ETH Zurich. As part of J.H. Ungerer's PhD at University of Basel, the data analysis and publication process was carried out by J.H. Ungerer and Pasquale Scarlino in collaboration with the co-authors. This chapter is published [137] in *Physical Review X* **12**, 031004 (2022).

In-situ tuning of the electric dipole strength of a double dot charge qubit: Charge noise protection and ultra strong coupling

P. Scarlino^{1,2,*}, J. H. Ungerer^{1,3,*}, D. J. van Woerkom¹, M. Mancini¹,
P. Stano^{4,5,6}, C. Müller⁷, A. J. Landig¹, J. V. Koski¹, C. Reichl¹,
W. Wegscheider¹, T. Ihn¹, K. Ensslin¹ and A. Wallraff^{1,8}

¹Department of Physics, ETH Zurich, CH-8093 Zurich, Switzerland,

²Institute of Physics, Ecole Polytechnique Fédérale de Lausanne, CH-1015 Lausanne, Switzerland,

³Swiss Nanoscience Institute and Department of Physics, University of Basel, CH-4056 Basel, Switzerland,

⁴RIKEN Center for Emergent Matter Science (CEMS), Wako, Saitama 351-0198, Japan,

⁵Department of Applied Physics, School of Engineering, University of Tokyo, 7-3-1 Hongo, Bunkyo-ku, Tokyo 113-8656, Japan,

⁶Institute of Physics, Slovak Academy of Sciences, 845 11 Bratislava, Slovakia,

⁷IBM Quantum, IBM Research–Zurich, CH-8803 Rüschlikon, Switzerland,

⁸Quantum Center, ETH Zurich, 8093 Zurich, Switzerland

*These authors contributed equally.

Abstract

Semiconductor quantum dots in which electrons or holes are isolated via electrostatic potentials generated by surface gates, are promising building blocks for semiconductor-based quantum technology. Here, we investigate DQD charge qubits in GaAs capacitively coupled to high-impedance SQUID array and Josephson junction array resonators. We tune the strength of the electric-dipole interaction between the qubit and the resonator *in-situ* using surface gates. We characterize the qubit-resonator coupling strength, the qubit decoherence and the detuning noise affecting the charge qubit for different electrostatic DQD configurations. We find that all quantities to be systematically tunable over more than one order of magnitude, resulting in reproducible decoherence rates $\Gamma_2/2\pi < 5$ MHz in the limit of high inter-dot capacitance. In the opposite limit, by reducing the inter-dot capacitance, we increase the DQD electric-dipole strength, and therefore its coupling to the resonator. Employing a Josephson junction array resonator with an impedance of ~ 4 k Ω and a resonance frequency of $\omega_r/2\pi \sim 5.6$ GHz, we observe a coupling strength of $g/2\pi \sim 630$ MHz, demonstrating the possibility to operate electrons hosted in a semiconductor DQD in the *ultrastrong coupling regime* (USC). The presented

results are essential for further increasing the coherence of quantum dot based qubits and investigating USC physics in semiconducting QDs.

5.1. Introduction

The semiconductor material platform [3, 138] promises scalable realizations of quantum bits (qubits) with long coherence time, fast operation, and a wide range of tunability [139]. Electrons and holes are confined on small islands, called quantum dots, defined by electrostatic gates fabricated on top of semiconducting host materials [3, 97, 140]. Quantum dot devices can be studied directly in transport or remotely by a nearby charge detector, such as a quantum point contact or another quantum dot [3]. Recently, semiconducting quantum dots have also been successfully embedded in circuit quantum electrodynamics (QED) architectures, enabling the study of double [17, 21] and triple quantum dots [27] via their electric dipolar interaction with a microwave resonator. Strong coupling between resonator microwave photons and charge [22, 24, 35] and spin [26, 27, 33] degrees of freedom in the quantum dots has been achieved. Although the spin degree of freedom is of particular interest for quantum information applications, charge noise in the host substrate remains a major limitation [141, 142]. Even operation of the quantum devices at sweet spots – configurations in the parameter space where critical system properties are minimally affected by noise in the control parameters [143–148] – can only mitigate its effects to a limited extent. Therefore, understanding and improving the coherence and control of the charge degree of freedom in semiconductor systems is of special interest also for future spin qubit applications. In fact, all recent successful circuit QED implementations of spins of electrons confined in quantum dots [26, 27, 33] rely on coupling the spin to the electric field of microwave photons via a controlled hybridization of the spin and orbital degrees of freedom, in effect allowing the spin qubit to acquire an electric-dipole moment. The strength of this dipole coupling can be tuned by controlling the spin-orbit degree of hybridization. This allows to find a compromise between a charge qubit with a short coherence but large coupling to cavity photons and the more protected pure spin qubit with small or negligible coupling to cavity photons [149].

In this work, we describe a strategy to systematically tune the DQD electric-dipole strength which controls the coupling rate between the DQD

charge system and a superconducting microwave resonator. The approach is based on altering the magnitude of the DQD inter-dot capacitance while maintaining the inter-dot tunneling rate close to the resonator frequency. We explore different configurations of the DQD confinement potential created by the surface metallic depletion gates, and demonstrate how to efficiently assess the magnitude of the DQD dipole strength in a given configuration. As we will explain in section 5.2, increasing the inter-dot capacitance lowers the electric-dipole strength of the DQD.

In this chapter, we present experiments on two distinct devices [reported in Fig. 5.1(a, c, d, e) and (b, e, f, g), respectively] with which we explore a range of the DQD electric-dipole strength and analyze the DQD decoherence, sensitivity to charge noise, and coupling to the resonator.

In a set of experiments performed with the first device, we systematically decrease the DQD electric-dipole strength by exploring regimes in which the inter-dot mutual capacitance C_m becomes the dominant contribution to the DQD capacitance. In all of these DQD configurations, the DQD-cavity system is in the strong coupling regime, namely in a configuration where the coupling strength between the radiation and the quantum two-level system (g) exceeds the total decoherence of the coupled systems.

In the first device [see Fig. 5.1(a, c, d, e)], the DQD is coupled to a SQUID array resonator. We systematically decrease the DQD electric-dipole strength by exploring regimes with increasing inter-dot mutual capacitance C_m . This allows us to generate a high degree of resilience against charge noise. We make extensive use of the frequency tunability of the SQUID-array resonator [see Fig. 5.1(a,d)]. We reproducibly achieve a decoherence rate of only a few MHz for DQD charge qubits in GaAs/AlGaAs operated in the tens of electrons regime [150], which substantially increases the visibility of the vacuum Rabi mode splitting for a DQD-resonator hybrid device, essential for spectroscopic characterization of the coherent electron-photon hybridization. Furthermore, we show that the reduced sensitivity to charge noise also considerably increases the qubit coherence even at finite DQD detuning.

In the second device a DQD is coupled to a Josephson junction array resonator [see Fig. 5.1(b, e, f, g)]. We explore the same tuning strategy of the DQD confinement potential as used in the first device, but aiming for maximizing the DQD electric-dipole strength. We increase the coupling rate of the DQD to the microwave resonator and approach the

Ultra Strong Coupling (USC) regime [151–153]. The USC is a configuration where the vacuum Rabi frequency (g) becomes an appreciable fraction of the uncoupled eigenfrequencies of the system (ω_r, ω_q), frequently characterized by the ratio $g/\omega_r \geq 0.1$. In contrast to standard cavity-QED scenarios, in the USC regime the routinely invoked rotating-wave approximation is no longer applicable, and the anti-resonant terms become significant [152, 153]. Given the small electric-dipole moment and high decoherence rates, reaching the USC regime with a semiconductor DQD system is more demanding than with superconducting qubits. Here, we demonstrate that careful design and tuning of the DQD confinement potential and using a junction array resonator with a characteristic impedance of $\sim 4\text{ k}\Omega$ allows us to reach a coupling strength of $g/2\pi \sim 600 - 650\text{ MHz}$ at a resonator frequency of $\omega_r/2\pi \sim 5.6\text{ GHz}$.

The chapter is structured as follows: In Sec. 5.2, we discuss the DQD charge qubit and derive its sensitivity to applied voltages and charge fluctuations, which is central to the understanding of the experiments presented in later sections. In Sec. 5.3, we present measurements aimed at maximizing the coherence of semiconductor charge qubits. In Sec. 5.4, we demonstrate that we can reach ultra-strong coupling to a superconducting resonator in a device with an identical quantum dot design. We conclude with Sec. 5.5 where we give an outlook towards future research enabled by our results. Technical details, derivations, and supporting measurements are discussed in Appendix D.

5.2. Double quantum dot charge qubit

In this work, we consider a DQD charge qubit [97] coupled to a microwave resonator. We investigate its coherence properties and coupling strength when systematically varying the electrostatic properties of the dots. The qubit is modeled with a Hamiltonian characterized by two parameters, the detuning between the two dots ϵ and the tunneling amplitude t_c coupling them:

$$H_q = \hbar \left(\frac{\epsilon}{2} \sigma_z + t_c \sigma_x \right) \equiv \frac{1}{2} \hbar \omega_q \boldsymbol{\sigma} \cdot (\cos \varphi, 0, \sin \varphi). \quad (5.1)$$

Here, we introduced the mixing angle through $\tan \varphi = \epsilon/2t_c$, the qubit energy $\omega_q = \sqrt{\epsilon^2 + (2t_c)^2}$ and the vector of Pauli matrices $\boldsymbol{\sigma}$. The Hamiltonian is written in the basis of position states $|l\rangle$ and $|r\rangle$, which differ in their charge configuration by a single electron transferred across the

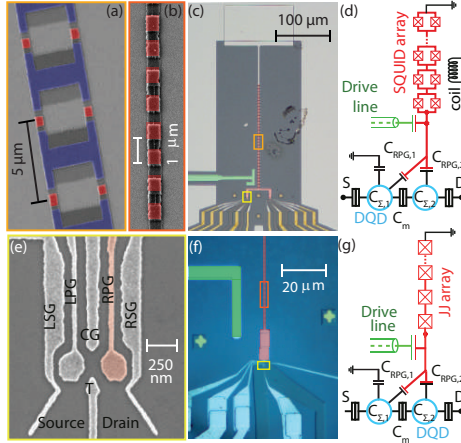


Figure 5.1. Simplified circuit diagram and micrographs of the devices. (a) [(b)] False-colored SEM micrograph of a section of the SQUID [Josephson-junction] array resonator indicated by the light [dark] orange rectangle in panel (c) [(f)]. Josephson junctions in the array are highlighted in red. (c) False-colored optical micrograph of the measured device described in Sec.II, with a SQUID array resonator (red), ground plane (light grey), fine (light grey) and coarse (gold) gates defining the DQD. (d) [(g)] Schematic of the device and control line indicating a simplified circuit diagram of the SQUID [Josephson-junction] array resonator (red), drive line (green), the DQD (cyan) and an external coil (black). $C_{\text{RPG},2}$, $C_{\text{RPG},1}$, $C_{\Sigma,2}$, $C_{\Sigma,1}$ and C_m are the capacitance between the QD_2 [QD_1] and the resonator, total capacitance of QD_2 [QD_1] and inter-dot capacitance, respectively. (e) Scanning electron micrograph of the areas indicated by yellow rectangles in panels (c) and (f) showing the DQD fine gates (light grey) on the GaAs mesa (dark grey). The plunger gate galvanically connected to the resonator is highlighted in red. (f) False-colored optical micrograph of the measured device described in Sec.III, showing the substrate (dark blue), the superconducting structures including the Al fine gate forming the DQD (light blue), the Josephson-junction array (red) and the microwave feedline (green).

double dot. The finite overlap of these position states results in the tunneling amplitude t_c , and their energy difference defines the detuning $\hbar\epsilon = E_r - E_l$.

The DQD is defined through electrostatic gates controlled via applied voltages. Its states can be characterised by the number of charges in each dot. We define a vector of charges $\mathbf{q} = -e(n_1, n_2)^T$ and gate voltages \mathbf{v} . The latter leads to induced gate charges on each dot through $\mathbf{q}_G = -e(n_{G,1}, n_{G,2})^T = -e\mathbf{C}_G\mathbf{v}$, with the gate capacitance matrix \mathbf{C}_G and the electron charge e (for details see Appendix D.3). For a given charge-voltage configuration, the electrostatic energy of the DQD results to[3]

$$E(n_1, n_2, \mathbf{v}) = \frac{1}{2}(\mathbf{q} - \mathbf{q}_G)^T \cdot \mathbf{C}_D^{-1} \cdot (\mathbf{q} - \mathbf{q}_G). \quad (5.2)$$

Here, we introduced the DQD capacitance matrix

$$\mathbf{C}_D = \begin{pmatrix} C_1 & -C_m \\ -C_m & C_2 \end{pmatrix}, \quad (5.3)$$

with the total capacitance of the k -th dot C_k and the mutual inter-dot capacitance C_m . In particular, the mutual capacitance C_m is a parameter which is experimentally tuneable through modifications of the shape and distance of the two dots.

The detuning $\hbar\epsilon$ in the Hamiltonian is defined as the energy difference between two states whose charge configuration differs by a single charge either on the left or right dot. We can thus write

$$\begin{aligned} \hbar\epsilon &= E(n_1, n_2, \mathbf{v}) - E(n_1 - 1, n_2 + 1, \mathbf{v}) \\ &= E_{C,1}(2n_1 - 2n_{G,1} - 1) - E_{C,2}(2n_2 - 2n_{G,2} + 1) \\ &\quad + 2E_{C,m}(n_2 - n_{G,2} - n_1 + n_{G,1} + 1), \end{aligned} \quad (5.4)$$

where we defined the charging energies $E_{C,1/2} = e^2 C_{2/1} / [2(C_1 C_2 - C_m^2)]$ and $E_{C,m} = e^2 C_m / [2(C_1 C_2 - C_m^2)]$. To elucidate the effect of variations and fluctuations in gate voltages δV_G on the Hamiltonian parameters, we define the induced variation in gate charge as $\delta \mathbf{q}_G = \delta V_G (C_{G,1}, C_{G,2})^T$. From Eq. (5.4), we then find the change in $\hbar\epsilon$ to be

$$\begin{aligned} \hbar\delta\epsilon &= 2\delta V_G [C_{G,1}(E_{C,1} - E_{C,m}) - C_{G,2}(E_{C,2} - E_{C,m})] / e \\ &\approx \frac{e \delta V_G}{C_\Sigma + C_m} (C_{G,1} - C_{G,2}), \end{aligned} \quad (5.5)$$

where in the last step, we assumed equal quantum dots with $C_{\Sigma,1} = C_{\Sigma,2} = C_{\Sigma}$. The generalization of Eq. (5.5) to the case of dissimilar quantum dots is given in Appendix D.1.

We will show that qubit electrical sensitivity, expressed in Eq. (5.5), appears as an essential parameter for both qubit-resonator coupling and coherence. Let us, therefore, analyze Eq. (5.5) in more detail. It states that the sensitivity to a given gate voltage is larger, if the two dots are coupled to it differently, $C_{G,1} \neq C_{G,2}$, and is smaller, if the dot mutual capacitance C_m grows. The more tightly the two dots are coupled, the less differently they respond to a voltage change on a gate and the smaller is the DQD effective dipole strength. This finding is a central point of this chapter.

On the first look, Eq. (5.5) suggest a reduction in electrical sensitivity by $1/(C_{\Sigma} + C_m)$. However, the reduction is stronger, due to a sum rule that the capacitances need to satisfy. To see that, we write a single dot total capacitance as

$$C_{\Sigma} = C_m + C_{\text{gnd}} + \sum_{\text{g}} C_{\text{g}} = C_m + C_{\text{out}}, \quad (5.6)$$

where we define its capacitance to ground as C_{gnd} , and to each gate as C_{g} . We also use C_{out} , the capacitance to the outside world, as the total capacitance to everything else except of the other single dot. With this notation, we write the variation of $\hbar\epsilon$ due to an applied voltage δV_G as

$$\hbar\delta\epsilon = e \delta V_G \frac{C_{G,1} - C_{G,2}}{C_{\text{out}}} \frac{C_{\Sigma} - C_m}{C_{\Sigma} + C_m}. \quad (5.7)$$

Here, we interpret the last term as the renormalization factor for the dipolar energy of the system (see Appendix D.2)

$$\eta = \frac{C_{\Sigma} - C_m}{C_{\Sigma} + C_m} = \frac{1 - C_m/C_{\Sigma}}{1 + C_m/C_{\Sigma}}. \quad (5.8)$$

If the dots have non-equal total capacitance ($C_{\Sigma,1} \neq C_{\Sigma,2}$), an additional contribution appears in Eq. (5.7). However, the definition of the factor η given in Eq. (5.8) remains the same, see App. D.3 for details. In the rest of the chapter, we refer to η as *dipole strength* for brevity. The quantities defining the dipole strength as given in Eq. (5.8) can be directly read off the standard charging diagram of the double dot as illustrated in Fig. 5.2 and Fig. D.2 in the appendix.

Note that here we are not considering the concomitant change in tunneling amplitude t_c when changing the electrostatic confinement of the dot. This is because the lever arm for changing the tunneling amplitude t_c in GaAs quantum dots similar to the one considered here is typically at least one order of magnitude smaller than for changes in ϵ [154]. Furthermore, in the experiments presented here, through independent tuning of the T and CP gate voltages [see Fig. 5.1(e)], we take care to keep t_c around 4.5 – 5.5 GHz in all measurements (see Table D.1). In this way, we can specifically investigate changes in the DQD coherence properties and coupling strength when tuning mainly the inter-dot capacitance C_m and, therefore, only the dipole strength η .

Equations (5.7) and (5.8) allow a straightforward derivation of the interaction between the charge qubit and the resonator by replacing the voltage fluctuations δV_G by the voltage vacuum fluctuations of a superconducting resonator of frequency $\omega_r = 1/\sqrt{L_r C_r}$, given by its capacitance C_r and inductance L_r :

$$\delta V_G = \sqrt{\frac{\hbar \omega_r}{2C_r}} (a + a^\dagger). \quad (5.9)$$

a is the annihilation operator of the resonator quantized electromagnetic field. The strength of the resulting qubit-resonator interaction $H_{q-r} = (1/2)g\sigma_z(a + a^\dagger)$ can be parameterized using the resonator impedance $Z_r = \sqrt{L_r/C_r}$ as

$$g = \omega_r \sqrt{\frac{2e^2}{\hbar}} Z_r \times \eta \frac{C_{G,1} - C_{G,2}}{C_{out}}, \quad (5.10)$$

separating the contributions from the resonator and the DQD charge qubit. Since instrumental constraints limit the resonator frequency, the crucial resonator parameter when aiming at maximizing the coupling strength is its impedance Z_r . The dot properties and system geometry enter through the second term.

Equation (5.5) also encodes the qubit coupling to electrical noise. To describe electrical noise, we consider uncontrolled fluctuations of voltage V_G , causing random fluctuations of the qubit energy and thus decoherence. The latter is a complex process, depending on the details of the time correlations in these fluctuations. After analyzing most typical scenarios [155], here we restrict ourselves to dephasing due to singular noise

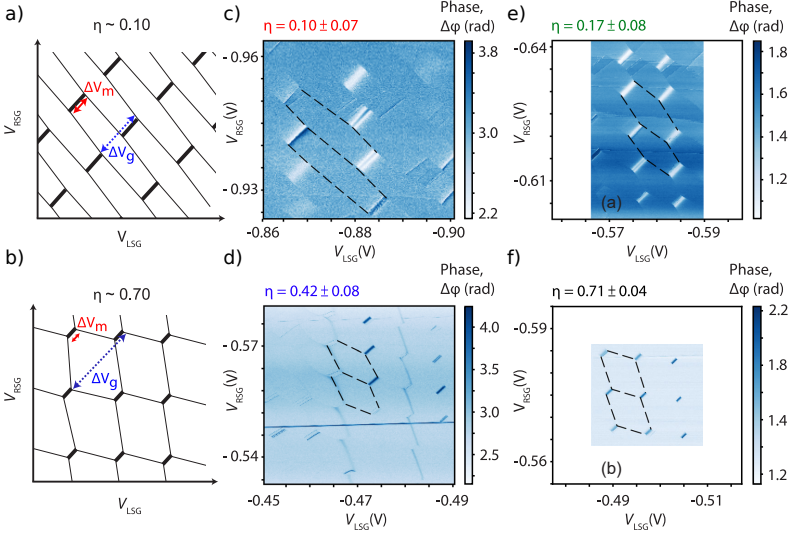


Figure 5.2. DQD charge stability diagrams. (a) A schematic of a DQD charge stability diagram for a configuration with a large mutual capacitance C_m , resulting in $\eta \sim 0.10$. The black areas (lines) represent inter-dot (QD_i -lead $_i$) charge degeneracy regions. The dipole strength η is determined directly from the charge stability diagrams. ΔV_m and ΔV_g are the voltage distance between the two triple points and QD-lead energy degeneracies, respectively. (b) Same as (a), but for smaller C_m , resulting in $\eta \sim 0.70$. (c-f) measured DQD charge stability diagrams obtained for four different DQD configurations in correspondence of four distinct values of C_m [decreasing from panel (c) to (f)]. Each charge stability diagram is measured by monitoring the change in the phase $\Delta\phi$ of the resonator reflectance in response to the DQD gate voltages. The axes scales of the LSG and RSG gate voltages are kept the same in the four panels for ease of comparison.

with a $1/f$ -type spectral function $S(\omega) = A/|\omega|$, $\omega_{ir} < \omega < \omega_c$, linearly coupled to the qubit. The low- and high-frequency cutoffs ω_{ir} and ω_c are typically defined through experimental timescales. In the quasi-static

approximation, where the noise is considered static in each individual run of the experiment, this leads to decay of the qubit off-diagonal density matrix element with a Gaussian form [155] as

$$\ln c_{in}^{1/f}(\tau) \equiv -\tau^2 \left(\frac{\partial \omega_q}{\partial \epsilon} \right)^2 \sigma_\epsilon^2 \quad (5.11)$$

$$\equiv -(\Gamma_\varphi \tau)^2. \quad (5.12)$$

Here, τ denotes the evolution time, and $c(\tau)$ is the decay envelope. Introducing the pure dephasing time Γ_φ , the expression can be written as a function of a dimensionless parameter $\Gamma_\varphi \tau$. Additionally, the noise parameter $\sigma_\epsilon \propto \partial \epsilon / \partial V_G$, given by Eq. (5.5), isolates the effects that are in our focus. Finally, the noise of semiconducting charge qubits is most probably not dominated by fluctuating voltages of the gates, but fluctuating charges of impurities. We show in Appendix D.3 that there is a relation analogous to Eq. (5.7) describing detuning response to charge impurity fluctuations.

The dipole strength as defined in Eq. (5.8) is experimentally easily accessible and provides useful qualitative predictions. Indeed, from Eq. (5.10) we see that the coupling to the resonator theoretically scales proportionally to η . Maximizing the coupling therefore calls for maximizing η , i.e. minimizing the mutual capacitance of the two dots. If the coherence of the DQD charge system is limited by electric noise-induced dephasing, the coherence time $1/\Gamma_2 \sim 1/\Gamma_\phi$ is, according to Eq. (5.12), expected to scale as $1/\eta$, since Eqs. (5.7) and (5.8) give $\partial \epsilon / \partial V_G \sim \eta$. Therefore, a maximally coherent charge qubit requires minimizing η . The scaling $1/\eta$ is a consequence of the singular noise resulting in a Gaussian decay form. Other relevant decay channels, like relaxation and non-singular noise, will lead to a scaling of the coherence time as $\propto 1/\eta^2$ [155]. We thus expect that depending on the details of the dominant noise source in the experiments, the qubit coupling quality factor $Q = g/\Gamma_2$ is either constant as a function of η (for singular noise dominating dephasing) or can be $\propto 1/\eta$ (for regular dephasing noise or if relaxation dominates). The latter situation would allow one to optimize Q by tuning the mutual dot capacitance. In the following Sec. 5.3, we investigate which specific scenario is realized in our system. We find that the charge-photon coupling strength g and decoherence rate Γ_2 are both *in-situ* tunable over an order of magnitude, while Q remains approximately constant. Minimizing the dipole

strength, we achieve a $\Gamma_2/2\pi < 5$ MHz. In section 5.4, aiming at maximizing the charge-photon coupling strength g , we employ a resonator with an even larger impedance. Making use of both terms in equation (5.10), we achieve a charge-photon coupling strength $g/2\pi \sim 630$ MHz for a fundamental mode resonator frequency of $\omega_r/2\pi \sim 5.6$ GHz.

5.3. Increasing charge qubit coherence

In this section, we describe experiments performed on the first device where we investigate a GaAs DQD charge qubit strongly coupled to a SQUID array resonator [see Fig. 5.1(a, c, d, e)] [35, 150]. We characterize the qubit coherence properties and its coupling strength g to the resonator. Aiming to reduce decoherence of the qubit, we *in-situ* explore different electrostatic confinement potentials of the DQD in the few-electron regime ($\sim 10 - 20$) obtained by tuning the voltages applied to the electrostatic gates defining the DQD [see Fig. 5.1(e)]. Each configuration leads to a different strength of the effective dipole interaction between DQD and resonator, characterized by a different dipole strength η as defined in Eq. (5.8).

We use a GaAs/AlGaAs heterostructure with a 2DEG ~ 90 nm below the surface. Depletion gates are used to define the DQD electrostatic potential. The right dot plunger gate is galvanically connected to the resonator [see Figs. 5.1(c, e)]. We measure the resonator response in reflection via the drive line [indicated in green in Fig. 5.1(c)] in a heterodyne detection scheme by monitoring the amplitude ($|S_{11}|$) and phase difference ($\Delta\phi = \text{Arg}[S_{11}]$) of the reflected signal [11]. An additional spectroscopy tone can be applied through the same line. The second DQD in the device [Fig. 5.1(c)] is tuned deeply into Coulomb blockade and does not participate in the reported experiment.

The impedance of the employed SQUID array resonator (see Fig. 5.1(a) and Fig. 5.1(c)) is estimated to be $Z_r^{\text{Sq}} = \sqrt{L_{\text{Sq}}/C_{\text{Sq}}} \sim 1$ k Ω . Similar high impedance resonators have been previously shown to enable the strong coupling regime between a DQD and microwave photons [35]. A magnetic flux, applied via a superconducting coil mounted on the sample box, is used to tune the resonator in the frequency range $\omega_r/2\pi \sim [4.2, 5.7]$ GHz (see Tab. D.1). The internal resonator dissipation κ_{int} and coupling to the microwave feedline κ_{ext} change with the resonator frequency, as shown in

5. Charge noise protection and ultrastrong coupling

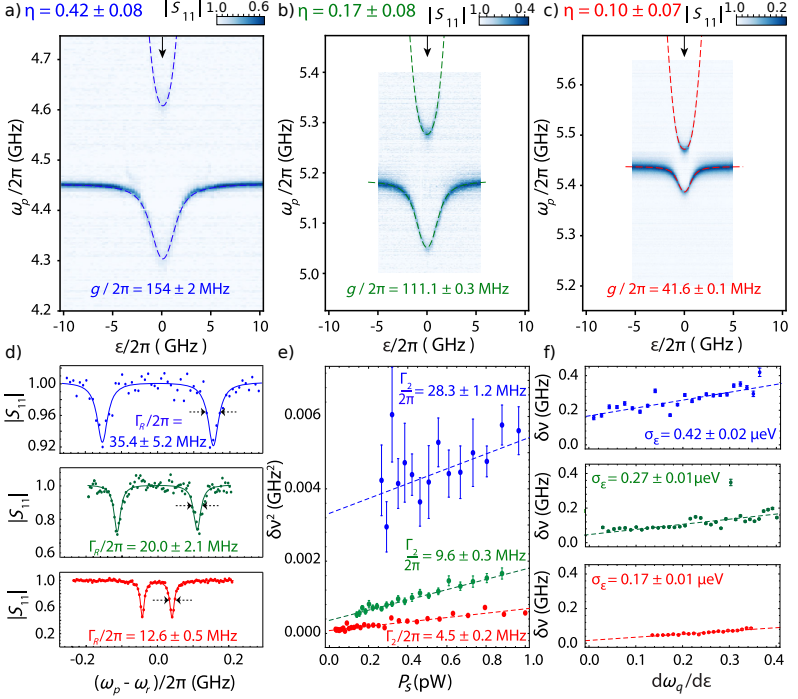


Figure 5.3. The dependence of the coupling strength g and DQD coherence rates Γ_R and Γ_2 for DQD configurations with dipole strengths $\eta = 0.42, 0.17, 0.10$. (a-c) Resonator reflectance amplitude $|S_{11}|$ versus DQD detuning ϵ for three representative values of the dipole strength $\eta \sim 0.42 \pm 0.08$ (blue), $\eta \sim 0.17 \pm 0.08$ (green) and $\eta \sim 0.10 \pm 0.07$ (red) [corresponding to the DQD charge stability diagrams in Fig. 5.2(c), (b) and (a), respectively]. (d) Resonator amplitude response $|S_{11}|$ (dots) *vs.* probe frequency $\omega_p/2\pi$ at $\epsilon = 0$ [see black arrow in the panels (a-c)], displaying well-resolved vacuum Rabi mode splittings. The solid line is a fit to the sum of two Lorentzian lines. The quoted Γ_R is computed as an average of the two linewidths. (e) Squared qubit linewidth $\delta\nu_q^2$ (dots) *vs.* spectroscopy drive power P_s , measured via two-tones spectroscopy [35]. The dashed lines are linear fits. The zero-power linewidths Γ_2 are given in the panel. (f) Qubit linewidth $\delta\nu_q$ (dots) *vs.* $d\omega_q/d\epsilon$ extracted from two-tones spectroscopy [35]. The dashed lines are linear fits. Their slopes define σ_ϵ according to Eq. (5.12).

Fig. D.3(c) in the appendix¹.

The DQD response to the gate voltages is characterized by charge stability diagrams [97] which we measure by recording the amplitude and phase response of the reflectance of the resonator [17]. From those diagrams, we extract the charging energies and capacitances of the DQD. In Figs. 5.2(c-f), we present four typical examples of DQD charge stability diagrams realized within the same device by *in-situ* tuning the voltages on the four gates defining the DQD [Fig. 5.1(e)]. The differences between the four configurations lie mainly in different voltages applied to the gates T and CG [cf. Fig. 5.1(e)] which control the inter-dot tunnel barrier, and are listed in Table D.2 in Appendix D.1. For ease of comparison, the axes scales are identical for the four panels of Fig. 5.2. We want to highlight that these four different configurations present similar inter-dot tunneling amplitudes t_c despite the different gate voltage values (see Table D.1 in the appendix).

Comparing the four DQD configurations shown in Figs. 5.2(c-f), we notice that the average spacing between the DQD triple points [97] [maximal in Fig. 5.2(c)] decreases relative to the spacing between two consecutive QD-reservoirs charge transitions [dashed lines in Fig. 5.2(c-f)]. This variation can be interpreted as a change in the contribution of the inter-dot coupling capacitance (C_m) to the total capacitance of the individual quantum dots (C_1 and C_2) [97]. This translates into the dipole strength η , Eq. (5.8), covering the interval [0.1, 0.7] in our experiments. Both C_m/C_Σ and the dipole strength η can be determined from the charge stability diagrams by considering the arrows indicated in the schematics in Figs. 5.2(a,b). The red arrow represents the distance of two adjacent DQD triple points and the blue arrow connects two consecutive electron transitions with the leads. As derived in Appendix D.1, in the simplified case of symmetric quantum dots, $C_{\Sigma,1} = C_{\Sigma,2} = C_\Sigma$, and neglecting gate-cross capacitances, one finds $C_m/C_\Sigma = \Delta V_m / (\Delta V_g - \Delta V_m)$ and $\eta = 1 - \frac{2\Delta V_m}{\Delta V_g}$. ΔV_m (ΔV_g) represents the length of the red (blue) arrow in Figs. 5.2(a,b). Furthermore, we emphasize that this striking change of the DQD inter-dot capacitance is obtained while keeping the inter-dot tunneling rate in the range $4 \text{ GHz} < 2t_c/2\pi < 6 \text{ GHz}$. The ability to control t_c and η independently allows us to probe the interaction with the resonator in both

¹The total dissipation of the SQUID array resonator is not constant as a function of the resonator frequency due to the presence of standing waves in its microwave feedline.

resonant and dispersive regimes.

In total, we study eleven different DQD configurations from which we extract the parameters summarized in Tab. D.1. For three of these configurations, we present in Fig. 5.3 the hybridized qubit-resonator energy spectrum [see Fig. 5.3(a-d)], a measurement of the intrinsic DQD charge qubit linewidth [see Fig. 5.3(e)], and a measurement of the root-mean-square amplitude of the detuning noise σ_ϵ defined in Eq. (5.12) [see Fig. 5.3(f)]. The data plotted in Fig. 5.3 (d) and 5.3 (e) were taken at charge degeneracy ($\epsilon = 0$).

In Fig. 5.3(a-c), we show three examples of hybridized spectra in the strong coupling regime for different dipole strengths. The DQD stability diagrams of the three configurations in Fig. 5.3(a,b,c) are shown in panels (e,d,c) of Fig. 5.2, respectively, in corresponding colors. We tune the DQD gate voltages and the SQUID array resonance frequency to reach the resonance condition $\omega_q = \omega_r$ at approximately zero detuning ϵ . Varying the DQD detuning, we observe the characteristic shifts in the dispersive regime and clear indications of an avoided crossing [22, 35] at resonance. We analyze the hybridized spectrum and extract the coupling strength g , resonator resonance frequency ω_r , and DQD tunneling amplitude t_c by fitting the observed resonances to the spectrum extracted from the system Hamiltonian (see Appendix D.5 for details). The Hamiltonian spectrum is plotted by dashed lines in Figs. 5.3(a-c).

When comparing these three configurations, we take note of a correlation between the coupling strength g and the visibility of the reflected signal (Rabi modes splitting) around the avoided crossing. Fig. 5.3(d) shows the linecuts at the resonance [detuning indicated by black arrows in Figs. 5.3(a-c)] visualizing the correlation between the coupling strength and the visibility of the Rabi modes splitting. Furthermore, increasing η , we observe a distinct increase of the linewidth of the Rabi modes [$\Gamma_R \sim (\kappa_{\text{ext}} + \kappa_{\text{int}})/2 + \Gamma_2$], extracted by fitting the data to a sum of two Lorentzian lines [see solid line in Fig. 5.3(d)], and a clear reduction in the depth of the two Lorentzian [compare the y-axis for the three panels of Fig. 5.3(d)]. This suggests that the dipole strength also has a strong influence on the system decoherence.

We investigate in more detail the correlations between the measured dipole strength η and the observed coherence of the charge qubit. Using two-tone spectroscopy [35, 156], we measure the intrinsic qubit linewidth at charge degeneracy ($\epsilon = 0$) and its sensitivity to the noise of the detun-

ing parameter induced by the charge noise of the DQD electromagnetic environment². Measuring the power dependence of the qubit linewidth, we extract the zero power linewidth ($P_S \rightarrow 0$) [see Fig. 5.3(e)] from which we determine the intrinsic DQD charge decoherence rate Γ_2 [35, 156]. In this experiment, we reached a DQD linewidth as low as 4.5 ± 0.2 MHz for a configuration with $\eta = 0.10 \pm 0.07$. In contrast, by *in-situ* tuning to a configuration with $\eta = 0.71 \pm 0.03$, the DQD charge qubit linewidth increases by a factor of eight.

At $\epsilon = 0$, the charge qubit is in first-order insensitive to charge noise since $\partial\omega_q/\partial\epsilon = 0$. Measuring the dependence of the qubit linewidth against the detuning ϵ , we extract the detuning noise σ_ϵ according to Eq. 5.12 [see Fig. 5.3(f) and Fig. 5.4(c) and also Refs. [148, 150]]. The extraction of σ_ϵ in two-tone spectroscopy was performed at a larger resonator read-out power explaining the lower error bars on the extracted linewidths and the higher value of qubit linewidth at $\epsilon = 0$ compared to Fig. 5.3(e). We notice that σ_ϵ clearly decreases for lower η .

The measurements presented in Fig. 5.3 indicate that increasing the capacitance ratio C_m/C_Σ reduces the resonator-DQD coupling strength g [Fig. 5.3(d)], the qubit decoherence $\Gamma_2 \equiv \delta\nu(P_S \rightarrow 0)$ [Fig. 5.3(e)], and the sensitivity of the qubit energy to detuning noise [Fig. 5.3(f)] [157]. The reduced sensitivity of the DQD to charge noise is engineered through a large mutual capacitance of strongly coupled QDs.

We summarize results of similar measurements for all eleven investigated DQD configurations in Fig. 5.4. In order to systematically compare the coupling strength g of the different configurations, we normalize it to³

$$\bar{g}_\perp = g(\omega_r = 2t_c = 2\pi \cdot 5 \text{ GHz}) = g \frac{2t_c}{\omega_r} \frac{5 \text{ GHz}}{\omega_r/2\pi}. \quad (5.13)$$

The normalization aims to systematically account for the small differences

²These measurements are implemented by changing the resonator frequency for performing these experiments in the dispersive regime, ensuring a negligible contribution of the Purcell induced decay ($\Gamma_{\text{purcell}}/2\pi < 0.05$ MHz). Also, we drive the resonator weakly so that its population is on average < 1 photon. The reflected signal is then amplified via a Josephson parametric amplifier with a gain of ~ 18 dB.

³From unpublished data, reported in Fig. D.6(a) in the appendix, which will be the topic of another manuscript, we observe an unexpected linear dependence of the coupling strength g on the resonator frequency $\omega_r (= \omega_q)$ measured at the sweet spot, $\epsilon = 0$. We take this into account by defining the normalized coupling \bar{g}_\perp , instead of the expected $\bar{g}'_\perp \propto \sqrt{\omega_r}$ dependence.

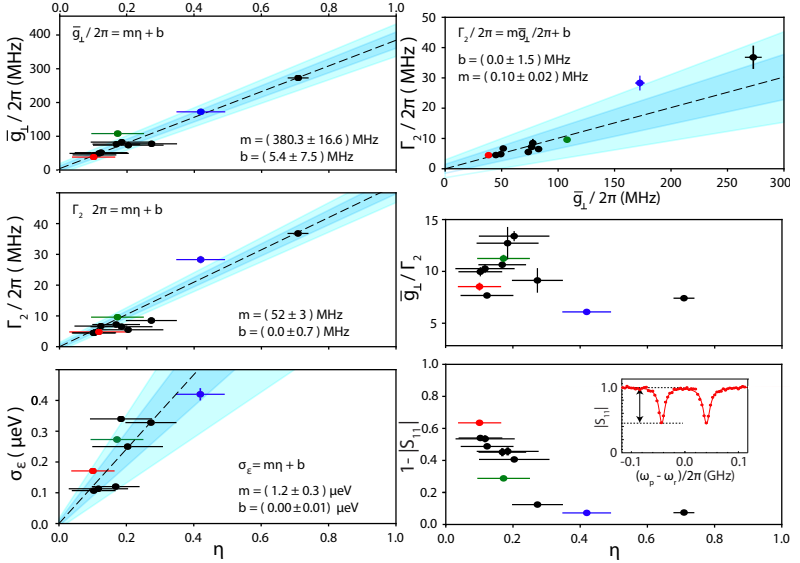


Figure 5.4. Coupling strength and decoherence parameters extracted for eleven DQD gate bias voltage configurations. (a) Normalized coupling \bar{g}_\perp [see Eq. (5.13)] of the DQD charge qubit to the resonator *vs.* the dipole strength η . (b) Qubit linewidth Γ_2 *vs.* η . The linewidth is extracted as in Fig. 5.3(e). (c) Effective detuning noise of the DQD charge qubit σ_ϵ *vs.* η , obtained as in Fig. 5.3(f). For two configurations with $\eta = 0.123$ and 0.709 , we could not extract σ_ϵ due to either spurious resonances and enhanced sensitivity to detuning noise, respectively. (d) DQD linewidth Γ_2 *vs.* the normalized coupling. The data in (a)-(d) were fitted to a linear model plotted as dashed lines and the fit parameters are stated in the panels. The dark [light] blue area represents the one-[two]-sigma confidence interval. (e) The quality factor \bar{g}_\perp/Γ_2 *vs.* η . (f) Visibility of the vacuum Rabi modes (at resonance) $(1 - |S_{11}|) = 2\kappa_{\text{ext}}/(\kappa_{\text{ext}} + \kappa_{\text{int}} + 2\Gamma_2)$ *vs.* η . The insert shows an example of a vacuum Rabi mode splitting with the black arrow indicating the visibility of a Rabi mode at the resonance.

in the resonator frequency/inductance and in DQD tunneling amplitude t_c [35] at which the experiments were performed (see Table D.1 and Appendix D.7). The normalized coupling strength ranges from 41.6 MHz to 250.6 MHz. The dependence of the normalized coupling \bar{g}_\perp on η agrees with the linear relation [see Fig. 5.4(a)] derived as Eq. (5.10).

A similar dependence on η is also observed for the DQD decoherence Γ_2 [Fig. 5.4(b)] and detuning noise σ_e [Fig. 5.4(c)], as modeled by Eq. (5.12). In order to display the linear relation between coupling strength \bar{g}_\perp and DQD decoherence Γ_2 , we plot both quantities in Fig. 5.4(d). The scattered (Γ_2, \bar{g}_\perp) data lies within the 3σ confidence interval of the linear fit. The proportionality relation is additionally highlighted by inspecting the quality factor of the resonator-qubit hybrid system $Q = \bar{g}_\perp/\Gamma_2$ [158]. In Fig. 5.4(e), we observe that Q does not show a strong dependence on the dipole strength η , but it is scattered around a mean value of 9.7 with a standard deviation of 2.2, indicating that the coherence of the system is likely dominated by dephasing due to singular charge noise (see Sec.I).

For a circuit QED architecture realized with semiconductor QDs and superconducting resonators, the strong coupling regime has been reached only recently [22, 35]. Intrinsic limitations are the high decoherence rate of the orbital-charge degree of freedom and the small electric-dipole moment of electrons confined in QDs. The high qubit decoherence implies low visibility of the vacuum Rabi mode splitting, even if the strong coupling is reached [35]. In Appendix D.5.4, we derive an expression for the visibility of the vacuum-Rabi mode splitting for a single port resonator coupled to a DQD and tested in reflection. In the case of a DQD and resonator being tuned into resonance, we find $(1 - |S_{11}|) = 2\kappa_{\text{ext}}/(\kappa_{\text{ext}} + \kappa_{\text{int}} + 2\Gamma_2)$. The estimated visibility is plotted in Fig. 5.4(f) for the different DQD configurations explored in this study. When tuning the DQD into a configuration where the inter-dot capacitance is the dominant contribution ($\eta \rightarrow 0$), the Rabi mode splitting visibility is considerably increased despite a reduction in the coupling strength. Furthermore, it is instructive to consider the system cooperativity, defined as $C = \bar{g}_\perp^2/[\Gamma_2(\kappa_{\text{ext}} + \kappa_{\text{int}})]$, representing a dimensionless measure of the light/matter interaction strength in our hybrid system. As reported in Appendix D.6 [see Fig. D.5(a)], we have achieved $C > 100$ by making use of the described tuning strategy for the DQD electric dipolar energy. It represents the highest cooperativity reported so far for hybrid QD-resonator systems (see Ref.[158] for a comparison), even when comparing to hybrid spin-photon systems.

Summarizing this section, we have realized a DQD coupled to a SQUID array resonator. We observed a striking and clear dependence of the DQD-resonator coupling strength, DQD charge decoherence rate, and DQD detuning noise on the dipole strength, parametrized by η , as defined in Eq. 5.8. The characterization of different DQD configurations, realized by changing *in-situ* the voltages applied to the DQD depletion gates over an extensive voltage range, demonstrates the possibility to reduce the charge qubit decoherence rate down to less than 5 MHz, thanks to the reduced DQD electric-dipole strength. The improved charge coherence allows to considerably increase the visibility of the charge qubit-resonator Rabi vacuum mode splitting at small coupling strengths (see Appendix D.5).

5.4. Ultrastrong coupling with a junction array resonator

In Sec. 5.3, we have investigated the possibility to *in-situ* tune the DQD dipolar coupling energy. We have explored the trade-off between the qubit-resonator coupling and the DQD charge decoherence rate. In this section, we show that the same strategy allows us to approach the ultrastrong coupling regime. With this goal in mind, we have realized a second device. The DQD of the second device is similar to the first, but the SQUID array resonator is replaced by a more compact Josephson-junction (JJ) array resonator [37]. Replacing SQUIDs with single Josephson junctions in the array makes the resonator fixed in frequency, reducing the flexibility on tuning parameters. On the other hand, as illustrated in Fig. 5.1(b) and explained in Appendix D.4, the change reduces the dimensions of the array unit. We thus achieve overall a higher total Josephson inductance with a shorter array: the length of the JJ resonator is $\sim 70 \mu\text{m}$, instead of $\sim 250 \mu\text{m}$ for the SQUID array [compare Fig. 5.1(a,b) and Fig. 5.1(c,f)]. The JJ array resonator has a lower stray capacitance to ground $C_{\text{gnd}}^{\text{JJ}} \sim 5 \text{fF}$, with a total inductance of $L_{\text{tot}}^{\text{JJ}} \sim 100 \text{nH}$ and, in turn, a resonator impedance $Z_r^{\text{JJ}} \sim 4 \text{k}\Omega$. Parameters of the SQUID and JJ arrays are compared in Tab. D.3.

Aiming at realizing the USC regime with semiconductor quantum dots, we investigate a DQD configuration corresponding to the largest dipole strength that we were able to achieve ($\eta \approx 0.72$). As discussed in Sec. 5.3, we detect the amplitude and phase of the signal reflected off the resonator. We configure the DQD tunneling amplitude close to $2t_c \sim \omega_r$ and change the DQD detuning. Upon bringing the qubit energy into resonance with

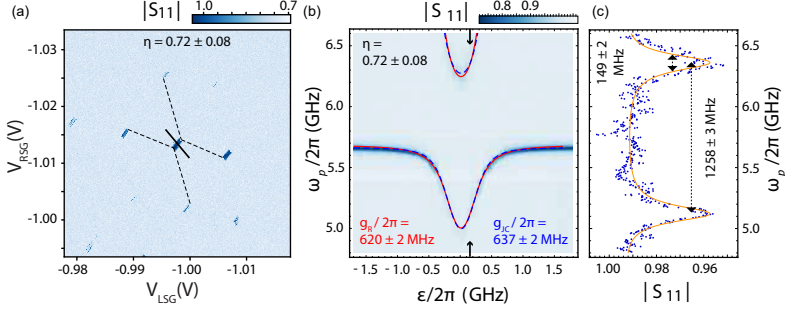


Figure 5.5. Investigation of a bias configuration approaching the ultrastrong coupling regime for a DQD coupled to a JJ array resonator. (a) Charge stability diagram of the DQD measured by monitoring the change in resonator reflectance amplitude $|S_{11}|$ for the extracted dipole strength $\eta = 0.72 \pm 0.08$. (b) Resonator amplitude response $|S_{11}|$ taken by varying the DQD detuning ϵ along the grey line indicated in panel (a) by applying appropriately chosen voltages to the two side gates. Red (blue) line represents a fit to the Rabi (JC) model (see Appendix D.5). (c) Measured resonator reflectance $|S_{11}|$ (dots) *vs.* probe frequency ω_p extracted at resonance for $\epsilon/2\pi = 0.15$ GHz (black arrows in panel (b)), displaying a vacuum Rabi mode splitting. The orange line represents a fit to a Rabi master equation model. The JJ array resonator losses are $\kappa_{int}/2\pi = 19.5 \pm 0.1$ MHz and $\kappa_{ext}/2\pi = 5.7 \pm 0.1$ MHz.

the resonator, $\omega_q \sim \omega_r$, a clear avoided crossing is observed in the resonator reflectance [see Fig. 5.5(b), and Fig. D.9(b)]. It is a sign of reaching the strong coupling regime.

The data are in excellent agreement with the spectrum of the hybridized system numerically calculated using g , ω_r and t_c as adjustable parameters. We fit a Rabi (red solid line) and a Jaynes–Cummings (blue dashed line) model and present the results in Fig. 5.5(b). We extract a coupling strength $g_R/2\pi \sim 620 \pm 2$ MHz ($g_{JC}/2\pi \sim 637 \pm 2$ MHz) from which we can estimate $g_{R,JC}/\omega_r \sim 0.11 \pm 0.01$, reaching the ultrastrong coupling regime [151–153]. The discrepancy between the values obtained from the Rabi and JC fits can be explained by the onset of the USC regime as the rotating-wave approximation starts to break down⁴. The resonator reflectance $|S_{11}|$ vs. probe frequency ω_p at the DQD-resonator detuning value indicated by the black arrow in Fig. 5.5(b) (resonant condition) is shown in Fig. 5.5(c). By fitting a master equation model [see solid orange line in Fig. 5.5(c)] to the measured $|S_{11}|$, we extract a DQD decoherence of $\Gamma_2/2\pi \sim 149 \pm 2$ MHz and a Rabi mode splitting of $2g/2\pi \sim 1258 \pm 3$ MHz. Resolving the two dips of the vacuum Rabi mode splitting indicates that the system is still in the strong coupling regime despite the extra decoherence introduced by the large DQD electric-dipole strength.

5.5. Conclusions

We have realized two hybrid devices with which we have studied charge configurations at the two extremes of the explored tunable DQD electric-dipole strength. We have demonstrated the systematic control of the DQD electric-dipole strength, allowing us to explore a broad range of different regimes in the same device. In particular, we have demonstrated that it is possible to decrease the electric dipolar coupling energy of the DQD by tuning it into a configuration in which the inter-dot mutual capacitance C_m becomes the dominant contribution of the total DQD capacitance. In such a configuration, the small dipole strength ($\eta \rightarrow 0$) reduces both the DQD coupling to the resonator and its decoherence rate, down to $g/2\pi \sim 40$ MHz and $\Gamma_2/2\pi < 5$ MHz, respectively.

⁴Fig. D.7 in Appendix D.8 reports the same analysis performed on a second DQD configuration characterized by $\eta \sim 0.5$. There we obtain comparable results from fits to the Rabi and JC models.

We have made use of the DQD dipole strength control reported here to reduce the decoherence rate of DQD devices used in some of our previous works. It has led to the observation of a DQD qubit linewidth down to $\Gamma_2/2\pi \sim 3$ MHz in a similar device [150, 159]. These decoherence rates are well below values reported typically for semiconductor charge qubits, usually observed to be above hundreds of MHz or even up to several GHz [35, 143, 160]. The possibility to achieve these remarkably low decoherence rates for a DQD charge qubit enabled the realization of time-resolved dispersive read-out [150], and distant qubit-qubit interaction mediated by virtual microwave photons [29, 159].

Here, we have provided a detailed explanation and a method to engineer low charge decoherence by modifying the contribution of the inter-dot capacitance C_m to the total QD capacitance, which we can easily assess and tune by exploring the DQD stability diagram. Furthermore, this work sheds new light on the puzzling observation reported by different experiments on QD-resonator hybrid system [150, 161] which reported that g and Γ_2 can vary considerably within the same device configured in different regions of the DQD charge stability diagrams.

In addition, we show that by using the same tuning strategy of the DQD confinement potential, but striving to maximize the DQD electric dipolar coupling energy, we can considerably increase the DQD-resonator coupling strength. This is achieved by configuring the DQD gates voltages to minimize the inter-dot capacitance C_m . To further increase the coupling strength, we implemented a more compact Josephson-junction (JJ) array resonator with reduced stray capacitance with respect to a SQUID array resonator. This results in a $Z_r^{JJ} \sim 4$ k Ω resonator impedance. The JJ array resonator enabled a maximum coupling of $g/2\pi \sim 630$ MHz for a fundamental mode resonator frequency of $\omega_r/2\pi \sim 5.6$ GHz. In this way, we realize the Ultra Strong Coupling regime between electrons hosted in a semiconductor DQD and a microwave resonator. By increasing the resonator impedance even further and by defining DQDs in shallower 2DEGs, or in semiconductor nanowires and Si-CMOS devices, where a higher gate lever-arm (up to 0.75 in [162]) has been demonstrated for QDs, it may well be possible to achieve $g/\omega_r \sim 0.4 - 0.5$. This could enable more advanced investigations of the effects of the breakdown of the rotating-wave approximation in this class of light-matter hybrid devices [151–153].

Recent experiments with holes confined in 2D-Ge heterostructures have reported effective charge/gate noise lower by a factor of 2-4 with respect

to Si and GaAs 2DEG systems [163], estimated by recording the current fluctuations of a charge detector over long waiting times. Applying the dipole strength tuning strategy described in this chapter to holes confined in QDs defined in 2D-Ge systems may enact a substantial improvement in the coherence properties of the charge degree of freedom. This could enable a more clear study of the ultrastrong coupling physics in the $\eta \rightarrow 1$ limit and the potential to extend the coherence for a DQD charge/spin qubit in the $\eta \rightarrow 0$ limit even further.

Understanding and improving the coherence and control of the electron/hole charge degree of freedom in semiconductor systems is of paramount importance also for future spin qubit applications, especially for systems where the spin is strongly hybridized with the orbital degree via a large real [46] or artificial spin-orbit field [164], enabling the coupling with microwave photons. We anticipate that these findings will be of great significance for state-of-the-art charge and/or spin qubits as well as any hybrid QD-cavity designs, which are currently all limited by electrical noise.

We acknowledge Christian Andersen, Mihai Gabureac, Theo Walter, Johannes Heinsoo, for the useful discussion and thank Christina Reisel for proof-reading. This work was supported by the Swiss National Science Foundation through the National Center of Competence in Research (NCCR) Quantum Science and Technology, the project Elements for Quantum Information Processing with Semiconductor/Superconductor Hybrids (EQUIPS) and by ETH Zurich.

6 Charge-sensing of a GeSi nanowire double quantum dot

In the previous Chapter 5 we demonstrated how the potential landscape of a double-quantum dot (DQD) can be engineered, while realizing record large charge qubit coherence times and charge qubit-photon coupling strengths. We now turn towards coupling magnetic-field resilient NbTiN resonators to nanowire DQDs.

The realization of high quality, magnetic-field resilient resonators has already been addressed in Chapter 4, and in this chapter we discuss how a high-impedance NbTiN resonator is used in order to detect the charge configuration of a DQD, eventually being able to detect the last hole in one of the quantum dots.

This chapter is a submitted paper [165].

Charge-sensing of a Ge/Si core/shell nanowire double quantum dot using a high-impedance superconducting resonator

J. H. Ungerer,^{1,2,*} P. Chevalier Kwon,^{1,*} J. Ridderbos,^{1,3} A. Kononov,¹
 D. Sarmah,¹ E. P. A. M. Bakkers,^{4,5} D. Zumbühl^{1,2} and
 C. Schönberger^{1,2}

¹Department of Physics, University of Basel, Klingelbergstrasse 82 CH-4056, Switzerland

²Swiss Nanoscience Institute, University of Basel, Klingelbergstrasse 82 CH-4056, Switzerland

³MESA+ Institute for Nanotechnology, University of Twente, P.O. Box 217, 7500 AE Enschede, The Netherlands

⁴Kavli Institute of Nanoscience, Delft University of Technology, Lorentzweg 1, 2628 CJ Delft, The Netherlands

⁵Department of Applied Physics, TU Eindhoven, Den Dolech 2, 5612 AZ Eindhoven, The Netherlands

*These authors contributed equally.

Abstract

Spin qubits in germanium are a promising contender for scalable quantum computers. Reading out of the spin and charge configuration of quantum dots formed in Ge/Si core/shell nanowires is typically performed by measuring the current through the nanowire. Here, we demonstrate a more versatile approach on investigating the charge configuration of these quantum dots. We employ a high-impedance, magnetic-field resilient superconducting resonator based on NbTiN and couple it to a double quantum dot in a Ge/Si nanowire. This allows us to dispersively detect charging effects, even in the regime where the nanowire is fully pinched off and no direct current is present. Furthermore, by increasing the electro-chemical potential far beyond the nanowire pinch-off, we observe indications for depleting the last hole in the quantum dot by using the second quantum dot as a charge sensor.

6.1. Introduction

The interest in group-IV semiconductor spin qubits is large because of their small footprint, a low concentration of nuclear spins and the available knowledge about their production in semi-conductor industry [1, 138, 139,

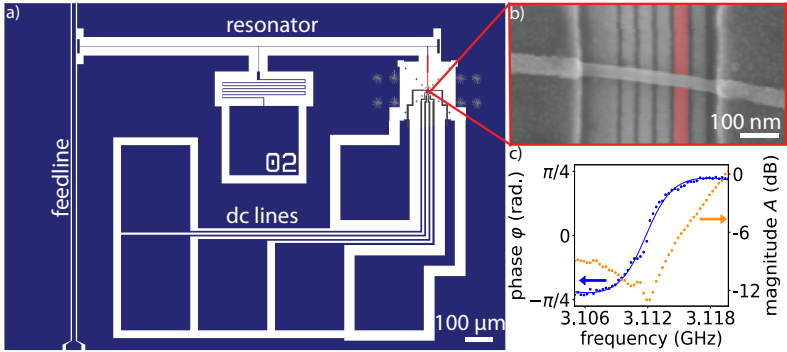


Figure 6.1. Device overview. a) Schematic of hybrid resonator architecture. NbTiN is shown in dark blue, the Si substrate is shown white. The feedline on the left is used for reading out the notch-type coplanar-waveguide half-wave resonator which is dc biased at its voltage node in the center. Additional dc lines are used for sending current through the nanowire and applying gate voltages on all bottom gates. b) False-colored scanning electron micrograph of the Ge/Si nanowire lying on top of bottom-gates covered with HfO₂ of a similar device. The gate colored red is connected to the resonator. c) Transmission (phase and magnitude) through the feedline as a function of frequency close to the resonator frequency. The solid blue curve indicates a fit from which we extract the resonance frequency and estimate the quality factor (see main text).

166, 167]. By integrating on-chip superconducting resonators, strong spin-photon coupling has been demonstrated for spins of confined electrons in a Si two-dimensional electron gas [25, 26]. Hole spins may offer the additional advantages of improved relaxation and decoherence times as they lack a valley degeneracy and exhibit a reduced wave-function overlap with nuclear spins [168, 169]. In particular, holes in one-dimensional Si or Ge nanowires [85, 170, 171] are of a special interest, because they possess strong spin-orbit interaction [86, 172, 173]. Strong spin-orbit interaction potentially simplifies qubit control and coupling to resonators by electric-dipole spin resonance (EDSR) [87, 90]. It thereby releases the need of implementing micromagnets and hence facilitates scaling-up.

Recently, the coherent manipulation of a hole-spin qubit in a gate-defined double quantum dot in a Ge/Si core/shell nanowire has been demonstrated [46]. However, in these experiments both the charge and the spin-state of the double quantum dot were determined by direct current measurements. This technique limits the capability of determining the total number of holes present in the nanowire. Furthermore, it requires long integration times and severely limits the maximum cycle length in pulsed-gate experiments.

Rather than measuring the current through the Ge/Si core/shell nanowire DQD, pioneering works have employed another quantum dot to determine changes in the charge-occupancy of the DQD and to perform spin read-out [43, 47].

A different approach for measuring the DQD is realized by probing a resonator coupled to the source contact of the DQD [174–176]. This approach is further simplified by connecting the resonator to a plunger gate, performing gate-dispersive sensing [177]. This technique has enabled measurements of the relaxation and dephasing times of hole spins in a Ge/Si core/shell nanowire DQD using a lumped-element resonator [44]. First attempts of coupling Ge/Si nanowires to on-chip superconducting resonators were based on low-impedance resonators with a weak charge-photon coupling and in a regime of many holes present in the nanowire [48].

In this work, we extend the existing measurements by coupling one of the two quantum dots to a high-impedance superconducting resonator, see Fig. 6.1. The used coupling scheme allows us to detect charging in the other dot by means of capacitive charge sensing [178–181]. We map the charge-stability diagram using both, direct current measurements and resonator spectroscopy. Furthermore, we gate the nanowire to a regime of low hole occupancy where no direct current through the nanowire can be observed (pinch-off). In this regime, the resonator spectroscopy signal reveals the presence of several more holes in the investigated dot. Finally, by further increasing the gate voltages, we find indications of the depletion of the last hole from the investigated dot.

6.2. Device description

An overview of the device under investigation is shown in Fig. 6.1a) and b). The device consists of a hybrid resonator-nanowire architecture. A notch-type half-wave ($\lambda/2$) resonator with a central frequency $f_0 \approx 3.1$ GHz is

defined in a NbTiN film of thickness ~ 10 nm, center conductor width of ~ 370 nm and a distance between center conductor and ground plane of ~ 35 μ m. The resonator is capacitively coupled at a voltage anti-node to a feedline which is used for resonator readout. At the middle of the center conductor (voltage node), the resonator is dc biased. In front of the dc bias pad, a meandered inductor ensures sufficient frequency detuning between the $\lambda/2$ mode and a second, quarter-wave mode that forms due to the T-shaped section of the resonator. Thereby, microwave-leakage through the dc bias line is reduced [105]. The resonator's second voltage anti-node is galvanically connected to one out of five bottom gates. The bottom gates are fabricated by Ti/Pd sandwiched by ALD-grown HfO₂ and have a width of approximately 25 nm. The gate pitch is 50 nm. On top of the bottom gates a Ge/Si core/shell nanowire is deterministically placed using a micromanipulator, see Fig. 6.1 b). All presented measurements are performed in a dilution refrigerator at a base temperature of 35 mK.

The transmission S_{21} through the feedline in proximity to the notch-type resonator as a function of frequency f is given by [72, 78]

$$S_{21}(f) = ae^{i\alpha}e^{-2\pi if\tau} \left[1 - \frac{e^{i\Phi}/(1 + Q_c/Q_{\text{loss}})}{1 + 2i(f/f_r - 1)/(1/Q_c + 1/Q_{\text{loss}})} \right], \quad (6.1)$$

where a , α and τ account for the microwave propagation through the wiring in the cryostat and the resonance is described by its resonance frequency f_0 , the coupling quality factor Q_c and the loss quality factor Q_{loss} . The term $e^{i\Phi}$ accounts for the Fano shape of the observed resonance arising from impedance mismatches in the feedline coupled to the resonator [77].

We identify the resonance of the superconducting resonator at around 3.1 GHz by considering its temperature dependence. The measured transmission (phase and magnitude) through the feedline around resonance is shown on Fig. 6.1c). The signal is superimposed on a large standing-wave background (see Fig. E.1 in the appendix.) which we attribute to an impedance mismatch between the feedline and the 50-Ohm environment of the cryostat. Despite the large fluctuations in the transmission magnitude, we are able to fit the phase of the transmission (solid, blue curve in Fig. 6.1c) and extract the resonance frequency $f_0 = 3.111$ GHz, and estimate the Q factors $Q_c \approx 600$ and $Q_{\text{loss}} \approx 600$. The uncertainty in these values originates from the large standing wave background.

We perform a finite-element simulation of the resonator using Sonnet and recover the resonance frequency of the central mode of the resonator half-wave mode when taking into account a sheet kinetic inductance of $70 \text{ pH}/\square$. Together with the stray line capacitance of $75 \text{ pF}/\text{m}$, this corresponds to a resonator impedance of $1.6 \text{ k}\Omega$, much larger than the standard 50Ω , hence improving the coupling strength between resonator and double quantum dot [12, 32]. We attribute the rather low Q_{loss} to microwave leakage from the resonator to the dc lines via capacitive coupling through the set of bottom gates [106]. Indeed, using Sonnet, we estimate the mutual capacitance between two neighbouring bottom gates to be $C_{\text{gg}}' \approx 800 \text{ aF}$. In future works, the mutual capacitance can likely be decreased with an optimised gate geometry and the resulting microwave leakage might be further reduced via improved filtering of the dc lines [105, 117].

6.3. Charge sensing

Due to the Fermi level pinning stemming from the staggered Si/Ge band-gap alignment, the Ge/Si core/shell nanowire is a hole conductor. Therefore, by applying positive gate voltages, we define the barrier potentials on the gates g_1 , g_3 and g_5 . This gives rise to the confinement potential of two quantum dots whose electrochemical potentials are tuned by the gates g_2 and g_4 [92].

In the following, we investigate two different confinement configurations. The first configuration is schematically depicted in Figure 6.2a). Here, two fairly symmetric quantum dots, the left and right dots, dot L and dot R, are formed between the gates g_1 and g_3 and between the gates g_3 and g_5 . In this configuration, each dot couples to its respective neighbors as shown on the sketch in Figure 6.2a). In Figure 6.2b), we plot a measurement of the direct current through the nanowire I_{sd} as a function of the voltages on gates g_2 and g_4 . Because of Coulomb blockade, we measure a finite current through the nanowire only at the triple points at which the electrostatic potential of both dots is aligned with the electrostatic potential of the leads. By connecting the triple points (dashed white lines in Figure 6.2b)), we find the charge-stability diagram in the shape of a honeycomb pattern [97].

Simultaneous to measuring the current through the nanowire, we send a microwave signal through the feedline at a frequency close to the resonance frequency f_0 . We perform dispersive gate sensing by measuring

6. Charge-sensing of a GeSi nanowire double quantum dot

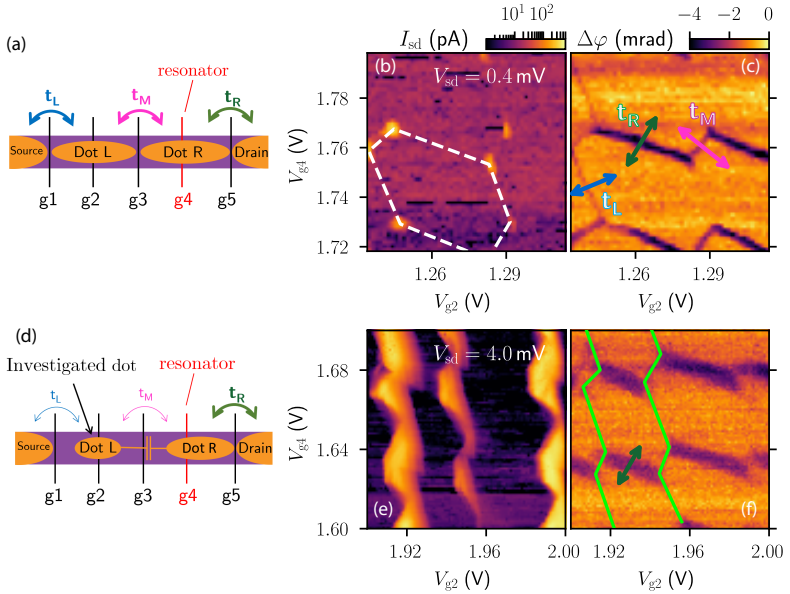


Figure 6.2. Charge sensing. a) Schematic of the gate-defined double quantum dot and the relevant tunnel couplings between dots and leads. b) Logarithmic current, I_{sd} , through the nanowire exhibiting the position of triple points. Here, the bias voltage is $V_{sd} = 400 \mu\text{V}$ and the values of the other gate voltages are $V_{g1} = 3.2 \text{ V}$, $V_{g3} = 1.175 \text{ V}$, $V_{g5} = 9.0 \text{ V}$ c) Phase difference, $\Delta\varphi$ of the resonator spectroscopy acquired at the same time as b). Tunnel couplings depicted in a) cause a phase shift of the resonator when any potentials of the system are aligned, as indicated by the colored double arrows corresponding to the tunnel transitions in a). d) Schematic of double quantum dot for a more isolated configuration. e) and f) correspond to b) and c) for the configuration depicted in d). Solid, green lines in f) indicate discharging lines of dot L. Here, the values of the other gate voltages are $V_{g1} = 3.2 \text{ V}$, $V_{g3} = 1.15 \text{ V}$ and $V_{g5} = 9.0 \text{ V}$. The bias voltage is $V_{sd} = 4 \text{ mV}$ and therefore bias triangles appear larger in e) compared to b). The microwave power at the input of the feedline is $\sim -60 \text{ dBm}$ for both measurements.

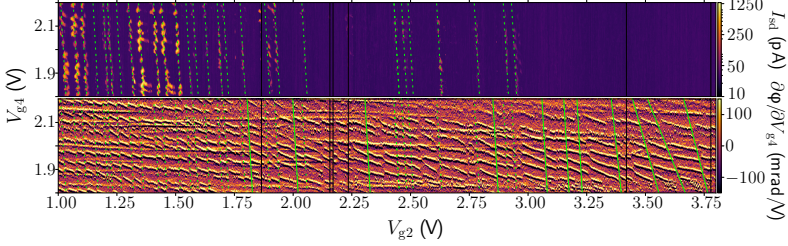


Figure 6.3. Nanowire pinch-off. top panel: Map of dc current through the nanowire as a function of gate voltages V_{g2} and V_{g4} , eventually vanishing completely above $V_{g2} \approx 3$ V as the nanowire is pinched off. The positions at which dot 1 is resonant with the lead are highlighted with white, dashed lines. bottom panel: Simultaneously measured resonator spectroscopy, $\partial\varphi/\partial V_{g4}$. The resonator spectroscopy shows the same resonance conditions as in the top panel (green, dashed lines). However, additional transitions are observed (green, solid lines). Gate jumps are marked with vertical, black, solid lines. In this measurement, the other gate voltages are $V_{g1} = 3.2$ V, $V_{g3} = 1.1$ V and $V_{g5} = 9.0$ V and the bias voltage is $V_{sd} = 2$ mV and the readout frequency is $f_{ro} = 3.1259$ GHz.

the phase change of the transmitted signal and plot it in Figure 6.2c) as a function of gate voltages. As the resonator is capacitively coupled to the quantum dots via one of the plunger gates, it is sensitive to their effective admittance [17, 107, 182]. Therefore, by sending a signal through the feedline at a frequency close to the resonator frequency, changes in the transmission amplitude and phase can be detected when the quantum dot admittance changes. Indeed, we note that in the plotted phase response, one can clearly identify the honeycomb pattern of the charge-stability diagram. Whenever the electrochemical potential between a dot and its respective lead, or between the two dots, is aligned, a shift in the phase response is observed. The charge-stability diagram that we gain from both dc and rf measurements are well described by a capacitance model [97]. By considering the change of the number of electrons when changing the gate potentials and using the source-drain bias triangles as an absolute energy scale, we fit the data according to the recipe described in Appendix A of Ref. [137]. We extract the capacitances that are specified in Tab. 6.1.

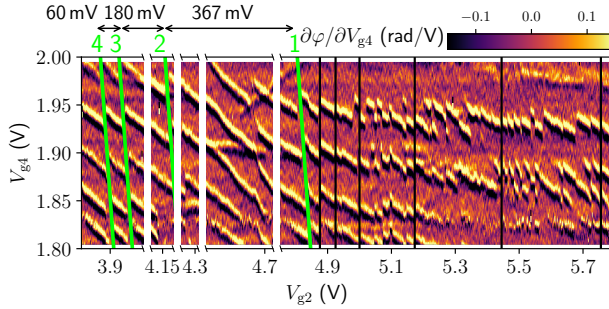


Figure 6.4. Indications of last hole depletion. Resonator spectroscopy, $\partial\varphi/\partial V_{g4}$ as a function of gate voltages, V_{g2} , V_{g4} . Resonances correspond to dot-lead transition and characteristic discontinuities correspond to hole discharging from the dot. For gate voltages, $V_{g2} > 4.9$ V, no further regular discontinuities are observed. Instead, random jumps dominate the signal indicating that the last hole has been depleted. For the green discharging lines, the corresponding numbers of holes is indicated with a green number. Data repetition due to gate switchers has been omitted in the graph. Here, the other gate voltages are $V_{g1} = 3.2$ V, $V_{g3} = 1.1$ V and $V_{g5} = 9.0$ V. The source drain bias voltage is $V_{sd} = 2$ mV and the readout frequency is $f_{ro} = 3.1259$ GHz.

	2a,b,c)	2d,e,f)
$C_{g2,dL}$ (aF)	3.4 ± 0.4	5.4 ± 0.8
$C_{g4,dL}$ (aF)	0.2 ± 0.4	0.8 ± 0.7
$C_{\Sigma,L}$ (aF)	51 ± 19	15 ± 7
$C_{g2,dR}$ (aF)	0.4 ± 0.4	0.1 ± 0.6
$C_{g4,dR}$ (aF)	4.1 ± 0.5	4.1 ± 0.5
$C_{\Sigma,R}$ (aF)	57 ± 20	20 ± 12
C_M (aF)	17 ± 8	8 ± 5

Table 6.1. Gate-to-dot capacitances, where C_{g_i,d_j} is the capacitance between gate g_i and dot j ($i \in \{2, 4\}$ and $j \in \{L, R\}$). $C_{\Sigma,j}$ denotes the total capacitance of dot j and C_M is the dot's mutual capacitance.

After, having demonstrated the possibility of detecting the charge-stability diagram by means of resonator spectroscopy, we tune the double quantum dot system into the configuration which is schematically depicted in Figure 6.2f). The main difference to the previous configuration relies in the larger voltage on the gate g_2 , while the barrier gate voltages V_{g1} and V_{g3} are not changed significantly. This corresponds to a geometrically smaller dot L with a lower number of holes. Hence, the tunneling rate t_L between the source and dot L, as well as the inter-dot tunneling rate t_M are reduced. In this configuration, it is therefore not possible to measure these transitions using resonator spectroscopy. However, the remaining tunnel rate t_R is, in first order, not affected, enabling us to use the dot R as a sensor for tracking Coulomb resonances of dot L [178–181]. When we progressively deplete dot L, the tunneling rate between the sensor dot and the drain always remains similar to the resonator frequency. This allows us to track discharging lines of dot L despite the fact that the tunneling involving dot L happens at much lower frequencies and can therefore not directly be detected by dispersive resonator sensing.

Figure 6.2d) shows the current through the nanowire in this configuration. Although the bias voltage is by an order of magnitude larger, the amplitude in Fig. 6.2d) stays relatively constant compared to the one in Figure 6.2b) as the tunnel couplings are suppressed. Nonetheless, we are still able to identify the locations of the triple points in the conductance measurement and calculate the capacitances as given in Table 6.1. Com-

parison of the conductance with the phase response in Figure 6.2e) shows that the transmission through the feedline clearly exhibits a change in phase whenever the electrochemical potential of the sensor R is resonant with the one in the drain. We note characteristic jumps in the observed resonances. These jumps correspond to discharging of a hole in the dot L. Therefore, by interconnecting jumps (green lines in Figure 6.2f)), we determine the Coulomb resonances of the dot L.

While staying in the same configuration, the top panel of Figure 6.3 shows the current through the nanowire in a large range of V_{g2} . Coulomb resonances of the dot L that are observable in the current are highlighted by dashed, green lines. We note that when considering only the current, the largest gate voltage, at which a Coulomb resonance of dot L is observed, is $V_{g2} \approx 3$ V. On the other hand, when examining the simultaneously measured resonator response in the bottom panel of Figure 6.3, we identify several sloped lines that correspond to the sensor being in resonance with the drain. Here, for better visibility, we plot the derivative of the phase response with respect to the gate voltage V_{g4} . These sloped lines have kinks upon removing a hole from dot L because of the dots mutual capacitance. Therefore, by interconnecting the kinks, a Coulomb resonance of dot L is found. We identify several more Coulomb resonances of the dot L than in the dc measurement. Note that the observed Coulomb resonances have a finite slope of $m = \Delta V_{g4} / \Delta V_{g2} \approx -18$ because of a finite capacitance between gate g4 and dot L. Inadvertent charge switching events occurring during this measurement can be rather easily identified because they happen suddenly, at a time scale smaller than the acquisition time of a single data point. Such a single event appears as a (vertical) jump in gate voltage shifting the data along the entire axis, which we refer to as a gate jump from here on. Some of these gate jumps are indicated by vertical, black lines in the figures (e.g. around $V_{g2} \approx 2.2$ V in Fig. 6.3). Even for gate voltages V_{g2} much larger than the nanowire pinch-off at 3 V, several Coulomb resonances are found which cannot be identified when only considering the current through the nanowire. We note that in the lower panel of Fig 6.3, several horizontal features without any kinks are visible. These are interpreted to originate from impurities coupling to the resonator, independent of the quantum dots.

Finally, with the goal in mind to deplete the last hole from dot L, we tune the gates into a third configuration in which we increase V_{g1} from 3.1 V to 5.8 V. In this configuration, the nanowire is fully pinched-off and

a direct current cannot be measured. In Figure 6.4, we plot the derivative of the phase on the resonator signal with respect to the gate voltages V_{g2} and V_{g4} . Once again, we identify resonances corresponding to tunnelling between dot R and the drain. When connecting the characteristic shifts of these resonances, we obtain the parallel discharging lines (solid, black lines in Figure 6.4) of the dot L with a slope of $m = \Delta V_{g4} / \Delta V_{g2} = -4.8$. The smaller slope as compared to Fig. 6.3 corresponds to a larger relative effect of gate g4 compared to gate g2 which makes sense as the large gate voltage of g2 pushes the dot away. The transition to smaller slopes is also clearly visible in Fig. 6.3 for voltages $V_{g2} \gtrsim 3.4$ V where the current is already suppressed.

Since we work with larger gate voltages and thus a decreasing number of charges present in the wire, there is less screening and the wire becomes less stable, suffering from several gate jumps. These gate jumps result in shifts along the V_{g2} -axis towards less positive voltages. In order to focus on the physics that corresponds to discharging of the dot L, those shifts are removed in Figure 6.4 where the removed regions are also clearly marked. For completeness, the full data set can be found in Fig. E.2 in the appendix. In Figure 6.4, we observe a total of four sloped, parallel lines; each corresponding to discharging of a single hole from the dot L. The penultimate charging line is observed at $V_{g2} = 4.2$ V (bottom axis) indicating the 2 to 1 hole transition in dot L, while the last charging line is found at $V_{g2} = 4.90$ V, showing the position of the 1 to 0 hole transition. We note that even after subtracting the additional voltage range, because of shifts along the V_{g2} -axis due to gate jumps, the effective voltage distance between these two lines is $\Delta V_{g2} \approx 370$ mV, much larger than the distance between any two previous discharging lines.

For voltages larger than $V_{g2} = 4.80$ V, beyond the last observed discharging line, the amount of gate jumps increases drastically. They randomly shift the observed resonances in the gate-gate map and yield vertical disruptions of dot-lead resonances, even within a single vertical gate sweep (fast scan axis). We therefore conclude that they correspond to the random charging and discharging of unwanted charge traps in proximity to the nanowire. The absence of any further dot discharging lines appearing with a slope can give some confidence that indeed, the last hole was depleted from the left dot. We speculate that after depletion of the last hole from the dot, the sensor is more susceptible to unwanted charge traps as the screening by dot L vanishes. Hence, the increase of random

gate jumps is consistent with the interpretation that the discharging line at $V_{g2} = 4.80$ V may correspond to discharging of the last hole.

6.4. Conclusions

We demonstrate charge sensing of a Ge/Si core/shell nanowire double quantum dot by using a superconducting, high-impedance, on-chip NbTiN resonator. Using bottom gates, we are able to define a double quantum dot in the nanowire and consistently map the characteristic charge-stability diagram by both direct current measurements and resonator spectroscopy. By changing the electrostatic potentials on the gates, we tune the double quantum dot into a regime of a more isolated dot and a second, sensor dot which together with the resonator, we employ as a charge sensor of the first dot. By increasing the gate voltages, we consecutively deplete holes from the dot. We find that even in the regime where no current through the nanowire could be detected, because it is pinched-off, the sensor reveals several more hole discharging events while increasing the gate voltages. Finally, we find indications of the depletion of the last hole from the nanowire. Our measurements confirm that observing only the direct current through these type of nanowires is not a sufficient criterion for counting the absolute number of holes present in a quantum dot in Ge/Si core/shell nanowires. The circuit-quantum electrodynamics architecture presented in this manuscript lies the foundations for realizing coherent charge-photon and spin-photon coupling based on semiconductor nanowires. We expect that a reduction of the gate-gate and resonator-feedline capacitances will result in resonator quality factors by an order of magnitude larger. Frequent gate jumps inhibited using the device as a spin qubit. However, the charge stability of the system might be improved in the future by working on the quality of the oxides and nanowires. Because similar nanowires have been employed as spin qubits [46], we anticipate that the improvements on the resonator in combination with a more stable nanowire device will enable strong charge photon and hole-spin photon coupling in Ge/Si core/shell nanowires.

This research was supported by the Swiss Nanoscience Institute (SNI), the Swiss National Science Foundation through grant 192027 and 179024, and the NCCR Spin Qubit in Silicon (NCCR-Spin). We further acknowledge funding from the European Union's Horizon 2020 research and innovation programme, specifically the FET-open project AndQC, agreement

No 828948, the FET-open project TOPSQUAD, agreement No 847471, and the European Microkelvin Platform (EMP), agreement No 824109. We also acknowledge support through the Marie Skłodowska-Curie CO-FUND grant QUSTEC, grant agreement N° 847471, and the Georg H. Endress foundation.

7 Dispersive interaction between a crystal-phase defined double quantum dot and a microwave photon

In the previous chapter, we have investigated how a superconducting resonator coupled to a double-quantum dot (DQD) in a Ge/Si core/shell nanowire can be used to detect the charge configuration inside the nanowire. However, the device which was presented, showed many gate-jumps inhibiting us from realizing a spin qubit. We now turn towards a DQD realization in another material system, namely a crystal-phase defined DQD in an InAs nanowire as was discussed in Section 2.3.1.

The pre-defined barriers of the crystal-phase engineered DQD allow us to reduce the number of gates used for operating the DQD. Because no gates are needed for electrostatically defining the DQD, photon losses of the resonator through the gate lines can be reduced as the resonator-to-gate capacitance can be designed to be much lower compared to implementations of DQDs in Ge/Si core/shell nanowires or DQDs in two-dimensional materials.

Because operating a spin quantum bit (qubit) in this structure is highly dependent on the properties of the charge qubit, in this Chapter, we investigate how the charge qubit decoherence rate γ and charge qubit photon coupling-strength g_0 depend on the inter-dot tunneling t_c . We do so while keeping the capacitances of the DQD approximately constant. This is complementary to Chapter 5 where we investigated how γ and g_0 depend on the capacitance configuration of the DQD while keeping t_c approximately constant.

This chapter is the result of a close collaboration with Alessia Pally and some of the data is also presented in her thesis [183].

7.1. Device description

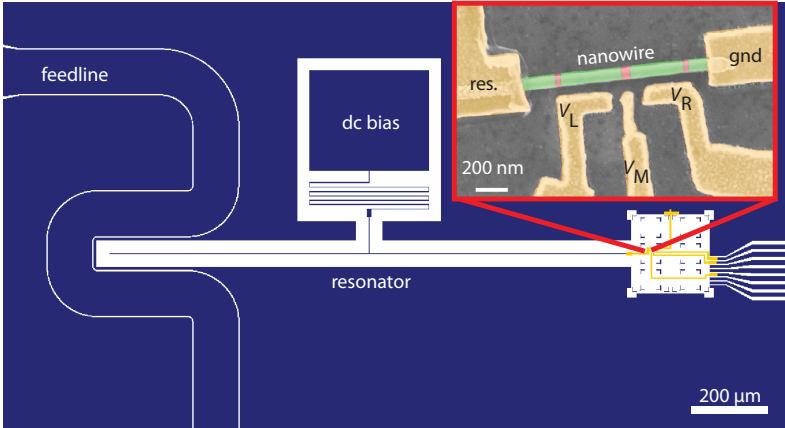


Figure 7.1. Device image. A notch-type half-wave resonator with a narrow center conductor is formed from thin NbTiN (blue). The resonator can be direct current (DC)-biased via a dc bias pad that is separated from the center conductor by a meandered inductor. The feedline on the left side of the figure is used for resonator readout. On the right-hand side the nanowire device is fabricated. The inset shows a false-colored scanning-electron micrograph. The zincblende segments of the nanowire are colored in green and the wurtzite barriers are colored in red. The lead contact labelled with ‘res.’ is connected to the resonator. The other lead is hard-grounded.

Figure 7.1 shows the device that is being measured and analyzed, which is fabricated in a collaboration with Alessia Pally. Because we are interested in measuring both the total quality factor of the resonator coupled to the DQD and the coupling to the feedline, a notch-type, high-impedance resonator is fabricated from a thin film of NbTiN on top of intrinsic silicon, and the resonator corresponds to the design presented in Figure 3.5 in Section 3.4. The DQD is formed by a zincblende InAs nanowire where the dc part of the device is fabricated in a designated area of the resonator chip as shown in the inset of Figure 7.1. In the nanowire, a DQD is formed

in the zincblende segments (green) separated with wurtzite tunnel barriers (red).

The resonator is coupled to the DQD via its right voltage anti-node, which is contacted to the source contact of the nanowire. The second nanowire lead is hard grounded to the ground plane and the electrochemical potentials of the quantum dots is varied by applying voltages to the side gates labelled with V_L and V_R in the figure. The voltage V_M on the side gate in the middle is not used and left close to zero for the measurements presented here. A 20 nm thick atomic-layer deposition (ALD)-grown hafnium oxide layer is located underneath the nanowire device, ensuring electrical isolation of the gates.

7.2. Device characterization

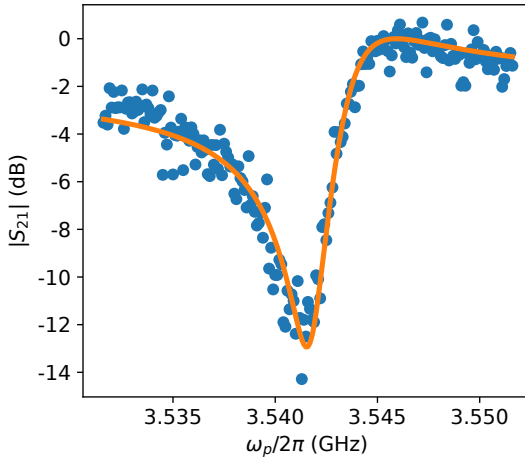


Figure 7.2. Bare resonator. Transmission $|S_{21}|$ through the feedline as a function of probe frequency ω_p , exhibiting the resonance of the notch-type resonator. The solid line is the amplitude of a circular fit [78].

Before characterizing the combined device, we first identify the resonance of the resonator at $\omega_p^0/2\pi = 3.543$ GHz and extract the external

7. Dispersive interaction between a crystal-phase defined double quantum dot and a microwave photon

quality factor $Q_c = 1290 \pm 40$ and loss quality factor $Q_{\text{loss}} = 2319 \pm 200$ (see Fig. 7.2). Compared to the test device without a nanowire (see Fig. 3.5), we notice that Q_c is similar, while Q_{loss} is reduced by an order of magnitude. We attribute this expected drop in Q_{loss} to the loss through the capacitive coupling between the resonator and the gate lines [21, 105, 117]. Nevertheless, Q_{loss} is still similar to similar resonator devices [22, 117], despite our larger impedance and our lack of on-chip gate filtering. We explain this by the limited number of gates required to operate the crystal-phase defined DQD, leading to a reduced resonator to gate capacitance. To characterize the coupled device, we measure the dc current through

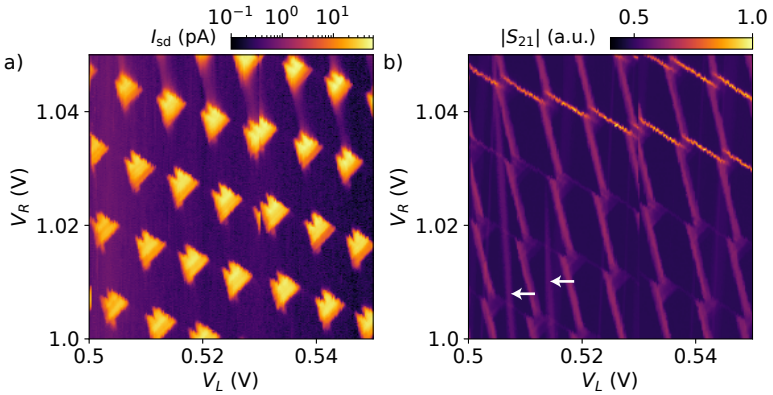


Figure 7.3. Comparison between transport and resonator response. a) current I_{sd} through the DQD at a bias voltage of $V_{\text{sd}} = 100 \mu\text{V}$ showing bias-triangles. b) Transmission through the feedline $|S_{21}|$ at the resonator frequency. The two measurements were performed simultaneously.

the nanowire at a fixed bias voltage as a function of the plunger gate voltages V_L and V_R . Simultaneously, we measure the transmission through the feedline at the resonance frequency. The results of the current and resonator spectroscopy are shown in Figure 7.3. In the measured current in Figure 7.3a), we can clearly identify bias triangles, where their size is proportional to the difference in the electro-chemical potentials of source

and drain, i.e., the applied bias. Therefore, when states are within this energy window, electrons can sequentially tunnel through the DQD [97]. Regular bias triangles are therefore a distinct signature of a well-defined DQD in the presence of a finite source drain bias voltage.

The resonator response is shown in Figure 7.3b). We note that the measured response of the resonator corresponds to the same charge-stability diagram as the measured current, but that the resonator is sensitive to different features than the current: While a current is measured dominantly at the bias triangles, the resonator senses dispersively whenever quantum dot states are resonant, either with each other or with a lead. This is a direct consequence of the dipolar coupling between the resonator and the tunneling charge in the DQD [17].

In addition, we also measure distinct features dispersing with the gate voltages that are not related to the charge-stability diagram. They present themselves as almost vertical lines indicated by white arrows in Figure 7.3b). Because they do not interact with the features corresponding to the DQD but still couple to the resonator, we attribute these lines to impurities in the substrate spatially separated from the DQD.

7.3. From double-dot to single dot

Identifying the correspondence between the dc transport and the dispersive response of the resonator, allows us to switch the bias voltage to zero and to focus purely on the resonator response. This is particularly useful as it allows investigation of the DQD also in configurations where no current to the leads can be measured. Figure 7.4 shows a high-resolution charge-stability diagram measured in a larger gate range. We note that while increasing the gate voltage V_R , we observe an evolution from a DQD (see Figure 7.4b) with clearly identifiable triple points, to a single Coulomb-blockaded quantum dot (see Figure 7.4c). Operating at more positive gate voltages implies that the dots are populated with more electrons occupying increasingly high energy states. For these higher energy states, the effective tunnel barrier due to the crystal phase is lower, resulting in a larger tunnel rate t_c . In the top right of Figure 7.4 an almost complete wave function overlap is realized and hence signatures of a single dot are measured [45, 184]. So the data presented in Figure 7.4 clearly demonstrates that it is possible to change the inter-dot tunnel rate t_c of the DQD by changing the gate voltages.

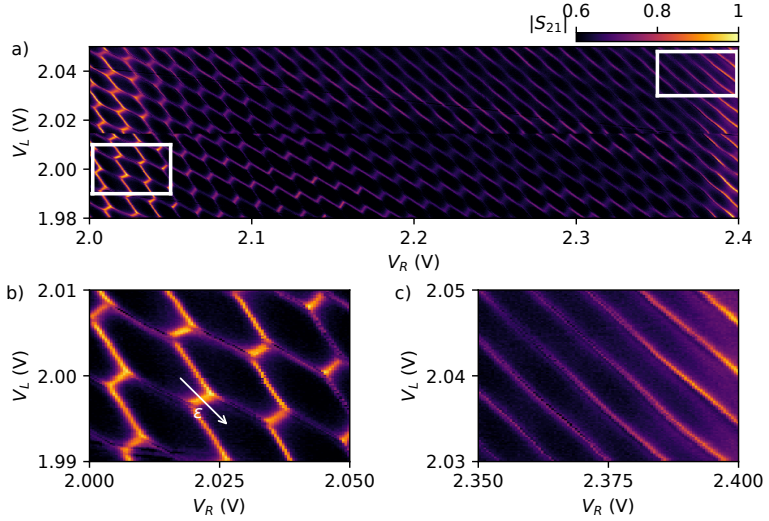


Figure 7.4. Charge-stability from DQD to single dot. a) Transmission $|S_{21}|$ through the feedline at the resonator frequency as a function of plunger gate voltages V_L and V_R . b) Zoom in the DQD regime. c) Zoom in the single dot regime. The position of b) and c) are indicated in a) by white rectangles. Here, it is $V_M = V_{sd} = 0$ V.

7.4. Resonator response versus tunnel rate.

The data presented in Figure 7.4 clearly demonstrates the ability to change the inter-dot tunnel rate t_c of the DQD by changing the dot occupancies. We will use the dispersive resonator response to investigate the dependence of the dipolar interaction strength g_0 , and the charge qubit linewidth γ on t_c . To gain a deeper understanding of the interdependencies of these variables we investigate five different inter-dot transitions, each with a different t_c . For each transition we measure according to the following protocol consisting of 5 steps:

(1) To quantitatively analyze the dispersive response of the resonator, we first measure a small charge-stability diagram similar to the one shown

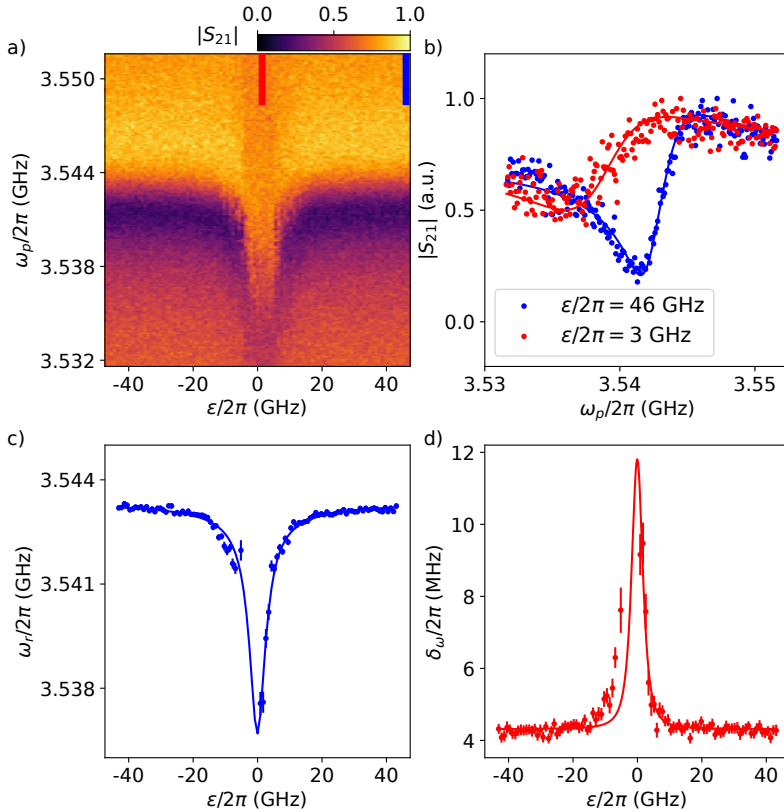


Figure 7.5. Large dispersive shift. a) Transmission $|S_{21}|$ through the feedline as function of detuning ϵ and probe frequency ω_p , showing a dispersive shift of the resonator and corresponding resonator broadening. b) Linecuts through a) at fixed ϵ as indicated by the bars in a). Solid lines are amplitude of a circular fit of $S_{21}(\omega)$. c) Extracted resonance frequency ω_r of the dressed resonator. d) Extracted linewidth δ_ω of the dressed resonator. Solid lines in c) and d) are fits to Equation (7.1) and Equation (7.2).

in Figure 7.4b).

(2) We then focus on one specific inter-dot transition. From the charge-stability diagram, we extract the system's capacitances according to the recipe described in Section D.1 [97, 137]. To calibrate the required energy scale for every investigated inter-dot transition, we apply a finite bias and measure a bias triangle similar to the one shown in Figure F.1 in the appendix. The bias voltage acts as an absolute energy scale and therefore from the size of the measured bias triangle, the conversion from gate voltages to detuning ϵ is realized (lever arm calibration). All extracted capacitances for the five different investigated inter-dot transitions are found in Table F.1 in the appendix.

(4) Then, at zero bias, we measure the resonator response along the detuning line ϵ of the specific inter-dot transition. Exemplary, this line is indicated for one inter-dot transition in Figure 7.3b).

(5) Finally, using the calibrated lever arm, we plot the resonator response as function of frequency and detuning ϵ in Figure 7.5a).

The resonator response shown in Figure 7.5a) exhibits two effects which become obvious when considering the two linecuts shown in Figure 7.5b): First, the resonance frequency of the dressed resonator decreases as the difference between the charge transition frequency $\omega_q = \sqrt{|2t_c|^2 + \epsilon^2}$ and the bare resonator frequency ω_r^0 decreases for decreasing $|\epsilon|$. Second, the linewidth of the dressed resonator increases for decreasing $|\epsilon|$. We quantify this by performing a circular fit [78] at every value of ϵ (solid lines in Figure 7.5b), extracting the dressed resonator frequency and linewidth as a function of detuning, and plotting it in Figure 7.5c) and d).

The combined system of a single microwave photon in the resonator and a charge qubit in the DQD is described by the Jaynes-Cummings model which is introduced in Section 2.1.1. In the dispersive case, when the bare qubit frequency is larger than the resonance frequency of the resonator, the transition frequency from the ground state to the dressed resonator state is given by [12]

$$\omega_r = \omega_r^0 - \frac{1}{2} \sqrt{4g^2 + (\omega_r^0 - \omega_q)^2}, \quad (7.1)$$

where $g = g_0 \cdot 2t/\omega_q(\epsilon)$ is the effective charge-photon coupling strength accounting for the finite mixing angle at positive detuning. Furthermore,

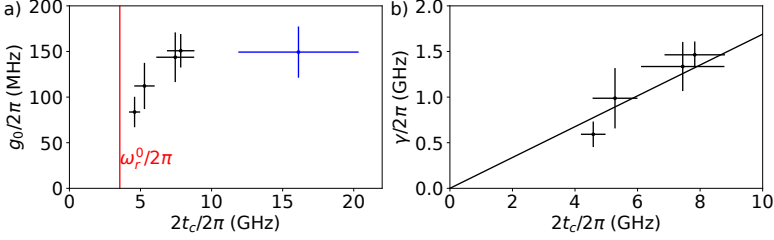


Figure 7.6. Dispersive coupling versus tunnel rate. a) Dipolar coupling g between the charge qubit and resonator mode versus DQD tunnel rate t_c . The red, solid line indicates the resonator frequency ω_r^0 . b) Charge qubit linewidth γ as a function of tunnel rate t_c . The black, solid line is a fit to $\gamma = m_\gamma \cdot t$ with $m_\gamma = 0.34 \pm 0.03$

the linewidth of the dressed resonator state is given by [12]

$$\begin{aligned} \delta_\omega &= |\langle \psi_- | g, 1 \rangle|^2 \kappa + |\langle \psi_- | e, 0 \rangle|^2 2\gamma \\ &= \cos^2(\theta) \kappa + \sin^2(\theta) 2\gamma, \end{aligned} \quad (7.2)$$

where κ is the decay rate of the resonator, γ is the bare qubit linewidth and $\theta = \frac{1}{2} \arctan\left(\frac{2g}{\omega_q - \omega_r^0}\right)$ [12]. We use Equation (7.1) to fit the extracted frequencies of the dressed resonator, which is shown as a solid line in Figure 7.5c). We keep the calibrated gate lever arm fixed in the fitting procedure, and extract the bare charge qubit-photon coupling strength g_0 and the inter-dot tunnel rate t_c as fit parameters.

Next, using the extracted values of g_0 and t_c , we fit Equation (7.2) to the dressed resonator linewidths. From the fit, we extract the bare qubit linewidth γ . The result of the analysis on the five analyzed inter-dot transitions is shown in Figure 7.6. Figure 7.6a) shows the charge-photon coupling strength at zero detuning g_0 versus the charge tunneling rate t_c , where we observe no clear trend.

For the configuration corresponding to very large t_c (blue data point in Figure 7.6a)), no broadening of the dressed resonator is measured and therefore, γ cannot be determined for this specific point. Figure 7.6b) shows the fitted values of γ versus t_c for all other investigated DQD configurations. We find that γ is proportional to t_c (see figure caption), which

implies that the qubit Q factor $Q \equiv 2t_c/\gamma \sim 6$ is constant and independent of t_c . We note that similar or even smaller values have been obtained for other realizations of charge qubits in nanowires [48, 185] and speculate that the proximity of the DQD to the nanowire surface could lead to large charge noise yielding charge qubit decoherence and hence a small Q factor.

7.5. Bloch-Siegert shift in the strong dispersive regime

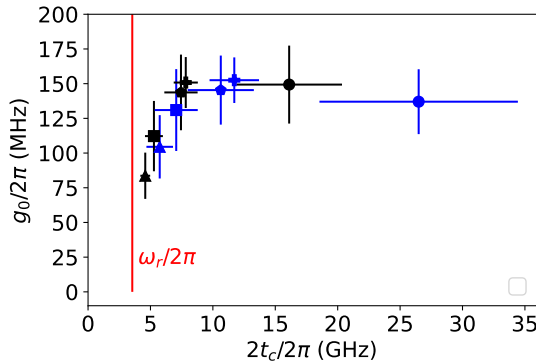


Figure 7.7. Comparison between Jaynes-Cummings model and Bloch-Siegert model. Coupling strength g_0 versus tunnel rate t_c extracted using a Jaynes-Cummings model (black points) and a model including the Bloch-Siegert shift (blue points). Data points with the same symbols correspond to the same configuration.

In the previous section, we have found strong dispersive resonance frequency shifts due to the dipolar interaction between the resonator and the charge qubit in the DQD and analyzed this interaction in the scope of a Jaynes-Cummings model (JCM). However, we note that in the very open regime, the extracted tunnel rates $2t_c$ and hence qubit transition frequencies are much larger than the resonator resonance frequency ω_r^0 . In this strong dispersive regime, the counter rotating terms that were neglected in the rotating-wave approximation in Section 2.1.1 matter, and now the

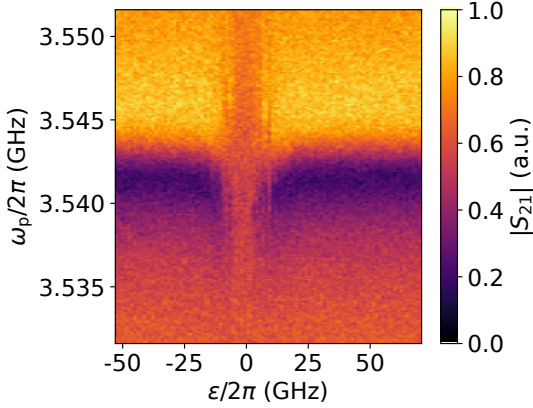


Figure 7.8. Charge-qubit crosses resonator. Transmission $|S_{21}|$ through the feedline as function of probe frequency ω_p and detuning ϵ . When the qubit frequency is similar to the resonator resonance frequency, the dressed resonator state broadens significantly and eventually fully vanishes.

dressed resonator frequency can be written as [2, 186]

$$\omega_r = \omega_r^0 - \left(\frac{g^2}{\omega_q - \omega_r^0} + \frac{g^2}{\omega_q + \omega_r} \right), \quad (7.3)$$

where the term proportional to $g^2/(\omega_q - \omega_r^0)$ is called Lamb shift and the term proportional to $g^2/(\omega_q + \omega_r)$ is called Bloch-Siegert shift. We repeat the analysis presented in the previous section while using Equation (7.3) instead of (7.1) and compare the results of the two analyses in Figure 7.7.

We note that while for low tunnel rates the results of the two analyses are similar, for large t_c , increasingly large differences in t_c are obtained while the obtained values of g_0 remain similar.

7.6. Entering the resonant regime

After having characterized the dispersive resonator-charge qubit regime, we find a configuration of gate voltages in which the charge qubit tun-

nel rate is smaller than the resonator frequency, $2t_c \lesssim \omega_r^0$. In this configuration and by tuning ϵ , the charge qubit transition frequency $\omega_q = \sqrt{|2t|^2 + \epsilon^2}$ can become equal to the resonator frequency, thus entering the resonant regime. Figure 7.8 shows the resonator spectroscopy as a function of detuning ϵ in this regime. Because the charge qubit linewidth ($\gamma \sim 1$ GHz) is much larger than resonator linewidth ($\kappa/2 \sim 10$ MHz), the dressed resonator broadens significantly when ω_q approaches ω_r^0 . For low ϵ , the dressed resonator broadening is so large that no distinct resonance curve can be measured anymore.

7.7. Conclusions and Outlook

We have demonstrated for the first time a dipolar interaction between a high-impedance resonator and a charge qubit defined in a crystal-phase engineered nanowire. We find large dispersive signals and measure the dipolar interaction strength g_0 between a charge-qubit and a resonator mode in the single photon regime by fitting the dispersive shift using a Jaynes-Cummings Hamiltonian. We measure charge-photon couplings as high as $g_0 = 150 \pm 30$ MHz.

These large coupling strengths are confirmed by considering not only the Lamb shift but also by using a more complete model that includes the Bloch-Siegert shift, which is relevant when the qubit-resonator interactions are in the strong dispersive regime.

Considering the broadening of the dressed resonator, we also extract the charge-qubit linewidth γ . By varying the number of electrons in the DQD, we change the charge tunnel rate between the quantum dots t_c while keeping the DQD capacitances approximately constant. While no clear dependence of g_0 on t_c is observed, we find that the qubit linewidth γ is proportional to the tunnel rate t_c and measure a qubit quality factor ~ 6 .

When working close to the resonant regime $2t_c \lesssim \omega_r^0$, the dressed resonator linewidth broadens substantially, eventually smearing out completely. In the same device presented in this chapter, attempts were made to measure the qubit parameters as a function of magnetic field. However, because of gate jumps, we are unable to perform measurements over time scales longer than a few hours which is essential for performing measurements at elevated magnetic-field strengths due to the slow nature of ramping up and down a large magnet. We attribute the large number of

gate jumps to the ALD-grown oxide which is located in direct vicinity to the nanowire and we therefore change the experiments in two aspects.

Firstly, we increase the coupling between the resonator and the feedline substantially, aiming on a strongly over-coupled resonator. Increasing the external coupling to the resonator ensures a better matching between the qubit linewidth and the resonator decay rate. To do so, we employ a resonator probed in transmission which has two advantages compared to a notch-type resonator. The first advantage is that despite aiming on large κ_c , the resonator can be designed fully symmetric ensuring low photon loss through the dc tap (see Section 3.3). The second advantage is that, as we read-out the resonator at its resonance frequency, the signal to noise ratio is substantially higher (see Section 2.2.6).

Secondly, we fabricate the next resonator generation on top of a wafer covered with 100 nm of silicon dioxide. The silicon dioxide is an established substrate material for operating the crystal-phase engineered DQDs [45, 93]. And, as demonstrated in Chapter 4, NbTiN resonators fabricated on top of silicon dioxide still show internal quality factors $Q_{\text{loss}} > 10^3$. Therefore the oxide does not limit the resonator quality, because of the intentionally large coupling to the feedline. A device incorporating these improvements is discussed in Chapter 8.

8 Strong coupling between a single photon and a singlet-triplet qubit

In the experiments described in Chapter 6 and in Chapter 7, the resonator had been fabricated on top of intrinsic silicon aiming on large internal quality factors. This made it necessary to cover the intrinsic silicon substrate below the nanowire device with atomic-layer deposition (ALD)-grown hafnium oxide. The resulting devices showed many gate jumps on the time scale of several minutes which inhibited operation as a spin quantum bit (qubit); stability on much longer timescales is required because of the involvement of an external magnetic field which can only be varied slowly.

However as demonstrated in Chapter 4, magnetic-field resilient, high-impedance resonators based on NbTiN can also be fabricated on a wafer covered with the much more ‘silent’ thermally grown silicon oxide, while maintaining internal quality factors $Q_{\text{loss}} > 10^3$. We connect these resonators to the side-gate of a crystal-phase defined double-quantum dot (DQD) in a zincblende InAs nanowire, resulting in fewer gate jumps, allowing us to investigate the resonator-qubit coupling at elevated magnetic field strengths. Because of the large spin-orbit interaction present in the nanowire, at magnetic fields $B > 500$ mT, a spin-orbit qubit is formed whose linewidth and coupling to the resonator is investigated both in the dispersive and resonant regime.

This chapter is a submitted paper [187]. It is the result of a collaboration with Alessia Pally and can therefore also be found in her thesis [183].

Strong coupling between a microwave photon and a singlet-triplet qubit

J. H. Ungerer,^{1,2,*} A. Pally,^{1,*} A. Kononov,¹ S. Lehmann,³
J. Ridderbos,¹ C. Thelander,³ K. A. Dick,⁴ V. F. Maisi,³ P. Scarlino,⁵
A. Baumgartner,^{1,2} and C. Schönenberger^{1,2}

¹Department of Physics, University of Basel, Klingelbergstrasse 82 CH-4056, Switzerland

²Swiss Nanoscience Institute, University of Basel, Klingelbergstrasse 82 CH-4056, Switzerland

³Solid State Physics and NanoLund, Lund University, Box 118, S-22100 Lund, Sweden

⁴Centre for Analysis and Synthesis, Lund University, Box 124, S-22100 Lund, Sweden

⁵Institute of Physics and Center for Quantum Science and Engineering, Ecole Polytechnique Fédérale de Lausanne, CH-1015 Lausanne, Switzerland

Abstract

Tremendous progress in few-qubit quantum processing has been achieved lately using superconducting resonators coupled to gate voltage defined quantum dots. While the strong coupling regime has been demonstrated recently for odd charge parity flopping mode spin qubits, first attempts towards coupling a resonator to even charge parity singlet-triplet spin qubits have resulted only in weak spin-photon coupling strengths. Here, we integrate a zincblende InAs nanowire double quantum dot with strong spin-orbit interaction in a magnetic-field resilient, high-quality resonator. In contrast to conventional strategies, the quantum confinement is achieved using deterministically grown wurtzite tunnel barriers without resorting to electrical gating. Our experiments on even charge parity states and at large magnetic fields, allow us to identify the relevant spin states and to measure the spin decoherence rates and spin-photon coupling strengths. Most importantly, at a specific magnetic field, we find an anti-crossing between the resonator mode in the single photon limit and a singlet-triplet qubit with an electron spin-photon coupling strength of $g = 114 \pm 9$ MHz, reaching the strong coupling regime in which the coherent coupling exceeds the combined qubit and resonator linewidth.

8.1. Introduction

Spin qubits in semiconductors are promising candidates for scalable quantum information processing due to long coherence times and fast manipulation [1, 3, 138, 139]. For the qubit readout, circuit quantum electrodynamics based on superconducting resonators [188], allows a direct and fast measurement of qubit states and their dynamics [21]. Recently, resonators were used to achieve charge-photon [22, 35], spin-photon [27, 33, 34] as well as coherent coupling of distant charge [29] and spin qubits [30, 31], enabling coherent information exchange between distant qubits. However, the small electric and magnetic moments of individual electrons require complicated device architectures such as micromagnets, and a large number of surface gates that render scaling up to more complex architectures challenging. These approaches typically achieve a relatively weak electron spin-photon coupling on the order of $\sim 10 - 30$ MHz. In addition to single electron spin-qubits, also spin qubits based on two electrons in a double quantum dot (DQD), e.g. in a singlet-triplet qubit have been demonstrated [5]. Spin qubits based on two electrons typically offer a large hybridization of the spin and charge degree of freedom compared to single-electron spin qubits in principle allowing even stronger coupling strengths. So far, however, the experimentally achieved coupling strengths in such systems [189, 190] remained well below the strong coupling limit in which the coherent coupling rate exceeds both, the cavity mode decay rate and the qubit linewidth.

Here, we demonstrate that the strong coupling regime between a singlet-triplet qubit and a superconducting resonator can be reached. We achieve this strong coupling by carefully designing the resonator and by using a DQD defined by in-situ grown tunnel barriers in a semiconductor with a large spin-orbit interaction. The tunnel barriers consist of InAs segments in the wurtzite crystal-phase with an atomically sharp interface to the zincblende bulk of the nanowire (NW) [40]. We make use of the large spin-orbit interaction in these wires [49] to define a singlet-triplet qubit at a finite magnetic field in which the $T_{1,1}^+$ and $S_{2,0}$ states hybridize, forming a quantum two-level system. For the qubit spectroscopy, we use a magnetic-field resilient resonator based on NbTiN that can be operated in magnetic fields exceeding 2 T [32, 113]. At $B \sim 1.7$ T, the singlet-triplet qubit hybridizes with the resonator with a record-high electron spin-photon coupling strength reaching the strong coupling limit.

8.2. Device characterization

The resonator-qubit system is shown in Figure 8.1a), including a false-colored SEM-image of the crystal-phase defined NW DQD. The DQD is hosted in the 280 nm and 380 nm long zinblende segments (green), separated by 30 nm long wurtzite (red) tunnel barriers with a conduction band offset of ~ 100 meV [93], as illustrated in Fig. 8.1(b). A high-impedance, half-wave coplanar-waveguide resonator is capacitively coupled to the DQD at its voltage anti-node via a sidegate. In addition, the same sidegate can be used to tune the DQD charge states using a dc voltage (V_R) applied at the resonator voltage node. The DQD state is probed by reading out the resonator rf-transmission. We extract the bare resonance frequency of the resonator $\omega_r/2\pi = 5.25308 \pm 0.00003$ GHz and the bare decay rate $\kappa/2\pi = 34.4$ MHz. The resonator design and fitting are described in detail in Section G.1 in the appendix.

In the following, we prepare the DQD in an even charge configuration in the many-electron regime (see appendix, Section G.2), described by a two-electron Hamiltonian given in the Section G.4 in the appendix. Figure 8.1(c) shows the eigenvalues of this Hamiltonian as a function of external magnetic field B at a fixed DQD detuning. At zero magnetic field, the detuning renders the singlet $S_{2,0}$ the ground state, for which both electrons reside in the same dot. Without spin-rotating tunneling, this, and the $S_{1,1}$ state, with the electrons distributed to different dots, form a charge qubit [191]. The subscripts describe the dot electron occupation of the left and right dot respectively. By applying an external magnetic field, the Zeeman effect can lower the energy of the triplet $T_{1,1}^+$ state, that becomes the ground state for sufficient high magnetic fields. However, the intrinsic spin-orbit interaction hybridizes the $S_{2,0}$ and $T_{1,1}^+$ states, with the two new eigenstates of the avoided crossing forming a singlet-triplet qubit shown schematically in Figs. 8.1(a) and (b).

Fig. 8.2(a) shows the charge stability diagram of the DQD detected as a shift in the transmission phase φ of the resonator, plotted as a function of the two gate voltages V_L and V_R at a fixed probe frequency of 5.253 GHz, close to resonance. We observe a slanted honeycomb pattern, in which the inter-dot transition lines exhibit a negative slope due to the specific gate geometry (see Fig. 8.1(a)), which results in the right gate (V_R) coupling stronger to both dots than the left (V_L). Using a capacitance model [97, 137], we extract the gate-to-dot capacitances $C_{R2} = 2.5 \pm$

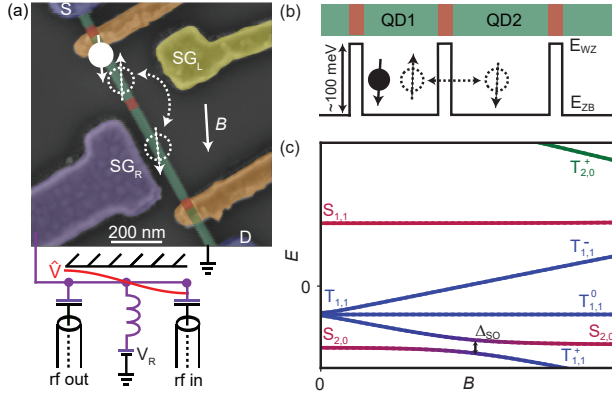


Figure 8.1. Coupled resonator-qubit system (a) False colored SEM image of the device. The NW (green) is divided into two segments by an in-situ grown tunnel barrier (red), thus forming the DQD system. The NW ends are contacted by two Ti/Au contacts (S,D) and the NW segments can be electrically tuned by two Ti/Au sidegates SG_R (purple) and SG_L (yellow). A high-impedance, half-wave resonator is connected to SG_R . Top gates (orange) are kept at a constant voltage of -0.05 V. The magnetic field is applied in-plane at an angle of $\sim 60^\circ$ to the NW. The arrows illustrate an even charge configuration with the two degenerate DQD states $T_{1,1}^+$ and $S_{2,0}$. (b) Schematic of the crystal-phase defined DQD. The conduction band of wurzite and zinblende are offset by ~ 100 meV, resulting in a tunnel barrier between the zinblende segments. The intrinsic spin-orbit interaction enables spin-rotating tunneling between these segments. (c) Energy levels of an even charge configuration as a function of magnetic field B at a fixed positive detuning ϵ between the dot levels. At finite magnetic fields, $T_{1,1}^+$ (blue) hybridizes with $S_{2,0}$ (red) defining a singlet-triplet qubit with an energy splitting given by the spin-orbit interaction strength Δ_{SO} .

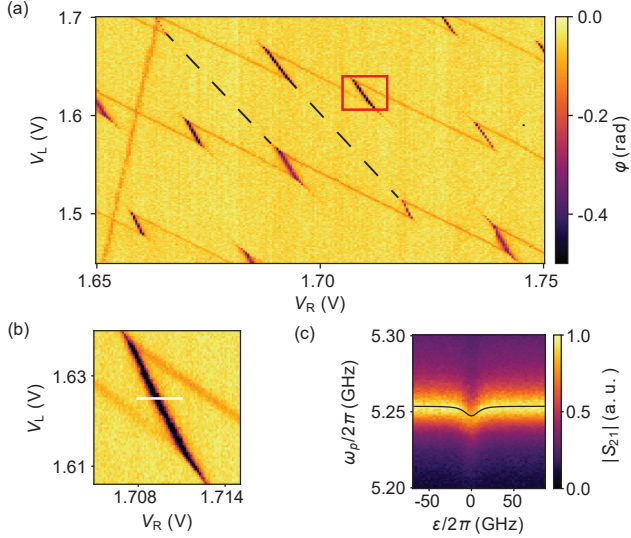


Figure 8.2. Dispersive sensing of the DQD at $B = 0$. (a) Charge stability diagram of the device, in which the resonator phase φ is measured as a function of the SG voltages V_R and V_L . The negative slopes of the interdot transitions are due to the strong cross-capacitance of the larger gate SG_R . A zoom on the interdot transition pointed out by the red rectangle is shown in (b). (c) Resonator transmission amplitude $|S_{21}|$ versus probe frequency ω_p and detuning ϵ along the white line in (b). At the charge degeneracy point of the DQD, we find a dispersive shift of $\chi = 6.9$ MHz with respect to the bare resonance frequency. The black line is a fit to the data.

0.4 aF, $C_{L2} = 1.65 \pm 0.08$ aF, $C_{R1} = 10.1 \pm 0.6$ aF and $C_{L1} = 2.0 \pm 0.2$ aF.

In Fig. 8.2(c) we show the resonator response while varying the probe frequency ω_p and changing the detuning ϵ along the white line in Fig. 8.2(b). An electron can now reside on either of the two tunnel-coupled dots thus forming a charge qubit. At the inter-dot transition (IDT), close to charge degeneracy, the electrical dipole moment of the charge qubit interacts with the resonator, resulting in a dispersive shift of the latter's resonance frequency. By fitting the parameters of a Jaynes-Cummings Hamiltonian (see Section G.3 in the appendix) to this particular IDT, we extract the dispersive shift $\chi_0 = 4.6$ MHz, an inter-dot tunnel coupling $t_c = 6.9 \pm 0.1$ GHz, charge-photon coupling $g_c = 235 \pm 3$ MHz, and charge qubit linewidth $\gamma = 7.9 \pm 0.6$ GHz.

8.3. Strong spin-photon coupling

When investigating the magnetic-field dependence of IDTs similar to the one shown in Fig. 8.2(b), we observe two qualitatively different behaviors which we identify as even and odd charge parity configuration as described in Section G.2 in the appendix. In the following, we investigate one single IDT with an even charge parity.

As illustrated in Fig. 8.1(c), the DQD can be operated as a singlet-triplet qubit when placed into a magnetic field. The qubit frequency $\omega_q = \Delta_{SO}/\hbar$ can be brought into resonance with the cavity frequency ω_r at $B \approx 1.7$ T, as discussed in more detail below. At the resonance condition ($\omega_q \sim \omega_r$), an anti-symmetric (bonding) and a symmetric (anti-bonding) qubit-photon superposition are formed. Consistently, at a field of $B \approx 1.7$ T, we observe an anti-crossing between the resonator and the singlet-triplet qubit. Figure 8.3(a) shows the anti-crossing as a function of the detuning ϵ at constant magnetic field $B = 1.67$ T, from which we extract the resonance frequency $\omega_{\Psi_{\pm}}$ and linewidth δ_{ω} by fitting a Lorentzian (amplitude and phase) to each trace of fixed ϵ . Then, we simultaneously fit the transition frequencies (dashed, white curves in Fig. 8.3(a)) and linewidths (solid, black curve in Fig. 8.3(b)) to the Jaynes-Cummings model as described in Section G.3 in the appendix. This allows us to extract a spin-photon coupling $g_{\epsilon}/2\pi = 75 \pm 4$ MHz, qubit linewidth $\gamma_{\epsilon}/2\pi = 135 \pm 30$ MHz and tunnel rate $t_{\epsilon} = 1.10 \pm 0.05$ GHz for Figs. 8.3(a,b). We note that the observed anti-crossing occurs at a finite detuning $\epsilon' \sim 4.8$ GHz and hence DQD polarization, which reduces the resonator-qubit coupling strength

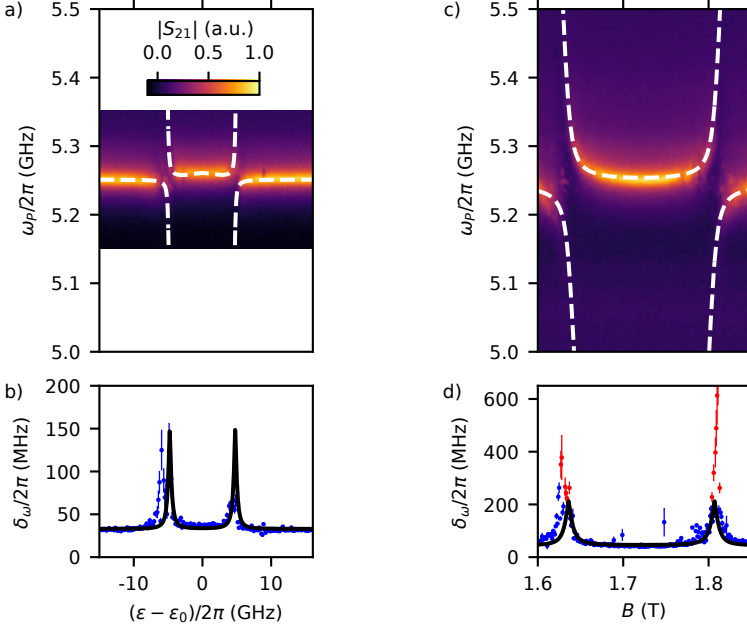


Figure 8.3. Strong spin-photon coupling. (a) Anti-crossing of the resonator and the qubit found when plotting the resonator transmission amplitude $|S_{21}|$ as a function of detuning ϵ and probe frequency ω_p at a magnetic field $B = 1.67$ T. The dashed white curves are fits to a Jaynes-Cummings model (Eq. (G.3) in Section G.3 in the appendix). (b) Dressed resonator linewidth δ_ω extracted from Fig. 8.3(a) with a fit to the Jaynes-Cummings model (Eq. (G.5) in Section G.3 in the appendix). (c) Anti-crossing of the resonator and the singlet-triplet qubit measured by varying the magnetic field B and the probe frequency ω_p , the constant detuning of ~ 1.65 GHz. (d) Dressed resonator linewidth δ_ω extracted from Fig. 8.3(c), analogous to Fig. 8.3(b). The red points were excluded from the fit, as they present a superposition of the hybridized qubit-photon state. Based on the dilution refrigerator attenuation, we estimate the average number of photons in the resonator during this measurement to be < 0.2 [192, 193].

8. Strong coupling between a single photon and a singlet-triplet qubit

as $g_\epsilon = g_0 \sin \theta$, with $\sin \theta = 2t_\epsilon / \sqrt{(2t)^2 + \epsilon'^2}$, where θ is the mixing angle [17, 21, 188]. After correcting for this mixing angle we obtain a spin-photon coupling strength $g_0/2\pi = 178 \pm 6$ MHz.

In Fig. 8.3(c), we show the same anti-crossing as a function of B at a fixed detuning of ~ 1.65 GHz. To extract the spin-photon coupling strength and qubit linewidth from this second measurement, we characterize the effective qubit transition frequency around the minimum $t_0 = t(B_0)$ by $\omega_q(B) = \sqrt{(2t_0)^2 + (\alpha_B(B - B_0))^2}$, where we introduce the heuristic scaling factor α_B . With this additional free parameter, we fit the Jaynes-Cummings model (dashed, white curves in Fig. 3(c) and solid, black curve in Fig. 3(d)) and extract a spin-photon coupling strength of $g_B/2\pi = 114 \pm 9$ MHz and linewidth $\gamma_B/2\pi = 190 \pm 24$ MHz for Fig. 8.3(c,d). The larger value of the coupling strength in the magnetic-field sweep compared to the detuning sweep is attributed to the smaller mixing angle and reflected by the larger splitting at the anti-crossing in Figure 8.3(c) compared to Figure 8.3(a).

These extracted coupling strengths demonstrate that the strong coupling limit between a superconducting resonator and a singlet-triplet qubit can be reached: In the strong coupling regime, a single photon coherently hybridizes with a two-level system. This limit is reached if the vacuum Rabi $2g$ splitting exceeds the linewidth $\gamma + \kappa/2$ of the hybridized bonding and anti-bonding states [2]. For our device we find a ratio $2g_\epsilon/(\gamma_\epsilon + \kappa/2) = 1.0 \pm 0.2$ for the detuning sweep (Fig 8.3(a,b)) and $2g_B/(\gamma_B + \kappa/2) = 1.1 \pm 0.2$ for the magnetic field sweep (Fig. 8.3(c,d)) reaching the strong coupling regime in both cases. After accounting for the mixing angle and using the larger extracted linewidth $\gamma \equiv \max(\gamma_B, \gamma_\epsilon) = \gamma_B$, we find $2g_0/(\gamma + \kappa/2) = 1.7 \pm 0.2$, now very clearly in the strong coupling regime.

8.4. Magnetspectroscopy

To further characterize the spin-orbit eigenstates and and to independently verify the character of the singlet-triplet qubit, we now study the magnetic field evolution of the IDT from 0 T up to 2 T. As described in Section G.1 in the appendix, we measure the resonator shift χ as a function of the detuning ϵ and the magnetic field, as plotted in Fig. 8.4(a). A finite $\chi \neq 0$ occurs at the IDT when tunneling between the dots is allowed and hence if the DQD obtains a non-zero dipole moment. As

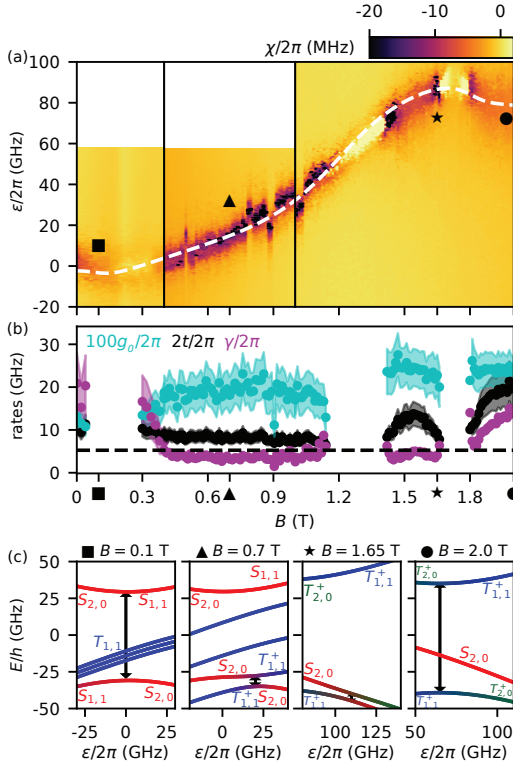


Figure 8.4. Magnetospectroscopy of the singlet-triplet qubit. a) Dispersive shift χ as a function of the magnetic field B and detuning ϵ . The white dashed line is a fit of the effective two-electron Hamiltonian (Eq. (G.4)) to the data. b) Extracted tunnel rate $2t/2\pi$ (black), qubit-photon coupling times hundred $100 \cdot g_0/2\pi$ (cyan) and qubit linewidth $\gamma/2\pi$ (purple). The bare resonator frequency is indicated by the dashed black line. (c) Two-electron energy level diagrams at various magnetic fields with the corresponding field strength indicated in (a) and (b) by the given symbols. A constant offset of 20 GHz and 30 GHz was added to the energy levels at 1.65 T and 2.0 T, respectively. We estimate the average photon number in these experiments as ~ 1 [192, 193].

described in the Section G.4 in the appendix, we model the DQD by an effective two electron Hamiltonian which allows us to fit the gate voltage and field dependence of the IDT (white dashed line in Fig. G.3(a)). We find that the magneto-dispersion of the IDT is well fitted using the following fit parameters namely the spin-conserving singlet and triplet tunnel rates $t_c^S/2\pi \approx 29$ GHz, and $t_c^T/2\pi \approx 37$ GHz, the singlet-triplet coupling rate $t_{\text{SO}}/2\pi \approx 5$ GHz, the electron g-factors of the right and left dots, $g_R \approx 1.8$ and $g_L \approx 2.8$, as well as the singlet-triplet energy splitting $\Delta_{\text{ST}}/2\pi \approx 79$ GHz. These fit parameters are consistent with parameters obtained previously in this material system [49, 111, 194–196]. We note, however, that the fit is under-determined and therefore, it does not provide accurate numbers. Nonetheless, the model gives a qualitative, physical understanding of the system and allows us to establish which DQD levels interact with the resonator.

We can gain additional independent information on the system by also using the other IDT characteristics. Especially, the resonator provides an absolute energy scale allowing for a quantitative analysis of the interaction between the DQD and the resonator [197] complementing the preceding DQD Hamiltonian fit. As described in Section G.3 in the appendix, by fitting a Jaynes-Cummings model to both the resonator shift χ and the dressed resonator linewidth δ_ω simultaneously, we extract the resonator decay κ as well as the qubit tunnel amplitude t , the qubit linewidth γ , and the qubit-photon coupling strength g as a function of B , which we plot in Figure 8.4(b).

Using the fits to both the 2-electron Hamiltonian model and the Jaynes-Cummings model in the 2-level approximation, allows to directly identify several regimes, in each of which the qubit has a different spin-character. Fig. 8.4(c) shows the corresponding DQD level structure based on the fit parameters as a function of ϵ for different magnetic field.

At a low magnetic fields around $B = 0.1$ T, the triplet states (blue curves) are Zeeman split and the ground-state curvature is dominated by the anti-crossing between $S_{1,1}$ and $S_{2,0}$ (red curves). We find a singlet charge qubit in the weak coupling limit, i.e. for which the linewidth exceeds the charge-photon coupling by a factor of hundred. The formation of a double-dip structure in $\chi(\epsilon)$ between $B \sim 0.03$ T and $B \sim 0.3$ T is explained by an interaction between the three states $S_{2,0}$, $S_{1,1}$ and $T_{1,1}^+$ as described in the supplementary material. Traces of $\chi(\epsilon)$ with a double-dip structure cannot be described by the Jaynes-Cummings Hamiltonian and

are therefore not analysed quantitatively.

As B is increased, the triplet state $T_{1,1}^+$ becomes the ground state for $\epsilon < 0$ as shown in the second panel of Fig. 8.4(c) for $B = 0.7$ T. The spin-orbit interaction couples the singlet and triplet states, leading to an anti-crossing between $S_{2,0}$ and $T_{1,1}^+$. A singlet-triplet qubit is created with $\omega_q = \Delta_{\text{SO}} = 2t_{\text{SO}}$ [101, 198]. In this regime, at larger B , the resonance condition between $S_{2,0}$ and $T_{1,1}^+$ occurs at larger ϵ , because the energy of the bare $T_{1,1}^+$ state decreases with larger B and the energy of $S_{2,0}$ decreases with larger ϵ . Therefore, the IDT is observed at larger ϵ for increasing B .

Consistent with the interpretation of the formation of a singlet-triplet qubit, we measure an approximately constant tunneling rate t between $B \sim 0.5$ T and $B \sim 1.1$ T. In this regime, we extract the average spin-orbit tunneling to be $\bar{t}_{\text{so}} = 4.0 \pm 0.3$ GHz. At $B \approx 1.3$ T, χ becomes positive. This is interpreted as a drop of the tunnel rate below the resonator frequency, $2t < \omega_r^0$. This decline in t is not captured by our simplified Hamiltonian model and we speculate that changes in the orbital structure of a many-electron DQD could be the reason.

At a magnetic field of $B \approx 1.7$ T, the resonator shift χ becomes positive again and we observe a resonant interaction between the resonator and the singlet-triplet qubit leading to the anti-crossing as discussed in Section 8.3. As seen in the level structure in Fig. 8.4(c) at $B = 1.65$ T, because the IDT happens at elevated magnetic-field strength and detuning, the triplet state $T_{2,0}^+$ becomes relevant. This results in a level repulsion between $T_{2,0}^+$ and $T_{1,1}^+$ and hence leads to a reduced splitting between the $S_{2,0}$ level and the $T_{1,1}^+$ states. In Fig. 8.4(c), this is illustrated by the smaller level gap (black arrow) compared to the one at $B = 0.7$ T.

The level structure at very large magnetic fields is plotted exemplarily for $B \approx 2$ T in the right panel of Fig. 8.4(c). In this regime, the ground-state of the DQD at the IDT is formed by a superposition of the $T_{2,0}^+$ and the $T_{1,1}^+$ states. Comparing this very-large magnetic-field regime with the lower field regimes, we find that the curve of Fig. 8.4(a) turns back towards lower ϵ for increasing B . This situation can be understood easily by noting that the spin-polarized triplets $T_{2,0}^+$ and $T_{1,1}^+$ form a charge qubit similar to the singlets at low field. While the transition is increasingly dominated by the triplet-charge qubit for increasing B , $|\chi|$ becomes smaller at the IDT, because the anti-crossing between the triplet states $T_{2,0}^-$ and $T_{1,1}^-$ happens at much larger frequencies $2t_c^T \gg 2t_{\text{SO}}$. Hence, the triplet charge qubit

has a larger frequency detuning from the resonator frequency than the singlet-triplet qubit, leading to a smaller resonator shift.

This large number of detailed findings justify the use and the parameters of the two-electron Hamiltonian introduced above, which, in turn, directly allows us to identify the singlet-triplet spin qubit, for which we find the strong coupling limit to the electromagnetic cavity. We note that the qubit linewidth γ and qubit-photon coupling strength are both related to the qubit rate as discussed in the supplementary material. An intuitive explanation is that the tunnel rate in our experiments increases as the qubit becomes more charge like and hence is more susceptible to charge noise. Another possible explanation is that the qubit linewidth is limited by qubit relaxation which scales proportional to the tunnel rate to the contacts.

8.5. Conclusion and Outlook

In summary, we demonstrate a semiconductor nanowire DQD device with crystal-phase defined tunnel barriers that can be operated as different types of qubits, coupled to a high-impedance, high magnetic field resilient electromagnetic resonator. As the main result, we find a singlet-triplet qubit for which we extract the relevant qubit parameters, especially a record high electron spin-photon coupling of $g/2\pi = 114$ MHz in the single photon limit, thus reaching the strong coupling regime $2g \geq \gamma + \kappa/2$.

Our experiments demonstrate that deterministically grown tunnel barriers allow for a reduced number of gate lines, and that, mediated by intrinsic spin-orbit interaction, singlet-triplet qubits can reach the strong coupling limit for low photon numbers, similar to flopping mode spin qubits [199, 200]. This finding is potentially applicable to other promising platforms with strong spin-orbit interactions, like holes in Ge [198]. Technologically, the large electron spin-photon coupling found in our experiments might become crucial for the implementation of two-qubit gates between distant spin qubits a milestone on the way towards scalable quantum computers. Moreover, our nanowire platform without depletion gates results in a significantly reduced gate-induced photon-leakage in the absence of on-chip filtering [21, 105, 117]. An optimized gate design with resonators with larger impedance [137] therefore presents an ideal platform to investigate new phenomena in the ultrastrong coupling regime [137, 153].

We acknowledge fruitful discussions with Simon Zihlmann, Roy Haller,

Andrea Hofmann, Stefano Bosco, Romain Maurand and Antti Ranni and support in setting-up the experiments by Fabian Opliger, Roy Haller, Luk Yi Cheung, and Deepankar Sarmah. This research was supported by the Swiss Nanoscience Institute (SNI), the Swiss National Science Foundation through grant 192027, the NCCR Quantum Science and Technology (NCCR-QSIT) and the NCCR Spin Qubit in Silicon (NCCR-Spin). We further acknowledge funding from the European Union's Horizon 2020 research and innovation programme, specifically the FET-open project AndQC, agreement No 828948 and the FET-open project TOPSQUAD, agreement No 847471. Furthermore, we acknowledge funding by NanoLund and the Knut & Alice Wallenberg Foundation (KAW).

9 Conclusions and Outlook

The goal of this thesis was improving the coupling strength between semiconductor quantum bits (qubits) and superconducting resonators, as well as addressing the scalability challenge of spin-based qubits by exploiting circuit quantum electrodynamics (QED) techniques. These goals were addressed by integrating semiconductor double-quantum dots (DQDs) in three material systems into high-impedance resonance circuits.

We demonstrated a systematic tuning strategy allowing to engineer the dipolar interaction strength between a resonator and a DQD charge qubit as well as the charge qubit coherence. This tuning-strategy is based on in-situ engineering of the DQD capacitances by means of electro-static gating, and allows us to reproducibly achieve record low decoherence rates of $\Gamma_2 < 5$ MHz for a DQD charge qubit in GaAs strongly coupled to a SQUID-array resonator. Using the same tuning protocol and by integrating a Josephson junction-array resonator with an impedance of ~ 4 k Ω , we measured an avoided crossing corresponding to a dipolar interaction strength $g_c \sim 630$ MHz. Together with the bare resonance frequencies of the resonator and the qubit $\omega_r \sim \omega_q \sim 5.6$ GHz, this represents the first demonstration of ultrastrong coupling (USC) between a DQD and a microwave photon where the dipolar interaction strength constitutes a non-negligible fraction of the bare transition frequencies.

These experiments form the basis of exploring the USC regime with semiconductor DQDs where novel and unexpected physical phenomena arise because of the breakdown of the rotating wave-approximation [153].

Turning towards spin qubits, we addressed the challenge imposed by micromagnets which are used in state of the art hybrid circuit QED architectures integrating spin qubits [25, 30, 31, 34]. Micromagnets inhibit scaling up to the qubit numbers that are projected for a universal quantum computer. This is, on the one hand, because the resulting spin-photon coupling strengths are relatively weak and, on the other hand, because of

a limited tunability of important qubit parameters such as the Landé g factor.

Addressing these disadvantages, we have developed an architecture incorporating magnetic-field resilient, high-quality and high-impedance resonators based on NbTiN, coupled to semiconductor nanowires. The latter are electrically tunable and possess a large spin-orbit interaction, thereby solving the problems imposed by the micromagnets [87].

Based on this architecture, we extended pioneering charge-sensing protocols of DQDs in Ge/Si nanowires [43, 44, 47, 48] by coupling one of the quantum dots to a high-impedance resonator. Reaching the last hole in this system is of particular interest, because of the subband-population dependent mixing of light and heavy holes [86, 91, 201]. In our experiments, we find indications of the depletion of the last hole from an isolated quantum dot in a Ge/Si core/shell nanowire and anticipate that similar experiments will enable the investigation of the underlying mechanisms of light-hole heavy-hole mixing.

These experiments on Ge/Si nanowires were performed in a dielectric configuration aiming on an optimized resonator performance with the drawback of non-ideal dielectrics in vicinity of the nanowire. The measurements therefore exhibited an insufficient electrostatic stability of the DQD for investigating spin properties. However, we discovered that our NbTiN resonators can also be implemented in dielectric environments that are ideally suited for the integration of semiconductor nanowires, without a deleterious reduction of the resonator quality in the hybrid device.

Moreover, larger lever arms and therefore larger coupling strengths were achieved by incorporating crystal-phase defined DQDs in InAs nanowires in the circuit QED architecture. These advances enabled us to infer the magneto-dispersion of a zincblende InAs DQD from its large dispersive interaction with the resonator, which we modeled by accounting for two electrons shared among the two dots in the presence of large spin-orbit interaction. At a field strength of ~ 1.7 T, we measured an avoided crossing between the DQD qubit and the resonator mode in the single-photon limit. This avoided crossing is consistent with the interpretation of strong coupling between a singlet-triplet qubit and a single photon in the resonator, mediated by the large spin-orbit interaction that is naturally present in zincblende InAs nanowires.

These results constitute a coherent spin-photon interface without the necessity of micromagnets. Furthermore, the spin-photon coupling strength

of $g/2\pi = 114 \pm 9$, extracted from the avoided crossing exceeds the spin-photon coupling based on micromagnets by an order of magnitude setting a record high electron spin-photon coupling strength. Therefore, our results can substantially contribute to scaling up spin-based quantum computers by facilitating the realization of entangling gates between distant spin qubits.

9.1. Outlook

The experiments presented in this thesis open up a number of possible routes, both for progressing towards the realization of scalable spin-based quantum computers and for fundamental research of light-matter interactions.

In terms of realizing a scalable spin-based quantum computer, superconducting resonators can constitute the missing link between clusters of qubits, especially if the interaction between the spin qubit and the resonator is based on intrinsic spin-orbit interaction rather than on micromagnets. Semiconductor nanowires naturally feature a large spin-orbit interaction and are therefore a useful technology for proof-of-principle experiments as demonstrated in this thesis. However, currently every single nanowire is deposited deterministically by means of micromanipulation. For creating a scalable platform, it is advantageous to use a top-down approach instead. Hole spin qubits with intrinsic spin-orbit interaction can be realized, for example, using silicon complementary metal-oxide-semiconductor (CMOS) transistors [202, 203] or in planar germanium [140, 198]. It is therefore highly desirable to couple spin qubits in these structures to a superconducting resonator. Indeed, very recent experiments demonstrated signatures of strong spin-photon coupling between a microwave photon and a hole in a CMOS transistor [199]. Demonstrations of a coherent coupling between a singlet-triplet qubit and a single microwave photon, as has been demonstrated in this thesis, are still to be realized in these material systems. Whichever material platform succeeds, the demonstration of an entangling gate between two distant spin qubits based on spin-orbit interaction will contribute a crucial piece to the puzzle of a scalable quantum computer.

In terms of fundamental understanding of light-matter interaction, it is of high interest to increase the dipolar interaction strength even further and to observe the breakdown of the rotating wave approximation [153].

In contrast to superconducting qubits, the quantum-dot two-level system features a very large anharmonicity allowing to perform analog quantum simulations [204] of quantum impurity models with quantum dots in the USC regime.

A tuning strategy for the qubit dipole moment has been presented in this work and enhancing it by a factor of two would allow investigations of the hybrid qubit-photon system deep in the USC regime. It turns out, there are several possibilities for further enhancing the dipolar coupling strength.

One way is increasing the lever arm of the resonator gate to the DQD, which is possible utilizing the crystal-phase defined nanowire DQDs which we have used in this thesis. Because no depletion or accumulation gates are needed for defining the DQD in this material system, spurious capacitance that would reduce the lever arm is avoided. By depositing gates on top of the nanowire rather than next to it, a substantial increase of the lever arm and thereby the coupling strength compared to the work presented in this thesis is expected.

Another possibility for increasing the coupling strength lies in connecting either end of the half-wave resonator to one of the two plunger gates of the DQD. Because the voltages on the two ends of the resonator oscillate out-of-phase, by doing so, a factor of two in the effective voltage fluctuations and hence in the coupling strength can be gained [34].

The coupling strength can be increased even further by utilizing resonators with even larger impedance such as granular aluminum (grAl) [205] resonators. When implementing these proposals, high-impedance resonators will enable the detection of novel phenomena due to the mixing of light and matter to an extreme degree deep in the USC regime.

Having said that, I am optimistic that numerous insights and plenty of intriguing results are ensued from the investigation of light-matter interaction in solid-state systems based on high-impedance resonators and eventually, they will contribute to the realization of a useful quantum computer with so-far unknown potential for addressing urgent challenges of humankind.

Bibliography

- [1] A. Chatterjee, P. Stevenson, S. De Franceschi, A. Morello, N. P. de Leon, and F. Kuemmeth, *Nature Reviews Physics* **3**, 157 (2021).
- [2] A. Blais, A. L. Grimsmo, S. M. Girvin, and A. Wallraff, *Reviews of Modern Physics* **93**, 25005 (2021).
- [3] R. Hanson, L. P. Kouwenhoven, J. R. Petta, S. Tarucha, and L. M. K. Vandersypen, *Reviews of modern physics* **79**, 1217 (2007).
- [4] D. D. Awschalom, L. C. Bassett, A. S. Dzurak, E. L. Hu, and J. R. Petta, *Science* **339**, 1174 (2013).
- [5] J. R. Petta, A. C. Johnson, J. M. Taylor, E. A. Laird, A. Yacoby, M. D. Lukin, C. M. Marcus, M. P. Hanson, and A. C. Gossard, *Science* **309**, 2180 (2005).
- [6] F. H. L. Koppens, C. Buizert, K.-J. Tielrooij, I. T. Vink, K. C. Nowack, T. Meunier, L. P. Kouwenhoven, and L. M. K. Vandersypen, *Nature* **442**, 766 (2006).
- [7] K. C. Nowack, M. Shafiei, M. Laforest, G. Prawiroatmodjo, L. R. Schreiber, C. Reichl, W. Wegscheider, and L. M. K. Vandersypen, *Science* **333**, 1269 (2011).
- [8] R. Brunner, Y.-S. Shin, T. Obata, M. Pioro-Ladrière, T. Kubo, K. Yoshida, T. Taniyama, Y. Tokura, and S. Tarucha, *Physical review letters* **107**, 146801 (2011).
- [9] M. D. Shulman, O. E. Dial, S. P. Harvey, H. Bluhm, V. Umansky, and A. Yacoby, *Science* **336**, 202 (2012).
- [10] S. G. J. Philips, M. T. Mkadzik, S. V. Amitonov, S. L. de Snoo, M. Russ, N. Kalhor, C. Volk, W. I. L. Lawrie, D. Brousse, and L. Trypuzen, *Nature* **609**, 919 (2022).
- [11] A. Wallraff, D. I. Schuster, A. Blais, L. Frunzio, R.-S. Huang, J. Majer, S. Kumar, S. M. Girvin, and R. J. Schoelkopf, *Nature* **431**, 162 (2004).

- [12] A. Blais, R. S. Huang, A. Wallraff, S. M. Girvin, and R. J. Schoelkopf, *Physical Review A - Atomic, Molecular, and Optical Physics* **69** (2004).
- [13] J. Chow, O. Dial, and J. Gambetta, *IBM Research Blog* (2021).
- [14] D. I. Schuster, A. P. Sears, E. Ginossar, L. DiCarlo, L. Frunzio, J. J. L. Morton, H. Wu, G. A. D. Briggs, B. B. Buckley, D. D. Awschalom, and Others, *Physical review letters* **105**, 140501 (2010).
- [15] A. A. Clerk, K. W. Lehnert, P. Bertet, J. R. Petta, and Y. Nakamura, *Nature Physics* **16**, 257 (2020).
- [16] M. R. Delbecq, V. Schmitt, F. D. Parmentier, N. Roch, J. J. Viennot, G. Fève, B. Huard, C. Mora, A. Cottet, and T. Kontos, *Physical Review Letters* **107**, 256804 (2011).
- [17] T. Frey, P. J. Leek, M. Beck, A. Blais, T. Ihn, K. Ensslin, and A. Wallraff, *Physical Review Letters* **108**, 46807 (2012).
- [18] H. Toida, T. Nakajima, and S. Komiyama, *Physical review letters* **110**, 66802 (2013).
- [19] J. J. Viennot, M. R. Delbecq, M. C. Dartiailh, A. Cottet, and T. Kontos, *Physical Review B* **89**, 165404 (2014).
- [20] G.-W. Deng, D. Wei, J. R. Johansson, M.-L. Zhang, S.-X. Li, H.-O. Li, G. Cao, M. Xiao, T. Tu, G.-C. Guo, and Others, *Physical Review Letters* **115**, 126804 (2015).
- [21] K. D. Petersson, L. W. McFaul, M. D. Schroer, M. Jung, J. M. Taylor, A. A. Houck, and J. R. Petta, *Nature* **490**, 380 (2012).
- [22] X. Mi, J. V. Cady, D. M. Zajac, P. W. Deelman, and J. R. Petta, *Science* **355**, 156 (2017).
- [23] A. Stockklauser, P. Scarlino, J. V. Koski, S. Gasparinetti, C. K. Andersen, C. Reichl, W. Wegscheider, T. Ihn, K. Ensslin, and A. Wallraff, *Physical Review X* **7**, 1 (2017).
- [24] L. E. Bruhat, T. Cubaynes, J. J. Viennot, M. C. Dartiailh, M. M. Desjardins, A. Cottet, and T. Kontos, *Physical Review B* **98**, 155313 (2018).
- [25] X. Mi, M. Benito, S. Putz, D. M. Zajac, J. M. Taylor, G. Burkard, and J. R. Petta, *Nature* **555**, 599 (2018).
- [26] N. Samkharadze, G. Zheng, N. Kalhor, D. Brousse, A. Sammak, U. C. Mendes, A. Blais, G. Scappucci, and L. M. Vandersypen, *Science* **359**, 1123 (2018).

- [27] A. J. Landig, J. V. Koski, P. Scarlino, U. C. Mendes, A. Blais, C. Reichl, W. Wegscheider, A. Wallraff, K. Ensslin, and T. Ihn, *Nature* **560**, 179 (2018).
- [28] J. Majer, J. M. Chow, J. M. Gambetta, J. Koch, B. R. Johnson, J. A. Schreier, L. Frunzio, D. I. Schuster, A. A. Houck, A. Wallraff, and Others, *Nature* **449**, 443 (2007).
- [29] D. J. van Woerkom, P. Scarlino, J. H. Ungerer, C. Müller, J. V. Koski, A. J. Landig, C. Reichl, W. Wegscheider, T. Ihn, K. Ensslin, and Others, *Physical Review X* **8**, 41018 (2018).
- [30] F. Borjans, X. G. Croot, X. Mi, M. J. Gullans, and J. R. Petta, *Nature* **577**, 195 (2020).
- [31] P. Harvey-Collard, J. Dijkema, G. Zheng, A. Sammak, G. Scappucci, and L. M. K. Vandersypen, *Physical Review X* **12**, 21026 (2022).
- [32] N. Samkharadze, A. Bruno, P. Scarlino, G. Zheng, D. P. DiVincenzo, L. DiCarlo, and L. M. K. Vandersypen, *Physical Review Applied* **5**, 44004 (2016).
- [33] X. Mi, M. Benito, S. Putz, D. M. Zajac, J. M. Taylor, G. Burkard, and J. R. Petta, *Nature* **555**, 599 (2018).
- [34] N. Samkharadze, G. Zheng, N. Kalhor, D. Brousse, A. Sammak, U. C. Mendes, A. Blais, G. Scappucci, and L. M. K. Vandersypen, *Science* **359**, 1123 (2018).
- [35] A. Stockklauser, *Strong Coupling Circuit QED with Semiconductor Quantum Dots*, Ph.D. thesis, ETH Zurich (2017).
- [36] A. Palacios-Laloy, F. Nguyen, F. Mallet, P. Bertet, D. Vion, and D. Esteve, *Journal of Low Temperature Physics* **151**, 1034 (2008).
- [37] N. A. Masluk, I. M. Pop, A. Kamal, Z. K. Mineev, and M. H. Devoret, *Physical review letters* **109**, 137002 (2012).
- [38] D. Delagebeaudeuf and N. T. Linh, *IEEE Transactions on Electron Devices* **29**, 955 (1982).
- [39] W. Lu, J. Xiang, B. P. Timko, Y. Wu, and C. M. Lieber, *Proceedings of the National Academy of Sciences* **102**, 10046 (2005).
- [40] S. Lehmann, J. Wallentin, D. Jacobsson, K. Deppert, and K. A. Dick, *Nano letters* **13**, 4099 (2013).

- [41] A. D. O'Connell, M. Ansmann, R. C. Bialczak, M. Hofheinz, N. Katz, E. Lucero, C. McKenney, M. Neeley, H. Wang, E. M. Weig, and Others, *Applied Physics Letters* **92**, 112903 (2008).
- [42] C. Fasth, A. Fuhrer, M. T. Björk, and L. Samuelson, *Nano letters* **5**, 1487 (2005).
- [43] Y. Hu, F. Kuemmeth, C. M. Lieber, and C. M. Marcus, *Nature nanotechnology* **7**, 47 (2012).
- [44] A. P. Higginbotham, T. W. Larsen, J. Yao, H. Yan, C. M. Lieber, C. M. Marcus, and F. Kuemmeth, *Nano Letters* **14**, 3582 (2014).
- [45] D. Barker, S. Lehmann, L. Namazi, M. Nilsson, C. Thelander, K. A. Dick, and V. F. Maisi, *Applied Physics Letters* **114**, 183502 (2019).
- [46] F. N. M. Froning, L. C. Camenzind, O. A. H. van der Molen, A. Li, E. P. A. M. Bakkers, D. M. Zumbühl, and F. R. Braakman, *Nature Nanotechnology* **16**, 308 (2021).
- [47] Y. Hu, H. O. H. Churchill, D. J. Reilly, J. Xiang, C. M. Lieber, and C. M. Marcus, *Nature nanotechnology* **2**, 622 (2007).
- [48] R. Wang, R. S. Deacon, J. Sun, J. Yao, C. M. Lieber, and K. Ishibashi, *Nano Letters* **19**, 1052 (2019).
- [49] M. Nilsson, F. V. Boström, S. Lehmann, K. A. Dick, M. Leijnse, and C. Thelander, *Physical Review Letters* **121**, 156802 (2018).
- [50] I. I. Rabi, *Physical Review* **49**, 324 (1936).
- [51] D. Braak, *Physical Review Letters* **107**, 100401 (2011).
- [52] E. T. Jaynes and F. W. Cummings, *Proceedings of the IEEE* **51**, 89 (1963).
- [53] S. Haroche, in *Proceedings of the Les Houches Summer School* (1992).
- [54] M. A. Castellanos-Beltran and K. W. Lehnert, *Applied Physics Letters* **91**, 83509 (2007).
- [55] C. Altimiras, O. Parlavacchio, P. Joyez, D. Vion, P. Roche, D. Esteve, and F. Portier, *Applied Physics Letters* **103**, 212601 (2013).
- [56] M. Tinkham, *Introduction to superconductivity* (Courier Corporation, 2004).
- [57] K. K. Likharev and J. Lukens, *Physics Today* **41**, 122 (1988).
- [58] M. Sigrist, *Superconductivity: lecture notes* (ETH Zürich, 2017).

- [59] J. Aumentado, IEEE Microwave magazine **21**, 45 (2020).
- [60] H. Weinstock, IEEE Transactions on Magnetics **27**, 3231 (1991).
- [61] J. Clarke and F. K. Wilhelm, Nature **453**, 1031 (2008).
- [62] B. D. Josephson, Physics letters **1**, 251 (1962).
- [63] P. W. Anderson and J. M. Rowell, Physical Review Letters **10**, 230 (1963).
- [64] C. K. Andersen and A. Blais, New Journal of Physics **19**, 23022 (2017).
- [65] K. C. Gupta, Artech house **7** (1979).
- [66] W. Hilberg, IEEE Transactions on Microwave Theory and techniques **17**, 259 (1969).
- [67] T. Hong, K. Choi, K. Ik Sim, T. Ha, B. Cheol Park, H. Yamamori, and J. Hoon Kim, Journal of Applied Physics **114**, 243905 (2013).
- [68] A. J. Annunziata, D. F. Santavicca, L. Frunzio, G. Catelani, M. J. Rooks, A. Frydman, and D. E. Prober, Nanotechnology **21**, 445202 (2010).
- [69] D. M. Zajac, T. M. Hazard, X. Mi, E. Nielsen, and J. R. Petta, Physical Review Applied **6**, 54013 (2016).
- [70] L. Grünhaupt, N. Maleeva, S. T. Skacel, M. Calvo, F. Levy-Bertrand, A. V. Ustinov, H. Rotzinger, A. Monfardini, G. Catelani, and I. M. Pop, Physical review letters **121**, 117001 (2018).
- [71] U. Patel, I. V. Pechenezhskiy, B. L. T. Plourde, M. G. Vavilov, and R. McDermott, Physical Review B **96**, 220501 (2017).
- [72] P. J. Petersan and S. M. Anlage, Journal of applied physics **84**, 3392 (1998).
- [73] J. Gao, *The physics of superconducting microwave resonators* (California Institute of Technology, 2008).
- [74] M. Göppl, A. Fragner, M. Baur, R. Bianchetti, S. Filipp, J. M. Fink, P. J. Leek, G. Puebla, L. Steffen, and A. Wallraff, Journal of Applied Physics **104**, 113904 (2008).
- [75] A. Megrant, C. Neill, R. Barends, B. Chiaro, Y. Chen, L. Feigl, J. Kelly, E. Lucero, M. Mariantoni, P. J. J. O'Malley, and Others, Applied Physics Letters **100**, 113510 (2012).
- [76] C. Deng, M. Otto, and A. Lupascu, Journal of Applied Physics **114**, 54504 (2013).

- [77] M. S. Khalil, M. J. A. Stoutimore, F. C. Wellstood, and K. D. Osborn, *Journal of Applied Physics* **111**, 54510 (2012).
- [78] S. Probst, F. B. Song, P. A. Bushev, A. V. Ustinov, and M. Weides, *Review of Scientific Instruments* **86**, 24706 (2015).
- [79] M. Nilsson, *Charge and Spin Transport in Parallel-Coupled Quantum Dots in Nanowires* (Division of Solid State Physics, Department of Physics, Lund University, 2018).
- [80] G. W. Bryant, *Physical review letters* **59**, 1140 (1987).
- [81] T. Brandes, W. Häusler, K. Jauregui, B. Kramer, and D. Weinmann, *Physica B: Condensed Matter* **189**, 16 (1993).
- [82] L. J. Lauhon, M. S. Gudiksen, D. Wang, and C. M. Lieber, *nature* **420**, 57 (2002).
- [83] S. Zhang, F. J. Lopez, J. K. Hyun, and L. J. Lauhon, *Nano letters* **10**, 4483 (2010).
- [84] F. N. M. Froning, *Hole Spin Qubits in Ge/Si Core/Shell Nanowires*, Ph.D. thesis, University of Basel (2021).
- [85] S. Conesa-Boj, A. Li, S. Koelling, M. Brauns, J. Ridderbos, T. T. Nguyen, M. A. Verheijen, P. M. Koenraad, F. A. Zwanenburg, and E. P. A. M. Bakkers, *Nano letters* **17**, 2259 (2017).
- [86] C. Kloeffel, M. Trif, and D. Loss, *Physical Review B - Condensed Matter and Materials Physics* **84**, 1 (2011).
- [87] C. Kloeffel, M. Trif, P. Stano, and D. Loss, *Physical Review B - Condensed Matter and Materials Physics* **88**, 1 (2013).
- [88] E. N. Osika, B. Szafran, and M. P. Nowak, *Physical Review B* **88**, 165302 (2013).
- [89] F. Froning, L. Camenzind, A. Li, E. Bakkers, D. Zumbühl, and F. Braakman, *Bulletin of the American Physical Society* **65** (2020).
- [90] F. Maier, C. Kloeffel, and D. Loss, *Physical Review B - Condensed Matter and Materials Physics* **87**, 1 (2013).
- [91] D. Csontos, P. Brusheim, U. Zülicke, and H. Q. Xu, *Physical Review B* **79**, 155323 (2009).
- [92] F. N. M. Froning, M. K. Rehmann, J. Ridderbos, M. Brauns, F. A. Zwanenburg, A. Li, E. Bakkers, D. M. Zumbühl, and F. R. Braakman, *Applied physics letters* **113**, 73102 (2018).

- [93] M. Nilsson, L. Namazi, S. Lehmann, M. Leijnse, K. A. Dick, and C. Thelander, *Physical Review B* **93**, 195422 (2016).
- [94] F. Glas, J.-C. Harmand, and G. Patriarche, *Physical review letters* **99**, 146101 (2007).
- [95] M. Nilsson, I.-J. Chen, S. Lehmann, V. Maulerova, K. A. Dick, and C. Thelander, *Nano letters* **17**, 7847 (2017).
- [96] S. Nadj-Perge, S. M. Frolov, E. Bakkers, and L. P. Kouwenhoven, *Nature* **468**, 1084 (2010).
- [97] W. G. der Wiel, S. De Franceschi, J. M. Elzerman, T. Fujisawa, S. Tarucha, and L. P. Kouwenhoven, *Reviews of modern physics* **75**, 1 (2002).
- [98] D. Loss and D. P. DiVincenzo, *Physical Review A* **57**, 120 (1998).
- [99] R. Ezzouch, *Gate reflectometry as readout and spectroscopy tool for silicon spin qubits*, Theses, Université Grenoble Alpes (2021).
- [100] T. Ihn, *Semiconductor Nanostructures: Quantum states and electronic transport* (OUP Oxford, 2009).
- [101] P. M. Mutter and G. Burkard, *Physical Review B* **104**, 195421 (2021).
- [102] T. Hayashi, T. Fujisawa, H.-D. Cheong, Y. H. Jeong, and Y. Hirayama, *Physical review letters* **91**, 226804 (2003).
- [103] D. M. Pozar, *Microwave engineering* (John wiley & sons, 2011).
- [104] B. A. Mazin, *Microwave kinetic inductance detectors* (California Institute of Technology, 2005).
- [105] P. Harvey-Collard, G. Zheng, J. Dijkema, N. Samkharadze, A. Sammak, G. Scappucci, and L. M. Vandersypen, *Physical Review Applied* **14**, 1 (2020).
- [106] X. Mi, J. V. Cady, D. M. Zajac, J. Stehlik, L. F. Edge, and J. R. Petta, *Applied Physics Letters* **110** (2017).
- [107] T. Frey, P. J. Leek, M. Beck, J. Faist, A. Wallraff, K. Ensslin, T. Ihn, and M. Büttiker, *Physical Review B* **86**, 115303 (2012).
- [108] M. E. Brinson and S. Jahn, *International Journal of Numerical Modelling: Electronic Networks, Devices and Fields* **22**, 297 (2009).
- [109] S. Krinner, S. Storz, P. Kurpiers, P. Magnard, J. Heinsoo, R. Keller, J. Luetolf, C. Eichler, and A. Wallraff, *EPJ Quantum Technology* **6**, 2 (2019).

- [110] C. H. Jünger, *Transport spectroscopy of semiconductor superconductor nanowire hybrid devices*, Ph.D. thesis, University_of_Basel (2019).
- [111] C. Jünger, R. Delagrangé, D. Chevallier, S. Lehmann, K. A. Dick, C. Thelander, J. Klinovaja, D. Loss, A. Baumgartner, and C. Schönenberger, *Physical Review Letters* **125**, 17701 (2020).
- [112] F. S. Thomas, M. Nilsson, C. Ciaccia, C. Jünger, F. Rossi, V. Zannier, L. Sorba, A. Baumgartner, and C. Schönenberger, *Physical Review B* **104**, 115415 (2021).
- [113] J. H. Ungerer, D. Sarmah, A. Kononov, J. Ridderbos, R. Haller, L. Y. Cheung, and C. Schönenberger, arXiv preprint arXiv:2302.06303 (2023).
- [114] G. Zheng, N. Samkharadze, M. L. Noordam, N. Kalhor, D. Brousse, A. Sammak, G. Scappucci, and L. M. K. Vandersypen, *Nature nanotechnology* **14**, 742 (2019).
- [115] V. Singh, B. H. Schneider, S. J. Bosman, E. P. Merckx, and G. A. Steele, *Applied Physics Letters* **105**, 222601 (2014).
- [116] C. X. Yu, S. Zihlmann, G. Troncoso Fernández-Bada, J.-L. Thomassin, F. Gustavo, É. Dumur, and R. Maurand, *Applied Physics Letters* **118**, 54001 (2021).
- [117] X. Mi, J. V. Cady, D. M. Zajac, J. Stehlik, L. F. Edge, and J. R. Petta, *Applied Physics Letters* **110**, 43502 (2017).
- [118] L. Petit, H. G. J. Eenink, M. Russ, W. I. L. Lawrie, N. W. Hendrickx, S. G. J. Philips, J. S. Clarke, L. M. K. Vandersypen, and M. Veldhorst, *Nature* **580**, 355 (2020).
- [119] C. H. Yang, R. C. C. Leon, J. C. C. Hwang, A. Saraiva, T. Tanttu, W. Huang, J. Camirand Lemyre, K. W. Chan, K. Y. Tan, F. E. Hudson, and Others, *Nature* **580**, 350 (2020).
- [120] L. C. Camenzind, S. Geyer, A. Fuhrer, R. J. Warburton, D. M. Zumbühl, and A. V. Kuhlmann, *Nature Electronics* **5**, 178 (2022).
- [121] M. J. Biercuk, D. J. Monsma, C. M. Marcus, J. S. Becker, and R. G. Gordon, *Applied Physics Letters* **83**, 2405 (2003).
- [122] E. Toomey, M. Colangelo, N. Abedzadeh, and K. K. Berggren, *Journal of Vacuum Science & Technology B, Nanotechnology and Microelectronics: Materials, Processing, Measurement, and Phenomena* **36**, 06JC01 (2018).
- [123] M. R. Vissers, J. Gao, D. S. Wisbey, D. A. Hite, C. C. Tsuei, A. D. Corcoles, M. Steffen, and D. P. Pappas, *Applied Physics Letters* **97**, 232509 (2010).

- [124] S. Ohya, B. Chiaro, A. Megrant, C. Neill, R. Barends, Y. Chen, J. Kelly, D. Low, J. Mutus, P. J. J. O'Malley, and Others, *Superconductor Science and Technology* **27**, 15009 (2013).
- [125] M. Sandberg, M. R. Vissers, J. S. Kline, M. Weides, J. Gao, D. S. Wisbey, and D. P. Pappas, *Applied Physics Letters* **100**, 262605 (2012).
- [126] W. A. Phillips, *Reports on Progress in Physics* **50**, 1657 (1987).
- [127] H. Wang, M. Hofheinz, J. Wenner, M. Ansmann, R. C. Bialczak, M. Lenander, E. Lucero, M. Neeley, A. D. O'Connell, D. Sank, and Others, *Applied Physics Letters* **95**, 233508 (2009).
- [128] D. P. Pappas, M. R. Vissers, D. S. Wisbey, J. S. Kline, and J. Gao, *IEEE Transactions on Applied Superconductivity* **21**, 871 (2011).
- [129] J. Goetz, F. Deppe, M. Haeberlein, F. Wulschner, C. W. Zollitsch, S. Meier, M. Fischer, P. Eder, E. Xie, K. G. Fedorov, and Others, *Journal of Applied Physics* **119**, 15304 (2016).
- [130] J. D. Brehm, A. Bilmes, G. Weiss, A. V. Ustinov, and J. Lisenfeld, *Applied Physics Letters* **111**, 112601 (2017).
- [131] F. W. Carter, T. Khaire, C. Chang, and V. Novosad, *Applied Physics Letters* **115**, 92602 (2019).
- [132] C. Müller, J. H. Cole, and J. Lisenfeld, *Reports on Progress in Physics* **82**, 124501 (2019).
- [133] M. Scigliuzzo, L. E. Bruhat, A. Bengtsson, J. J. Burnett, A. F. Roudsari, and P. Delsing, *New Journal of Physics* **22**, 53027 (2020).
- [134] J. M. Sage, V. Bolkhovsky, W. D. Oliver, B. Turek, and P. B. Welander, *Journal of Applied Physics* **109**, 63915 (2011).
- [135] P. Coumou, M. R. Zuddam, E. F. C. Driessen, P. J. De Visser, J. J. A. Baselmans, and T. M. Klapwijk, *IEEE transactions on applied superconductivity* **23**, 7500404 (2012).
- [136] Quantum Device Lab, www.qudev.phys.ethz.ch .
- [137] P. Scarlino, J. H. Ungerer, D. J. van Woerkom, M. Mancini, P. Stano, C. Müller, A. J. Landig, J. V. Koski, C. Reichl, W. Wegscheider, T. Ihn, K. Ensslin, and A. Wallraff, *Phys. Rev. X* **12**, 31004 (2022).
- [138] F. A. Zwanenburg, A. S. Dzurak, A. Morello, M. Y. Simmons, L. C. Hollenberg, G. Klimeck, S. Rogge, S. N. Coppersmith, and M. A. Eriksson, *Reviews of Modern Physics* **85**, 961 (2013).

- [139] L. M. K. Vandersypen, H. Bluhm, J. S. Clarke, A. S. Dzurak, R. Ishihara, A. Morello, D. J. Reilly, L. R. Schreiber, and M. Veldhorst, *npj Quantum Information* **3**, 1 (2017).
- [140] G. Scappucci, C. Kloeffel, F. A. Zwanenburg, D. Loss, M. Myronov, J.-J. Zhang, S. De Franceschi, G. Katsaros, and M. Veldhorst, *Nature Reviews Materials* **6**, 926 (2021).
- [141] O. E. Dial, M. D. Shulman, S. P. Harvey, H. Bluhm, V. Umansky, and A. Yacoby, *Physical review letters* **110**, 146804 (2013).
- [142] J. Yoneda, K. Takeda, T. Otsuka, T. Nakajima, M. R. Delbecq, G. Allison, T. Honda, T. Kodera, S. Oda, Y. Hoshi, and Others, *Nature nanotechnology* **13**, 102 (2018).
- [143] K. D. Petersson, J. R. Petta, H. Lu, and A. C. Gossard, *Physical Review Letters* **105**, 246804 (2010).
- [144] D. Vion, A. Aassime, A. Cottet, P. Joyez, H. Pothier, C. Urbina, D. Esteve, and M. H. Devoret, *Science* **296**, 886 (2002).
- [145] B. M. Maune, M. G. Borselli, B. Huang, T. D. Ladd, P. W. Deelman, K. S. Holabird, A. A. Kiselev, I. Alvarado-Rodriguez, R. S. Ross, A. E. Schmitz, and Others, *Nature* **481**, 344 (2012).
- [146] J. Medford, J. Beil, J. M. Taylor, E. I. Rashba, H. Lu, A. C. Gossard, and C. M. Marcus, *Physical review letters* **111**, 50501 (2013).
- [147] J. Medford, J. Beil, J. M. Taylor, S. D. Bartlett, A. C. Doherty, E. I. Rashba, D. P. DiVincenzo, H. Lu, A. C. Gossard, and C. M. Marcus, *Nature nanotechnology* **8**, 654 (2013).
- [148] B. Thorgrimsson, D. Kim, Y.-C. Yang, L. W. Smith, C. B. Simmons, D. R. Ward, R. H. Foote, J. Corrigan, D. E. Savage, M. G. Lagally, and Others, *npj Quantum Information* **3**, 1 (2017).
- [149] M. Benito and G. Burkard, *Applied Physics Letters* **116**, 190502 (2020).
- [150] P. Scarlino, D. J. Van Woerkom, A. Stockklauser, J. V. Koski, M. C. Collodo, S. Gasparinetti, C. Reichl, W. Wegscheider, T. Ihn, K. Ensslin, and Others, *Physical review letters* **122**, 206802 (2019).
- [151] T. Niemczyk, F. Deppe, H. Huebl, E. P. Menzel, F. Hocke, M. J. Schwarz, J. J. Garcia-Ripoll, D. Zueco, T. Hümmer, E. Solano, and Others, *Nature Physics* **6**, 772 (2010).
- [152] A. Frisk Kockum, A. Miranowicz, S. De Liberato, S. Savasta, and F. Nori, *Nature Reviews Physics* **1**, 19 (2019).

- [153] P. Forn-Diaz, L. Lamata, E. Rico, J. Kono, and E. Solano, *Reviews of Modern Physics* **91**, 25005 (2019).
- [154] E. Paladino, Y. M. Galperin, G. Falci, and B. L. Altshuler, *Reviews of Modern Physics* **86**, 361 (2014).
- [155] G. Ithier, E. Collin, P. Joyez, P. J. Meeson, D. Vion, D. Esteve, F. Chiarello, A. Shnirman, Y. Makhlin, J. Schrieffer, and Others, *Physical Review B* **72**, 134519 (2005).
- [156] D. I. Schuster, A. Wallraff, A. Blais, L. Frunzio, R.-S. Huang, J. Majer, S. M. Girvin, Schoelkopf, and RJ, *Physical Review Letters* **94**, 123602 (2005).
- [157] J. Q. You, X. Hu, and F. Nori, *Physical Review B* **72**, 144529 (2005).
- [158] A. Cottet, M. C. Dartiailh, M. M. Desjardins, T. Cubaynes, L. C. Contamin, M. Delbecq, J. J. Viennot, L. E. Bruhat, B. Douçot, and T. Kontos, *Journal of Physics: Condensed Matter* **29**, 433002 (2017).
- [159] P. Scarlino, D. J. Van Woerkom, U. C. Mendes, J. V. Koski, A. J. Landig, C. K. Andersen, S. Gasparinetti, C. Reichl, W. Wegscheider, K. Ensslin, and Others, *Nature communications* **10**, 1 (2019).
- [160] J. Basset, D.-D. Jarausch, A. Stockklauser, T. Frey, C. Reichl, W. Wegscheider, T. M. Ihn, K. Ensslin, and A. Wallraff, *Physical Review B* **88**, 125312 (2013).
- [161] D. J. Ibberson, T. Lundberg, J. A. Haigh, L. Hutin, B. Bertrand, S. Barraud, C.-M. Lee, N. A. Stelmashenko, G. A. Oakes, L. Cochrane, and Others, *PRX Quantum* **2**, 20315 (2021).
- [162] D. De Jong, J. Van Veen, L. Binci, A. Singh, P. Krogstrup, L. P. Kouwenhoven, W. Pfaff, and J. D. Watson, *Physical Review Applied* **11**, 44061 (2019).
- [163] M. Lodari, N. W. Hendrickx, W. I. L. Lawrie, T.-K. Hsiao, L. M. K. Vandersypen, A. Sammak, M. Veldhorst, and G. Scappucci, *Materials for Quantum Technology* **1**, 11002 (2021).
- [164] E. Kawakami, P. Scarlino, D. R. Ward, F. R. Braakman, D. E. Savage, M. G. Lagally, M. Friesen, S. N. Coppersmith, M. A. Eriksson, and L. M. K. Vandersypen, *Nature nanotechnology* **9**, 666 (2014).
- [165] J. H. Ungerer, P. Chevalier Kwon, T. Patlatiuk, J. Ridderbos, A. Kononov, D. Sarmah, E. P. A. M. Bakkers, D. Zumbühl, and C. Schönenberger, *arXiv preprint arXiv:2211.00763* (2022).

- [166] C. Kloeffel and D. Loss, Annual Review of Condensed Matter Physics **4**, 51 (2013).
- [167] G. Scappucci, C. Kloeffel, F. A. Zwanenburg, D. Loss, M. Myronov, J. J. Zhang, S. De Franceschi, G. Katsaros, and M. Veldhorst, Nature Reviews Materials **6**, 926 (2021).
- [168] C. H. Yang, A. Rossi, R. Ruskov, N. S. Lai, F. A. Mohiyaddin, S. Lee, C. Tahan, G. Klimeck, A. Morello, and A. S. Dzurak, Nature Communications **4** (2013).
- [169] J. H. Prechtel, A. V. Kuhlmann, J. Houel, A. Ludwig, S. R. Valentin, A. D. Wieck, and R. J. Warburton, Nature Materials **15**, 981 (2016).
- [170] J. Xiang, W. Lu, Y. Hu, Y. Wu, H. Yan, and C. M. Lieber, nature **441**, 489 (2006).
- [171] M. Brauns, J. Ridderbos, A. Li, W. G. Van Der Wiel, E. P. Bakkers, and F. A. Zwanenburg, Applied Physics Letters **109**, 1 (2016).
- [172] C. Kloeffel, M. J. Rančić, and D. Loss, Physical Review B **97**, 1 (2018).
- [173] F. N. M. Froning, M. J. Rančić, B. Hetényi, S. Bosco, M. K. Rehmann, A. Li, E. P. A. M. Bakkers, F. A. Zwanenburg, D. Loss, D. M. Zumbühl, and Others, Physical Review Research **3**, 13081 (2021).
- [174] S. J. Chorley, J. Wabnig, Z. V. Penfold-Fitch, K. D. Petersson, J. Frake, C. G. Smith, and M. R. Buitelaar, Physical review letters **108**, 36802 (2012).
- [175] M. D. Schroer, M. Jung, K. D. Petersson, and J. R. Petta, Physical review letters **109**, 166804 (2012).
- [176] K. D. Petersson, C. G. Smith, D. Anderson, P. Atkinson, G. A. C. Jones, and D. A. Ritchie, Nano letters **10**, 2789 (2010).
- [177] J. I. Colless, A. C. Mahoney, J. M. Hornibrook, A. C. Doherty, H. Lu, A. C. Gossard, and D. J. Reilly, Physical review letters **110**, 46805 (2013).
- [178] L. Hutin, B. Bertrand, E. Chanrion, H. Bohuslavskiy, F. Ansaloni, T.-Y. Yang, J. Michniewicz, D. J. Niegemann, C. Spence, T. Lundberg, and Others, in *2019 IEEE International Electron Devices Meeting (IEDM)* (IEEE, 2019) p. 37.
- [179] F. Ansaloni, A. Chatterjee, H. Bohuslavskiy, B. Bertrand, L. Hutin, M. Vinet, and F. Kuemmeth, Nature communications **11**, 1 (2020).

- [180] E. Chanrion, D. J. Niegemann, B. Bertrand, C. Spence, B. Jadot, J. Li, P.-A. Mortemousque, L. Hutin, R. Maurand, X. Jehl, and Others, *Physical Review Applied* **14**, 24066 (2020).
- [181] F. Borjans, X. Mi, and J. R. Petta, *Physical Review Applied* **15**, 1 (2021).
- [182] V. Ranjan, G. Puebla-Hellmann, M. Jung, T. Hasler, A. Nunnenkamp, M. Muoth, C. Hierold, A. Wallraff, and C. Schönenberger, *Nature communications* **6**, 1 (2015).
- [183] A. Pally, *Crystal-phase defined nanowire quantum dots as a platform for qubits*, Ph.D. thesis, University of Basel (in preparation).
- [184] C. Livermore, C. H. Crouch, R. M. Westervelt, K. L. Campman, and A. C. Gossard, *Science* **274**, 1332 (1996).
- [185] R. Wang, R. S. Deacon, D. Car, E. Bakkers, and K. Ishibashi, *Applied Physics Letters* **108**, 203502 (2016).
- [186] F. Bloch and A. Siegert, *Physical Review* **57**, 522 (1940).
- [187] J. H. Ungerer, A. Pally, A. m. Kononov, S. Lehmann, J. Ridderbos, C. Thelander, K. A. Dick, V. F. Maisi, P. Scarlino, A. Baumgartner, *et al.*, arXiv preprint arXiv:2303.16825 (2023).
- [188] L. Childress, A. Sørensen, and M. D. Lukin, *Physical Review A* **69**, 042302 (2004).
- [189] A. J. Landig, J. V. Koski, P. Scarlino, C. Reichl, W. Wegscheider, A. Wallraff, K. Ensslin, and T. Ihn, *Physical Review Letters* **122**, 2 (2019).
- [190] C. Böttcher, S. Harvey, S. Fallahi, G. Gardner, M. Manfra, U. Vool, S. Bartlett, and A. Yacoby, *Nature Communications* **13**, 4773 (2022).
- [191] W. G. van der Wiel, S. De Franceschi, J. M. Elzerman, T. Fujisawa, S. Tarucha, and L. P. Kouwenhoven, *Reviews of Modern Physics* **75**, 1 (2002).
- [192] A. Palacios-Laloy, *Superconducting qubit in a resonator: test of the Leggett-Garg inequality and single-shot readout*, Ph.D. thesis, Université Pierre et Marie Curie-Paris VI (2010).
- [193] T. Weißl, B. Küng, É. Dumur, A. K. Feofanov, I. Matei, C. Naud, O. Buisson, F. W. J. Hekking, and W. Guichard, *Physical Review B* **92**, 104508 (2015).
- [194] C. Fasth, A. Fuhrer, L. Samuelson, V. N. Golovach, and D. Loss, *Physical review letters* **98**, 266801 (2007).

- [195] S. Nadj-Perge, S. Frolov, J. Van Tilburg, J. Danon, Y. V. Nazarov, R. Algra, E. Bakkers, and L. Kouwenhoven, *Physical Review B* **81**, 201305 (2010).
- [196] M. Trif, V. N. Golovach, and D. Loss, *Physical Review B* **77**, 045434 (2008).
- [197] F. Borjans, X. Zhang, X. Mi, G. Cheng, N. Yao, C. A. C. Jackson, L. F. Edge, and J. R. Petta, *PRX Quantum* **2**, 20309 (2021).
- [198] D. Jirovec, A. Hofmann, A. Ballabio, P. M. Mutter, G. Tavani, M. Botifoll, A. Crippa, J. Kukucka, O. Sagi, F. Martins, and Others, *Nature materials* **20**, 1106 (2021).
- [199] C. X. Yu, S. Zihlmann, J. C. Abadillo-Uriel, V. P. Michal, N. Rambal, H. Niebojewski, T. Bedecarrats, M. Vinet, É. Dumur, M. Filippone, *et al.*, *Nature Nanotechnology*, 1 (2023).
- [200] G. Burkard, T. D. Ladd, J. M. Nichol, A. Pan, and J. R. Petta, *arXiv preprint arXiv:2112.08863* (2021).
- [201] F. Maier, T. Meng, and D. Loss, *Physical Review B* **90**, 155437 (2014).
- [202] R. Maurand, X. Jehl, D. Kotekar-Patil, A. Corna, H. Bohuslavskiy, R. Laviéville, L. Hutin, S. Barraud, M. Vinet, M. Sanquer, and Others, *Nature communications* **7**, 1 (2016).
- [203] A. Crippa, R. Ezzouch, A. Aprá, A. Amisse, R. Laviéville, L. Hutin, B. Bertrand, M. Vinet, M. Urdampilleta, T. Meunier, and Others, *Nature communications* **10**, 1 (2019).
- [204] C. W. Kim, J. M. Nichol, A. N. Jordan, and I. Franco, *PRX Quantum* **3**, 40308 (2022).
- [205] L. Grünhaupt, M. Spiecker, D. Gusenkova, N. Maleeva, S. T. Skacel, I. Takmakov, F. Valenti, P. Winkel, H. Rotzinger, W. Wernsdorfer, and Others, *Nature materials* **18**, 816 (2019).
- [206] B. Cord, J. Lutkenhaus, and K. K. Berggren, *Journal of Vacuum Science & Technology B: Microelectronics and Nanometer Structures Processing, Measurement, and Phenomena* **25**, 2013 (2007).
- [207] D. S. Macintyre, O. Ignatova, S. Thoms, and I. G. Thayne, *Journal of Vacuum Science & Technology B: Microelectronics and Nanometer Structures Processing, Measurement, and Phenomena* **27**, 2597 (2009).
- [208] J. Ridderbos, *Quantum dots and superconductivity in Ge-Si nanowires*, Ph.D. thesis, University of Twente (2018).

-
- [209] B. Yurke and E. Buks, *Journal of lightwave technology* **24**, 5054 (2006).
- [210] C. Lang, *Quantum microwave radiation and its interference characterized by correlation function measurements in circuit quantum electrodynamics*, Ph.D. thesis, ETH Zurich (2014).
- [211] D. M. Glowacka, D. J. Goldie, S. Withington, H. Muhammad, G. Yassin, and B. K. Tan, arXiv preprint arXiv:1401.2292 (2014).
- [212] A. Bordoloi, *Spin Projection and Correlation Experiments in Nanoelectronic Devices*, Ph.D. thesis, University of Basel (2021).
- [213] J. Combes, J. Kerckhoff, and M. Sarovar, *Advances in Physics: X* **2**, 784 (2017).
- [214] C. Müller, J. Combes, A. R. Hamann, A. Fedorov, and T. M. Stace, *Physical Review A* **96**, 53817 (2017).
- [215] A. R. Hamann, C. Müller, M. Jerger, M. Zanner, J. Combes, M. Pletyukhov, M. Weides, T. M. Stace, and A. Fedorov, *Physical review letters* **121**, 123601 (2018).
- [216] R. Ezzouch, S. Zihlmann, V. P. Michal, J. Li, A. Aprá, B. Bertrand, L. Hutin, M. Vinet, M. Urdampilleta, T. Meunier, and Others, *Physical Review Applied* **16**, 34031 (2021).
- [217] S. Park, C. Metzger, L. Tosi, M. F. Goffman, C. Urbina, H. Pothier, and A. L. Yeyati, *Physical Review Letters* **125**, 077701 (2020).
- [218] F. K. Malinowski, F. Martins, T. B. Smith, S. D. Bartlett, A. C. Doherty, P. D. Nissen, S. Fallahi, G. C. Gardner, M. J. Manfra, C. M. Marcus, and Others, *Physical Review X* **8**, 11045 (2018).
- [219] B. W. Shore and P. L. Knight, *Journal of Modern Optics* **40**, 1195 (1993).

A Fabrication protocols

This chapter provides detailed information about the fabrication of the devices described throughout this thesis.

A.1. Fabrication of resonator devices with GaAs dots

The devices described in Chapter 5 were fabricated by Pasquale Scarlino. Detailed fabrication protocols can be found in the thesis of Anna Stockklauser [35].

A.2. Fabrication of high-impedance NbTiN resonators

NbTiN resonators are described in Chapter 3, in Chapter 4, in Chapter 6, in Chapter 7, and in Chapter 8.

While fabricating the high-impedance NbTiN resonators, a special attention has to be given to the wafer processing before the sputtering of the superconducting film (see Section A.2.2, and Section A.2.3) and to the sputtering process itself (see section A.2.4). This section aims on providing a detailed description of every step involved in the fabrication of these resonators enabling the reader to reproduce the results.

A.2.1. Wafer characteristics

- Substrate material: intrinsic silicon (resistivity: 10 k Ω cm)
- Optional capping layer: 100 nm thermally grown silicon oxide

A.2.2. Cleaning of wafer with capping layer

- Sonication in an aquatic solution of tripotassium orthophosphate (time: 5 min)

- Sonication in water (time: 5 min)
- Sonication in acetone (time: 5 min)
- Sonication in isopropanol (time: 5 min)
- Blow-drying with nitrogen
- Ozone plasma cleaning (time: 5 min)

A.2.3. Cleaning of wafer without capping layer

In advance at the facilities of Paul-Scherrer Institute

- Piranha etching (solution: $\text{H}_2\text{SO}_4:\text{H}_2\text{O}_2 - 2:1$, temperature: 90°C , time: 10 min)
- Oxide removal: solution (10% HF in water, time: 1 min)
- Piranha etching: (solution: $\text{H}_2\text{SO}_4:\text{H}_2\text{O}_2 - 2:1$, temperature: 100°C , time: 10 min)
After the second Piranha etching step, the wafer is left with a thin layer of protecting oxide which is removed right before sputtering.
- Rinsing in water
- Vacuum sealing

Immediately before sputtering at University of Basel

- Oxide removal (solution: 10% HF in water, time: 1 min)
- Rinsing in water
- Blow-drying with nitrogen

A.2.4. Sputtering

- Loading of wafer and small wafer piece with PMMA mask which is used for determining the thickness of the sputtered film
- Pre-sputtering of titanium (power: 50 W, time: 15 min, background pressure: 4 mTorr , Ar flow: 50 sccm, sample shutter closed)

- Waiting 12 h to reach base pressure $\lesssim 10^{-9}$ mTorr
- Pre-sputtering of NbTi (power: 50 W, time: 5 min, background pressure: 2 mTorr, Ar flow: 50 sccm, N₂ flow: 3.5 sccm, sample shutter closed)
- Sputtering of NbTi (power:250 W, time:45 s, background pressure: 2 mTorr, Ar flow: 50 sccm, N₂ flow: 3.5 sccm, sample shutter open, sample rotation)

A.2.5. Two-step e-beam lithography

The etch mask used for defining the high-impedance superconducting resonators is created by means of electron beam lithography using a 30kV scanning electron microscope (SEM). In order to minimize the effects of beam-fluctuations during the lithography of the narrow center conductor, the lithography is performed in two steps: In a first lithography step, large structures such as bond pads and feedlines are patterned using a low dose. The sample is then developed at room-temperature before being loaded to the SEM for a second time. A second exposure step is performed with much larger charge doses minimizing the effect of beam fluctuations and proximity exposure [206]. This ensures that the mask for the narrow center conductor is well defined. The sample is then developed for a second time at a reduced temperature. While patterning, the script `Multisample` is used which enables us to pattern several structures in batches.

Sample preparation

- Cleaving of wafer to a sizeable piece ($\sim 1.5\text{ cm} \times 3\text{ cm}$)
- Sonication in acetone (time: 5 min)
- Rinsing in isopropanol
- Blow-drying with nitrogen
- Spin coating (solution: 4.5% PMMA in anisole, rotation speed: 6000 rpm, time: 45 s)
- Baking (temperature: 180°C, time: 5 min)

First e-beam step for large structures

- Exposure (dose: 300 μC , acceleration voltage: 30 kV)
- Warm development (solution: methylisobutylketon:isopropanol - 1:3, temperature: 20°C, time: 45 s)
- Rinsing (solution: isopropanol, temperature: 20°C, time: 10 s)
- Blow-drying with nitrogen

Second e-beam step for narrow center conductor

- Exposure (dose: 2000 μC , acceleration voltage: 30 kV)
- Cold development (solution: methylisobutylketon:isopropanol - 1:3, temperature: -20°C, time: 30 s)
- Rinse (solution: isopropanol, temperature: -20°C, time: 10 s)
- Blow-dry with nitrogen

A.2.6. Dry-etching

- Filling ICP-RIE plasma etcher chamber with argon (flow: 25 sccm) and chlorine (flow: 40 sccm) until reaching 10^{-5} bar.
- Plasma (source power: 100 W, rf generator power: 125 W, time: 10 s)

A.2.7. Resist removal

- Sonication in N-ethyl pyrrolidone [207] (temperature: 80°C, time: 60 min)
- Sonication in acetone (temperature: 50°C, time: 20 min)
- Rinsing in isopropanol
- Oxygen plasma cleaning (power: 30 W, time: 1 min)

A.3. Fabrication of nanowire devices

After fabricating the NbTiN resonator, a nanowire device is fabricated in a designated area of the chip at which the NbTiN has been etched away.

A.3.1. Fabrication of Ge/Si core/shell nanowire device

Narrow finger gates are fabricated by means of electron-beam lithography. The finger gates are isolated by 20 nm of hafnium/aluminium oxide grown by means of atomic layer deposition. The nanowire is then deterministically placed using a micromanipulator. As a last step, the nanowire is contacted using titanium/gold after removing the native silicon oxide from the shell using hydrofluoric acid. Details are found in the theses of Joost Ridderbos [208] and Florian Froning [84].

A.3.2. Fabrication of InAs nanowire device

Several nanowires are deterministically deposited using a micromanipulator. A suitable nanowire is then chosen using electron-beam microscopy and the position of the double-quantum dot (DQD) is identified on the basis of GaSb markers that had previously been selectively grown on the zincblende segments of the nanowire [45]. After having identified the position of the tunnel barriers, gold is deposited on top of the end of the nanowire, clamping it and hence protecting it from moving in the consecutive wet-etching step. As a next step, the gallium antimony shell is etched away using low-concentrated TMAH ($C_4H_{13}NO$). As a last step, titanium/gold side gates are deposited in proximity to the nanowire and the nanowire is contacted using titanium/gold after milling the indium arsenide oxide covering the nanowire using an argon plasma. Details about the fabrication of InAs nanowire devices can be found in the thesis of Alessia Pally.

B Supplementary information: Designing high-impedance microwave circuits

This chapter provides supplementary information corresponding to Chapter 3 in the main text.

B.1. Designing the coupling capacitor

In section 3.4 in the main text, we describe how we use Sonnet for designing the coupling between the feedline and a notch-type resonator.

Aiming for a resonance frequency of roughly 3.5 GHz and a total Q factor on the order of $Q_{\text{tot}} \gtrsim 10^3$, Q_c is desirable to be approximately 3,000. We perform a simulation study of different capacitor designs which are shown in Figure B.1. For each of these coupling capacitor designs, we simulate the transmission through the feedline as a function of frequency. From the simulation, we find S_{21} as a function of frequency which is then fitted to extract f_r and Q_c .

The capacitor designs between Figure B.1a) and Figure B.1c)) differ in the width of the capacitor plate attached to the end of the resonator's center conductor. The length, l of the resonator center conductor that is specified in the caption of Figure B.1 is slightly different to partly adjust for the frequency pull due to the different capacitor plates at the center conductor ends. We notice that even the largest capacitor plate (Figure B.1c)) results in a coupling $Q_c \gg 10,000$. Further increasing the capacitor size reduces the resonance frequency and hence the effective impedance of the resonator. Therefore, the designs shown in Figure B.1d) and Figure B.1e) do not rely on a capacitor plate at the end of the center conductor and feature a large proximity to the feedline instead. In this approach, the resonator frequency can be well determined by an analytic coplanar-waveguide model and is approximately independent of the coupling capacitance. The capacitor in Figure B.1e) together with a res-

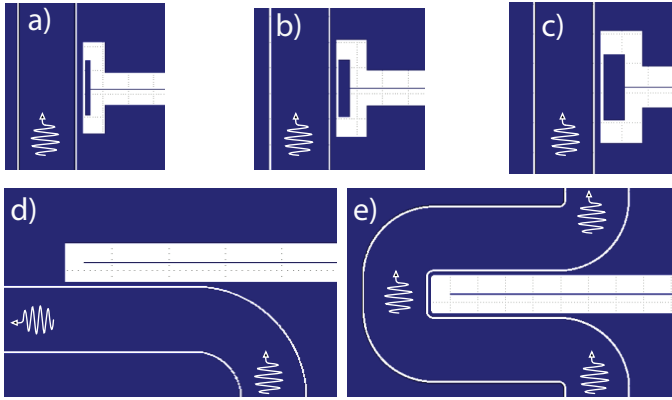


Figure B.1. Capacitor designs. The width of the feedline center conductor is $110\ \mu\text{m}$ in all figures. The width of the capacitor plate, w , and the length, l , of the resonator center conductor is varied as specified in each subcaption. The subcaption also indicates the simulated resonance frequency f_r and coupling Q factor Q_c . a) $l = 1.3\ \text{mm}$, $w = 8.5\ \mu\text{m}$, $f_r \approx 2.8\ \text{GHz}$, $Q_c \approx 20500$ b) $l = 1.1\ \text{mm}$, $w = 20\ \mu\text{m}$, $f_r \approx 3.0\ \text{GHz}$, $Q_c \approx 13500$ c) $l = 1.0\ \text{mm}$, $w = 40\ \mu\text{m}$, $f_r \approx 2.1\ \text{GHz}$, $Q_c \approx 14500$ d) $l = 1.3\ \text{mm}$, $f_r \approx 3.5\ \text{GHz}$, $Q_c \approx 12500$ e) $l = 1.3\ \text{mm}$, $f_r \approx 3.5\ \text{GHz}$, $Q_c \approx 3500$

onator length of $1.3\ \text{mm}$, results in a resonance frequency of $3.5\ \text{GHz}$ and a $Q_c \approx 3,500$, hence perfectly matching our requirements.

B.2. Alternative measurement setup

The experiments presented in Chapter 5 were performed in a different dilution refrigerator using a modified setup compared to the one described in Section 3.5 in the main text and we briefly explain the main differences. The schematic setup can be seen in Figure B.2 and the largest difference compared to the setup shown in Figure 3.7 in the main text lies in the way the microwave tone is generated and analyzed. In this case, the microwave tone (radio frequency (RF)) is generated at room temperature by a microwave generator instead of a vector network analyzer (VNA). Af-

ter passing the sample, the microwave tone passes three circulators and is then reflected by a Josephson parametric amplifier (JPA) providing quantum limited amplification [23, 54, 209]. The JPA is driven by an external pump tone which, upon reflection, is cancelled by an additional tone that is split off the pump line and fed into the fourth port of the directional coupler. Destructive interference between pump tone and cancellation tone is achieved by tuning amplitude and phase of the cancellation tone using a displacer board [23].

For signal acquisition, the signal is down-converted to an intermediate frequency (IF) by mixing the signal with a local oscillator (LO) detuned from the RF signal tone. A phase-reference is gained by performing the same mixing with a reference tone which is split-off from the RF input signal. After down-conversion, the signals are consecutively amplified and low-pass filtered. Finally, they reach the analog-to-digital converter (ADC) inputs of an Acqiris high-speed digitizer acquisition card which performs digital down-conversion to zero frequency and the Q and I quadratures are obtained. Combining them gives the complex transmission $S = I + iQ$ [11, 23, 210].

B

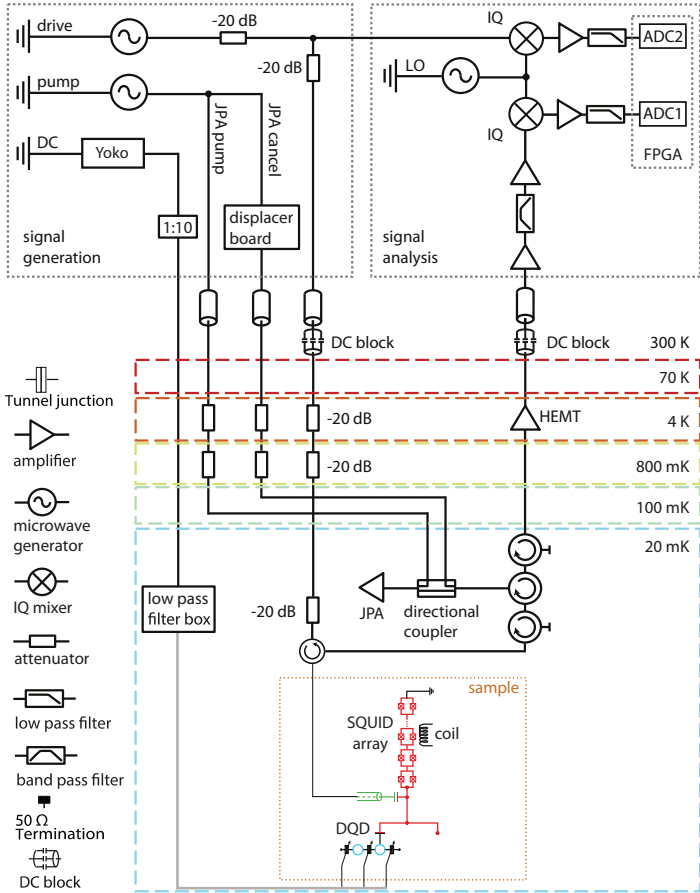


Figure B.2. Cryogenic and room-temperature equipment. A coherent microwave signal is generated by a microwave generator. After passing the resonator, it is amplified by a JPA, a cryogenic high electron mobility transistor (HEMT) amplifier and two room-temperature HEMT amplifiers. It is then downconverted and detected using an ADC acquisition card. Figure adapted from [23].

C Supplementary information: The effect of dielectrics on the quality of high-impedance resonators

This chapter provides supplementary information corresponding to Chapter 4 in the main text.

C.1. Investigation of sputtering parameters

In this appendix, we give detailed background information about the choice of sputtering parameters that are used while fabricating the resonators as described in Section 4.3 in the main text.

In order to minimize the impurity density of the sputtered NbTiN film, it is desirable to maximize the growth rate γ , because a shorter sputtering time results in less gettered contaminants in the film. While sputtering, the plasma power, P , the background pressure ρ_{bg} , the argon flow J_{Ar} and the nitrogen flow J_{N_2} can be controlled. In Figure C.1, we investigate the dependence of the growth rate γ and the voltage between the plasma source and the target V_{dc} on these parameters. The growth rate increases as a function of P . Therefore, the power should be chosen as high as possible while maintaining a stable plasma which is the case in our chamber for $P \lesssim 250$ W. As a function of J_{N_2} , a maximum in the growth rate is found, corresponding to the stoichiometric ratio [211] (see Figure C.1a) and Figure C.1b)). The position of the optimum depends on P and ρ_{bg} . When increasing ρ_{bg} , γ decreases (see Figure C.1c)). Therefore, the background pressure should be chosen as small as possible before the plasma becomes unstable. In our sputtering chamber, this is the case for $\rho_{bg} \lesssim 2$ mTorr. We choose $P = 250$ W, $\rho_{bg} = 2$ mTorr, $J_{Ar} = 50$ sccm, $J_{N_2} = 3.5$ sccm for the sputtering of both films.

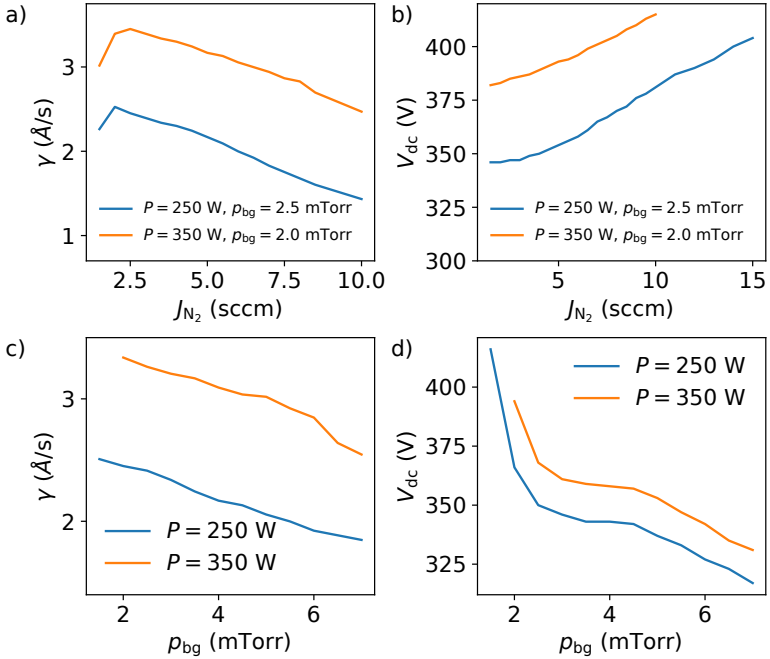


Figure C.1. Sputtering parameters. a) growth rate γ as function of nitrogen flow J_{N_2} at different back-ground pressures ρ_{bg} and plasma power P . b) dc voltage V_{dc} between plasma source and target as function of J_{N_2} for two values of ρ_{bg} and P . A kink in the curve is observed in all both a) and b) at the same values of J_{N_2} . This kink corresponds to sputtering at a stoichiometric ratio. c) growth rate γ as a function of background pressure ρ_{bg} showing a monotonous decay as lower ρ_{bg} correspond to larger mean-free paths and therefore to a smaller scattering of the sputtered material. d) dc voltage V_{dc} between the plasma source and the target as a function of background pressure ρ_{bg} . When lowering $\rho_{bg} < 2$ mTorr, V_{dc} increases drastically and the plasmas becomes unstable. All traces were measured at a fixed argon flow rate $Q_{Ar} = 50$ sccm.

C.2. Frequency shift in power dependence

In the inset of Figure 4.3b) in the main text, we observe a substantial positive resonance frequency shift as a function of temperature with a peak at approximately 0.5 K. We attribute this shift to a saturation of TLS with a transition frequency of approximately 10 GHz dispersively interacting with the resonator. Figure C.2 shows the resonance frequency shift as a function of number of photons in the resonator. The observed positive shift is smaller by an order of magnitude compared to Figure 4.3.

For very large drive powers with $\langle n_{\text{ph}} \rangle \gtrsim 10^5$, a negative relative frequency shift is observed in Figure C.2. We attribute this negative shift to the onset of the bifurcation of the resonator due to a finite non-linearity.

C

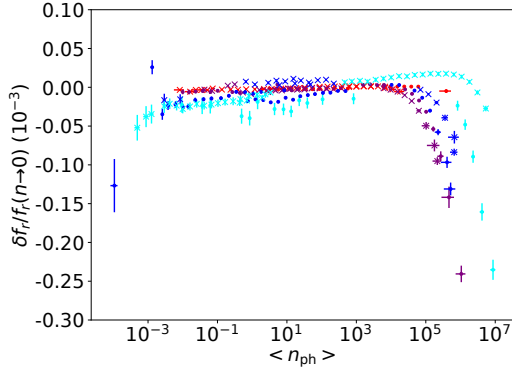


Figure C.2. Relative frequency shift $\delta f_r = f_r - f_r(n \rightarrow 0)$ as function of average number of photons in the resonator $\langle n_{\text{ph}} \rangle$. We do not observe a noteworthy positive frequency shift, and therefore exclude a simple saturation of two-level fluctuators as reason for the observed resonance frequency shifts as a function of temperature in Figure 4.3 in the main text. For $\langle n_{\text{ph}} \rangle \gtrsim 10^5$, an increasingly negative relative frequency shift is observed which we attribute to the finite non-linearity of the resonators.

D Supplementary information: Charge noise protection and ultrastrong coupling

This chapter provides supplementary information corresponding to Chapter 5 in the main text. Section D.1 provides the methodology of quantitative charge-stability diagram analysis which was used in most chapters of this thesis.

D.1. Determining the system capacitances

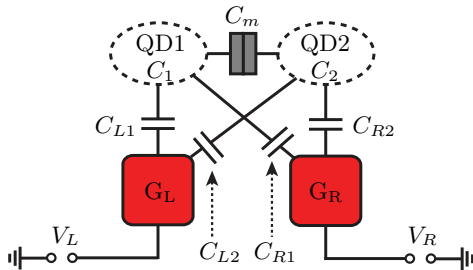


Figure D.1. Capacitance model of a double-quantum dot (DQD). In the figure, all the capacitance parameters relevant for us are indicated. Figure adapted from [97, 212].

The charge-stability diagram can be understood quantitatively by considering a capacitance model [97] as depicted in Figure D.1. This section aims on providing simple expressions for determining the relevant capacitance parameters from the measured charge-stability diagram which are

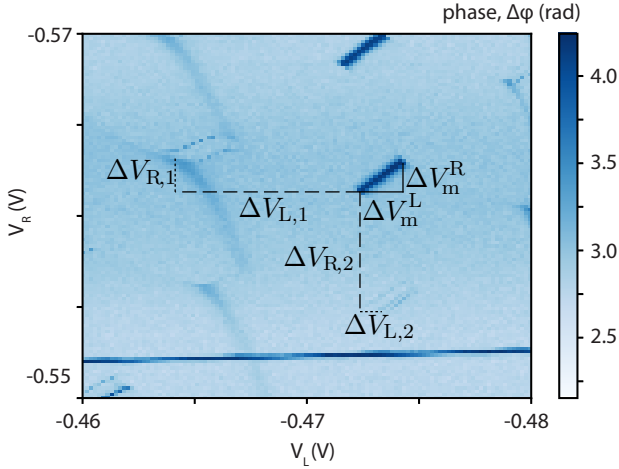


Figure D.2. An example of a DQD charge stability diagram. It shows the phase response of the resonator reflectance while changing the voltage of gates L R [see Fig. 5.1(e)]. The six voltage differences indicated allow extraction of the QDs capacitances and the dipole strength η .

used throughout this thesis. Then, from the system capacitances, the dipole strength which is used in Chapter 5 is calculated explicitly.

In the following, we describe how the set of capacitance parameters $C_{L,1}, C_{R,1}, C_1, C_{L,2}, C_{R,2}, C_2$ and C_m corresponding to Figure D.1, are determined from the DQD charge stability diagram. Here $C_{L,i}$ [$C_{R,i}$] is the capacitance between the left [right] side plunger gate and the i th dot and C_i is the total capacitance of the i th dot. C_m describes the inter-dot mutual capacitance.

Dashed lines labelled with $\Delta V_{L,i}$ [$\Delta V_{R,i}$] in the charge stability diagram [191] in Figure D.2 represent the plunger gate voltage differences between two consecutive sets of triple points for which the only difference is that the effective charge of dot i changes by one electron charge e , while the total electro-static energy remains constant. I.e. changing the left and right gate potentials by $\Delta V_{L,1}$ and $\Delta V_{R,1}$ according to the figure brings the charge configuration from (N, M) to $(N \pm 1, M)$, where N and M

are integers. Changing the number of charges by one in dot 2 $((N, M)$ to $(N, M \pm))$ is realized by adjusting the gate potentials by $\Delta V_{L,2}$ and $\Delta V_{R,2}$. Hence one finds the four equations

$$\begin{pmatrix} C_{L,1} \\ C_{R,1} \\ C_{L,2} \\ C_{R,2} \end{pmatrix} = \begin{pmatrix} \Delta V_{L,1} & -\Delta V_{R,1} & 0 & 0 \\ 0 & 0 & \Delta V_{L,1} & -\Delta V_{R,1} \\ -\Delta V_{L,2} & \Delta V_{R,2} & 0 & 0 \\ 0 & 0 & -\Delta V_{L,2} & \Delta V_{R,2} \end{pmatrix}^{-1} \cdot \begin{pmatrix} e \\ 0 \\ 0 \\ e \end{pmatrix} \quad (\text{D.1})$$

The charging energy, can be rewritten as

$$E_{n_1, n_2}(n_{G,i}) = E_{C,1}(n_1 - n_{G,1})^2 + E_{C,2}(n_2 - n_{G,2})^2 + E_{C,m}(n_1 - n_{G,1})(n_2 - n_{G,2}), \quad (\text{D.2})$$

where n_i is the number of electrons in dot i . Here, we introduced $n_{G,i}$ representing the effective number of electrons induced on dot i by the voltages on the gates. A voltage change on the left (right) side gate, denoted by ΔV^L (ΔV^R), results in a change $\Delta n_{G,1}$ ($\Delta n_{G,2}$) of $n_{G,1}$ ($n_{G,2}$) according to

$$\begin{pmatrix} \Delta n_{G,1} \\ \Delta n_{G,2} \end{pmatrix} = \frac{1}{e} \begin{pmatrix} C_{L,1} & C_{R,1} \\ C_{L,2} & C_{R,2} \end{pmatrix} \cdot \begin{pmatrix} \Delta V^L \\ \Delta V^R \end{pmatrix}. \quad (\text{D.3})$$

and the charging energy matrix is represented by

$$\begin{pmatrix} E_{C,1} & E_{C,m}/2 \\ E_{C,m}/2 & E_{C,2} \end{pmatrix} = \frac{e^2}{2} \begin{pmatrix} C_1 & -C_m \\ -C_m & C_2 \end{pmatrix}^{-1}. \quad (\text{D.4})$$

Now we consider the solid black lines in Figure D.2 labelled with ΔV_m^L [ΔV_m^R] that connect adjacent triple points which are split due to the mutual inter-dot capacitance C_m . In the following, we use them to extract C_m , C_1 and C_2 . Because we conduct ourselves on relative occupancies, without losing generality, we consider the triple point at the intersects of the $\{(0,0), (0,1), (1,0)\}$ charge stability regions. The electrostatic energy at these triple point is given by

$$E_{0,0}(n_{G,i}^{(1)}) = E_{0,1}(n_{G,i}^{(1)}) = E_{1,0}(n_{G,i}^{(1)}). \quad (\text{D.5})$$

Similarly, the charging energy at the adjacent triple point corresponding to the intersect of the $\{(1,1), (0,1), (1,0)\}$ charge stability regions is given by

$$E_{1,1}(n_{G,i}^{(2)}) = E_{0,1}(n_{G,i}^{(2)}) = E_{1,0}(n_{G,i}^{(2)}). \quad (\text{D.6})$$

The voltage differences between these two triple points are denoted by ΔV_m^L and ΔV_m^R (lengths of solid black lines in Figure D.2). Plugging these voltage differences into Eq. (D.3) as $\Delta V^L = \Delta V_m^L$ and $\Delta V^R = \Delta V_m^R$, we calculate the difference of the effective electron numbers induced by the gates $\Delta n_{G,1}^{(m)}$ and $\Delta n_{G,2}^{(m)}$ between the two triple points. In order to calculate the three parameters C_m , C_1 and C_2 , additionally to Eqs. (D.5) and (D.6), we consider the following relation which allows to calibrate the energy scale in the DQD stability diagram:

$$\hbar\epsilon = E_{1,0} - E_{0,1} \quad (\text{D.7})$$

at a specific set of gate voltages. Throughout the experiments presented in this thesis, the detuning ϵ is measured in three different ways:

1. By two-tone spectroscopy of a charge qubit (see Figure 2.19)
2. By measuring a bias triangle at a given source drain bias voltage V_{sd} (see Figure F.1)
3. By measuring an anti-crossing of the resonator and a charge qubit as a function of ϵ (see e.g. Fig. 5.3a-c))

We label the difference in the voltage on the left (right) gate corresponding to ϵ extracted from any of these methods. By plugging these voltage differences into Eq. (D.3) as $V^L = \Delta V_\epsilon^L$ and $V^R = \Delta V_\epsilon^R$, we again convert the voltage differences into differences in the effective number of electrons induced by the gates which we call $\Delta n_{G,1}^{(\epsilon)}$ and $\Delta n_{G,2}^{(\epsilon)}$. Here, the superscript (ϵ) highlights the correspondence to one specific set of ϵ , ΔV_ϵ^L and ΔV_ϵ^R .

Combining Eqs. (D.2), (D.5), (D.6) and (D.7), we find the charging energies as

$$\begin{pmatrix} E_{C,1} \\ E_{C,2} \\ E_{C,m} \end{pmatrix} = \begin{pmatrix} \Delta n_{G,1}^{(m)} & 0 & \left(\Delta n_{G,2}^{(m)} - 1 \right) / 2 \\ 0 & \Delta n_{G,2}^{(m)} & \left(\Delta n_{G,1}^{(m)} - 1 \right) / 2 \\ -2\Delta n_{G,1}^{(\epsilon)} & 2\Delta n_{G,2}^{(\delta)} & \Delta n_{G,1}^{(\epsilon)} - \Delta n_{G,2}^{(\epsilon)} \end{pmatrix}^{-1} \cdot \begin{pmatrix} 0 \\ 0 \\ \hbar\epsilon \end{pmatrix}. \quad (\text{D.8})$$

From the charging energies, the capacitances C_1 , C_2 and C_m can be de-

duced from Eq. (D.4) as

$$C_m = \frac{e^2 (\Delta V_\epsilon^L \Delta V_m^R + \Delta V_m^L \Delta V_\epsilon^R)}{\hbar\epsilon (\Delta V_{L,1}^L \Delta V_{R,2}^R - \Delta V_{L,2}^L \Delta V_{R,1}^R)}, \quad (\text{D.9})$$

$$C_1 = \frac{e^2 (\Delta V_\epsilon^L \Delta V_m^R + \Delta V_m^L \Delta V_\epsilon^R) (\Delta V_{L,1}^L \Delta V_{R,2}^R - \Delta V_m^L \Delta V_{R,2}^R - \Delta V_{L,2}^L \Delta V_m^R - \Delta V_{L,2}^L \Delta V_{R,1}^R)}{\hbar\epsilon (\Delta V_m^L \Delta V_{R,1}^R + \Delta V_{L,1}^L \Delta V_m^R) (\Delta V_{L,1}^L \Delta V_{R,2}^R - \Delta V_{L,2}^L \Delta V_{R,1}^R)}, \quad (\text{D.10})$$

$$C_2 = \frac{e^2 (\Delta V_\epsilon^L \Delta V_m^R + \Delta V_m^L \Delta V_\epsilon^R) (\Delta V_{L,1}^L \Delta V_{R,2}^R - \Delta V_m^L \Delta V_{R,1}^R - \Delta V_{L,1}^L \Delta V_m^R - \Delta V_{L,2}^L \Delta V_{R,1}^R)}{\hbar\epsilon (\Delta V_m^L \Delta V_{R,2}^R + \Delta V_{L,2}^L \Delta V_m^R) (\Delta V_{L,1}^L \Delta V_{R,2}^R - \Delta V_{L,2}^L \Delta V_{R,1}^R)}. \quad (\text{D.11})$$

After having found these equations for the system capacitances, we calculate the dipole strength is given according to Eq. (5.5) as

$$\eta = \frac{1 - 2C_m/(C_1 + C_2)}{1 + 2C_m/(C_1 + C_2)}. \quad (\text{D.12})$$

When dividing the capacitances by each other, the terms involving the lever arm calibration cancel. Hence, η can be determined directly from the charge stability diagram without considering the energy calibration step.

In the simplified case of identical dots, $C_1 = C_2 = C_\Sigma$, with a symmetric coupling to their respective gates, $C_{L,1} = C_{R,2}$, and neglecting cross-gate capacitances, $C_{R,1} = C_{L,2} = 0$, the expressions further simplify to

$$\frac{C_m}{C_\Sigma} = \frac{\Delta V_m}{\Delta V_g - \Delta V_m}, \quad (\text{D.13})$$

$$\eta = 1 - \frac{2\Delta V_m}{\Delta V_g}, \quad (\text{D.14})$$

where $\Delta V_m/\sqrt{2} \equiv \Delta V_m^L = \Delta V_m^R$ and $\Delta V_g/\sqrt{2} \equiv \Delta V_{L,1} = \Delta V_{R,2}$.

The error bars assigned to the extracted capacitances and to η are determined by attributing, in the above procedure, an uncertainty to the positions of the four triple points in the stability diagram (see Fig. D.2). The errors were then propagated to the final results in Eqs. (D.12), (D.9), (D.10) and (D.11) using Gaussian error propagation.

D. Supplementary information: Charge noise protection and ultrastrong coupling

index	$C_{\Sigma,1}$ [fF]	$C_{\Sigma,2}$ [fF]	C_m [fF]	η	$g/2\pi$ [MHz]	$\Gamma_2/2\pi$ [MHz]	σ_c [μ eV]	$\epsilon/2\pi$ [MHz]	$\omega_r/2\pi$ [MHz]
1	0.561±0.034	0.634±0.071	0.488±0.041	0.101±0.064	41.63±0.06	4.5±0.2	0.171±0.006	5420.8±0.2	5437.0±0.1
2	0.433±0.037	0.474±0.061	0.358±0.041	0.117±0.088	54.9±0.1	4.8±0.2	0.113±0.009	5568.6±0.3	5575.6±0.14
3	0.599±0.056	0.565±0.034	0.473±0.038	0.103±0.065	48.8±0.2	4.5±0.2	0.107±0.007	5435.1±0.5	5578.6±0.11
4	0.554±0.068	0.41±0.075	0.364±0.060	0.204±0.105	75.7±0.2	5.5±0.2	0.250±0.008	5137.4±0.4	5117.6±0.14
5	0.656±0.065	0.70±0.053	0.506±0.052	0.123±0.079	56.4±0.5	6.7±0.2	-	5482±3	5578.4±0.4
6	0.611±0.053	0.54±0.058	0.443±0.046	0.168±0.071	86.3±0.2	7.2±0.2	0.120±0.007	5633.5±0.4	5649.0±0.2
7	0.265±0.045	0.31±0.051	0.191±0.034	0.184±0.092	87.2±0.4	6.5±0.8	0.34±0.007	5276±1	5283.7±0.6
8	0.333±0.031	0.27±0.041	0.250±0.026	0.172±0.078	111.1±0.3	9.6±0.3	0.273±0.005	5145±1	5180.3±0.2
9	0.136±0.045	0.32±0.037	0.058±0.017	0.419±0.073	153.6±1.9	28.3±1.2	0.42±0.02	4453±4	4440.9±0.3
10	0.330±0.050	0.20±0.023	0.048±0.007	0.709±0.031	260.5±3.5	36.8±0.9	-	4772.7±9	4745.5±0.9
11	0.412±0.029	0.20±0.050	0.257±0.029	0.273±0.076	65.9±0.7	8.5±1.1	0.328±0.005	4243±2	4271.6±0.2

Table D.1. Extracted parameters for the eleven DQD configurations presented in Fig 5.4 in Sec. 5.3 of the main text.

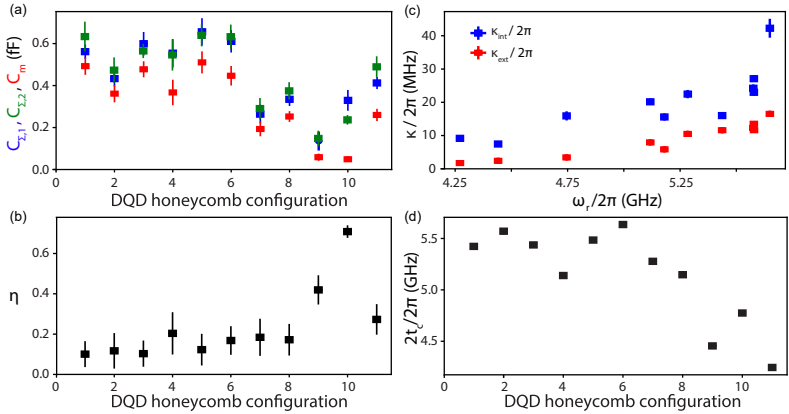


Figure D.3. Parameter comparison between the eleven configurations analyzed in the main text. (a) DQD capacitances C_1 , C_2 and C_m . (b) Dipole strength η . (c) κ_{ext} and κ_{int} , extracted by fitting the reflectance of the bare SQUID array to a Lorentzian with the DQD deep in Coulomb blockade. (d) Inter-dot tunneling rates Δ/h obtained from the JC model [see dashed lines in Fig. 5.3(a-c)]. In (c) the data are ordered according to the resonator frequency. In remaining panels, the x axis is the configuration index.

index	V_{CG} (mV)	V_T (mV)	V_{LSG} (mV)	V_{RSG} (mV)
1	-823.00	-623.00	-881.32	-946.48
2	-823.00	-623.00	-883.236	-937.35
3	-823.00	-727.00	-884.445	-789.79
4	-823.00	-818.00	-691.47	-751.60
5	-847.00	-847.00	-671.525	-641.20
6	-882.00	-882.00	-602.14	-648.68
7	-936.00	-936.00	-795.71	-593.76
8	-982.00	-982.00	-576.544	-613.92
9	-1040.00	-1040.00	-473.037	-562.02
10	-1050.00	-1050.00	-496.28	-574.92
11	-1030.00	-1030.00	-525.56	-494.35

Table D.2. The DQD gate voltages for the eleven configurations investigated in Sec. 5.3 of the main text.

D.2. Considerations about the definition of the dipole strength η

Here, we report some further considerations about the definition of the dipole strength for a DQD, introduced in Eq. (5.8). First of all, η is dimensionless and independent on scales, such as the dot size or material constants. Second, since $C_\Sigma \geq C_m \geq 0$, its value ranges between zero and one. Third, we notice that zero mutual capacitance, $C_m/C_\Sigma \rightarrow 0$, gives no suppression, $\eta \rightarrow 1$, and maximal mutual coupling $C_m/C_\Sigma \rightarrow 1$ gives perfect suppression $\eta \rightarrow 0$. Here, it is useful to point out two possible limiting scenarios of increasing the inter-dot coupling to $C_m/C_\Sigma \rightarrow 1$. Among other options, one can take this limit with either C_Σ or C_{out} fixed. In the former, the numerator in Eq. (5.8) is decreasing, reflecting the sum rule in Eq. (5.6). The numerator is constant in the latter, and its only role is to render the dipole strength dimensionless and normalized to one. Finally, and what we deem most important, the definition of η as given in Eq. (5.8) is practical: the quantities defining η can be directly read off the standard charging diagram of the double dot, as illustrated in Fig. 5.2 and Fig. D.2.

For illustration, we make the analogy with the typical microscopic

model used to describe the origin of the coupling of the DQD electrical dipole moment $e \times d$ to the electrical field \mathcal{E} generated by the resonator. In this case, we can write the coupling term as

$$g = \eta \times g_0 \equiv \eta \times e \times d \times \mathcal{E}, \quad (\text{D.15})$$

where we identified the *bare* dipole energy of the DQD and resonator as $g_0 = ed\mathcal{E} = 2e \sqrt{\frac{\hbar\omega_r}{2C_r} \frac{C_{G,1} - C_{G,2}}{C_{out}}}$, defined through bare quantities e , d and \mathcal{E} . Thus, Eq. (D.15) expresses the coupling strength as the dipole energy arising from displacement of an electron by distance d in the electric field \mathcal{E} , modified by the dipole strength $\eta \in \langle 0, 1 \rangle$. Such a definition anticipates the three different possible microscopic origins of the dipole strength for the dipolar interaction: the dot background (core) electrons can partially screen the electric field acting on the hopping (valence) electron ($\eta \times \mathcal{E}$); screening effects can reduce the effective hopping charge ($\eta \times e$); electrostatic tuning of the system may result in a configuration with reduced effective inter-dot distance ($\eta \times d$). Experimentally, we cannot distinguish these scenarios. We refer to them collectively as *renormalization of the dipolar coupling energy*. Eq. (5.10) defines the dipole coupling g using more accessible parameters.

D.3. Detuning sensitivity to charge and voltage fluctuations

This appendix shows how the DQD detuning energy responds to a change in the electrostatic environment in correspondence with voltage or charge fluctuations of a nearby impurity. Our goal is to shed light on Eq. (5.5), especially in the case where the two dots have non-equal capacitance contributions. The first line of Eq. (5.5) can be cast into

$$\delta\epsilon = e\delta V_G \frac{C_G [d_\Sigma C_\Sigma + d_G (C_\Sigma - C_m)]}{C_\Sigma^2 (1 - d_\Sigma^2/4) - C_m^2}. \quad (\text{D.16})$$

We have introduced $C_G = (C_{G,1} + C_{G,2})/2$ and $C_\Sigma = (C_1 + C_2)/2$ for the average capacitances, and $d_G = (C_{G,1} - C_{G,2})/C_G$ and $d_\Sigma = (C_1 - C_2)/C_\Sigma$ for fractional differences. The formula further simplifies upon introducing “polarizations” of the dot capacitances to the gate and to the outside of

the DQD, $C_{\text{out},d} = C_d - C_m$. Namely, we define the polarizations

$$P_G = \frac{C_{G,1} - C_{G,2}}{C_{G,1} + C_{G,2}}, \quad P_{\text{out}} = \frac{C_{\text{out},1} - C_{\text{out},2}}{C_{\text{out},2} + C_{\text{out},2}}. \quad (\text{D.17})$$

They relate to the fractional differences by $P_G = d_G/2$ and $P_{\text{out}} = d_\Sigma C_\Sigma / 2(C_\Sigma - C_m)$ and they take values between -1 and 1. $P_G \approx 1$ corresponds to the magnitude of the left dot capacitance to the gate V_G being much larger than that of the right dot and analogously for P_{out} . Since we aim at the leading order result, we neglect the $d_\Sigma^2/4$ term in the denominator of Eq. (D.16), being higher-order in the difference of the two total capacitances. With that, and using the polarizations, the detuning change is

$$\delta\epsilon = e\delta V_G \frac{C_{G,1} + C_{G,2}}{C_\Sigma + C_m} (P_G + P_{\text{out}}) \quad (\text{D.18})$$

, which is a generalization of the second line of Eq. (5.5): The difference of the two dots gives rise to an additional polarization, P_{out} . Using Eq. (D.18) instead of Eq. (D.16), the expression in Eq. (5.7) would read

$$\delta\epsilon = eV_G \frac{C_{G,1} + C_{G,2}}{C_{\text{out}}} (P_G + P_{\text{out}}) \eta, \quad (\text{D.19})$$

where $C_{\text{out}} = C_\Sigma - C_m$ and the last term is the dipole strength as given in Eq. (5.8). In other words, our definition of η remains the same even if the dots are not equal.

We now derive the detuning change with respect to a charge impurity fluctuation. Concerning the electrostatic description, a charge impurity is an object similar to a dot: its primary variable is the charge and the voltage is a derived variable. Postponing the derivation and discussion of a model containing charge impurities to a separate publication, we state here only the result; the analog of Eq. (D.16) with changing impurity i charge by δQ_i is

$$\delta\epsilon = e \frac{\delta Q_i}{C_i} \frac{C_{i,1} + C_{i,2}}{C_\Sigma + C_m} (P_i + P_{\text{out}}), \quad (\text{D.20})$$

where $C_{i,d}$ is the capacitance between the impurity i and the dot d , the polarization of these capacitances is $P_i = (C_{i,1} - C_{i,2}) / (C_{i,1} + C_{i,2})$, and C_i is the impurity self-capacitance. We conclude that there is a complete analogy between Eq. (D.18) and Eq. (D.20) upon interpreting $\delta Q_i / C_i$ as the equivalent voltage fluctuation.

D.4. SQUID and junction array high impedance resonators

High impedance resonators represent a valuable tool to increase the vacuum voltage fluctuations to maximize the coupling strength with the two-level electrical dipole moment. They allow to reach the strong coupling regime for electrons confined in semiconductor DQDs [23]. For superconducting artificial atoms electrically coupled to the microwave radiation, it has been recently demonstrated that high impedance resonators enable reaching a much higher coupling strength, which brings the system in the ultrastrong and deep strong coupling regimes [152, 153].

The SQUID and JJ array resonators, represented in Fig. D.4, are 1D Josephson-junction metamaterials with a multimode spectrum [37]. The choice of design parameters ensures that the array exhibits its fundamental mode within the measurement bandwidth and well separated in frequency from its second mode [37]. In Fig. D.4 (a) and (b) [(c) and (e)], we report a micrograph of [a circuit model for] the SQUID and JJ array resonators, respectively. The base unit of the SQUID [JJ] array resonator is enclosed by the dashed red [blue] line in Fig. D.4(a), (c-d) [(b), (e-f)]. The fabrication process of the SQUID array, based on the shadow evaporation technique, generates the two small Josephson junctions in parallel (the SQUID junctions, in red) that are in series with an extra larger junction (in blue), of ~ 11 times larger footprint, as we can see in Fig. D.4(a).

We realized SQUID junctions with inductance $L_S \sim 1.25$ nH and capacitance $C_S \sim 80$ fF, while the large junctions have $L_J^* \sim 0.11$ nH and $C_J^* \sim 880$ fF. Each section of the SQUID array contributes on average a stray capacitance to ground of $C_0 \sim C_{\text{gnd}}/N = C_0^J + C_0^S$ (see table D.3), where $C_0^J \sim 6C_0^S$ is the average capacitance to ground of the series junction. Therefore, the part of the base unit containing the extra junction dominates the stray capacitance to the ground per section, but adds a negligible contribution to the total array inductance. This limits the impedance of the resonator array's fundamental mode.

We model the arrays as distributed $\lambda/4$ resonators, being shunted to ground on one end [see Fig. 5.1(c) and (d)]. The capacitance between the array resonator and the right QD, the microwave feedline and the rest of the DQD depletion gates are estimated to be $C_{\text{RPG}} \sim 0.07$ fF, $C_c \sim 3$ fF and $C_g \sim 1.5$ fF, respectively.

As shown in Fig. D.4(f) and reported in Table D.3, we model each unit

cell of the JJ array with a parallel circuit of an inductance $L_J \sim 1.5$ nH and a capacitance $C_J \sim 40$ fF, connected in series with a capacitance C_0^{JJ} to ground. For $N = 70$ junctions in series, we obtain a total array resonator length of about $70 \mu\text{m}$, with an estimated total array inductance of $L_{\text{tot}} \sim 102$ nH and a total stray capacitance to ground of $C_{\text{gnd}} \sim 4.9$ fF. This allows to estimate a JJ array resonator impedance $Z_{rJJ} \sim \sqrt{L_{\text{tot}}/(C_{\text{gnd}} + C_c + C_g + C_{\text{RPG}})} \sim 3.8$ k Ω , which is almost four times higher than the SQUID array impedance and allows to increase the coupling strength with the DQD electric-dipole moment of a factor $\sqrt{Z_r^{JJ}/Z_r^{\text{Sq}}} \sim 2$.

	SQUID Array	Junction Array
Z_r (k Ω)	1.1	3.8
$\omega_r/2\pi$ (GHz)	6.2 (tunable)	5.665
$\kappa_{\text{int}}/2\pi$ (MHz)	Fig. D.3(c)	23.0
$\kappa_{\text{ext}}/2\pi$ (MHz)	Fig. D.3(c)	4.0
N	34	72
$\omega_p/2\pi$ (GHz)	16.6	16.1
Length (μm)	200	70
K_{00} (kHz)	5	60
L_{tot} (nH)	31	102
C_{gnd} (fF)	19	5
C_c (fF)	2.5	1.5
C_g (fF)	1.5	1.5

Table D.3. Comparison between SQUID and JJ array resonators.

D.5. Master equation - dissipative dynamics of DQD and resonator

Here, we give a short introduction to the theoretical modeling of the experimental data presented in Chapter 5. The model includes the DQD, the resonator, and the microwave drive through a transition line. For simplicity, we use the convention $\hbar = 1$ in this section. The dissipative

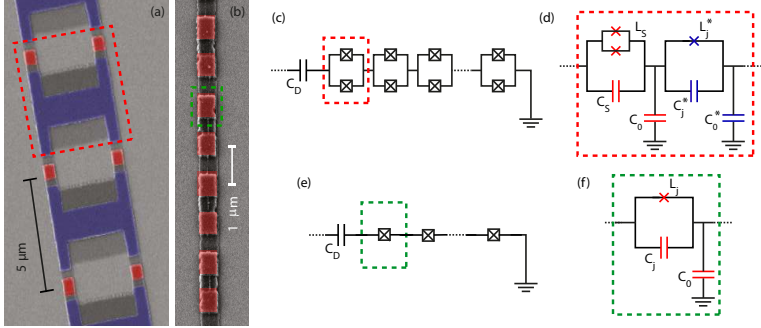


Figure D.4. Comparison between a SQUID and a junction array resonator. (a) False-colored SEM micrograph of a section of a SQUID array. The dashed red line encloses the unit cell of the SQUID array. (b) False-colored SEM micrograph of a section of a Josephson junction array. The dashed green line encloses the unit cell of the array, with a single $0.5 \times 0.9 \mu\text{m}^2$ Josephson junction. (c) Schematic circuit for a $\lambda/4$ SQUID array resonator. $C_D = C_c + C_{RPG} + C_g$ represents the capacitive coupling between the resonator array and the microwave feedline, the DQD device, and the rest of the DQD gates. The other end of the array is grounded. (d) Circuit schematic of the unit cell of the SQUID array. L_S and L_J^* represent the inductance of each SQUID junctions (red) and of the extra Josephson junction (blue) connected in series, while C_S (red) and C_J^* (blue) represent their junction capacitance. C_0 and C_0^* are their respective capacitance to the ground. (e) Schematic circuit for a $\lambda/4$ JJ array. (f) Circuit schematic of the JJ array's unit cell. L_J represents the Josephson inductance, while C_J and C_0 are the junction capacitance and the stray capacitance to ground, respectively.

dynamics of the system are described by the master equation

$$\dot{\rho} = -i[H, \rho] + \sum_k \mathcal{L}_k \rho, \quad (\text{D.21})$$

where H is the Hamiltonian of the system and $\mathcal{L}_k \rho$ describe different dissipative channels introduced in the following.

D.5.1. Hamiltonian

The DQD is well described by the Hamiltonian

$$H_{\text{DQD}} = \frac{\hbar}{2}\epsilon\sigma_z + \hbar t_c\sigma_x = \frac{1}{2}\hbar\omega_q\tilde{\sigma}_z, \quad (\text{D.22})$$

with the Pauli matrices σ in the DQD position basis and $\tilde{\sigma}$ in its eigenbasis, and where ϵ is the detuning and t_c is the tunnel splitting between the two dots. The DQD level splitting is $\omega_q = \sqrt{\epsilon^2 + (2t_c)^2}$. The resonator is described by

$$H_{\text{res}} = \hbar\omega_r a^\dagger a, \quad (\text{D.23})$$

with its resonance frequency ω_r and the bosonic annihilation operator a . The coupling between DQD and resonator corresponds to the quantum dots dipole moment and the electric field of the harmonic oscillator mode, so we write

$$\begin{aligned} H_{\text{DQD-res}} &= g_0\sigma_z(a + a^\dagger) \\ &= g_0(\cos\varphi\tilde{\sigma}_z + \sin\varphi\tilde{\sigma}_x)(a + a^\dagger), \end{aligned} \quad (\text{D.24})$$

with the DQD mixing angle $\tan\varphi = \epsilon/2t_c$. The total system Hamiltonian is then

$$H = H_{\text{DQD}} + H_{\text{res}} + H_{\text{DQD-res}}. \quad (\text{D.25})$$

D.5.2. Dissipative processes

The quantum dot and resonator are unavoidably coupled to the environment, leading to energy loss and dephasing. For the resonator, incoherent photon loss can be described in the master equation through a dissipative term

$$\mathcal{L}_{\text{res}}\rho = \kappa_{\text{int}}\mathcal{D}[a]\rho, \quad (\text{D.26})$$

with the internal photon loss rate κ_{int} . In practice, the resonator decay consists of an internal component κ_{int} , resulting from coupling to the intrinsic environment, and an external coupling rate, κ_{ext} , resulting from coupling to external modes, such as the transmission lines used for driving. Here, the external coupling will be taken into account through the SLH cascading of an external driving field, described in the next section, so that we only include the intrinsic losses κ_{int} . For the DQD, we assume a transversal decay channel, leading to energy relaxation at rate Γ_1 , as

well as a pure dephasing process due to fluctuations in the level splitting, leading to dephasing at rate $\Gamma_2 = \frac{1}{2}\Gamma_1 + \Gamma_\varphi$. The contributions to the master equation due to the dissipative dynamics of the DQD are then given by

$$\mathcal{L}_{\text{DQD}}\rho = \Gamma_1\mathcal{D}[\tilde{\sigma}_-]\rho + \frac{1}{2}\Gamma_\varphi\mathcal{D}[\tilde{\sigma}_z]\rho. \quad (\text{D.27})$$

D.5.3. SLH model - driven, dissipative dynamics of DQD and resonator

We use the SLH cascaded quantum systems approach to model scattering of microwave photons in the transmission line off the $\lambda/4$ resonator [29, 213, 214]. We cascade in a drive field for the resonator, which adds an effective drive term to the Hamiltonian as

$$H_{\text{drive}} = \frac{1}{2i}\sqrt{\kappa_{\text{ext}}}\left(\alpha a^\dagger - \alpha^* a\right), \quad (\text{D.28})$$

where we assumed a single-sided, $\lambda/4$ -type cavity driven with a coherent state of amplitude α . Here, we have additionally transformed the system into the rotating frame at the drive frequency ω_d of the coherent field input α . The cascading also adds another dissipative part to the master equation, which describes the decay of the resonator modes into the transmission line, which is assumed to have a constant spectrum. This term can be written as

$$\mathcal{L}_{\text{SLH}}\rho = \mathcal{D}[\hat{L}]\rho \quad (\text{D.29})$$

with the decay operator

$$\hat{L} = \sqrt{\kappa_{\text{ext}}}\,a + \alpha\mathbb{1}. \quad (\text{D.30})$$

Using this formalism, we can now calculate the amplitude β and photon flux n of the field scattered off the resonator as

$$\beta = \text{Tr}\{\hat{L}\rho\} \quad , \quad n = \text{Tr}\{\hat{L}^\dagger\hat{L}\rho\} \quad (\text{D.31})$$

where ρ is the solution of the total master equation, Eq. (D.21), now also including the drive and decay term from the cascading procedure, Eqs. (D.28) and (D.29). As equilibration of the field in the transmission lines happens typically very fast, we can assume that scattering in experiments happens in the steady-state of the system, so that we only need to calculate the steady-state density matrix $\bar{\rho}$ for all cases.

D.5.4. Visibility of vacuum Rabi splitting

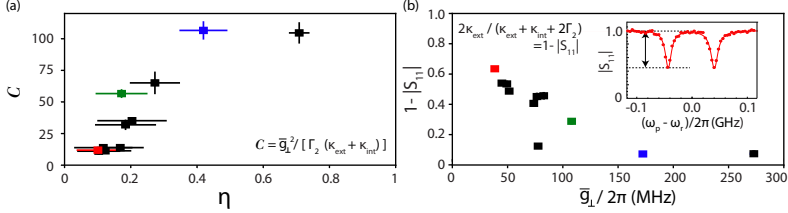


Figure D.5. Extracted figures of merit of light-matter hybridization. (a) System cooperativity $C = \bar{g}_\perp^2 / (\Gamma_2 (\kappa_{\text{ext}} + \kappa_{\text{int}}))$. (b) Visibility of the vacuum Rabi modes at resonance $(1 - |S_{11}|) = 2\kappa_{\text{ext}} / (\kappa_{\text{ext}} + \kappa_{\text{int}} + 2\Gamma_2)$ vs. the DQD-SQUID array coupling strength \bar{g}_\perp .

In order to find analytical expressions for the scattered field in the special case where DQD and resonator are tuned to resonance, we take the analogy to the case of a two-level system embedded in a waveguide, c.f the supplementary material of Ref. [215]. For exact resonance between DQD and resonator, $\omega_r = \omega_q = \omega_0$, the eigenstates of the coupled system are $|\pm\rangle = \frac{1}{\sqrt{2}} (|0, e\rangle \pm |1, g\rangle)$. We are focussing on driving the transition between the total system groundstate $|0, g\rangle$ and one of the coupled eigenstates $|\pm\rangle$, analogous to the two-level system case. We diagonalise the total Hamiltonian of the resonator plus the DQD, and consider the relevant operators in the diagonal basis, when reduced to a subset of states, i.e. the total system groundstate $|0, g\rangle$ and either of the two maximally mixed eigenstates $|\pm\rangle$. For each of these transitions, we write the input-output relations in the SLH formalism analogously to the case of a driven two-level system to find the reflectance of the $\lambda/4$ -type resonator in resonance with the DQD. For small drive amplitudes α far from saturation, we find to lowest order in α

$$r_\pm = \beta/\alpha = 1 - \frac{2\kappa_{\text{ext}}}{(\kappa_{\text{ext}} + \kappa_{\text{int}} + 2\Gamma_2 + 4i(\omega_0 - \omega_d \pm \frac{1}{2}g_0))}, \quad (\text{D.32})$$

where ω_d is the frequency of the drive field and g_0 is the coupling strength between resonator and DQD. As we assume perfect resonance between DQD and resonator, the two expressions differ only in the position of

the resonance. For resonant driving of either transition, i.e when $\omega_d = \omega_0 \pm \frac{1}{2}g_0$, r_{\pm} reduces to

$$\begin{aligned} r_{\pm, \text{res}} &= 1 - |S_{11}| = 1 - \frac{2\kappa_{\text{ext}}}{(\kappa_{\text{ext}} + \kappa_{\text{int}} + \Gamma_1 + 2\Gamma_{\varphi})} \\ &= 1 - \frac{\kappa_{\text{ext}}}{2\Gamma_{2, \pm}}. \end{aligned} \quad (\text{D.33})$$

Thus, the depth of the reflection peak on resonance is given by the ratio of the external coupling of the resonator to twice the total linewidth of the DQD-resonator hybridised states, $\Gamma_{2, \pm} = \frac{1}{4}(\kappa_{\text{ext}} + \kappa_{\text{int}} + \Gamma_1 + 2\Gamma_{\varphi})$, analogous to the case of scattering off a two-level system [215]. A plot of the visibility of the Rabi modes, extracted according to Eq. (D.33), is reported as a function of η in Fig. 5.4(f) in the main text and as a function of the renormalized coupling strength \tilde{g}_{\perp} in Fig. D.5(b).

D.5.5. Fits

Peaks from experiments are fitted to the Hamiltonian level structure, i.e. the position of levels in Eq (D.25). When fitting the full transmission curve as function of frequency, the SLH model is used, where for simplicity we set $\gamma_1 = 0$, as only the total DQD linewidth is relevant for these fits.

D.6. System Cooperativity

A high-fidelity technology must exchange information with preserved coherence, i.e., demonstrate the so-called strong-coupling regime. This criterion, which must be met for any useful quantum application, are characterized by a coupling between two subsystems that is stronger than the mean of the losses in both of them. Such, it is useful to introduce the cooperativity, $C = \tilde{g}_{\perp}^2 / [\Gamma_2(\kappa_{\text{ext}} + \kappa_{\text{int}})]$ to characterize the strength of a light-matter interaction in our hybrid system and to compare to what was already achieved for similar devices deployed in previous experiments [158]. The strong coupling regime corresponds to a cooperativity which is greater than unity. Thus, the coupling is strong in the sense that at resonance nearly every photon entering the cavity is coherently transferred into the matter system.

In Fig. D.5(a), we report the system cooperativity extracted for the eleven studied DQD configurations as a function of the dipole strength η .

We notice how despite increasing η increases the DQD decoherence rate Γ_2 (see Fig. 5.4), the cooperativity overall increases with η . This is in line with what is illustrated in the main part of the manuscript, where we reported that $\tilde{g}_\perp, \Gamma_2 \propto \eta$, therefore $C \propto \eta$. Making use of the described tuning strategy for the DQD electric-dipole strength, we push the limits for the cooperativity achieved for the semiconductor QD-resonator hybrid device above 100, representing the current record of cooperativity for a QD-resonator hybrid system. Furthermore, by adequately filtering the DQD gate lines, it has been shown that it is possible to keep a resonator linewidth < 1 MHz [105, 106], which, if implemented in our device, could allow achieving a cooperativity of up to $C \sim 1500$.

D.7. Renormalization of the coupling strengths (Eq. 5.13)

In the following, we describe the strategy used to renormalize the coupling strengths extracted from the eleven studied DQD configurations in Sec. 5.3 [see Eq. (5.13)]. Renormalization of the coupling strengths is necessary for comparison, because the hybridized spectra for the investigated DQD configurations are taken at not exactly the same resonator frequency and DQD tunneling amplitude (see Table D.1). The first term in Eq. (5.13), $2t_c/\omega_r$, originates from the mixing angle renormalization of the DQD dipole strength [17] [see Eq. (5.1)]. In Fig. D.6(a), we report a study of the coupling strength between a DQD and a resonator as a function of the resonator frequency. The data originates from a similar device with a nominally identical DQD coupled to a SQUID array resonator. The data is acquired by spectroscopically measuring avoided crossings between the resonator and the DQD charge qubit while keeping the DQD at its sweet spot ($\epsilon = 0$). The resonance frequency of the DQD charge qubit is changed systematically by changing its inter-dot tunneling amplitude t_c via the voltages applied to the depletion gates, and the frequency tunability of the SQUID array allows to bring the resonator into resonance with the charge qubit.

The extracted evolution of the coupling rate g as a function of the resonator frequency $\omega_r \sim \omega_q$ can be modeled accurately by a simple linear dependence [see blue dotted line in Fig. D.6(a)]. Instead, considering that $Z_r = 1/(\omega_r C_r)$, from Eq. (5.10), $g \propto \sqrt{Z_r} \omega_r \propto \sqrt{\omega_r}$ is expected assuming a simple lumped-element equivalent model of the resonator under the condition that the tuning process of the inter-dot tunneling rate does

neither appreciably modify the DQD electrical dipole moment nor its capacitive coupling to the resonator gate (DQD lever-arm). The linear scaling of g against ω_r suggests that other mechanisms take place in either the resonator impedance or the DQD electric-dipole moment during the tuning procedures of the inter-dot tunneling and SQUID array resonance. The change in tunnel rate or DQD shape could present a considerable influence on the magnitude of the electrical dipole moment of the DQD and thereby on the coupling strength. A complete understanding of these mechanisms will require further investigations.

Fig. D.6(b) shows a comparison of the extracted coupling strengths corrected for the mixing angle $g_0 = g\Delta/\omega_r$ and with the normalized $\bar{g}_\perp \propto g_0(5 \text{ GHz}/\omega_r)$ and $\bar{g}'_\perp \propto g_0\sqrt{5 \text{ GHz}/\omega_r}$. We notice that in our dataset, the correction originating from the normalization choice does not exceed 10% of the bare extracted coupling rates.

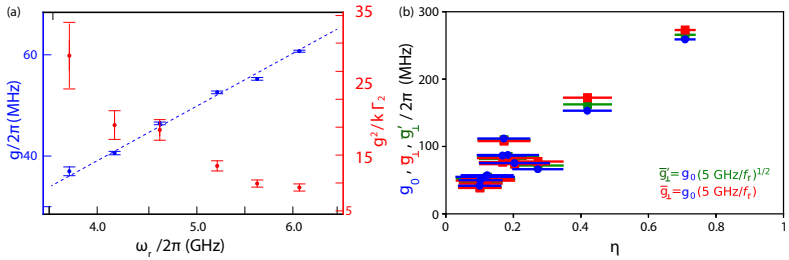


Figure D.6. (a) (Left axis) $g/2\pi$ extracted by measuring a Rabi mode splitting for the DQD qubit in resonance at $\epsilon = 0$ with the SQUID array fundamental mode, for different resonator frequency ω_r . (Right axis) system cooperativity, $g^2/(\kappa\Gamma_2)$, at different resonator frequency. During these measurements, the DQD system is kept at the sweet spot $\epsilon = 0$. (b) Comparison of the extracted coupling strengths corrected only for the mixing angle $g_0 = g\Delta/\omega_r$ with normalized $\bar{g}_\perp \propto g_0 \frac{5 \text{ GHz}}{\omega_r/2\pi}$ and $\bar{g}'_\perp \propto$

$$g_0 \sqrt{\frac{5 \text{ GHz}}{\omega_r/2\pi}}.$$

D.8. Additional data

Here, we report some additional measurements and datasets which the reader can find useful to better interpret the measurements reported in the main text.

Figure D.7(a) reports a study of a DQD configuration, distinct from the one reported in Fig. 5.5 in the main text. This new configuration has been obtained by *in-situ* tuning the DQD dipole strength to $\eta \sim 0.5$. The red (blue) line in Fig. D.7(b) represents a fit to the data obtained using the Rabi (JC) model from which we extract $g_{\text{R}}/2\pi = 350 \pm 3$ MHz ($g_{\text{JC}}/2\pi = 351 \pm 2$ MHz). A fit of a master equation model [solid orange line in Fig. D.7(c)] to the Rabi mode spectrum, obtained by changing the probe frequency along the DQD detuning value indicated by the black arrows in Fig. D.7(b), yields a splitting of $g/2\pi \sim 373.4 \pm 0.3$ MHz, with a DQD charge decoherence of $\Gamma_2/2\pi \sim 56.3 \pm 0.2$ MHz. For this DQD electrostatic configuration, the system is in the strong coupling regime ($g > \kappa/2 + \Gamma_2$), but comes with $g_{\text{R},\text{JC}}/\omega_{\text{r}} \sim 0.062$ which, despite being very high for a DQD-resonator hybrid device, does not promote the system in the USC regime.

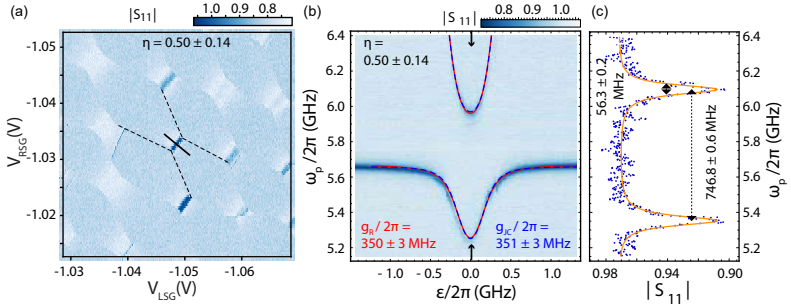


Figure D.7. Investigation of a configuration approaching the ultrastrong coupling regime for a DQD with $\eta \sim 0.50 \pm 0.14$ coupled to a JJ array. (a) Charge stability diagram of the DQD measured by monitoring the change in resonator reflectance amplitude $|S_{11}|$ for the extracted dipole strength $\eta \sim 0.50 \pm 0.14$. (b) Resonator amplitude response $|S_{11}|$ taken by varying the DQD detuning ϵ along the grey line indicated in panel (a) by applying properly chosen voltages to the two side gates. The red (blue) lines are independent fits to the Rabi (JC) model (see Appendix D.5).

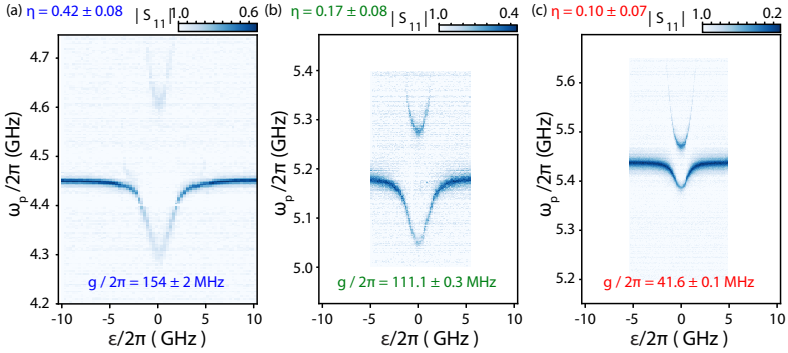


Figure D.8. Response of the SQUID array resonator reflectance amplitude $|S_{11}|$ vs. DQD detuning ϵ in correspondence of three distinct dipole strengths (a) $\eta \sim 0.42 \pm 0.08$ (blue), (b) $\eta \sim 0.17 \pm 0.08$ (green) and (c) $\eta \sim 0.10 \pm 0.07$ (red) [the corresponding DQD charge stability diagrams are reported in Fig. 5.2(e), (d) and (c)]. The three resonant spectrums are obtained by tuning the SQUID array in resonance with the DQD charge excitation frequency for $\epsilon = 0$. Data already reported in Fig. 5.3(a-c).

D

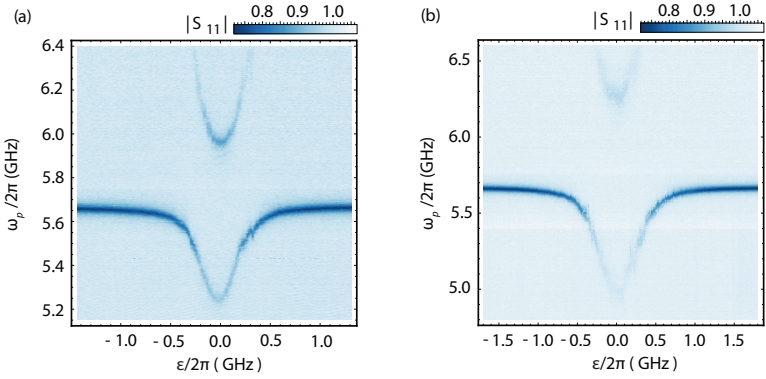


Figure D.9. Response of the Josephson junction array resonator reflectance amplitude $|S_{11}|$ versus DQD detuning ϵ in correspondence of a DQD configuration characterized by parameter (a) $\eta \sim 0.50 \pm 0.14$ and (b) $\eta \sim 0.72 \pm 0.08$. Data already reported in Fig. 5.5(b) and Fig. D.7(b).

E Supplementary information: **Charge-sensing of a GeSi nanowire double quantum dot**

This chapter provides supplementary information corresponding to Chapter 6 in the main text.

E.1. Additional data

In Figure 6.1 in the main text, we show the resonance curve of the resonator. When looking at a wider spectral range, which is shown in Fig. E.1, it becomes apparent that the resonance is superimposed on a large standing wave background. Nonetheless, the resonator can be identified by considering a temperature-dependence scan, because its resonance frequency depends on the the large temperature-dependent kinetic inductance. During the measurement of the data presented in Fig. 6.4 in the main text, several gate jumps occurred. These gate jumps results shifts along the V_{g2} -axis. In order to focus on the relevant physics, we have omitted those shifts in Fig. 6.4. Fig. E.2 shows the complete data set where white annotations highlight which data was omitted in Fig. 6.4 (see caption of the figure).

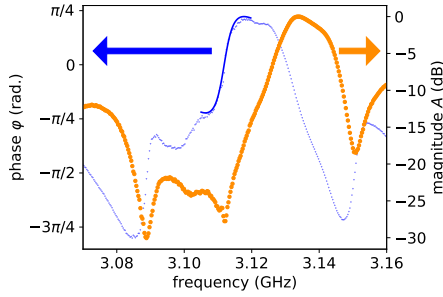


Figure E.1. Transmission through the feedline in wide frequency range

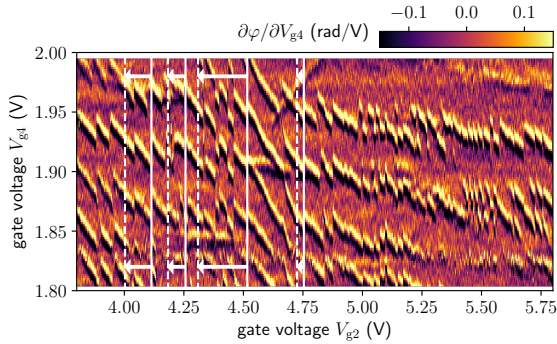


Figure E.2. Resonator response as a function of gate voltage V_{g2} and V_{g4} . This data set was used to create Fig. 6.4. The solid, white lines show the positions of the gate jumps. In Fig. 6.4, the data between the white, solid lines and the white, dashed lines, indicated by arrows, was omitted.

F Supplementary information: Dispersive interaction between a crystal-phase defined double quantum dot and a microwave photon

This chapter provides supplementary information corresponding to Chapter 7 in the main text.

F.1. Bias triangle

Figure F.1 shows the measurement of the current through the DQD shown in Figure 7.1 at a finite bias voltage of $V_{sd} = 250$ mV. A typical bias triangle is observed [97]. From the bias triangle, the detuning ϵ corresponding to the solid black line in the figure can be determined as $\epsilon = eV_{sd}/\hbar$.

F.2. Extracted capacitances of five inter-dot configurations

label	C_{L1} (aF)	C_{R1} (aF)	C_{L2} (aF)	C_{R2} (aF)	C_1 (aF)	C_2 (aF)	C_m (aF)
1	22 ± 2	3.3 ± 1.3	6.3 ± 1.5	12.8 ± 0.9	66 ± 16	53 ± 12	26 ± 9
2	22 ± 2	3.3 ± 1.4	5.7 ± 1.5	13.4 ± 0.9	102 ± 30	90 ± 30	30 ± 12
3	22 ± 1	2.8 ± 0.6	4.5 ± 1.2	12.3 ± 0.7	110 ± 30	100 ± 30	22 ± 8
4	22 ± 1	2.8 ± 0.5	2.9 ± 1.2	11.9 ± 0.7	110 ± 20	90 ± 12	22 ± 5
5	22 ± 1	2.7 ± 0.6	5.91.3	12.7 ± 0.8	84 ± 14	100 ± 20	10 ± 9

Table F.1. Extracted capacitances of the five different configurations.

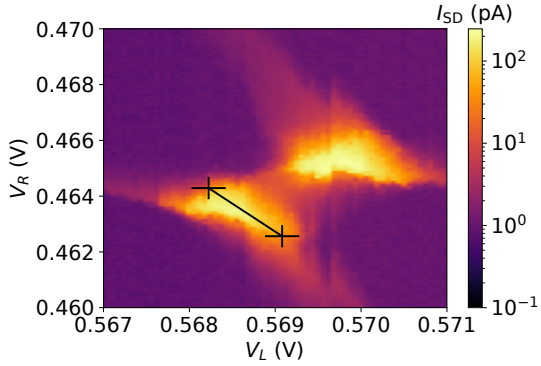


Figure F.1. Lever arm calibration from bias triangle. Current I_{sd} through the double-quantum dot (DQD) as a function of plunger gate voltages V_L , V_R at a bias voltage of $V_{sd} = 250$ mV. From the clearly visible bias triangles, the detuning $\hbar\epsilon = eV_{sd}$ can be read off (black line with error bars).

G Strong coupling between a single photon and a singlet-triplet qubit

This is the appendix to Chapter 8.

G.1. Resonator characterization and analysis

The resonator is fabricated from a thin-film NbTiN, sputtered onto a Si/SiO₂ (500 μm/100 nm) substrate [113]. The large sheet kinetic inductance of the NbTiN film of $L_{\text{sq}} \approx 90$ pH together with the narrow center conductor width of ~ 380 nm, and the large distance to the ground plane of ~ 35 μm results in the impedance value of 2.1 kΩ. The resonator can be dc biased using a bias line which contains a meandered inductor ensuring sufficient frequency detuning between the half-wave resonance used in the experiment and a second, low quality resonance mode at a lower frequency that forms due to the finite inductance of the bias line [105]. An optical microscopy image of a similar resonator is shown in Fig. G.1(a). One of the two resonator voltage anti-nodes is galvanically connected to gate SG_R shown in Fig. 8.1(c) of the main text.

We measure the transmission $S_{21}(\omega)$ of the resonator, to which we simultaneously fit the amplitude and phase of a Lorentzian:

$$|S_{21}|(\omega) = a_0 \cdot \frac{\frac{\delta_\omega}{2}}{((\omega - \omega_r)^2 + \frac{\delta_\omega^2}{4})}, \quad (\text{G.1})$$

$$\varphi(\omega) = -\arctan\left(\frac{\omega^2 - \omega_r^2}{\frac{\delta_\omega}{2}\omega}\right) + \varphi_0. \quad (\text{G.2})$$

From the fit (see Fig. G.1(b) in the extended data), we extract the resonator decay rate δ_ω and resonance frequency ω_r which we identify as the bare resonator decay rate $\kappa/2\pi = \delta_\omega/2\pi = 34.4 \pm 0.1$ MHz and resonance frequency $\omega_r/2\pi = 5.25308 \pm 0.00003$ GHz, respectively. In addition, we

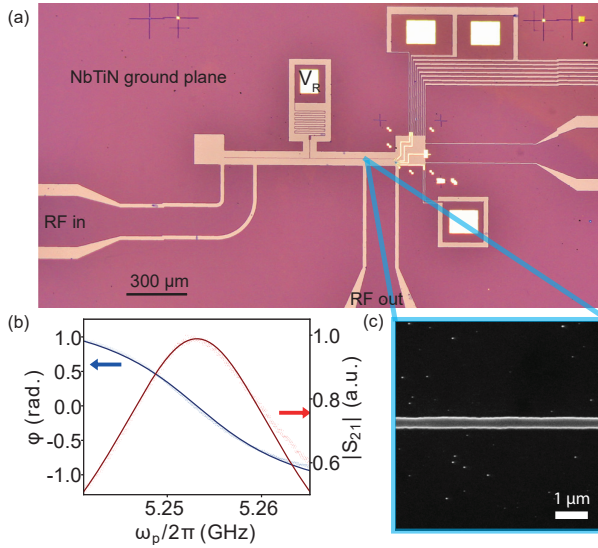


Figure G.1. Resonator of a similar device. (a) Optical microscope image of a similar device including the resonator. (b) Resonance curve of the resonator in phase (blue) and magnitude (red), as well as a fit to the data (black). (c) Same false-colored SEM image of the device as in Fig. 8.1(a). Scanning electron micrograph of the resonator center conductor of a similar device

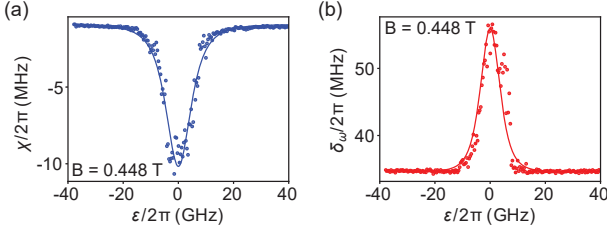


Figure G.2. Dispersive shift and dressed linewidth extraction. Extracted dispersive shift χ (a) and dressed resonator linewidth δ_ω (b) as a function of detuning ϵ of the even configuration at 0.448 T.

extract the transmission amplitude a_0 and phase offset φ_0 to calibrate our system. Gate voltages are converted to DQD detuning by using the lever arm $\alpha \approx 0.21$ eV/V ≈ 51 THz/V extracted from the Jaynes-Cummings fit to the anti-crossing shown in Fig. 8.3(a). This calibration allows us to convert a measured complex transmission $S_{21}(\omega)$ into a decay rate δ_ω and the frequency shift $\chi = \omega_r - \omega_r^0$ by numerically solving Eqs. (G.1) and (G.2) which results in Fig. 8.4(a) and Fig. G.2(a,b).

G.2. Charge parity determination

We measure the phase φ of the resonator transmission $S_{21}(\omega)$ as a function of detuning ϵ and magnetic field B at a readout-frequency $\omega_{\text{ro}}/2\pi = 5.253$ GHz close to the bare resonator frequency. A change in φ reflects the dispersive interaction between the resonator and two anticrossing levels of the DQD [17, 203]. Therefore, the non-zero phase response of the resonator tracks the position of the IDT along the detuning axis. The comparison of the magnetic field dependence of the position of the IDT to a Hamiltonian model of the DQD systems allows one to determine the charge parity [203, 216]. Figures G.3 (a) and (b) in the extended data show two typical low field IDT characteristics.

For an odd number of electrons (Fig. G.3(b)), the DQD resonance gate voltage V_R , at which the IDT is observed, disperses linearly with magnetic field starting from zero. This can be understood considering the Zeeman-splitting of the unpaired electron energy levels and two non-equal Landé

g-factors of the two dots. Fig. G.3(c) shows the energy level diagram of a one-electron Hamiltonian including Zeeman-splitting with a g-factor difference of 1.0 and spin-orbit interaction $t_{SO}/2\pi = 5$ GHz at a magnetic field of $B = 0.5$ T (green, dashed line in Fig. G.3(b)). The one-electron Hamiltonian is explicitly discussed in the supplementary material. The arrow points out the center of the IDT (largest curvature of the ground-state [217]) which corresponds to the largest dipole moment of the DQD and thus to the largest change in φ . This point shifts with B towards increasingly negative values.

For an even number of electrons in the DQD at zero field (Fig. G.3(a)), a single dip in phase is observed, but at a low magnetic fields, $B \approx 60$ mT, a double dip structure emerges as a function of ϵ (see supplementary material for details). This double-dip originates from an interaction between $S_{2,0}$, $S_{1,1}$ and $T_{1,1}^+$ as explained in detail in the supplementary material. The dependence of the IDT on magnetic field for an even number of electrons can be understood using an effective two electron Hamiltonian including spin-orbit interaction as described in more detail in section G.4. In Fig. G.3(c), we plot the energy levels at a magnetic field $B = 0.15$ T. In contrast to the odd filling, starting at zero field, the arrow marking the center of the IDT barely changes, consistent with our measurement. The double dip vanishes when further increasing the magnetic field, because of an increasing occupation of the polarized triplet states. Once the Zeeman energy of the triplet state $|T_{1,1}^+\rangle$ becomes comparable to the singlet charge tunneling t_C^S , the position of the IDT as a function of B disperses towards larger ϵ [175, 216, 218]. This transition is marked by the white dashed line at 0.2 T in G.3(a).

Based on the good qualitative agreement between our data and the one electron and two electron Hamiltonian, respectively, we can clearly identify the even and odd charge parities.

G.3. Jaynes-Cummings model

In the regime of only two DQD levels being relevant, we model the DQD Hamiltonian as an effective two-level system (qubit) interacting with a single photon in the resonator. The combined system is described by the Jaynes-Cummings model [219]. In which, a single excitation from the

ground state has the transition frequency [12]

$$\omega_{\psi_{\pm}} = \frac{\omega_r^0 + \omega_q}{2} \pm \frac{1}{2} \sqrt{4g^2 + (\omega_r^0 - \omega_q)^2}, \quad (\text{G.3})$$

with the qubit frequency $\omega_q = \sqrt{(2t(B))^2 + \epsilon^2}$ [191] and the effective qubit-photon coupling strength $g = g_0 \cdot 2t/\omega_q$, where g_0 is the bare qubit-photon coupling accounting for the mixing angle [12, 35]. In the experiments, we detect the transitions from the ground state to the predominantly photon-like dressed state $|\psi_{-}\rangle$. Its linewidth is given by

$$\delta_{\omega} = |\langle \psi_{-} | g, 1 \rangle|^2 \kappa + |\langle \psi_{-} | e, 0 \rangle|^2 2\gamma \quad (\text{G.4})$$

$$= \cos^2(\theta) \kappa + \sin^2(\theta) 2\gamma, \quad (\text{G.5})$$

where $\theta = \frac{1}{2} \tan^{-1} \left(\frac{2g}{\omega_q - \omega_r^0} \right)$ [12].

In order to extract the qubit tunneling rate t , and linewidth γ as well as qubit-photon coupling strength g , we simultaneously fit $\chi(\epsilon)$ and $\delta_{\omega}(\epsilon)$ using Eq. (G.3) and Eq. (G.5). An exemplary fit is shown in Fig. G.3(e,f).

G.4. Effective two-electron Hamiltonian model

We model an effective two-electron Hamiltonian in the presence of spin-orbit interaction and magnetic field. We write the Hamiltonian in the basis of singlet and triplet states $\{|S_{1,1}\rangle, |S_{2,0}\rangle, |T_{1,1}^{\pm,0}\rangle, |T_{2,0}^{\pm,0}\rangle\}$, with the subscripts indicating the charge distribution in the DQD. The Hamiltonian reads

$$\mathcal{H} = \mathcal{H}_0^S + \mathcal{H}_0^T + \mathcal{H}_Z + \mathcal{H}_{\text{so}}, \quad (\text{G.6})$$

with the spin quantum-number conserving Hamiltonians

$$\begin{aligned} \mathcal{H}_0^S / \hbar &= -\epsilon |S_{2,0}\rangle \langle S_{2,0}| + t_c^S |S_{1,1}\rangle \langle S_{2,0}| + \text{h.c.}, \\ \mathcal{H}_0^T / \hbar &= (\Delta_{\text{ST}} - \epsilon) \sum_{\pm,0} |T_{2,0}^{\pm,0}\rangle \langle T_{2,0}^{\pm,0}| + t_c^T \sum_{\pm,0} |T_{1,1}^{\pm,0}\rangle \langle T_{2,0}^{\pm,0}| + \text{h.c.} \end{aligned}$$

Here, $t_c^{S,T}$ are the tunnel rates between the two singlets, and between the two triplet states respectively, and Δ_{ST} is the single dot singlet-triplet

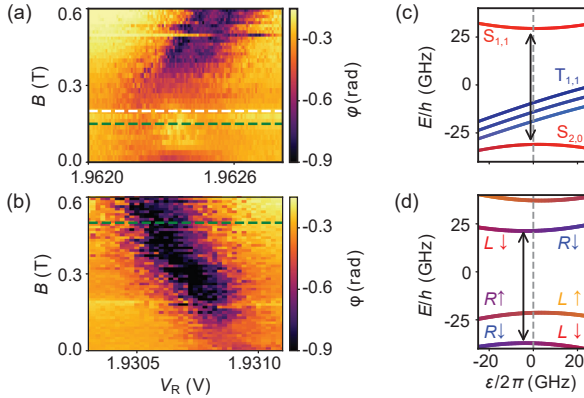


Figure G.3. Dispersive read-out at low magnetic field. Resonator phase in dependence of the right gate voltage V_R and magnetic field B for even (a) and odd (b) occupation of the DQD. For the odd occupation the IDT shifts to lower V_R from $B = 0$. The IDT of the even occupation stays nearly independent of magnetic field until around 0.2 T (white dashed line), from where it starts moving to more positive V_R . Energy level diagram for the even (c) and odd (d) configuration at 0.15 T and 0.5 T (green dashed line). The arrow marks the transition the resonator is sensitive to, where the ground state energy level has maximum curvature.

splitting that separates the $T_{2,0}$ states from the $S_{2,0}$ states. The Zeeman Hamiltonian is given by

$$\mathcal{H}_Z/\mu_B = B \sum_{\pm} \left(\pm \frac{g_l + g_r}{2} |T_{1,1}^{\pm}\rangle \langle T_{1,1}^{\pm}| \pm g_l |T_{2,0}^{\pm}\rangle \langle T_{2,0}^{\pm}| \right), \quad (\text{G.7})$$

where g_l (g_r) is the Landé g-factor of the left (right) dot. Because of the large intrinsic spin-orbit interaction in the NW, we include the spin-orbit Hamiltonian that couples the singlet and triplet states with opposite charge configuration using the spin-orbit tunnel rate t_{SO} as

$$\mathcal{H}_{\text{SO}}/\hbar = t_{\text{SO}} \left(|T_{1,1}^0\rangle \langle S_{2,0}| + \sum_{\pm} \pm |T_{1,1}^{\pm}\rangle \langle S_{2,0}| \right) + \text{h.c.}$$

G.5. Hamiltonian in the odd charge parity

In Section G.4, we elaborate on the Hamiltonian describing the double quantum dot (DQD) for an even charge occupation. This section provides the description for an *odd* number of electrons which is used in order to obtain Fig. G.3(d). In this case, the total electron spin is 1/2 which can be modelled by one electron with a half spin. This electron can reside either on the left dot or on the right dot [191]. Therefore, a suitable basis is $\{|L \uparrow\rangle, |L \downarrow\rangle, |R \uparrow\rangle, |R \downarrow\rangle\}$, where L/R denotes whether the charge resides in the left dot or on the right dot, and \uparrow/\downarrow denotes whether the spin is aligned parallel or anti-parallel with the magnetic field B .

The Hamiltonian describing the electron can be decomposed into three parts as

$$\mathcal{H}_{\text{odd}} = \mathcal{H}_{\text{odd}}^0 + \mathcal{H}_{\text{odd}}^Z + \mathcal{H}_{\text{odd}}^{\text{SO}} \quad (\text{G.8})$$

The first part of the Hamiltonian describes the spin-independent charge which can be written using the the charge Pauli matrices $\hat{\tau}_{x,y,z}$ as

$$\mathcal{H}_{\text{odd}}^0 = \frac{\hbar\epsilon}{2} \hat{\tau}_z + \hbar t_c \hat{\tau}_x. \quad (\text{G.9})$$

Here, the diagonal terms are proportional to the detuning $\hbar\epsilon = E_R - E_L$ which is the difference between the electro-static potential of the electron residing in the right and left dot. The off-diagonal terms are given by $\hbar t_c$, which is the spin-conserving tunnel rate.

In the presence of a magnetic-field, $\mathcal{H}_{\text{odd}}^Z$ comes into effect. This term describes the Zeeman energy of the electron and is given by

$$\mathcal{H}_{\text{odd}}^Z = \frac{1}{2}g_{L,R}\mu_B B\hat{\sigma}_z, \quad (\text{G.10})$$

where g_L and g_R are the site-dependent Landé g-factors, μ_B is the Bohr magneton and $\hat{\sigma}_{x,y,z}$ are the spin Pauli matrices. The Zeeman energy lifts the spin degeneracy and hence four spin-polarized levels are observed as shown in Fig. G.3(d). As explained in the Section G.2, unequal g factors $g_L \neq g_R$ result in a shift of the avoided level crossings originating from spin-conserving tunneling. This results in a slope of the observed inter-dot transition as a function of gate voltage (detuning) and field from zero field onward.

Spin-orbit interaction results in a spin-rotating tunneling amplitude t_{SO} entering the third part of the Hamiltonian as [101]

$$\mathcal{H}_{\text{odd}}^{\text{SO}} = \hbar t_{\text{SO}} \hat{\tau}_y \hat{\sigma}_y \quad (\text{G.11})$$

The spin-rotating tunneling amplitude results in a hybridization of the levels $|L \uparrow\rangle$ and $|R \downarrow\rangle$ and of the levels $|R \uparrow\rangle$ and $|L \downarrow\rangle$.

G.6. Singlet-triplet hybridization at low fields

In the main text, we explained the double-dip structure in ξ as a function of ϵ , which emerges at low field strength in Fig. 8.3(a) of the main text, by a finite hybridization between the singlet and triplet states at these field strengths. For making this feature more visible, Fig. G.4(a) shows a cross section through Fig. 8.3(a) of the main text at a magnetic field strength of 80 mT, which shows an asymmetry with respect to the detuning. Figure G.4(b) shows the corresponding linewidth of the dressed resonator. The level diagram for this situation is plotted in Fig. G.4(c) and exhibits an anticrossing of the singlet charge states $S_{1,1}$ and $S_{2,0}$ (red) close to zero detuning. At more negative detuning, the singlet $S_{2,0}$ and triplet $T_{1,1}$ states hybridize, as illustrated by the color gradient. These two different anti-crossing occurring at different detuning values, create an asymmetric double-dip resonator response when plotted as function of the detuning. The dip at more negative detuning is more pronounced due to the level splitting being closer to the resonance frequency.

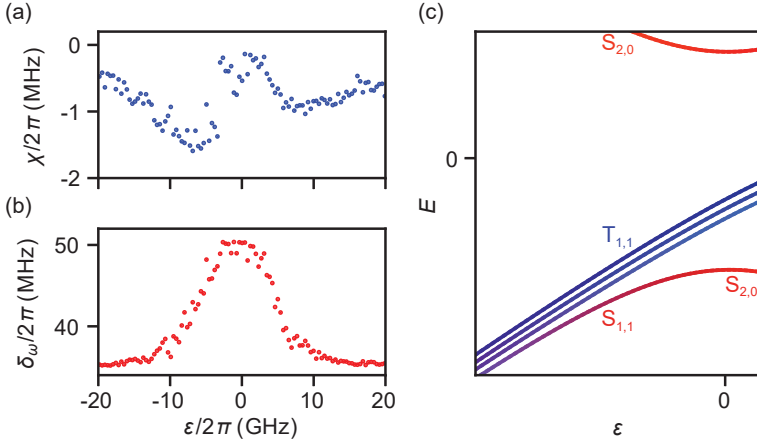


Figure G.4. Linecut through Fig. 4(a) at $B = 80$ mT. (a) Dispersive shift χ as a function of detuning ϵ . The data exhibits an asymmetric double-dip structure which is explained by the hybridization between the triplet and singlet states concurrently with the hybridization of the singlet charge qubit at different detuning values. (b) Linewidth $\delta\omega$ (full width at half maximum) extracted from the same trace. (c) Level structures using the fit parameters from the fit in Fig. 4(a) in the main text. Spin-orbit interaction couples $S_{2,0}$ and $T_{1,1}^+$. Because $S_{1,1}$ anti-crosses with $S_{2,0}$ due to spin-conserving tunneling, $S_{1,1}$ is dressed with $S_{2,0}$ when resonant with $T_{1,1}^+$. It therefore exhibits a second anti-crossing explaining the asymmetric lineshape observed in (a) and in (b).

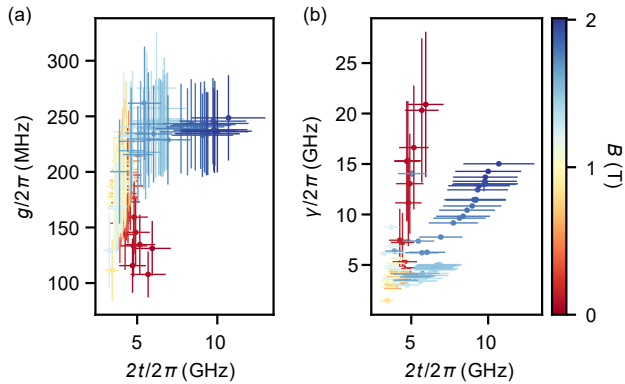


Figure G.5. Tunnel rate dependence of qubit linewidth and coupling strength. (a) Qubit linewidth γ as a function of interdot tunnel rate t . The color of the data points indicates the magnetic field strength B . No clear dependence is observed. (b) Spin-photon coupling strength g in dependence of the interdot tunnel rate t and magnetic-field strength B . Two different linear scalings are found (see text).

G.7. Linear dependence between tunnel rate and linewidth

Figure G.5 shows the qubit linewidth γ and the qubit-photon coupling strength g as a function of tunnel rate t and magnetic-field strength. The figure shows the same data as presented in Fig. 8.3 in the main text, plotting the extracted parameters one against another. We do not find a clear dependence of the coupling strength g on the tunnel rate t . However, the values of g saturate at ~ 250 MHz. In contrast the qubit linewidth γ saturates at low t and scales linearly as a function of tunnel rate for rates $2t/2\pi \gtrsim 6$ GHz. Two different linear dependencies are found for low fields ($B \sim 0.25$ T) where the singlet-triplet qubit acquires an increasing character of a singlet charge qubit ($S_{2,0}$ to $S_{1,1}$) for increasing tunnel rates and for large magnetic-fields where the singlet-triplet qubit acquires an increasing character as a triplet charge qubit ($T_{2,0}^+$ to $T_{1,1}^+$).

Curriculum Vitae

Jann Hinnerk Ungerer

Born on 4th November 1993 in Hannover (Germany)

Education

- 2018–2022 **PhD in Physics at University of Basel**
- Dissertation with Prof. Dr. C. Schönberger
"High-impedance circuit quantum electrodynamics with semiconductor quantum dots"
- 2016–2018 **Master of Science in Physics at ETH Zürich**
- Master's thesis with Prof. Dr. A. Wallraff
"Scaling up quantum dot-based qubits using a circuit QED architecture"
 - Project work with Prof. Dr. K. Ensslin
"Controlling Backscattering in the Quantum Hall Regime"
- 2013–2016 **Bachelor of Science in Physics at University of Göttingen**
- Bachelor's thesis at the Max Planck Institute for Dynamics and Self-Organization with Prof. Dr. U. Parlitz
"Intermittency in excitable media"
- 2013 **Abitur at St.-Ursula-Schule Hannover**
- 2010–2011 **Exchange student in Tlaxcala, Mexico**
- Scholarship by the Rotary Club Hannover-Luisenhof

Positions

- 2022 **Lecturer at University of Basel**
- *Physics III lecture* (Quantum and atomic physics)
- 2018–2022 **Teaching assistant at University of Basel**
- Main assistant for *Physics I* lecture in 2018, 2019, 2020 and 2021
 - Main assistant for *Physics III* lecture in 2022
 - *Quantum Transport* lecture in 2019
- 2014–2015 **Teaching assistant at University of Göttingen**
- Propaedeutic course of Mathematics for Mathematicians and Physicists

Extracurricular activity

- 2020 **Organizer of poly-e-fair 2020**
- [online job fair](#) (2281 participants)
 - organized in a team of 5 people
- 2019 **Organizer of NNCR QSIT Junior Meeting**
- [4 days conference](#) (44 participants)
 - organized together with Olivier Faist
- 2011-2013 **Member of Rotex 1800**
- Organizer of several seminars for Rotary exchange students from all over the world

Awards

- 2021 Head of winner team at PhD start-up challenge of the Swiss Nanoscience Institute
- 2021 [Nano Image Award 2021](#)
- 2020 [Nano Image Award 2020](#)
- 2019 Junior membership of the Swiss Nanoscience Institute

Publications

- “*Strong coupling between a microwave photon and a singlet-triplet qubit*”
J. H. Ungerer^{*}, A. Pally^{*}, A. Kononov, S. Lehmann, J. Ridderbos, C. Thelander, K.A. Dick, V. Maisi, P. Scarlino, A. Baumgartner, and C. Schönenberger
[arXiv:2303.16825 \(2023\)](#)
- “*Performance of high impedance resonators in dirty dielectric environments*”
J. H. Ungerer, D. Sarmah, A. Kononov, J. Ridderbos, R. Haller, L. Y. Cheung, and C. Schönenberger
[arXiv:2302.06303 \(2023\)](#)
- “*Charge-sensing of a Ge/Si core/shell nanowire double-quantum dot using a high-impedance superconducting resonator*”
J. H. Ungerer^{*}, P. Chevalier Kwon^{*}, T. Patlatiuk, J. Ridderbos, A. Kononov, D. Sarmah, E. P. A. M. Bakkers, D. Zumbühl and C. Schönenberger
[arXiv:2211.00763 \(2022\)](#)
- “*In situ Tuning of the Electric-Dipole Strength of a Double-Dot Charge Qubit: Charge-Noise Protection and Ultrastrong Coupling*”
P. Scarlino^{*}, **J. H. Ungerer**^{*}, D. J. van Woerkom, M. Mancini, P. Stano, C. Müller, A. J. Landig, J. V. Koski, C. Reichl, W. Wegscheider, T. Ihn, K. Ensslin, and A. Wallraff
[Physical Review X **12**, 031004 \(2022\)](#)
- “*’Recesion of ’Helgoland’ by Carlo Rovelli*” (in German)
J. H. Ungerer
[iX **1**, 140 \(2022\)](#)

- “Phase-dependent microwave response of a graphene Josephson junction”
R. Haller, G. Fülöp, D. Indolese, J. Ridderbos, R. Kraft, L. Y. Cheung, **J. H. Ungerer**, K. Watanabe, T. Taniguchi, D. Beckmann, R. Danneau, P. Virtanen, and C. Schönenberger
[Physical Review Research 4, 013198 \(2022\)](#)
- “Quantum computing: How to implement qubits” (in German)
[iX Special Quantencomputer \(2021\)](#) **J. H. Ungerer**
- “Crash course Quantum Mechanics” (in German)
J. H. Ungerer
[iX Special Quantencomputer \(2021\)](#)
- “Microwave photon-mediated interactions between semiconductor qubits”
D. J. van Woerkom*, P. Scarlino*, **J. H. Ungerer**, C. Müller, J. V. Koski, A. J. Landig, C. Reichl, W. Wegscheider, T. Ihn, K. Ensslin, A. Wallraff
[Physical Review X 8, 041018 \(2018\)](#)

* Equal contribution

Talks

- “Quantum computers”
Outreach event of the Swiss Nanoscience Institute, Basel (Switzerland), December 2022
- “Coupling a high-impedance resonator to crystal-phase defined quantum dots in a zincblende InAs nanowire”
[APS March Meeting 67, Y39.00009](#), Chicago (USA), March 2022
- “Coupling a high-impedance resonator to a crystal phase-defined double-quantum dot”
Winter School of the Swiss Nanoscience Institute, Zermatt (Switzerland), January 2022
- “Capacitive Coupling between an on-chip resonator and a semiconductor nanowire”
[Joint annual meeting of the Austrian Physical Society and Swiss Physical Society](#), Innsbruck (Austria), September 2021

-
- “*Coupling a Ge/Si quantum dot to a high-impedance resonator*”
NCCR SPIN Annual Meeting, Pontresina (Switzerland), August 2021
 - “*Spin Quantum Computers*”
Winter School of the Swiss Nanoscience Institute, online, January 2021
 - “*Quantum Computers*”
Meeting of the Rotaract club 'Zurich International', Zurich (Switzerland), January 2021
 - “*Circuit quantum electrodynamics architecture for semiconducting nanowires*”
Winter School of the Swiss Nanoscience Institute, Lauenen (Switzerland), January 2020
 - “*Having fun with quantum physics*”
Outreach event of the Swiss Nanoscience Institute, Basel (Switzerland), September 2018

Poster Contributions

- “*Coherent coupling between a microwave photon and spinful states of a crystal-phase defined double-quantum dot in a spin-orbit nanowire*”
5th International Conference on Spin-Based Quantum Information Processing, Pontresina (Switzerland), September 2022
- “*Coupling spin qubits to a high-impedance superconducting resonator*”
Site visit of the NCCR spin, Basel (Switzerland), November 2021
- “*Implementation of a circuit-quantum-electrodynamics architecture for qubit-photon coupling*”
Annual Event of the Swiss Nanoscience Institute, Lenzerheide (Switzerland), September 2021
- “*Capacitive Coupling between a resonator and a semiconductor nanowire*”
Swiss NanoConvention, online, June 2021

- “*Engineering of a semiconductor charge qubit coupled to a resonator – From coherence protection to ultrastrong coupling*”
737. WE-Heraeus-Seminar / Advances in Scalable Hardware Platforms for Quantum Computing, online, January 2021
- “*A circuit QED architecture for semiconductor nanowires*”
Annual Event of the Swiss Nanoscience Institute, Lenzerheide (Switzerland), September 2020
- “*Circuit QED for long-range spin-photon coupling using Ge-Si nanowires*”
5th School and Conference on Spin-Based Quantum Information Processing, San Sebastian (Spain), September 2019
- “*Circuit quantum-electrodynamics with semiconducting nanowires*”
Annual Event of the Swiss Nanoscience Institute, Lenzerheide (Switzerland), September 2019
- “*Circuit quantum-electrodynamics with semiconducting nanowires*”
The Capri Spring School on Transport in Nanostructures, Anacapri (Italy), May 2019
- “*Towards circuit-quantum electrodynamics with spins by means of magnetic-field resilient high-impedance superconducting resonators*”
Winter School of the Swiss Nanoscience Institute, Braunwald (Switzerland), January 2019

Acknowledgements

None of the work presented in this thesis would have been possible without the support of many exceptional people whom I would like to dedicate these lines to.

First of all, I would like to thank my PhD advisor Prof. Dr. Christian Schönenberger for being such a strong enabler and for making me the researcher I am today. Thank you for your continuous support, for sharing your passion for physics and science with me (not only, but also in many Monday morning meetings) and for creating such a pleasant work environment.

Moreover, I would like to thank the other members of my doctoral advisory committee Prof. Dr. Martino Poggio, Prof Dr. Ferdinand Kümmerth and Prof. Dr. Jason Petta for accepting this role and for the time you dedicate to reading my thesis (especially in the busy end-of-the-year period). I feel honored to have you as exceptional scientists in my doctoral advisory committee and I am looking forward to your comments from which this thesis will surely benefit.

My PhD work was kindly sponsored by the Swiss Nanoscience Institute of which I have had the great privilege to be part of. The scholarship has not only financially enabled my work, but during many amazing events, I had the pleasure to meet researchers working in different areas of nanoscience, many of whom also became friends.

I am very grateful to Dr. Joost Ridderbos for being such a great mentor and friend. Your joyful way of doing Science is an inspiration to me and I very well remember the countless nights that we spent together at the scanning electron microscope. Many thanks also to Dr. Artem Kononov who joined the project as a postdoc in the second half of my PhD. Thank you for the wonderful time, all the great discussions and fun that we had together!

Furthermore, I would especially like to thank Dr. Joost Ridderbos, Dr. Artem Kononov, Christina Reissel, Dr. Roy Haller, and Dr. Andreas

Baumgartner for proof-reading parts of this thesis. Dr. Roy Haller, you are also the one person to ask anything related to the clean room or cryostats in our lab and I owe you a big thank your for your help.

The work presented in this thesis is based on collaboration and Alessia Pally, Pierre Chevalier Kwon, and Luk Yi Cheung have been very close collaborators. Thank you not only for the great work, but for always keeping the mood up and being so fun to work with.

My thanks is extended to the whole 'RF team', to the group of Prof. Dr. Christian Schönenberger and to the former group members, in particular everyone not mentioned so far. I enjoyed working with all of you and sharing even our free time in form of barbecues at the Rhine, the group excursions and sports events like SOLA. Thank you for making my time in Basel very enjoyable!

Parts of this thesis were conducted in collaboration with the group of Prof. Dr. Andreas Wallraff at ETH Zurich and Prof. Dr. Pasquale Scarlino at EPF Lausanne. Thanks to both of you for not only sharing your broad knowledge about superconducting resonators and quantum bits with me, but also for providing the excellent infrastructure of your labs. You are great mentors and I enjoyed working with both of you a lot!

Further thanks to Peter Stano and Clemens Müller for the theory support, to Fabian Oppliger who has helped to set up experiments in a cryostat at EPFL and to Dario Marty who helped us with the wafer etching in the facilities of Paul Scherrer Institute.

The whole field of nanoelectronics would be non-existent without the crystals of very highest quality which are provided by marvellous scientist. Throughout my PhD I had the chance to work with GaAs substrates grown by Dr. Christian Reichl in the group of Prof. Dr. Werner Wegscheider. The Ge/Si core/shell nanowires reported in this thesis were provided by the group of Prof. Dr. Erik Bakkers. Moreover, Prof. Dr. Jesper Nygård and Dr. I-Ju Chen enabled me to work with hybrid aluminium/InAs nanowires. In the end, the experiments which we have performed on these nanowires did not make it into this thesis, but they will be used in future studies. The experiments which we performed based on crystal-phase defined double quantum dots were enabled by Dr. Sebastian Lehmann in the group of Prof. Dr. Kimberly Dick and Prof. Dr. Claes Thelander. Thank you for growing these amazing nanowires exactly tailored to our needs and for sharing your vast experience with us. I am grateful for the many discussions including Prof. Dr. Claes The-

lander, Prof. Dr. Ville Maisi, Dr. Sebastian Lehmann and Antti Ranni. They have pushed forward the experiments on crystal-phase defined double quantum dots reported in this thesis.

Throughout the time of my PhD I have had many insightful and fruitful discussions with very gifted scientists. In particular I would like to thank Dr. Simon Zihlmann, Dr. Mihai Gabureac, Prof. Dr. Andrea Hofmann, Dr. Andreas Baumgartner, Dr. Sergey Amitonov, Dr. Subhomoy Haldar, Prof. Dr. Valla Fatemi, Dr. Stefano Bosco, Prof. Dr. Romain Maurand and Prof. Dr. Christian Kraglund Andersen. Special thank you also to Prof. Dr. Dominik Zumbühl, Dr. Taras Patlatiuk and Raffael Egli from the Quantum Coherence Lab who are part of the very collaborative Basel Physics Department. The insights I got from these people have accelerated our research by a lot.

During a PhD, many things happen in the background. I would like to thank Patrick Stöcklin and Sascha Martin from the mechanical workshop for all the copper pieces which they manufactured for us and for the technical support. Moreover, thank you to Sascha Linder from the electronics workshop for the soldering of printed circuit boards. Thank you also to Michael Steinacher for his support with respect to the low-noise amplifiers.

A big thank you also goes to the administration team at University of Basel, in particular to Barbara Kammermann, Astrid Kalt, Claudia Wirth and Mile Mirkovic. Thank you also to Claudia Wirth and Klara Berg for their help in organizing the QSIT Junior Meeting.

A special thank you goes to the Master students Vera Jo Weibel and Reto Willi who I had the pleasure to supervise during my PhD. The thanks is also extended to Deepankar Sarmah who I mentored in the beginning of his PhD. I hope you learned as much from me as I did by supervising you!

On the other hand, I would like to thank my own teachers and mentors during my education at ETH Zurich. In particular, I would like to mention Prof. Dr. Klaus Ensslin and Prof. Dr. Thomas Ihn who sparked my interest in the field of Quantum Physics and Dr. David van Woerkom as well as Dr. Beat Bräm who have introduced me to the work as an experimental solid state physicist.

Last, but not least, I would like to thank my friends and family: I thank the CaPhy-Forscher for being a very great team during our Bachelor studies. Without you, I would probably not have gotten so far. Furthermore,

Acknowledgements

thank you to my house mates from Rotaryhaus Zurich for supporting me tremendously (not only with amazing food) during my masters program and the first two years of my PhD. Special thanks also to everyone, who helped babysitting my daughter during the last weeks of writing this thesis. Thank you to my parents for fostering my interest in science and always representing a safe haven. Finally, I thank my wife Christina Reissel for always pushing me to being a better version of myself, for her continuous and invaluable support and for being one of the most brilliant and inspiring physicists I know. Without all these people I would not be where I am today.

G